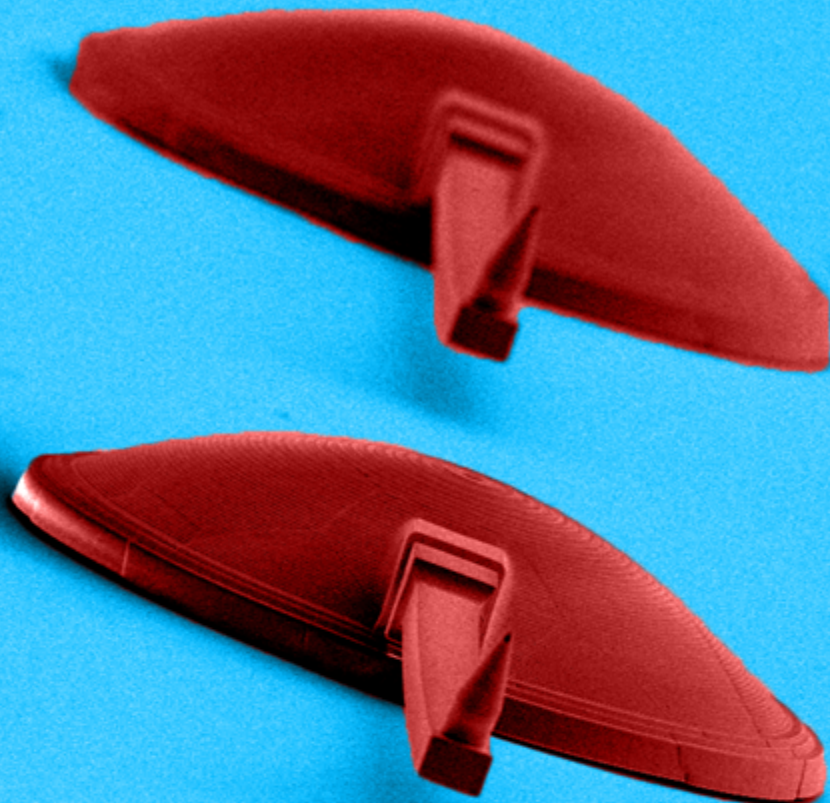


**Department of Precision and Microsystems Engineering
& Department of Biomedical Engineering**

Multiscale 3D printed polymer probes for single cell experiments

Pieter Frederik Jacobus van Altena

Report no : 2021.077
Coach : dr. M.K. Ghatkesar
dr. ir. E.L. Fratila-Apachitei
dr. ir. L. Angeloni
dr. ir. T. Manzanegue
Professor : dr. M.K. Ghatkesar
Specialization : Micro and Nano Engineering
Type of report : Master thesis
Date : 14 October 2021



2021

Multiscale 3D printed polymer probes for single cell experiments

**A rapid prototyping method to fabricate
microfluidic atomic force microscopy
cantilevers for single-cell studies**

by

Pieter Frederik Jacobus van Altena

in partial fulfilment of the requirements for the degree of Master of Science
in Mechanical Engineering,
at the Department of Precision and Microsystems Engineering,
and the Department of Biomedical Engineering,
of the Delft University of Technology.
To be defended publicly on Thursday, October 14, 2021 at 13:00 CEST.

Student number: 4233735
Defence Date: 14-10-2021
Thesis Supervisors: dr. M.K. Ghatkesar, TU Delft, First Supervisor (PME¹)
dr. ir. E.L. Fratila-Apachitei, TU Delft, Second Supervisor (BME²)
dr. ir. L. Angeloni, TU Delft, Daily Supervisor (PME¹)
dr. ir. T. Manzaneque Garcia, TU Delft, Daily Supervisor (PME¹)

*This thesis is confidential and cannot be made public until December 31, 2022.
An electronic version of this thesis is available at <http://repository.tudelft.nl/>*

¹ Department of Precision and Microsystems Engineering (PME)

² Department of Biomedical Engineering (BME)

Abstract

The nucleus regulates almost all the activities of the cell. Errors in the genetic code within the nucleus can disrupt its regulatory process and cause irreparable cell damage to the cell. If the damage is too severe, the cell may die, eventually leading to impaired tissue function.

An example of a medical condition in which this genetic malfunctioning is at play is Facioscapulothoracic muscular dystrophy (FSHD). This hereditary disease causes the skeletal muscle tissue to break down, leading to increasing physical impairments. A cure to effectively stop or reverse the symptoms of this genetic disease has not yet been found. Treatments and devices that are currently available can only alleviate the symptoms.

Biomechanical technologies may provide new possibilities to research a cure. Since FSHD originates from the cell's nucleus, it is necessary to isolate it to study this organelle's characteristics in greater detail. This will provide a better understanding of the cascade of events that lead to the cell's malfunctioning. However, the fact that skeletal muscle cells are multinucleated and only a limited number of nuclei are affected by the disease makes it even more challenging to understand and subsequently treat this condition. Therefore, it is necessary first to target and isolate one specific nucleus to study its characteristics. The behaviour of the cells without the disrupted nucleus can be studied in the second instance. At the core of this research is the technology to subtract a nucleus from a living cell while keeping the cell alive.

So far, efforts to remove the nucleus while keeping the cell alive have not been successful. Therefore, a mechanism is needed to remove a nucleus intact, ideally without causing permanent damage to the cell. This tool could then be used to understand the principles behind FSHD and multinuclear systems.

An existing tool to study single cells is FluidFM. FluidFM uses microfluidic AFM cantilevers in combination with an atomic force microscope (AFM) to aspirate and dispense fluids from or into cells. The microfluidic cantilevers have an internal channel that can be connected to a microfluidic pressure controller and have a sharp tip with an aperture. The AFM allows for precise force feedback during experiments, while the microfluidic pressure controller allows for precise fluid handling. The combination of force feedback and fluid manipulation provides an excellent advantage for single-cell experiments. These single-cell experiments contribute to a better understanding of cell behaviour and phenotype. More importantly, they help us understand diseased cells and find new cures for a variety of diseases.

Typically, microfluidic AFM cantilevers, used for single-cell experiments, are fabricated using classical micromachining techniques and then bonded to a microfluidic interface. This is an expensive approach with limited design freedom. More importantly, state-of-the-art microfluidic AFM cantilevers cannot be used for total nucleus removal.

In this study, two sequential 3D printing methods are used: high-resolution (resolution of 250 nm) two-photon polymerization (2PP) printing to fabricate hollow sharp-tipped microfluidic AFM cantilevers and direct light processing (DLP), which has a lower resolution of 30 microns but can print larger volumes relatively quickly, to fabricate microfluidic interfaces. The combination of printing methods enables the fabrication of devices that can be used for cell puncture experiments and cell nucleus aspiration using the FluidFM technique.

The DLP printed microfluidic interfaces have three main roles. It serves as a substrate for the two photon polymerization printing (2PP), allows for handling and mounting of the 2PP print on an AFM system, and connects the microfluidic pressure controller to the 2PP print. The latter was achieved using a technique that does not require adhesives but results in a connection that can withstand high pressures (tested up to 6.9 bar). By optimizing and coating the DLP prints, highly automated 2PP printing was achieved, enabling rapid prototyping of 3D-printed microfluidic AFM cantilevers.

The design for 2PP printing consists of three modules, namely a dome, a cantilever, and a sharp tip. Each of these modules is printed with different settings. The modular design of the probe allows for easy design adjustments, design flexibility, allows the technique to be used for different types of cell experiments, including cell adhesion studies, but more importantly, allows the print settings to be

changed for each part of the print. An intermediate dome structure was printed to connect the cantilever to the microfluidic interface. The hollow cantilever was printed attached to the side of this dome, with a length of $500\mu\text{m}$, a height of $20\mu\text{m}$, and a width of $30\mu\text{m}$. The cantilever has a continuous elliptical channel with a height of $15\mu\text{m}$ and a width of $25\mu\text{m}$. These cantilevers have a stiffness of 1.84 ± 0.24 N/m. Sharp tips were achieved with a tip radius of 270 nm . An elliptical aperture, with a width of $3.1\mu\text{m}$ and a height of $3.8\mu\text{m}$ was created next to the apex of the tip.

These 3D-printed microfluidic AFM cantilevers were used to successfully demonstrate AFM surface imaging, cell membrane puncturing, fluid dispensing and aspiration, nucleus aspiration, and cell adhesion studies. The printing methods can be used to fabricate various types of suspended microfluidic devices to perform single-cell biopsy and biophysical characterization of single-cells.

Preface

Since the beginning of my thesis, the world has been under the spell of the COVID-19 pandemic. With an almost complete disruption of daily life activities, the world has experienced times rarely seen before. In retrospect, performing this research has helped me get through the times of lockdown, stay fascinated, keep me in touch with friends, and make new friends.

I would like to express my sincere gratitude to my supervisors Murali Ghatkesar, Lidy Fratila-Apachitei, Livia Angeloni and Tomas Manzaneque Garcia, for their supervision but most of all for their cooperation, discussions and help during my thesis. Without them, this research would not have been possible. They inspired me to get the best out of this research and not quit when things did not work out as planned. They also inspired me to continue working in academic research.

I would like to thank Anita van den Heuvel for her efforts and flexibility in providing the cells for experiments and answering all my biologically related questions. Without these supervisors' enthusiasm, ideas, guidance, and discussions, this research would not have been possible.

Although the pandemic resulted in the university being almost completely closed for students and staff, the department's flexibility and resourcefulness helped me continue my research. Without the efforts of the Department of Precision and Microsystems Engineering (PME) and Biomedical Engineering (BME), the continuation of my research would not have been possible.

My sincere thanks to the technical staff of PME, Rob Luttjeboer, Spiridon van Veldhoven, Patrick van Holst, Gideon Emmaneel and Bradley But, for their technical support during my thesis. I would like to thank the PME staff and students for the fruitful discussions during the weekly meetings. In particular, I want to thank Ahmed, Dan, and Saleh for their help on the 3D printing aspects and the conversations on the nonwork related topics.

I would like to express my gratitude to my friends Pieter, Dirk, Damla, Rutger, Chelsea, Brian, Bogdan, Qais, Niek G., Niek R., Sofeke, Jikke, Niels and Remie, for their discussions, support and help.

My research would have been impossible without the aid and support of my family, who have supported me throughout my studies and were there for me in the good and bad times. Without them, I would never have gotten this far in life, and would never have been able to become the third generation at TU Delft without them.

I want to thank our family dog Puck for her unconditional love and support over the past 17 years. Sadly, she is not here to see my graduation, but Loeki will do the honours on her behalf. I would like to thank Loeki for the inspiring walks we had over the past months, which definitely led to some new printing ideas.

Last but not least, I would like to thank my girlfriend, Emily, who still motivates me every day to get the most out of myself.

As this research would not have been possible without the people mentioned above, I would like to end with a quote from Sir Isaac Newton: *"If I have seen further, it is by standing upon the shoulders of giants."*

*Pieter Frederik Jacobus van Altena
Delft, October 2021*

Contents

Abstract	ii
Preface	iii
Contents	v
List of Figures	xii
Nomenclature	xiii
List of Abbreviations	xiv
List of Derived SI units	xv
Division PME - BME	xvii
1 Introduction	1
1.1 Background & motivation	1
1.2 Report outline	2
I Literature review	3
2 The link between FSHD and the nucleus of the cell	5
2.1 Facioscapulohumeral Muscular Dystrophy	5
2.2 The genetic basis of the disease	5
2.3 Muscle Cells	7
2.4 Important components of the muscle cell	8
2.4.1 The Cell Nucleus	8
2.4.2 The Cell Membrane	10
2.4.3 Structure	10
2.4.4 Function	12
2.5 The cytoplasm	12
2.5.1 Cytosol	13
2.5.2 Organelles	13
2.6 Mechanical properties of cells	14
2.6.1 Mechanics of Cells	14
2.7 Penetrating the plasma membrane	15
2.7.1 Mechanics of the Nucleus	17
2.8 Self repair	17
2.9 Different applications for cell penetration devices	18
2.10 Preparation of the cell and nucleus	19
3 Micromechanical probes for single cell research	21
3.1 State of the Art	21
3.1.1 Classical glass pipette	21
3.1.2 Silicon pipettes	22
3.2 Silicon cantilever fabrication techniques	24
3.2.1 Silicon micromachining	24
3.2.2 Bulk micromachining	24
3.2.3 Surface micromachining	24
3.2.4 Nanofabrication	25
3.2.5 Limitations	25
3.2.6 Application of silicon micromachining in cantilevers	26

3.2.7	Polymeric pipettes	27
3.2.8	SU-8 micro cantilever pipette	27
3.2.9	2PP micro cantilever pipette	28
3.2.10	Other pipette types	30
3.2.11	Different applications of (hollow) cantilevers	30
3.3	Two Photon Polymerization	31
3.3.1	2PP method	34
3.3.2	Interface Finding	35
3.4	Digital Light Processing	36
3.4.1	Materials for DLP printing	37
3.4.2	DLP as 2PP substrate	37
3.5	Atomic Force Microscope	38
3.5.1	AFM modes	38
3.5.2	AFM actuation	40
4	Research question	41
	Bibliography	43
II	Paper	49
	List of figures included in the paper	51
1	Introduction	52
2	Materials and Methods	54
3	Results	60
4	Discussion	64
5	Conclusion	66
	References	68
	Outlook	69
	Thesis conclusion	69
	Recommendations	70
	Future work	72
III	Appendices	73
	Appendix A: Digital light processing (DLP)	75
A.1	Introduction	77
A.2	Workflow	77
A.3	Materials for DLP printing	78
A.4	Slicing	79
A.5	Design & print iterations	82
A.5.1	Test structures	82
A.6	Microfluidic interface	85
A.6.1	The AFM mounting	85
A.6.2	Microfluidic channel and aperture	89
A.6.3	Microfluidic coupling	92
A.6.4	Interface holder	95
A.6.5	Nanoscribe test substrates	98
A.6.6	Sample development holder	99

A.7	Developing	99
A.8	Parameters affecting the print	100
Appendix B: Two photon polymerization (2PP)		103
B.1	Introduction	105
B.2	Workflow	105
B.3	Materials and substrates for 2PP printing	106
B.4	Slicing	107
B.5	Design and print approach	108
B.6	Printing on top of a 3D printed substrate	109
B.6.1	Interface finding	109
B.6.2	Printing at the interface: parameter sweep	110
B.6.3	Chemical compatibility	114
B.7	Dome	114
B.7.1	Unique print parameters for the dome	117
B.7.2	Alignment of dome on aperture	118
B.7.3	Print results	119
B.8	Cantilever	121
B.8.1	Unique print parameters for the cantilever	123
B.8.2	2PP print results	127
B.9	Tip	130
B.9.1	Design	130
B.9.2	Describe for the tip	133
B.9.3	Dose test for the tip	134
B.9.4	Print results	135
B.9.5	Other tip ideas	139
B.10	Overview of final print parameters	141
B.11	Developing	142
B.12	Coding	143
B.12.1	Galvo acceleration	144
Appendix C: Atomic force microscopy (AFM)		145
C.1	Introduction	147
C.2	Protocol	147
C.3	Signal	148
C.3.1	Drift	148
C.4	Force curve on a flat substrate	149
C.5	Imaging	150
C.6	Flow from cantilever	152
C.7	Puncture	153
C.8	Aspiration	154
C.9	Adhesion	156
C.10	Measurement of the gold layer on prints	158
C.11	Recommendations	158
Appendix D: Laser Doppler vibrometer (LDV)		158
D.1	Introduction	159
D.2	Laser Doppler vibrometer	159
D.3	Frequency spectrum measurement	160
D.4	Power spectral density measurement	161
D.5	Influences on the measurement	163
Appendix E: Simulations - COMSOL		163
E.1	Introduction	165
E.2	COMSOL for mechanical characterization	165
E.3	COMSOL for fluidic characterisation	169
E.3.1	Laminar flow justification	169

E.3.2	Flow simulations	169
E.4	Comparison simulations and Polytec experiment	174
E.5	Influence of gold on the stiffness measurement	176
E.6	Recommendations	176

List of Figures

(2.1)	Affected Muscles FSHD	5
(2.2)	Mechanism at molecular level of FSHD	6
(2.3)	Fusion steps of myoblasts to myotubule	7
(2.4)	Fluorescence microscopy of myotubes	8
(2.5)	The nucleus of the cell	9
(2.6)	The bilipid layer	10
(2.7)	Schematic drawing of the structure of a cell	12
(2.8)	Optical and electron microscopy image of a cell	13
(2.9)	Three parameter solid model of a cell	14
(2.10)	Cell aspiration FEM simulation	15
(2.11)	Schematics of a cell puncture experiment	15
(2.12)	Cell puncture force	16
(2.13)	Typical force curve of cell puncture experiment	16
(2.14)	Penetration of cell using a nanoneedle (side view)	17
(3.1)	Glass Pipettes	21
(3.2)	Nanofountain probe	22
(3.3)	Nanosyringe and Nanopipette	22
(3.4)	Cantilver tip manufactured using FIB	23
(3.5)	Microfluidic AFM cantilever using FIB	23
(3.6)	Steps in micromachining	24
(3.7)	Bulk etching	25
(3.8)	Nanofountain production flow chart	26
(3.9)	SU-8 cantilever production flow chart	27
(3.10)	SU-8 cantilever	28
(3.11)	2PP microfluidic AFM cantilever	28
(3.12)	2PP solid cantilever	29
(3.13)	2PP tip on silicon (nitride) cantilever	29
(3.14)	Cytosurge's FluidFM tip pickup of particles	30
(3.15)	Particle at aperture of cantilever	31
(3.16)	UV versus NIR absorption	32
(3.17)	Light intensity distribution and polymerization	33
(3.18)	2PP quantum mechanical scheme	33
(3.19)	2PP setup	34
(3.20)	Youngs modulus 2PP	34
(3.21)	Schematic 2PP setup	35
(3.22)	Zeiss Definite Focus 2	35
(3.23)	DLP setup	36
(3.24)	Schematic printing principle of the DMD used for DLP printing	37
(3.25)	Schematic principle of the AFM	38
(3.26)	AFM modes	39
(3.27)	Comparison between AFM modes	39

Appendix A: Digital light processing (DLP) Printing

(A.2.1)	EnvisionTEC workflow	77
(A.3.2)	3DM - HTM140V2 comparison	78
(A.4.3)	Support settings EnvisionTEC	79
(A.4.4)	Perfactory slicer	79
(A.4.5)	DLP print on the build plate	80
(A.4.6)	SEM image of DLP print roughness	80
(A.4.7)	Surface comparison DLP print	81

(A.5.8)	DLP square hole test	82
(A.5.9)	DLP circular hole test	83
(A.5.10)	Channel test print	83
(A.5.11)	Distance between aperture and edge test print	84
(A.5.12)	Array of 3DM microfluidic interfaces	84
(A.6.13)	BioAFM holder mounting	85
(A.6.14)	CAD model of microfluidic interface	85
(A.6.15)	Microfluidic interface drawing front view	86
(A.6.16)	Microfluidic interface drawing top view	87
(A.6.17)	Microfluidic interface drawing isometric view	87
(A.6.18)	Microfluidic interface drawing side view	88
(A.6.19)	Microfluidic interface drawing bottom view	88
(A.6.20)	Channel through the microfluidic interface	89
(A.6.21)	Influence of ceiling height on aperture	90
(A.6.22)	Close up of aperture	91
(A.6.23)	Smallest aperture	91
(A.6.24)	Microfluidic couplers	92
(A.6.25)	Microfluidic connector design principle	93
(A.6.26)	Microfluidic connector drawing	94
(A.6.27)	CAD render of DLP print assembly and real assembly	95
(A.6.28)	Schematic drawing of substrates in Nanoscribe holder	95
(A.6.29)	DLP print in Nanoscribe holder	96
(A.6.30)	SEM image of DLP printed supports	96
(A.6.31)	Holes in bottom of DLP print	97
(A.6.32)	Interface in holder with plateau	97
(A.6.33)	Schematic explanation of resin plateau	98
(A.6.34)	Side view of the interface holder	98
(A.6.35)	Various views of a substrate with slits	99
(A.6.36)	3D printed sample holders	99
(A.7.37)	Equipment used for DLP print development	100
(A.8.38)	Proper UV calibration of EnvisionTEC	101
(A.8.39)	Before and after calibrating EnvisionTEC	101
(A.8.40)	FEP Foil	102
(A.8.41)	Pixels in sliced image	102
(A.8.42)	Prusa SL1 print	103
 Appendix B: Two photon polymerization (2PP)		
(B.2.1)	Nanoscribe workflow	105
(B.3.2)	Nanoscribe parameters per objective	106
(B.4.3)	Slicing and hatching Describe	107
(B.4.4)	Block splitting in Describe	108
(B.6.5)	Scorching gold coating	109
(B.6.6)	Absorption intensity gold layer	110
(B.6.7)	2PP dose test on fused silica	110
(B.6.8)	2PP dose test on gold coated fused silica	111
(B.6.9)	2PP dose test on plasma treated gold coated fused silica	111
(B.6.10)	2PP dose test on 3DM Tough Clear	112
(B.6.11)	2PP dosetest on HTM140V2	112
(B.6.12)	2PP dosetest on HTM140V2 with blocks and domes	113
(B.6.13)	Recording dosetest data in Excel	113
(B.7.14)	Dome with baseplate on HTM140V2	114
(B.7.15)	Schematic aperture and influenced area	114
(B.7.16)	Ring printed around aperture	115
(B.7.17)	CAD drawing of dome	115
(B.7.18)	Dome drawing side view	116
(B.7.19)	Dome drawing top view	116

(B.7.20)	Dome drawing cross section	116
(B.7.21)	Dome drawing bottom view	117
(B.7.22)	Dome block splitting in describe	117
(B.7.23)	Dome block splitting rectangular versus hexagonal	118
(B.7.24)	Alignment of the dome with the aperture	118
(B.7.25)	SEM images of the dome	119
(B.7.26)	SEM images of cross section of the dome	120
(B.7.27)	Microscope images of the dome	120
(B.8.28)	Cantilever drawing side view	121
(B.8.29)	Cantilever drawing top view	122
(B.8.30)	Cantilever drawing isometric view	122
(B.8.31)	Cantilever cross section	123
(B.8.32)	Cantilever block splitting	124
(B.8.33)	Sawtooth cantilever	124
(B.8.34)	Cantilever block splitting angle	125
(B.8.35)	Cantilever dose test	125
(B.8.36)	Too high cantilever dose	126
(B.8.37)	Cantilever printing results	127
(B.8.38)	Cross section of cantilevers	128
(B.8.39)	Measured length of cantilever	129
(B.8.40)	Cantilever protruding further	129
(B.8.41)	2PP with hair as size reference	130
(B.9.42)	Schematic top view of tip on cantilever	130
(B.9.43)	CAD drawing of tip	131
(B.9.44)	Side view drawing tip	131
(B.9.45)	Front view drawing tip	132
(B.9.46)	Top view drawing tip	132
(B.9.47)	Cross section drawing tip	133
(B.9.48)	Tips with various settings in Describe	133
(B.9.49)	Comparison model, describe, and print	134
(B.9.50)	Array of tips - dose test	134
(B.9.51)	SEM images tip	135
(B.9.52)	SEM images of aperture at the tip	136
(B.9.53)	SEM images aperture and cross section tip	137
(B.9.54)	SEM images with tip dimensions	137
(B.9.55)	SEM images with tipless cantiliver for adhesion experiment	138
(B.9.56)	Tip visible on AFM	138
(B.9.57)	SEM images smallest printed aperture	139
(B.9.58)	Sliced images of alternative tips	139
(B.9.59)	Sealing nucleus in a vesicle	140
(B.9.60)	Bifurcated needle	140
(B.10.61)	Laser power and scan speed	141
(B.11.62)	2PP development workflow	142
(B.11.63)	2PP development sample holder	142
(B.12.64)	Files generated by Describe	143
(B.12.65)	Changes to datafile	143
(B.12.66)	Describe Job File	144
(B.12.67)	Print time with various galvo accelerations	145

Appendix C: Atomic force microscopy (AFM)

(C.2.1)	AFM protocol	147
(C.2.2)	Cell disposal and AFM cleaning procedure	148
(C.3.3)	Cantilever coating	148
(C.3.4)	Signal drift showing in a measurement	149
(C.4.5)	Force curves in air and liquid	149
(C.5.6)	Imaging using AFM in three modes	150

(C.5.7)	QI imaging	150
(C.5.8)	Imaging using AFM in QI mode	151
(C.5.9)	Imaging of cells using AFM in QI mode	151
(C.6.10)	Flow from aperture	152
(C.7.11)	Force curve of cell puncture experiment	153
(C.7.12)	Typical force curve of cell puncture experiment	153
(C.7.13)	Puncture experiment protocol	154
(C.8.14)	Rupture of a cell during aspiration	154
(C.8.15)	Enlarged nucleus removal	155
(C.8.16)	Nucleus removal	155
(C.8.17)	Partial nucleus removal	156
(C.9.18)	Adhesion experiment graph	157
(C.9.19)	Adhesion experiment cells	157
(C.9.20)	SEM images with tipless cantilever for adhesion experiment	157
(C.10.21)	Gold film thickness	158
Appendix D: Laser Doppler vibrometer (LDV)		
(D.2.1)	Polytec view of the cantilever	159
(D.2.2)	Polytec cantilever and laser view	160
(D.3.3)	Frequency spectrum Polytec in air	160
(D.3.4)	Frequency spectrum Polytec in vacuum	161
(D.4.5)	Polytec PSD measurement in air	162
(D.4.6)	Polytec PSD measurement in vacuum	162
Appendix E: Simulations - COMSOL		
(E.2.1)	Boundary conditions for cantilever simulation	165
(E.2.2)	Mesh of the cantilever	166
(E.2.3)	Simulated deflection of the cantilever	166
(E.2.4)	First mode of the cantilever	167
(E.2.5)	Second mode of the cantilever	167
(E.2.6)	Third mode of the cantilever	167
(E.2.7)	Fourth mode of the cantilever	168
(E.2.8)	Convergence plot of the COMSOL cantilever simulation	168
(E.3.9)	Channel for the COMSOL simulation	170
(E.3.10)	Mesh of the channel through the tip	170
(E.3.11)	Convergence plot of the COMSOL simulation (NL)	171
(E.3.12)	Convergence plot of the COMSOL simulation (GMRES)	171
(E.3.13)	Velocity simulation plot	172
(E.3.14)	Velocity simulation plot DLP print	172
(E.3.15)	Velocity simulation plot of cantilever channel	172
(E.3.16)	Pressure contour simulation plot of cantilever channel	173
(E.3.17)	Pressure contour simulation plot of tip channel	173
(E.4.18)	Comparison simulations and experimental data	174
(E.4.19)	25kHz cantilever data simulation	175
(E.4.20)	165kHz cantilever data simulation	175

Nomenclature

η	Damping coefficient
λ	Wavelength of photon
ν	Photon frequency
ω	Angular frequency
ω_0	Angular resonant Frequency
ω_i	Incident light optical frequency (angular)
ρ	Density
A	Area
E	Young's modulus
f_0	Resonant frequency
h	Planck constant
I	Moment of inertia
I_L	Intensity of the light
k_{eff}	Effective stiffness
m_{eff}	Effective mass
n	Refractive index
V	Volume
X	Auto spectral density
c	Speed of light in vacuum
f	Frequency
k	Stiffness
k_b	Boltzmann constant
m	Mass
T	Temperature

List of Abbreviations

1PP	One photon polymerization
2PP	Two photon polymerization
AFM	Atomic force microscope
AM	Additive manufacturing
ATP	Adenosine triphosphate
CAD	Computer-aided design
DiLL	Dip-in laser lithography
DLP	Digital light processing
DMD	Digital micromirror device
DNA	Deoxyribonucleic acid
ER	Endoplasmatic reticulum
FEBID	Focused electron beam induced deposition
FEM	Finite element method
FEP	Fluorinated ethylene propylene
FIB	Focussed ion beam
FluidFM	Fluidic force microscopy
FSHD	Facioscapulohumeral muscular dystrophy
GMRES	Generalized minimal residual method
ID	Inner diameter
LDV	Laser Doppler vibrometer
LPCVD	Low-pressure chemical vapour deposition
MEMS	Microelectromechanical system
NIR	Near-infrared
OD	Outer diameter
PI	Photoinitiator
PSD	Power spectral density
RNA	Ribonucleic acid
SEM	Scanning electron microscope
SLA	Stereolithography apparatus (also known as SL)
SLE	Selective laser etching
SOI	Silicon on insulator
SMR	Suspended microchannel resonator
SR	Sarcoplasmatic reticulum
UV	Ultraviolet

Derived SI Units

SI Derived Units of Length

Multiple	Name	Symbol
10^0	Metre	m
10^{-3}	Millimetre	mm
10^{-6}	Micrometre	μm
10^{-9}	Nanometre	nm

SI Derived Units of Volume

Multiple	Name	Symbol	Equivalent volume
10^0	Litre	L	dm^3
10^{-3}	Millilitre	mL	cm^3
10^{-6}	Microlitre	μL	mm^3
10^{-9}	Nanolitre	nL	$10^6 \mu\text{m}^3$
10^{-12}	Picolitre	pL	$10^3 \mu\text{m}^3$
10^{-15}	Femtolitre	fL	μm^3

Division High Tech Engineering & Biomedical Engineering

Part	Chapter	PME	BME
	Introduction	V	V
1) Literature review	The link between FSHD and the nucleus of the cell	–	V
	Micromechanical probes for single cell research	V	–
2) Paper	Paper	V	V
	Outlook	V	V
3) Appendices	Appendix A: Digital light processing (DLP)	V	–
	Appendix B: Two photon polymerization (2PP)	V	V
	Appendix C: Atomic force microscopy (AFM)	V	V
	Appendix D: Laser Doppler vibrometer (LDV)	V	–
	Appendix E: Simulations - COMSOL	V	–
V = involved	– = not or little involved		

Introduction

1.1. Background & motivation

Every cell in the human body is unique. Even if cells in certain tissues are morphologically and genetically identical, the individual cells can behave dramatically differently. These cell-to-cell variations can occur due to differences in cell development and cell cycles, genetic drift, transcription events, and the intrinsic stochastic nature of cellular processes [1]. Heterogeneity between cells can have important consequences for tissue function and health. It also makes the development of disease models extremely complex [2].

These disease models are needed to understand the mechanisms behind diseases and discover new cures targeting specific cells. Traditional cell experiments do not capture the individual characteristics of cells but rather show the average response of a population of cells [1]. Single-cell analysis tools are essential to study cells in tissues that are either genetically, functionally or compositionally heterogeneous [2]. These tools allow the behaviour of a single-cell to be explored, which is of paramount importance as a large number of biological and medical questions can be investigated using single-cell analysis [1].

State-of-the-art tools have been developed to perform single-cell experiments, but there is not yet a tool that can be used to remove a single nucleus from a living multinuclear cell. To develop these tools for single-cell analysis, knowledge of biological, physics, and technical aspects must be combined. By combining the knowledge of these fields in technological breakthroughs, scientific questions can be answered at a whole new level.

To create devices that can be used to study and manipulate cells, very fine structures are required. State-of-the-art devices are often fabricated using silicon micro machining techniques, which are based on repetitive steps such as mask application, layer depositing and chemical etching. This is a time-consuming and costly process with limited design freedom, and only limited design iterations are possible as new masks need to be made for every iteration.

A solution is needed that allows rapid and reproducible fabrication of probes for single-cell experiments. A production method is needed that provides larger design freedom and allows the fabrication of many different probe geometries to be produced.

Additive manufacturing (AM) is a rapidly growing technology that can overcome the limitations of conventional silicon microfabrication techniques. AM machines (commonly known as 3D printers or rapid prototyping machines) have enabled engineers to fabricate geometries that were often not feasible using traditional fabrication techniques. The last few decades have seen a rapid development of various deposition techniques that have allowed engineers to 3D print at a variety of scales, ranging from macro-scale objects down to nanometre-scale objects. Printer costs have also plummeted due to innovative machine and material designs, leading to greater availability and allowing researchers to use the techniques more broadly. The potential of 3D printing is still being explored by researchers around the world and by people at home.

Inexpensive fused deposition modelling (FDM) printers are available for anyone to experiment with 3D printing. More precise printers with smaller achievable feature sizes are mainly found in research institutes or companies. Researchers are exploring new combinations of machines, materials, and

printers that can replace (expensive) classical techniques and allow the production of a wide range of geometries that cannot be produced with existing techniques. One important 3D printing technology that can be used for single-cell experiments is two-photon polymerization (2PP). With achievable feature sizes in the range of tens of nanometres, the potential applications in cell biology are enormous. Using 2PP to fabricate instruments for single-cell analysis, which are currently made using classical micromachining techniques, allows researchers to customize and optimize the instruments for their specific experiments.

The use of high-resolution 3D printing technologies for scientific research provides low-cost and highly customizable tools for a wide variety of experiments. It allows researchers to customize the design to meet the requirements of each experiment and to fabricate the tools in house. 3D printing solutions for single-cell manipulation and cell puncture studies have barely been explored, and there remains a knowledge gap.

This work focuses on developing a fabrication process that can be used to produce tools for single-cell analysis while maintaining a high degree of design flexibility. The main focus of this research was to develop a multiscale 3D printed tool that can remove a nucleus from a multinucleated skeletal muscle cell, thus proving that the fabrication process can be applied for single-cell research.

The methods developed and the obtained results show that the foundations have been laid to develop a variety of 3D printed probes for single-cell experiments. These probes can be tailored for each experiment to answer scientific questions related to single-cell manipulation, injection, chemical or mechanical stimulation, puncture or (partial) aspiration. These tools can enhance precision medicine by creating a better understanding of the single-cells. The knowledge gained from single-cell experiments using 3D printed probes can help to select specific targets for new drugs.

Exploring the capabilities of high-resolution 3D printing for single-cell experiments can provide new insights and tools for performing experiments that are impossible with state-of-the-art tools.

1.2. Report outline

The goal of producing a functional multiscale 3D print for single-cell experiments can only be achieved through a thorough understanding of both the biological and technical aspects. Therefore, at the beginning of this research, a systematic literature review was conducted, investigating both the biological and technical aspects of single-cell studies. A summary of the literature review can be found in part 1.

Part 2 discusses the methods developed and the results obtained from this research, in a paper format. The research and 3D printing strategy are discussed, and the results of the experiments are presented. A variety of topics are addressed, including materials and methods, results, conclusion, and a discussion. Also included are the recommendations for future research. The paper should be seen as the core part of this report as it summarizes the essential parts of this research.

The appendices, in part 3, provide additional information to the paper. The appendices cover a variety of topics, from 3D printing to simulations. They show the steps taken during this research to optimize the design and manufacturing process and the pitfalls encountered. This part contains in-depth knowledge required for reproducing the results.

Part I

Literature review

2

The link between FSHD and the nucleus of the cell

2.1. Facioscapulohumeral Muscular Dystrophy

Muscular dystrophies affect the lives of many people on earth. These diseases, usually hereditary, often lead to a certain degree of loss of muscle strength, increasing disability, and sometimes body deformities. This is the result of the weakening and breakdown of muscle tissue, and in some diseases, the loss of nerve tissue [4]. Currently, most muscular dystrophies cannot be treated, sometimes slowed down, and in some diseases, the symptoms can be relieved by certain treatments.

Facioscapulohumeral Muscular Dystrophy (FSHD) is one of these inherited diseases and has a major impact on patients' lives. FSHD is the third most common inherited neuromuscular disease (after Duchenne and myotonic muscular dystrophy) [4, 5]. Studies have shown that the prevalence of FSHD ranges from 1 in 8,333 to 1 in 15,000 depending on the population [6]. The patients suffering from FSHD mainly develop weakness in the skeletal muscles of the face (facio), the muscles that move the shoulder bone (scapula) and the muscles in the upper arm (which position the humerus) [6]. In many patients, the first symptoms resulting from the weakening of these three muscle groups appear in their teens. However, the disease can also start and be diagnosed throughout the patient's lifetime [7]. It is important to note that FSHD does not usually affect the life expectancy of the patients. However, the side effects of FSHD (morbidity, 20% of the patients older than 50 being wheelchair bound and losing the ability to make a living), are linked to reduction in life expectancy [7].

In later stages of the disease, other skeletal muscles, typically in the abdomen and lower legs, may also be affected, leading to an abnormal posture and abnormal gait (e.g. foot drop). Figure 2.1 shows the muscles that are typically affected by FSHD.

The rate at which the disease progresses, the severity and the onset vary from patient to patient, ranging from slowly progressive with early-onset (infantile) to fast progressive with an onset around young adulthood [6]. In many of these patients, the symptoms become apparent in the muscles at the upper part of the body (cranial) and then progress downwards (caudal).

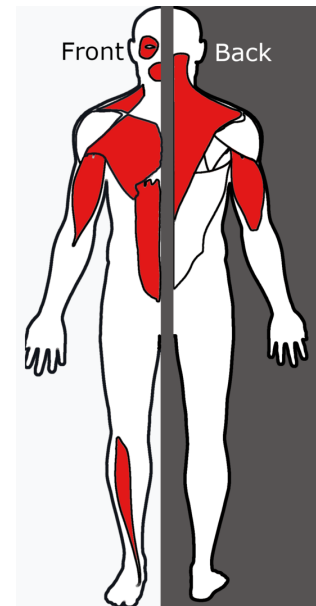


Figure 2.1: Muscles that are most often affected by facioscapulohumeral muscular dystrophy [3].

2.2. The genetic basis of the disease

The cause of FSHD can be traced back to the DNA, more precisely to the 4q chromosome [4]. Patients with FSHD lack a certain number of repetitive units (D4Z4) on this fourth chromosome. In healthy patients, between 11 and 150 of these repeating units are typically present (generally between 2 and 35) [6]. Normal amounts of D4Z4 units, in combination with a high degree of methylation, prevent

transcription of the DUX4 gene (DNA methylation represses the gene transcription). In healthy patients, this means the DUX4 locus is dormant.

However, in patients with FSHD type 1, the number of D4Z4 units is reduced to only 1 to 10 (due to contraction of the D4Z4 units) [6]. This contraction enables the transcription of the DUX4 gene (see figure 2.2). DUX4 is a transcription factor that can “turn on” a variety of other genes. These genes then initiate the production of the DUX4 protein and other proteins, causing toxic protein concentrations inside the cell. This eventually leads to cell death and, if it occurs in many cells, also muscle impairment. In FSHD2 (5% of the FSHD cases), the methylation level of the D4Z4 units is too low (hypomethylation), enabling the transcription of the DUX4 gene [4, 6].

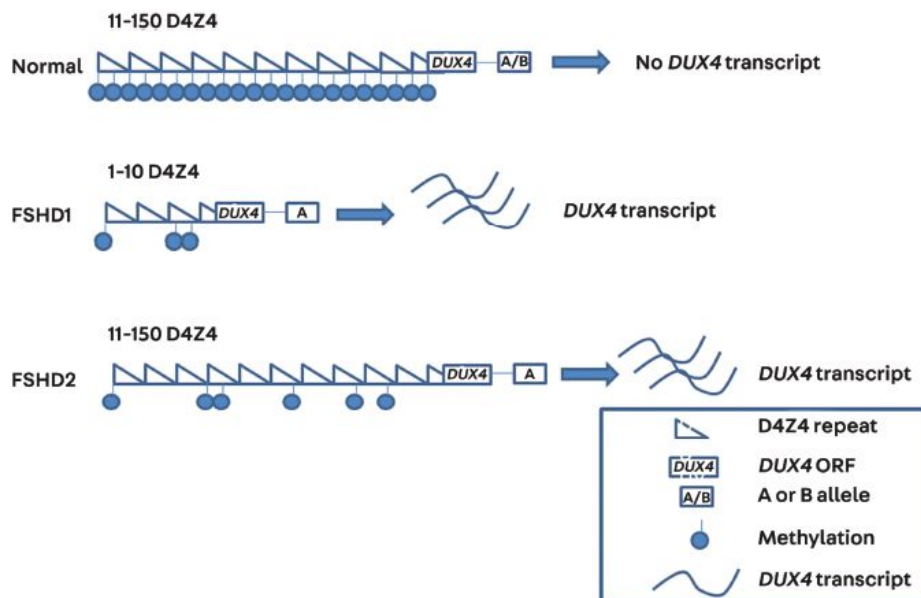


Figure 2.2: Mechanism behind FSHD at the molecular level. With contracted D4Z4 units (FSD1) and allele A or a low degree of methylation (FSDH2) and allele A, DUX4 can be transcribed. In healthy patients, enough D4Z4 repeats and methylation prevent transcription of the DUX4 gene [6].

The product of the DUX4 gene transcription in combination with the cascade of genes that are activated by the DUX4 leads to toxic amounts of proteins in the muscle cell. These toxic amounts lead to oxidative stress and induce apoptosis (self-induced cell death) [8].

In normal operation, DUX4 functions as a transcription factor (a protein that controls the transcription of DNA into mRNA) that specifically controls processes in the testis (e.g. germline and early stem cell development) [9]. This process is abnormal for muscle cells, and therefore it triggers apoptosis, as it recognizes it is not functioning correctly [8].

However, more research is needed to gain new insights into the mechanism that causes the pathological state of FSHD and find new biomarkers that can help uncover the basic principles of the disease. This could help to find a treatment or cure.

Rickard et al. [10] have shown that if only a few of the nuclei synthesize the DUX4 protein, the other nuclei are also affected (starts in a sentinel nucleus and spreads to neighbouring nuclei). It has been shown that only 1/1000 to 1/200 of the nuclei in a muscle cell show the DUX4 expression [11–13]. Rickard et al. [10] state: “DUX4 protein is present in a small subset of FSHD muscle cells, making its detection and analysis of its effects historically difficult”.

Therefore, it is interesting to investigate what happens if these nuclei are removed or replaced. That is one of the motivations for doing this research into the aspiration of a single nucleus from a cell. Understanding the mechanisms in this nucleus could lead to the development of drugs that target this specific nucleus. By stopping the secretion of the DUX4 protein and controlling the other processes caused by DUX4, one might delay or cure the disease. Ideally, one would be able to develop a cure that alters or destroys the specific nucleus. Studying the behaviour and response of an extracted nucleus could help find this cure.

2.3. Muscle Cells

Since FSHD occurs in the skeletal muscle cell (also called myocyte), it is important to understand the characteristics and features of this cell type.

The muscle cell has many of the general characteristics of a cell. It has similar organelles such as the ribosomes, the Golgi apparatus and the endoplasmic reticulum. However, some organelles are referred to differently when they are part of a muscle cell. For example, the cytoplasm in a muscle cell is called the sarcoplasm, the mitochondria are called the sarcosome and the plasma membrane is called the sarcolemma. The structure and composition of the muscle cell has some special (additional) features compared to other cell types so that the tissue can function as a muscle and exert forces.

The main function of muscle cells is to generate body movement [14]. The composition of the muscle cell is therefore specialized to produce this movement by enabling the contraction of the cell, which is carried out by the myofilaments (consisting of actin and myosin filaments). Other features inside the muscle cell that provide the muscle function are myofibrils, sarcoplasmic reticulum, and T-tubules [14, 15]. How these organelles work together to let the muscle cell contract is out of the scope of this research and will not be discussed in further detail.

There are three different types of muscle cells [14, 16]: skeletal muscle cells (attached to bones, voluntary muscle that we can consciously control, multinucleate), cardiac muscle cells (can only be found in the heart, involuntary contraction, uninucleate), and smooth muscle cells (mainly in walls of hollow organs, uninucleate). This work will focus on skeletal muscle cells, as these are affected by FSHD.

Skeletal muscle cells (also: myocytes) consist of fused myoblasts (early muscle cells with a single nucleus). This fusion creates a cell with multiple nuclei. The myocytes in turn, fuse together to form myotubule (the functional units of the muscle. Figure 2.3 shows the fusion steps from the myoblast to the myocyte.

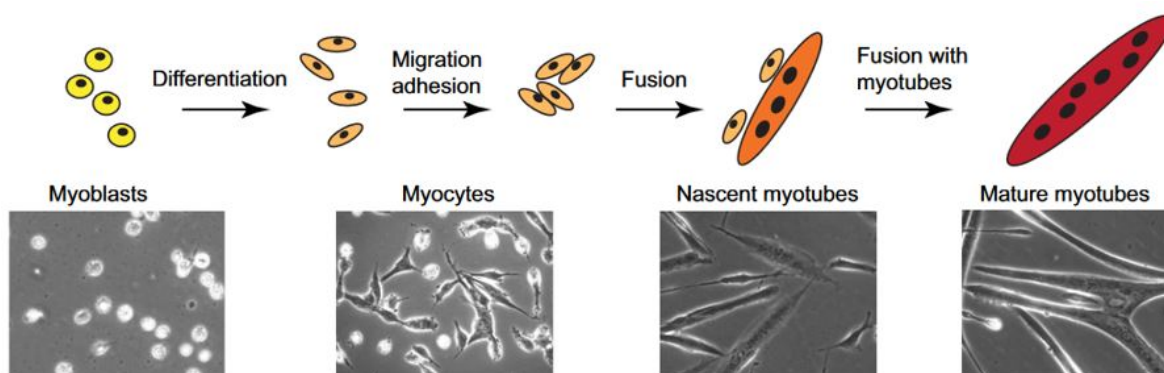


Figure 2.3: Myoblasts proliferate in medium containing growth factors (in-vitro). The myotube formation is initiated by removing the growth factors. This results in the majority of myoblasts to terminally differentiate into myocytes. The myocytes migrate, adhere and fuse to each other to form small myotubes with multiple nuclei [17].

The nuclei of the myocyte are distributed throughout the cell, which has an elongated shape [14]. The nuclei also have this elongated oval shape and are often called “myonuclei”. In the myotubes, the nuclei tend to come together in the widest part of the cell. The nuclei can be clearly be seen in figure 2.4.

The exact position of the nuclei, which are evenly distributed along the inner surface of the cell, results from cellular and nuclear movements [18]. Incorrectly positioned and functioning nuclei can lead to various muscle diseases (e.g. Duchenne muscular dystrophy and FSHD [18]). According to Perillo et al. [18], the position of each nucleus is critical to its function, and the cell attempts to restore displaced nuclei. If the cell fails to do this, diseases can occur that can be life-threatening or severely affect the quality of life. One such disease is FSHD, which explains why the skeletal muscle cell is of interest to this research. FSHD was discussed into more detail in section 2.1 and section 2.2.

It is important to elaborate on the size and shape of the muscle cell and its nuclei, as it sets the boundary conditions for this research. A human skeletal muscle consists of a bundle of muscle cells. These cells can range in size from 1 mm (stapedius muscle, in the middle ear) to 30 cm (sartorius muscle, along the thigh) [19]. The average muscle cell is usually about 30 mm long. The diameter

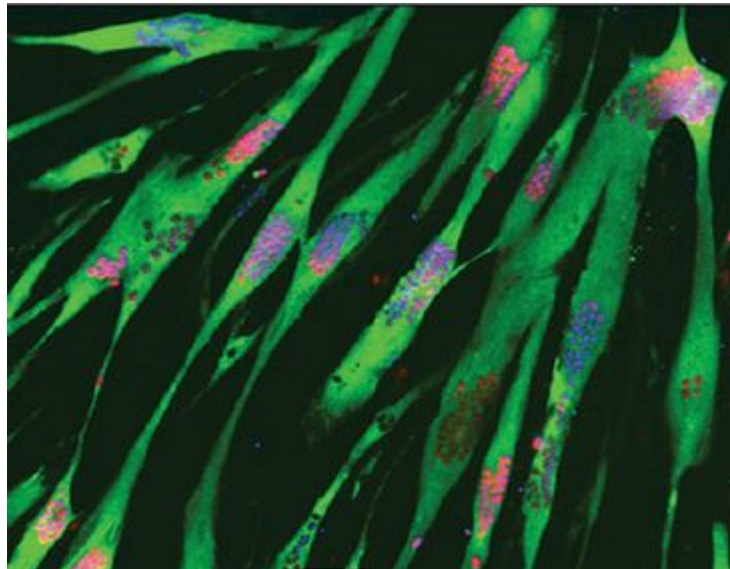


Figure 2.4: Fluorescence microscopy image of myotubes (green) with different protein binding sites used to stain nuclei. The DUX4 protein is stained red (no scale bar included in the original paper) [10].

of a muscle cell can vary between 10 and 100 μm [19]. Myocytes, grown in Petri dishes, are typically smaller than those in the human body.

In the skeletal muscle cell, the number of nuclei (arranged peripherally to maximize the internuclear distance [20]) can vary between a few and several hundred [19]. The shape of the nuclei is somewhat similar to that of the muscle cell (elongated ellipse) with an average length of the nucleus of about 11.75 μm and a cross-sectional area of 10.39 μm^2 [21]. Assuming that the cross-section has a circular shape, this would result in a diameter of approximately 3.6 μm . Assuming that the nucleus is a prolate ellipsoid, the volume can be calculated to be about 0.65pL.

There is little data on the average size of skeletal muscle cell nuclei. Kramer et al. [22] report that the average length of a myoblasts nucleus is around 10 μm , which is in the same range reported by Watkins et al. [21]. However, Watkins et al. [21] also show that the size of the nucleus is significantly affected in cells of patients with Duchennes disease. No data are available on the size of the nucleus in FSHD patients, which remains to be determined.

2.4. Important components of the muscle cell

Note in advance: this section discusses the components of the cell at a basic textbook level. This detail is required to understand the cell, establish boundary conditions and predict the response of a cell to a microfluidic AFM cantilever. However, this detail is not required to understand the rest of the report and can be skipped if the reader has basic knowledge of the components of the cell.

For cell puncture studies and nucleus aspiration studies, it is essential to understand the cell components that can affect the experiment. There are three important main cell components: the nucleus, the cell membrane and the cytoplasm.

2.4.1. The Cell Nucleus

The nucleus is the largest organelle of the cell, with a diameter ranging between 3 and 10 μm [15, 16, 23] (with an average size of 5 μm [14]). Note that many nuclei are oval rather than circular, and therefore, the length dimension can be larger. Often, the shape of the nucleus corresponds more or less to the shape of the cell. The nucleus is enclosed by two concentric lipid bilayer membranes, which together are called the nuclear membrane or nuclear envelope [23]. Within this envelope, most of the deoxyribonucleic acid (DNA) is contained. DNA is an extremely long polymer that encodes the genetic (hereditary) information of the organism. The nucleus is the control centre of the cell, controlling

the cell's activity, structure, and function. The nucleus controls the number of proteins synthesized in response to a specific signal and uses the information from the DNA to build the proteins.

Most cells contain only one of these nuclei, but some cells (e.g. liver and skeletal muscle cells) are multinucleated, meaning they have more than one nucleus [14]. Multiple nuclei are often associated with a larger volume of cytoplasmic fluid that needs to be regulated. There are also cells (red blood cells) that contain no nucleus (anucleate). A distinction can be made between three regions in the nucleus [14]: the nuclear envelope, the nucleolus, and the chromatin. This can be seen in figure 2.5.

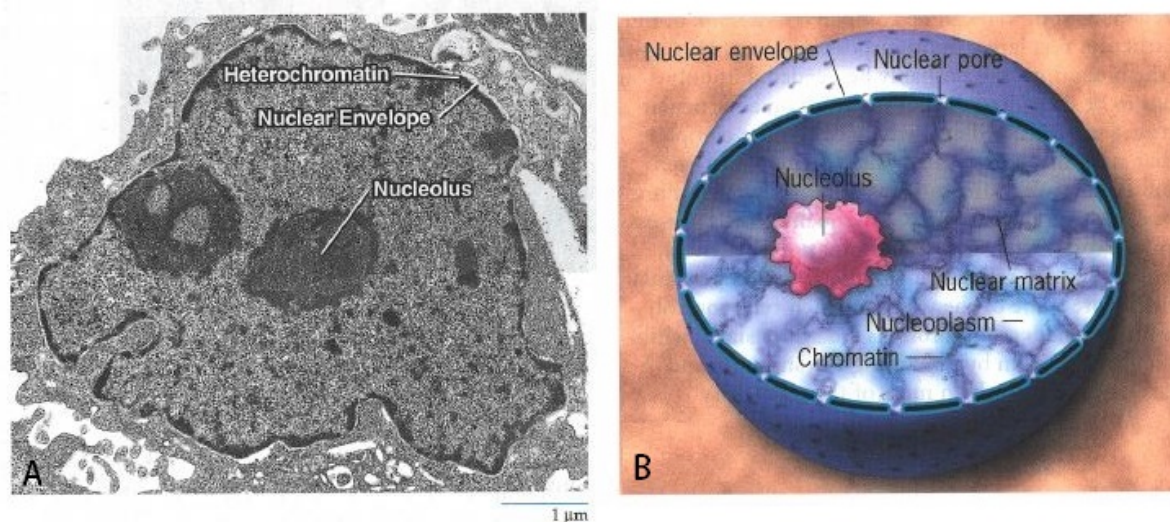


Figure 2.5: The nucleus of the cell, **A)** Optical microscopy image of the nucleus, **B)** Schematic drawing of the nucleus [15].

- **Nuclear envelope:** The nuclear envelope is a double membrane barrier with a distance between the membranes of about 10 to 50 nm [15]. In some places, the membranes are fused together and form pores. Proteins at these pores regulate the exchange of molecules between the cytoplasm and the nucleus [14]. There are often many ribosomes in the outer membrane of the nuclear envelope. The membrane itself is selectively permeable, but small molecules can pass much more freely than other membranes (due to the relatively large channels in proteins). The fluid inside the nucleus is enclosed by the nuclear envelope and is called the nucleoplasm. It contains dissolved nutrients, salts, ions, and other essential solutes. A network of thin protein filaments (nuclear lamina) provides mechanical support to the nuclear envelope [15].
- **Nucleoli:** Nucleoli are small, irregularly shaped bodies within the nucleus that produce ribosomal subunits [15]. The ribosomal subunits are transported to the outside of the nucleus, where they are assembled into ribosomes. The size of the nucleoli depends on the state of the cell. As the cell grows, the nucleoli will be large (they require large amounts of protein production for cell growth). If the cell has finished growing, the size of the nucleoli decreases. Typically, the nucleus has one or two nucleoli, but there can be more [14].
- **Chromatin:** Chromatin is about 30% DNA (genetic material), 60% globular histone protein (used as packaging and regulator of DNA), and 10% ribonucleic acid (RNA, "single-stranded nucleic acid composed of a polymeric chain of ribose containing nucleotides" [14, 15]). When the cell divides, the chromatin is coiled up into chromosomes (compact chromatin strands, this shape protects it from being torn apart during cell division) [14].

Understanding the nucleus can explain many of the processes that take place in the cell. Studying what goes in and what comes out of the nucleus can be very interesting for determining the cause of a disease and explaining certain cellular activities. The effects of specific genetic mutations can then be coupled with the cell nucleus's output of specific (messenger) proteins. The presence of these proteins can then be used to explain certain cell behaviour or malfunctioning. Especially in cells with multiple nuclei, it can be interesting to see how each nucleus affects the function of the cell. Studying the nucleus outside the cell could therefore offer great potential for understanding disease mechanisms.

It may also be valuable to see how a multinucleate cell responds to a removed or added nucleus. Currently, the only method to study a nucleus is to isolate it by breaking down the plasma membrane using detergents, leaving the nucleus in the medium. This method kills the cell and therefore prevents the study of the behaviour of the cell with the nucleus removed.

2.4.2. The Cell Membrane

The cell membrane (also called the plasma membrane) is the flexible outer surface of a cell that separates the internal environment (inside the cell) from the external environment (outside the cell). It consists of a lipid bilayer in which different types of proteins are embedded. It forms a selective barrier, that regulates the transport of material in and out of the cell. Additionally, it gives the cell its structure and plays a role in communication between cells and the environment.

The plasma membrane is a thin and flexible (yet fragile!) barrier between the intracellular fluid (inside the cell) and the extracellular fluid (outside the cell) [14]. It is an active barrier, i.e. it not only passively regulates whether molecules can pass through the barrier, but can also actively select whether a molecule can pass through the barrier at that moment (“as a pump”). Its function is provided by its unique structure, which is explained in section 2.4.3 [14]. The plasma membrane is only 5-10 nm wide, which making it impossible to see under an optical microscope (you can stack about 5000 membranes on top of each other to get the same thickness of the sheet of paper this is printed on) [15]. It took until the late 1950s before the plasma membrane could be resolved under the electron microscope with appropriate preparation and staining [15]. An important distinction must be made between the plasma membrane and the membrane that some organelles have. This membrane will be referred to as an internal membrane but will not be treated. The exact components of the plasma membrane and its functions will be addressed as relevant for this research (not in detail).

2.4.3. Structure

Plasma membranes are dynamic structures with constant activities on the surface and movements across and along the membrane. The plasma membrane consists of three main groups of components: lipids, proteins and carbohydrates [24].

The **lipids** (mainly phospholipids, but also cholesterol and glycolipids) are arranged in two closely opposed sheets [23]. The resulting combination of the sheets is called “the lipid bilayer” (see figure 2.6). This lipid bilayer forms the structural backbone of the cell and acts as a permeable barrier to most water-soluble molecules (by simple diffusion while preventing random movements of larger molecules in and out of the cell) [15]. The assembly of lipid molecules into sheets (and the combination of these sheets) occurs because the lipid molecules are amphipathic [15]. Amphipathic means that the molecule contains both a hydrophobic and a hydrophilic part. These amphipathic molecules are subjected to two main forces which conflict with each other [23]: the hydrophilic part is attracted to water, while the hydrophobic part is repelled by water.

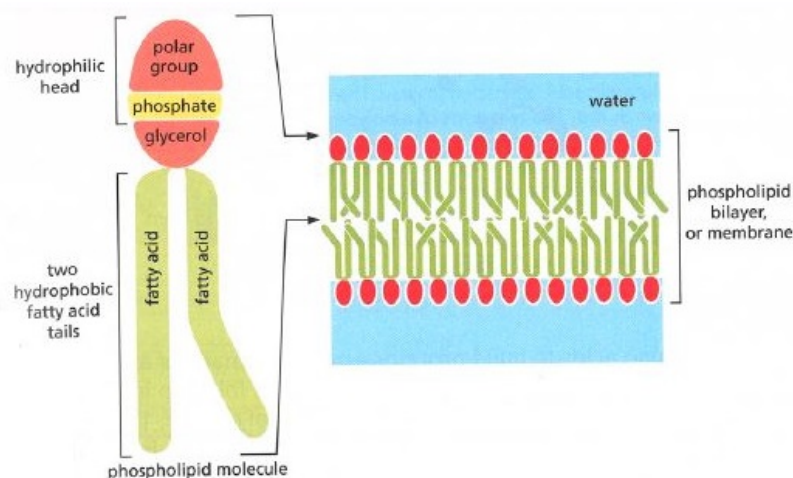


Figure 2.6: A schematic drawing of the bilipid layer of the plasma membrane. The hydrophilic head is attracted to the water, while hydrophobic tails are repelled by the water. The configuration of the bilipid layer is energetically most favourable [23].

To solve the problem of the conflicting forces, a bilayer is formed that is energetically most favourable and satisfies both the hydrophilic (facing the water on both sides of the layer) and the hydrophobic (shielded from the water by facing each other) parts. Because of these forces, the plasma membrane is self-sealing as it seeks to return to the most favourable energy state. When a rupture occurs in the plasma membrane, two situations can occur [23]:

- If the rupture is small, the rearrangement of the lipid molecules “pushes away” the water molecules, restoring the continuous sheet of lipids.
- If the rupture is too large, the plasma membrane may fold in on itself and disintegrate into several closed vesicles (often the end of the line for that cell, but the components can be degraded and the molecules reused).

Each cell type has its own characteristic composition of lipids in its bilayer, giving it specific properties required for the activities and function of that cell. The lipid molecules in the plasma membrane cannot leave the bilayer because of the water inside and outside the cell. If the lipid molecule would then leave the layer, higher forces would act on the lipid molecule, which results in an unfavourable energy state [23]. However, the lipids can move around in the plasma membrane and exchange places with other lipids. The plasma membrane can therefore be modelled as a flexible two-dimensional fluid, which is called the “fluid-mosaic model” [15]. The fluidity of the plasma membrane depends on the composition of the membrane and is kept within strict limits by the cell.

The **proteins** in a plasma membrane make up about 50% of the mass of the membrane [14]. The proteins are responsible for the specialized function of the membrane and therefore differ depending on the cell type. For example, the proteins can function as transporters (e.g. Na⁺ pump), ion channels (e.g. K⁺ leak channel), anchors (e.g. integrins), receptors or enzymes. There are three main groups of proteins classified according to their position in or on the plasma membrane [14, 15].

- Integral proteins (integrins) - Penetrate the bilipid layer (have parts in both the intracellular as the extracellular space). They function either as a receptor, a channel or a transporter.
- Peripheral proteins - Located entirely outside the bilipid layer, but may be either intracellular or extracellular. They are bound to the plasma membrane by non-covalent bonds.
- Lipid anchored proteins - Protein is in the intracellular or extracellular space and bound to a lipid molecule by covalent bonds.

The **carbohydrates** coat the cells' surface and can be bound either to lipids (then called glycolipids) or to proteins (called glycoprotein if they are short sugar molecules and proteoglycans if they are long polysaccharide chains). They include simple sugars (monosaccharides) and all larger molecules (polysaccharide chains) composed of simple sugars [15]. All these carbohydrates are attached on the extracellular side of the membrane [23]. Together, they form the carbohydrate layer (also called: glycocalyx) on the membrane. This layer serves to protect the cell surface from mechanical damage. It is also used by some cells (e.g. white blood cell) to create a slimy layer that acts as lubrication for passage through narrow spaces.

The repair of damage to the plasma membrane by the cell is a complex process. The underlying principles of membrane repair are beyond the scope of this research, as it involves not only passive phenomena (minimum energy state) but also active repair processes (e.g. Ca²⁺ dependent endocytosis [25]). Exploring the membrane repair after mechanical puncture and nucleus extraction would be interesting, but the latter needs to be proven first. McNeil et al. [26] have investigated the addition of Ca²⁺ and cytoskeletal depolymerizing chemicals to the external environment of the cell, which induces puncture “patching” and reduces the membrane tension respectively, which could help to reseal the membrane. Special particles were introduced into the environment that fluoresces so that the viability of the cell after puncture could be assessed (no puncture means no particles inside the cell, puncture and reseals means that particles are inside the cell, dead cell means no particles and ruptured membrane). The mechanics of the plasma membrane can not be discussed separately, as many other components of the cell influence it. It is therefore much more relevant to look at the mechanics of the whole cell, which is done in section 2.6.

2.4.4. Function

Before discussing the functions of the plasma membrane, it is important to note that each type of cell can have a membrane with a specific function (e.g. the brush border membrane in the intestine absorbs nutrients, and the rod plasma membrane in the eye captures light [24]), but this section will only discuss the general functions of the plasma membrane. The plasma membrane generally has seven main functions [14, 15]:

- **Mechanical barrier and compartmentalization:** It separates the internal environment of the cell from the external environment of the cell. It allows the cell to carry out its activities independently without interference from the outside.
- **Selective permeability:** The plasma membrane restricts the exchange of molecules between the internal and external environment. It can restrict or allow the diffusion of ions and molecules.
- **Transport:** The plasma membrane contains proteins that can “pump” solutes against the concentration gradient, allowing the cell to accumulate a reserve of nutrients
- **Electrochemical gradient:** Creates and maintains an electrochemical gradient required for the proper function of muscle and neuronal cell (e.g. by pumping against the gradient, opening channels to let in certain ions, etc.)
- **Communication:** cell-to-cell interaction and recognition. Cells can adhere to each other and then exchange materials or information (if the cells recognize each other, and the appropriate cell is found, e.g. sperm and egg cell).
- **Cell signalling:** the proteins in or on the plasma membrane can interact with certain specific chemicals called messengers. The proteins then relay the message to the inside of the cell.
- **Movement and expansion:** The flexibility of the membrane allows the cell to change shape, grow and move [23], making it very resistant to perturbations.

2.5. The cytoplasm

Between the plasma membrane and the nucleus, most cellular activity takes place (see figure 2.7) [14]. The fluids and components in this region are referred to as the cytoplasm. The cytoplasm can be divided into two groups: the cytosol (section 2.5.1) and the organelles (section 2.5.2). Each type of organelle has its own function within the cell and has a characteristic shape. Note again that for this research it is important to know the basics of the cell, but not all the details of the organelles.

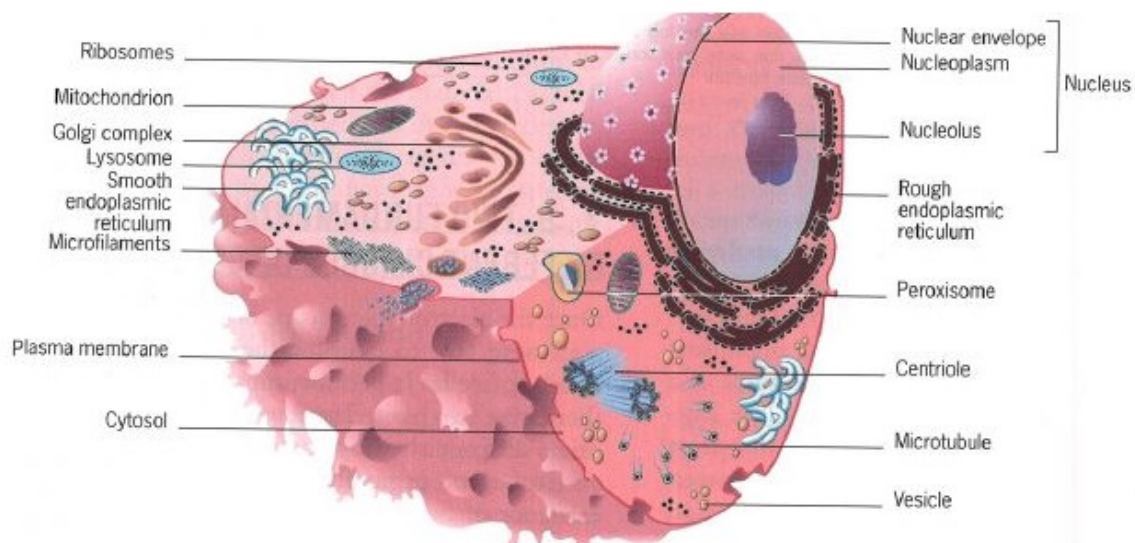


Figure 2.7: A schematic drawing of the structure of a cell, with the organelles indicated [15].

2.5.1. Cytosol

The cytosol is a viscous (gel-like), and semitransparent fluid in which the organelles are suspended (see figure 2.7) [14, 23]. The cytosol contains large amounts of small and large water-soluble molecules, which make the cytosol so viscous. The cytosol, therefore, behaves like a combination of a true solution and a colloid (insoluble or soluble particles of a substance are suspended in another substance). Various proteins, ions, salts, sugars, and other dissolved substances can be dissolved in the cytosol, which consists mainly of water. Inclusions are chemical substances of whose presence depends on the type of cell (e.g. glycogen granules in muscle cells or lipid droplets in fat cells) [14]. Many chemical reactions can take place in the cytosol (e.g. break down of nutrients or protein formation by ribosomes), which are essential for the functioning of the cell.

2.5.2. Organelles

Just as the human body has specialized organs for specific functions, the cell also has organelles. These organelles will not be treated in this report, but a schematic drawing of the cell with its organelles is shown in figure 2.7. A microscopy image of the cell and its components is shown in figure 2.8.

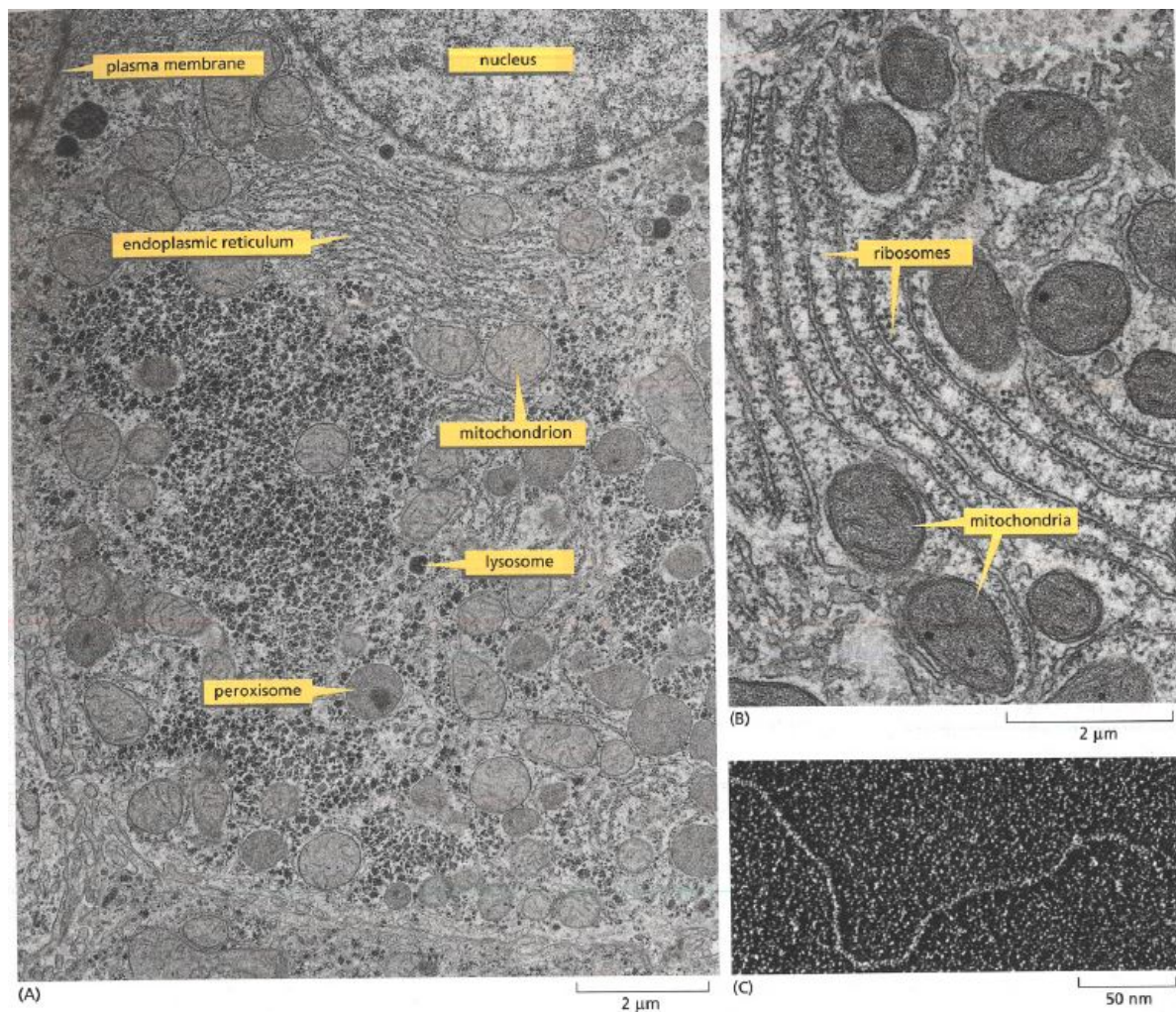


Figure 2.8: Microscopy images of a cell with its components. **A+B)** Optical microscopy image showing the components of a cell, **C)** Electron microscopy image showing a DNA molecule isolated from a cell. [23].

2.6. Mechanical properties of cells

In chapter 2.4, the structure of the cell has been discussed in order to get an overview of its characteristic components. In chapter 2.3, a more detailed overview of the muscle cell was given, including the important dimensions, which will be used in a later (design) stage. Before an engineering design can be made, the requirements need to be defined. For these requirements, it is important to understand the mechanical properties of the cell. This section gives an overview of the mechanics of cells (mainly looking at a general cell). Important parameters that determine the mechanical response of cells to physical manipulation and perturbation are discussed in this section. This section starts with the mechanics of the cell (section 2.6.1) as a single entity, followed by the puncture mechanics of the plasma membrane (section 2.7) and will conclude with the mechanics of the nucleus of a cell (section 2.7.1).

2.6.1. Mechanics of Cells

Cells exhibit both elastic and viscous properties and are therefore referred to as viscoelastic (only applies under physiological relevant time scales) [27]. The elastic behaviour is caused by the structures inside the cell (e.g. cytoskeletal filaments anchored to the plasma membrane) and is independent of time. The viscous properties of the cell originate from the fluid contained in the cell (time-dependent). The fluid can flow and redistribute if stress is applied, which means that no energy is stored [27]. The combination of elastic and viscous behaviour means the material continuously stores and dissipates energy, resulting in relaxation of stress, while deformation increases with time [27]. It should be noted that cells are prestressed by both the fluid pressure and the cytoskeleton. A “three parameter solid” model has been proposed for the interpretation of experimental data, using a spring-damper model in figure 2.9.

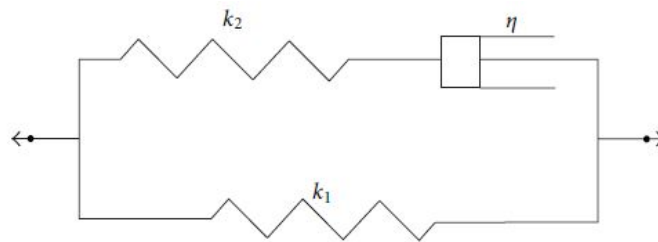


Figure 2.9: Three parameter solid model of a cell with k spring stiffness and η the damping coefficient [28].

Caille et al. [29] have performed compression tests on HeLa cells to determine the mechanical properties. They report a nonlinear relationship between stress and strain of a cell, as it is influenced by the relatively high elastic modulus of the nucleus (for round cells in the order of 5000 N/m^2 , while the cytoplasm has an elastic modulus in the order of 500 N/m^2 , for spread cells 5500 N/m^2 and 1250 N/m^2 respectively). A relatively linear behaviour was observed for very small deformations. These measurements were performed by compressing the HeLa cell and nuclei between two microplates. Takaza et al. [30] report a Poisson's ratio of 0.47 for skeletal muscle cells (using porcine samples). Dejous et al. [31] report a Young's modulus for biological materials in the range of $10 \text{ kPa} - 10^2 \text{ kPa}$ (living cells) by performing atomic force microscope (AFM) measurements. Collinsworth et al. [32] report a Young's modulus of skeletal muscle cells ranging from 11.5 kPa to 45.3 kPa ($11500 - 45300 \text{ N/m}^2$), which falls within the range mentioned by Dejous et al.

Kramer et al. [22] also found a Young's modulus for skeletal muscle cells in this range (44.3 kPa).

Bidhendi et al. [28] developed a finite element model to simulate cell aspiration using a Neo-Hookean viscohyperelastic material. This material model was used to account for the nonlinear mechanical behaviour of cells at large strains and strain-hardening phenomena. With these simulations, Bidhendi et al. were able to verify the experimental data and explain any discrepancies found by using models for the fluid outflow from the cell (Neo-Hookean porohyperelastic model). A result of their simulation can be seen in figure 2.10.

This last model shows the complexity of the cell mechanics, as fluids can leave the cell through pores, and many other complex aspects should be taken into account for proper simulations. However, the previously mentioned properties of the cell remain valid for the simplified models.

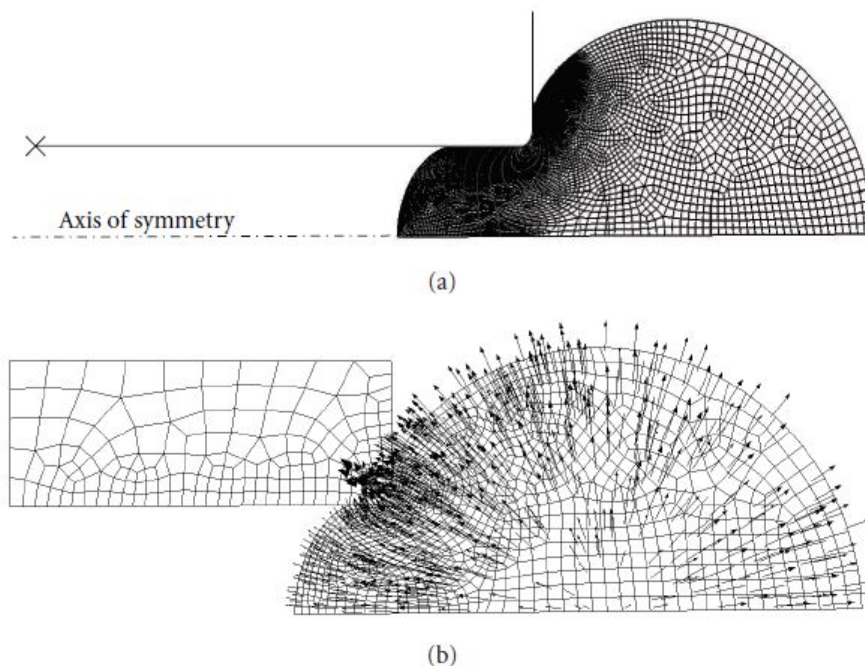


Figure 2.10: FEM simulation of cell aspiration using a micropipette, **A**) Simulation of cell aspiration using a micropipette with an axisymmetric mesh, **B**) Neo-Hookean porohyperelastic model of a micropipette simulating the fluid exchange and velocity in the boundary of the cell [28].

2.7. Penetrating the plasma membrane

As described in section 2.4.2, the plasma membrane forms a selective barrier between the internal and external environment of the cell. This barrier can resist all kinds of forces. Angle et al. [33] performed penetration tests on both bare membranes and on liquid-filled membranes. They found that the force required to penetrate the plasma membrane ranged from 5 to 20 nN depending on the sharpness of the tip (tip radius of 50 to 150 nm). However, it was found that by the time the probe penetrated the membrane, the cell was already compressed to such an extent that the upper and lower bilipid layer of the cell was in contact (if the nucleus was not directly between the membranes at the location of puncture, see figure 2.11a and b). This can be explained by the great compliance of the cell and the movement of the fluid inside the cell towards the sides. Angle et al. [33] report that the surface chemistry (coating) did not influence the puncture force.

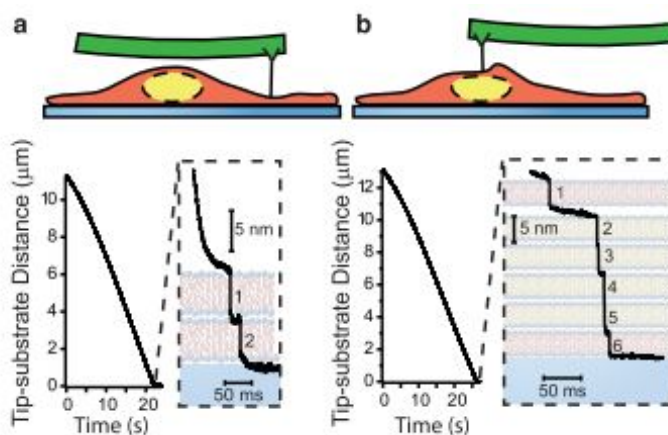


Figure 2.11: Cell membrane penetration, with plots showing the distance to the substrate and the penetration events. **A**) Penetration far away from the nucleus, **B**) Penetration on top of the nucleus [33].

Meister et al. [34] punctured the plasma membrane using an atomic force microscope (AFM) and measured a membrane perforation force of about 3.3 nN for a myoblast cell. A glass cantilever (with internal channel) attached to a silicon chip was used for this experiment. In part 3 section 3.1, the fabrication of microfluidic probes will be treated in more detail. Comparing these values with the ones found by Kramer et al. [22], one can see that the shape of the curve is more or less similar, but the magnitudes differ (see figure 2.12). This could be explained by the difference in tip size (frontal tip area) as Kramer et al. tested with probes with tips in the micrometre range, while Meister et al. worked with tip radii in the nanometre range.

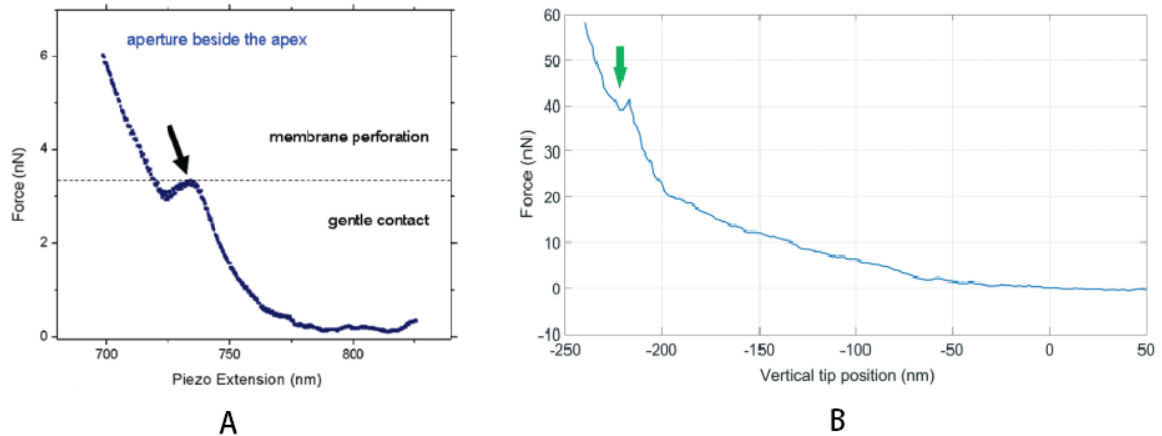


Figure 2.12: Plots of cell membrane puncture experiments. **A)** Puncture force measured by Meister et al. [34] with a glass cantilever (pyramid tip), **B)** Puncture force measured by Kramer et al. [22] with polymer cantilever. Overall plot shape is comparable, but force magnitude differs due to tip size.

McCreery et al. [35] performed a cell puncture experiment on top of a nucleus using a commercial probe. Figure 2.13 shows a typical force curve for puncture experiments on top of the nucleus found by McCreery et al. [35]. The puncture of both the plasma membrane and nucleus are visible in the plots. The required puncture force is in the same range as reported by Kramer et al. [22] in figure 2.12B.

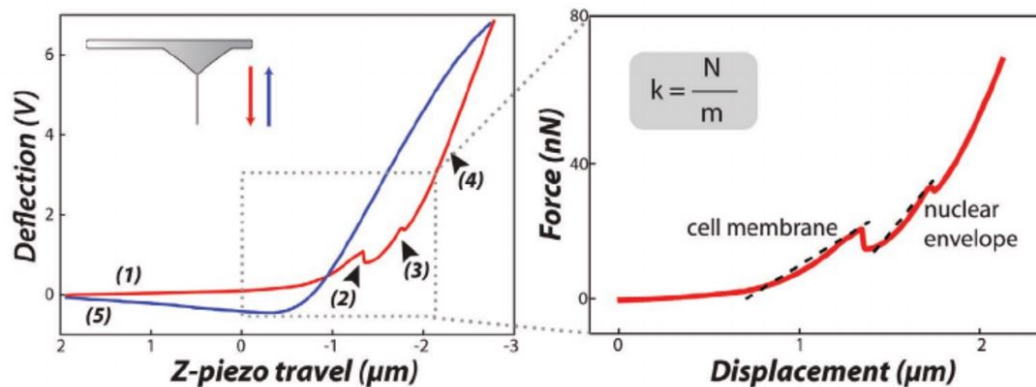


Figure 2.13: Typical force curve of cell puncture experiment on top of the nucleus [35].

Yum et al. [36] were able to visualize the membrane penetration from the side using a nanoneedle with a diameter of 30 nm (silicon nanoneedle made using focussed ion beam). The forces required for penetration were in the range of 3-4 nN (see figure 2.14).

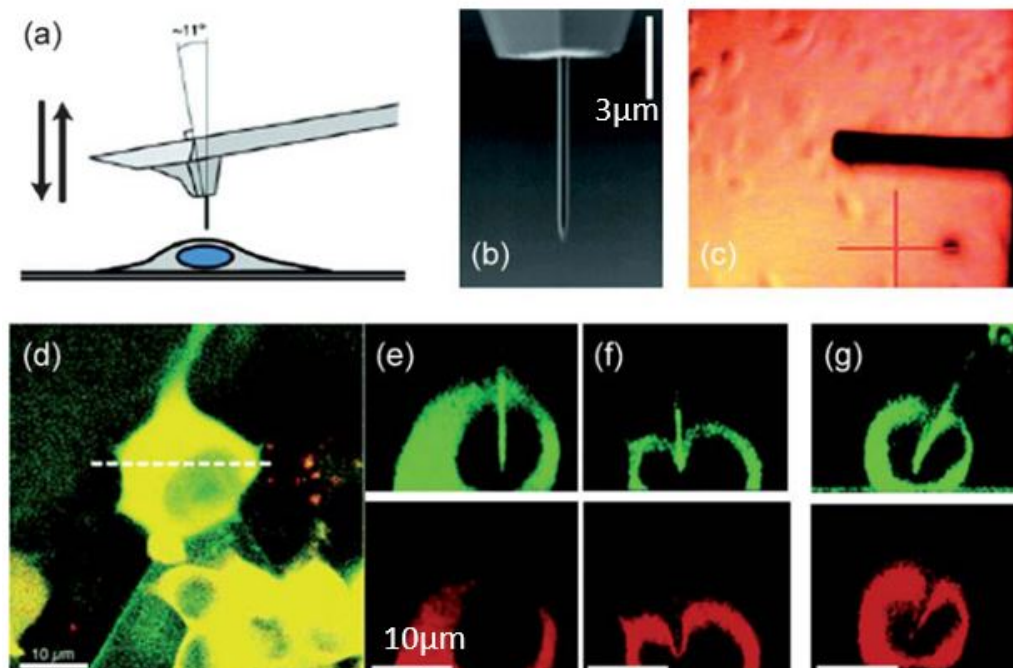


Figure 2.14: Penetration of a cell using a nanoneedle. **A)** A schematic overview of the setup, **B)** SEM close up of nanoneedle manufactured using focused ion beam manufacturing, **C+D)** View through microscope of cantilever and cell respectively, **E)** Penetration of membrane (side view), **F+G)** Failure to penetrate (membrane being deformed severely, side view) [36].

2.7.1. Mechanics of the Nucleus

Guilak et al. [37] found that the nucleus also behaves like a solid viscoelastic material, but is stiffer than the cell itself (which was also found in section 2.6.1). An interesting addition was found by Rowat et al. [38] who used micromanipulation of cell nuclei to show that the nuclei can withstand large deformations without large-scale rupture. The nucleus retains its structural stability even when subjected to mechanical stress caused by this manipulation. The maximum aspiration pressure was found to be 510Pa. The results of Guilak et al. and Rowat et al. were confirmed by Vaziri et al. [39] using computer models that studied the behaviour of the nucleus during aspiration.

2.8. Self repair

The ability of the cell to recover after a cytosurgical procedure is vital for the research on cell manipulation. In this regard, one of the essential features of a cell is its ability to repair damage and disruption to its surface. McNeil et al. [40] state that cells have the ability to quickly reseal a very large disruption in its plasma membrane (with disruption areas of up to $1000 \mu m^2$). This resealing allows the cells to survive a microneedle puncture: a key feature for this research.

Several factors can influence or potentially promote the viability of a cell after a puncture. For example, it has been suggested that environmental conditions, such as large quantities of Ca^{2+} in the surroundings of the cell, may promote the recovery and viability of the cell [40]. In literature, other compounds can be found that help decrease membrane damage. However, many other aspects can influence the viability of the cell. For example, McNeil et al. [40] do not specify the duration of the disruption of the cell membrane and the consequences for the cell's ability to heal itself, which is a factor that in all likelihood has a large effect on the cell survival rate. Many hypotheses have been put forward about how a better membrane repair can be achieved, but no consensus could be found [40]. Many of the properties and environmental conditions that affect cell viability are therefore still unknown and need to be studied in more detail in laboratory experiments.

Important studies on cell viability after puncture were carried out by Guillaume-Gentil et al. [41]. They showed that cell death occurred only in 19% of the cells with their needle if less than 4pL was aspirated from the cell. By injecting (fluorescent) markers into the cell or in its environment, viability could be detected using an optical microscope. The penetration devices used by Guillaume-Gentil et al. will be explained in more detail in chapter 3.1 in combination with the techniques employed.

2.9. Different applications for cell penetration devices

Recent innovations such as high-resolution imaging and fabrication techniques that can produce nanometre-sized features have enabled researchers to study the cell in much greater detail and, for example, to introduce or remove substances from a cell. In this section, the different applications for these membrane penetrating techniques will be discussed. Section 3.1, discussed the techniques and fabrication methods used to create these probes.

There are four main research topics that use membrane penetrating tools:

- Intracellular drug delivery
- Intracellular measurement/stimulation
- Removal of cellular components
- Addition of cellular components

Intracellular drug delivery: Used to study the response of a cell to certain drugs or molecules. Research into drug delivery at the cellular level has been most prevalent in membrane puncture studies. Studying the behaviour of a group of cells when only one cell is injected with a particular drug can help to understand the cascade effect and communication between cells [42, 43]. Another advantage of directly dispensing the drug into the cell is that one does not need to take into account how the drug is transported across the membrane (one does not need transport proteins to pass through the membrane) [36, 44]. For injecting cells with drugs, needle tips are fabricated with apertures in the range of tens to hundreds of nanometres. Guillaume-Gentil et al. [44] report that the tedious handling involved in manually injecting single-cells, the lack of feedback when penetrating the cell with classical methods, and precise dispensing form the main challenge for the injection of drugs at the cellular level. Research is also being conducted on the use of needle arrays to provide treatment to cells in larger areas, which requires less handling [45]. More details on the probes used by Guillaume-Gentil et al. can be found in section 3.1.

Intracellular measurement and stimulation: One of the most interesting properties of cells is their ability to communicate internally (e.g. between organelles) and externally (transmitting and receiving signals from other cells). Measuring and understanding the signals helps us to understand the cell. With the help of electrodes, it is possible to monitor the electro-physiological processes within the cell [36]. One could even think of stimulating the cell by applying a current. Yum et al. [36] give examples of conducting nanoneedles and carbon nanotubes that could be used for in-cell sensing and stimulation.

Removal of cellular components: Removing and testing certain components of a cell can help in understanding the cell and its activities. Nadappuram et al. [46] succeeded in able to removing a mitochondrion and RNA molecules (many researchers are currently focussing on the removal of nanosized components). Kramer et al. [22] have been able to aspirate whole cells using a 3D printed microfluidic AFM cantilever. Commercial products are now also available [47] for the puncturing of cells for the extraction and injection of small molecules. There are now also commercial microfluidic AFM cantilevers, like those of Cytosurge [43], that can be used to grab a cell and move it (by applying suction to keep the cell at the aperture of the pipette).

Addition of cellular components: Uses similar tools as the removal of cellular components (see above). A combination of the two can be seen in cloning, as mentioned earlier. There is little research in this field of adding cellular components to other cells, as many researchers focus on removing components and then performing tests on these components outside of the cell.

2.10. Preparation of the cell and nucleus

Many complex steps must be taken to prepare the cells for single-cell experiments. These steps can include cell differentiation, selection, staining, multiplication, and preservation. For this research, these steps are too complex to cover in detail. Cell growth must be carried out by professionals with the right equipment and skills in a certified biomedical laboratory. It is sufficient for the reader to know that the right circumstances are required to keep the cells alive (environmental conditions) and that different staining agents can be used to visualize the different components of the cell. More details will be given if needed when this topic is addressed. For nuclear transfer, the right environment is also of great importance. Nuclei that have been removed from the cell are missing their protective plasma membrane. Environmental circumstances must be kept within strict limits to prevent damage to the nucleus (e.g. evaporation of fluids can damage the nucleus, especially since we are handling picolitres). The cytocompatibility of the tools used is a very important aspect to investigate. This means that the materials used for cell penetration must not be toxic to the cell. Nouri-Goushki et al. [48] and Kramer et al. [49] researched patterned substrates for organized and orderly growth of cells. Using a substrate with pillars or trenches could help orient the cells in a certain direction and anchor them. This could be used to prevent movement of the cell when forces are applied and align them for the experiments. In research on cell penetration, such as that carried out by Guillaume-Gentil et al. [41], such surface structuring was not necessary, but it could be used if required.

3

Micromechanical probes for single cell research

3.1. State of the Art

In section 2.9, the various applications for cell-penetrating devices were discussed. This chapter focuses on different probes that are used for cell penetration, but also on microfluidic probes with a different purpose. First, the classical glass pipette will be discussed, followed by more recently developed probes. The manufacturing techniques are briefly touched upon in this chapter, but a more detailed account will be provided in section 3.2.

3.1.1. Classical glass pipette

Glass pipettes (microcapillary pipettes) come in many different sizes, each with its own application. The internal diameter of the tip can range from $0.1\mu\text{m}$ to $30\mu\text{m}$ [50]. The smaller diameter pipettes are often used for cell penetration, while the larger diameter pipettes are used for cell positioning and fixation (also called micromanipulator) [51]. Larger pipette diameters can also be used for aspiration of whole cells [52]. Figure 3.1 shows an injection procedure with a glass micropipette under direct visual control using an optical microscope.

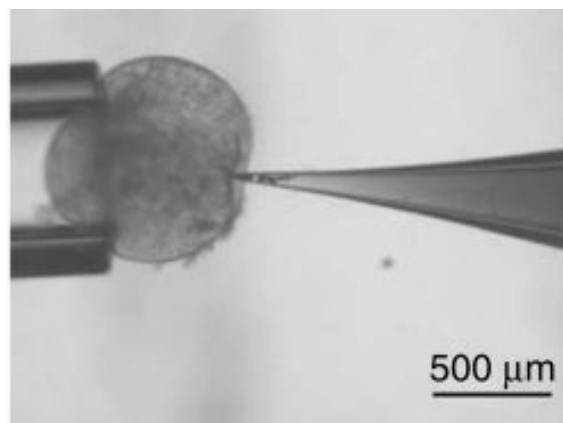


Figure 3.1: Glass pipettes: On the left is a holding pipette with a large diameter ($450\mu\text{m}$ internal diameter). On the right is a penetrating pipette with $5\mu\text{m}$ internal diameter (at the tip). The cell is indented (before the puncture). Direct visual control through an optical microscope (X, Y position directly visible, Z position through focusing), but no force feedback is possible [51, 53].

The tip of the glass pipette is flat, which is mainly due to the manufacturing process and seems favourable for the holding pipette, but not for the penetration pipette (the penetration forces would be higher due to the larger frontal area). To make these glass pipettes, a glass capillary (1 mm outer diameter) is heated and pulled [52]. This causes the glass capillary to expand longitudinally while the

diameter decreases in the middle. The result is two micropipettes connected at the tips. The glass is then broken at the desired point to separate the pipettes. The inner diameter of the tip must then be checked, and those that do not meet the requirements are discarded [52].

One of the disadvantages of the glass micropipette for penetrating cells is the lack of force feedback, which can lead to more damage to the cell [34]. The limited possibilities in the design of a glass pipette, which can thus only have a basic tip shape, results in more damage to the cell than necessary. Because the technique also requires manual control, throughput in cell experiments is low [51]. However, progress has been made in automating cell injection [54].

3.1.2. Silicon pipettes

Using microfabrication and nanofabrication methods, hollow cantilever pipettes can be made from silicon oxide (SiO_2) with a silicon nitride (Si_3N_4) tip [22, 55–57]. Kim et al. [56] developed a nanoprobe (called “Nanofountain Pen”) with a cone-shaped tip (tip radii as small as 50 nm [58]) using standard surface and bulk micromachining techniques. These Nanofountain probes have been studied mainly for drug delivery but not for cellular component extraction. The Nanofountain probe can be seen in figure 3.2.

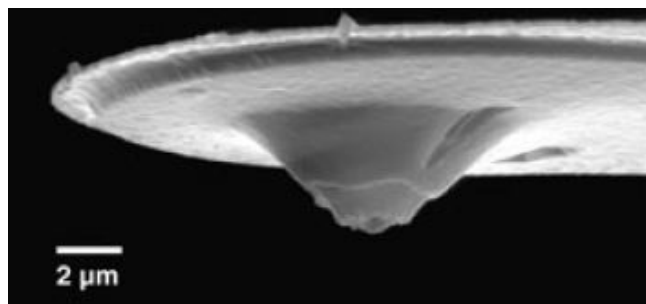


Figure 3.2: SEM image of a Nanofountain probe with a pyramidal (volcano) tip on a hollow cantilever [59].

Commercially available are silicon nitride (Si_3N_4) nanosyringes and pipettes from Cytosurge, which can be seen in figure 3.3 [60]. These probes have apertures in the 300-600 nm range near the apex of a pyramidal shape (made by focussed-ion-beam milling [34]). These probes can be used for nano-injection and nano-extraction without affecting cell viability (according to Cytosurge [47])

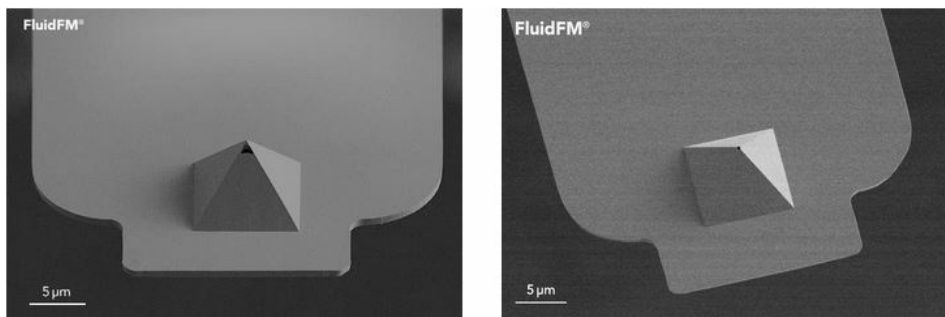


Figure 3.3: SEM image of Nanosyringe (left) with an aperture of 600nm and a nanopipette (right) with an aperture of 300 nm [60].

The silicon nitride cantilevers produced by Cytosurge (FluidFM line) have been tested for many different applications. Guillaume-Gentil et al. [44] have shown that a lesion of up to a few μm is formed in the plasma membrane after penetration of the probe. It was demonstrated that the leakage through the gap between the tip and the cell surface was minimal and that after a controlled retraction, the lesion closed immediately. Guillaume-Gentil et al. [44] state: “The lack of leakage was shown by injection of fluorescently labelled dextran into the cell nucleus, which cannot penetrate an intact nuclear envelope”. Frederix et al. [61] relate the recovery of the plasma membrane to the pyramidal tip, as this shape ensures that the lesion gradually changes as the tip is inserted and removed from the cell, which allows the membrane to reorganize slowly.

A lot can be learned from the research of Guillaume-Gentil et al. [41] who used the Cytosurge probes. First of all, they were able to aspirate fluids with volumes in the sub-picolitre range from single living cells and nuclei (nucleoplasm, not whole nuclei). They also found that for their cells, extracted volumes of cytoplasm greater than 4.5pL always resulted in cell death and volumes less than 4pL resulted in 19% cell death. Nucleoplasm could be extracted with volumes of up to 0.6 pL with little risk of cell death. The probe used by Guillaume-Gentil et al. [41] was coated with Sigmacote [62] and filled with mineral oil to prevent adsorption of cellular components in the surface of the microchannel. Other coatings were also tested, but this coating showed the best results. The mineral oil allowed the researchers to confine the extracts to the front of the cantilever channel. The research of Guillaume-Gentil et al. [41, 44] could serve as a basis for the development of a device for total nucleus extraction. However, their results are valid for HeLa cells, which have a single nucleus and have a cell size of 20 to 40 μm in diameter. It will be necessary to compare the results with the same probes on muscle cells, as these differ in many aspects.

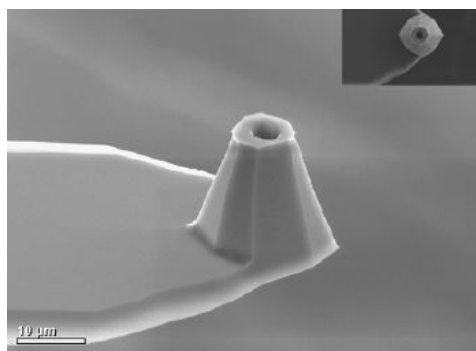


Figure 3.4: SEM image of a cantilever with 2.5 μm sized aperture. Tip manufactured using FIB (scale bar = 10 μm) [63].

Hsu et al. [63] fabricated a cantilever from silicon oxide and used a focused-ion-beam (FIB) to create a 2.5 μm aperture (see figure 3.4). Although this technique allows for a greater variety in the geometries of the tip of the cantilever (compared to the pyramidal shape), the design freedom remains limited (not fully defined 3D design possible). Another example of FIB was seen in figure 2.14, where a nanoneedle with a diameter of 30 nm was achieved.

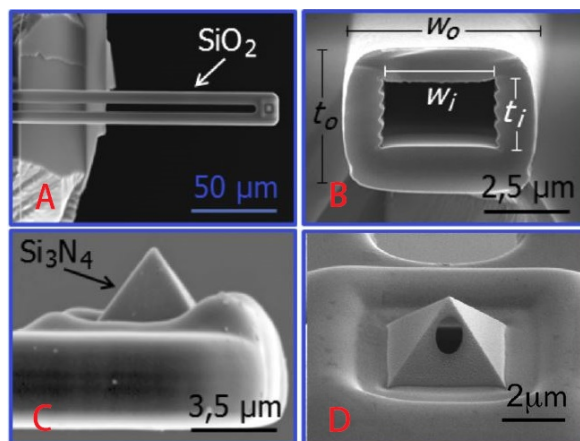


Figure 3.5: SEM image of a microfluidic AFM cantilever pipette (U-shaped). **A**) Cantilever overview, **B**) Cross-section of a leg of the cantilever $W_0 = 6.4\mu\text{m}$, $W_i = 3.7\mu\text{m}$, $t_0 = 4.9\mu\text{m}$, $t_i = 2.2\mu\text{m}$, **C**) Side view of pyramidal tip, **D**) Aperture near the apex manufactured using FIB (adapted from [57]).

Ghatkesar et al. [57] also created an aperture at the cantilever tip using FIB. The resulting microfluidic atomic force microscope (AFM) cantilever, made out of SiO_2 , can be seen in figure 3.5. With this microfluidic AFM cantilever, they were able to aspirate and inject fluids (minimum flow rate of 5 fL/s) and simultaneously perform force spectroscopy and imaging with the same atomic force microscope (AFM) [57].

3.2. Silicon cantilever fabrication techniques

Note upfront: this section discusses silicon micromachining at a fundamental textbook level. This detail is required to understand the complexity and the limitations of silicon micromachining for probe fabrication. However, this detail is not required to understand the rest of the report and can be skipped by readers with micromachining knowledge.

The microfluidic AFM cantilevers mentioned in section 3.1 are fabricated using various techniques. The interface, connecting the cantilever to the actuator clamp and the microfluidic controller, can also be fabricated using several techniques. This section discusses the different techniques used to fabricate microfluidic AFM cantilevers. Section 3.2.1 discusses micro and nanomachining for fabricating cantilevers and tips, and section 3.3 discusses two-photon polymerization (2PP). Both techniques are covered to a level of detail required for good decision-making on production techniques at the design stage. Despite the advances that these techniques have made in recent decades, the variety of microfluidic AFM cantilevers is limited due to the costly and complex production steps, resulting in high costs per probe [22].

3.2.1. Silicon micromachining

Silicon micromachining comprises two technologies: surface micromachining and bulk micromachining. Silicon-based cantilevers (e.g. the SiO_2 or the aforementioned Si_3N_4) can be fabricated using these surface and bulk micromachining techniques. In this section, the basic principles of these techniques are explained. SU-8 cantilever can also be fabricated using these techniques and uses silicon as a basis for the production (sacrificial) rather than structural material. The SU-8 cantilever production will be covered at the end of this section. First, the main overview will be given on the surface and bulk micromachining techniques.

3.2.2. Bulk micromachining

The process is called bulk micromachining if the mechanical part is produced by (an)isotropic etching of the bulk silicon substrate. In this process, the required features are created by removing (deposited) material from a (silicon) wafer [65]. Figure 3.6 shows the general steps for micromachining.

In bulk micromachining, significant amounts of bulk are selectively removed by either wet or dry etching (vapour or plasma) [66, 67]. Photopatterning steps must be performed to protect the parts that are to be kept. Anisotropic etching often results in flat surfaces and sharp angles, while isotropic etching results in more rounded features due to the same etch rate in all directions (see figure 3.7 [66]). Bulk micromachining can produce features with thickness between submicron and wafer thickness (200-500 μm) [67]. The lateral features can range in size from submicron to full wafer size.

One of the advantages of bulk micromachining is that it can be performed with a minimum of capital equipment and is often compatible with the fabrication infrastructure at universities [65].

3.2.3. Surface micromachining

Micromechanical structures can be fabricated from thin films [68]. These films are deposited on a substrate using various materials and techniques and can then be selectively removed. This process is called surface micromachining. An example of a deposition technique is chemical vapour deposition, which can be used to deposit polycrystalline silicon or silicon nitride (and some other materials). Physical vapour deposition can also be used to deposit a layer on a substrate, and oxide layers can be formed by dry or wet oxidation of a film or substrate.

A selective patterning technique called "photolithography" can be used to transfer a pattern from a photomask to a photosensitive photoresist on a wafer (for both bulk and surface micromachining) [69].

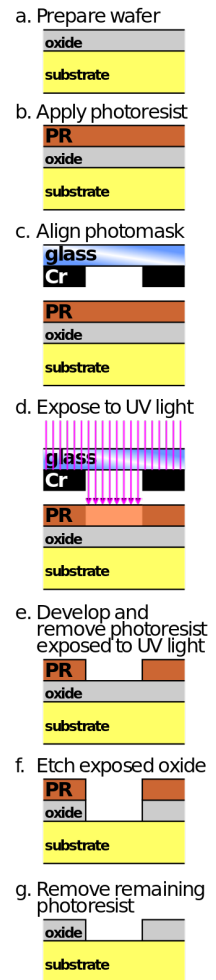


Figure 3.6: General steps for micromachining using photolithography [64].

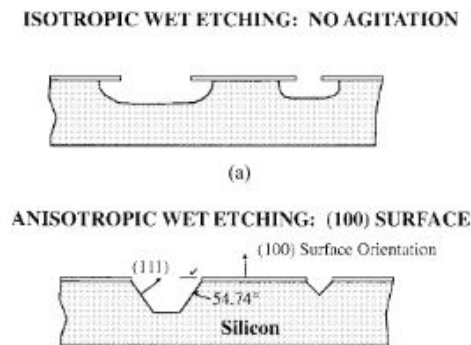


Figure 3.7: Bulk micromachining: Isotropic (top figure) and anisotropic wet etching (bottom figure) resulting in different geometries for the same mask due to the crystal lattice [66].

Photopolymerisation uses light (visible or ultraviolet light) to initiate a polymerization reaction in the photoresist that produces a linear or cross-linked polymer structure (for negative resist) [70]. Polymerization is explained in more detail in section 3.3. If the photomask blocks the light, that part of the wafer will not be polymerized (again for a negative resist). This unpolymersized resist can then be removed from the wafer so that it is only partially covered by polymerized photoresist. After applying the mask(s), etching or deposition steps can be performed depending on the design. The photoresist protects the underlying layer from the etchant, but a layer can also be deposited on top of the photoresist to create suspended structures.

The entire process is performed in a cleanroom to avoid any contamination. The photolithography steps are shown in figure 3.6. The deposition, patterning, and removal steps can be repeated several times to create the desired shape. Sacrificial layers can be used to create hollow or suspended structures [68]. Features with film thickness can be shaped using this technique. The surface micromachining technique is more complex than bulk micromachining and requires a more expensive manufacturing infrastructure [65]. However, it allows the fabrication of much more complex structures. The main difference with bulk micromachining is the successive deposition. These layers can either be structural or serve as sacrificial layers (built upon and removed at a later stage). The steps of photopatterning and selectively etching are quite similar in bulk and surface micromachining [65]. Examples of the layers used are polycrystalline silicon (e.g. structural layer) and silicon dioxide (here: sacrificial layer). After all structures have been formed, the silicon dioxide can be removed by an etchant (e.g. hydrofluoric acid), leaving the polysilicon untouched. The dimensions of the surface micromachined structures can be orders of magnitude smaller than the bulk micromachined structures [67].

3.2.4. Nanofabrication

Using Extreme Ultraviolet (EUV) lithography, Mojarad et al. [71] were able to achieve patterning with a resolution of 7 nm when fabricating dense periodic line-space structures with a periodicity of 14 nm. This enables the fabrication of even smaller features than the aforementioned microfabrication techniques can achieve (about 22nm feature size). Nanofabrication uses the same principles as the microfabrication but with better resolution and smaller feature sizes. Electron beam lithography could also be an option to reduce the feature sizes and obtain a very high resolution (almost to the atomic level) [65]. However, this is a very expensive and slow technique. Focused ion beam bombardment (FIB) was used by Hsu et al. [63] to fabricate the tip aperture shown in figure 3.4. They used FIB only to make the hole in the tip (the rest of the cantilever was made using regular micro and nanomachining methods). With FIB, features with a lateral size less than 50 nm can be machined [72].

3.2.5. Limitations

One of the main limitations of using surface and bulk micromachining for prototyping is the required masks. Every new design requires new masks, which increases the cost and limits the possibility of many design iterations. Another disadvantage is the reduced design freedom in 3D, as only simple shapes and edges are possible (as it is a layer by layer approach). The cost of the whole process and the developing time (mainly because of the repeated steps in the production phase) also make it

a less feasible option for shape design optimizations. Fabricating a batch of microfluidic cantilevers (a wafer full of devices), takes approximately two weeks [22, 49]. The geometries that can be achieved, especially in the z-direction, are limited by the fabrication process, the crystal lattice of the silicon, and the deposited layers' height. Many of the cantilevers mentioned earlier were produced with nanoscale apertures. Microscale apertures are possible, but the pyramidal or cone shape could be a restricting factor.

3.2.6. Application of silicon micromachining in cantilevers

As mentioned in chapter 3.1, the aforementioned production techniques can be used to produce microfluidic cantilevers. The Nanofountain probe is produced with silicon nitride as a structural layer. Repeated etching and deposition produces the final shape of the Nanofountain pen. This process is shown in figure 3.8. For the production of SU-8 cantilevers, silicon is only used as the base material for the production. The production flowchart of these SU-8 cantilevers can be seen in figure 3.9. It is clear that the production process of cantilevers using surface and bulk micromachining techniques is an elaborate process with many intermediate steps, which require specialized equipment.

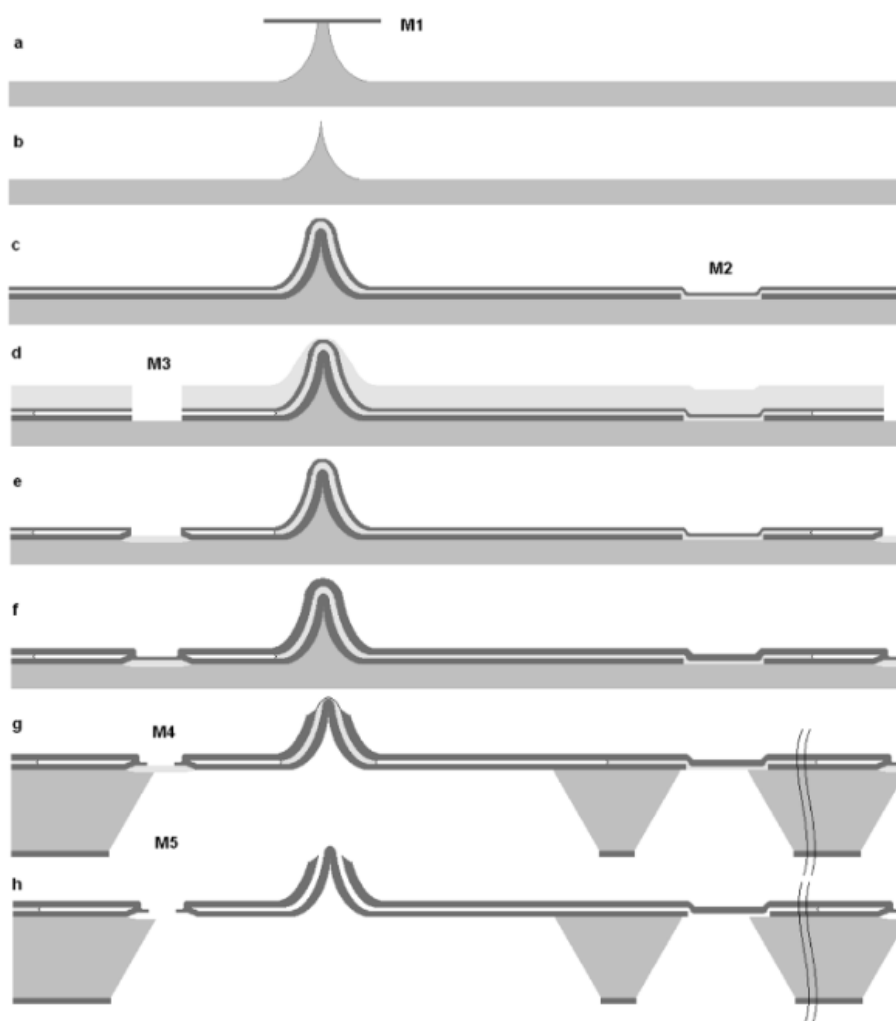


Figure 3.8: Nanofountain production process flow chart (see figure 3.2). **A,B)** Formation of tip precursor using mask M1 (for selective etching) and isotropic etching, **C)** deposition of Si_3N_4 followed by a layer of silicon oxide (SiO) and then again a layer of Si_3N_4 using low-pressure chemical vapour deposition (LPCVD) [22, 56]. This creates a channel filled with oxide, **D)** Mask M3 is applied and etched with potassium hydroxide (KOH), **E)** oxidation to close channel sides, **F)** sealing layer deposited, **G,H)** Etching to create tip, reservoir and release cantilever [56].

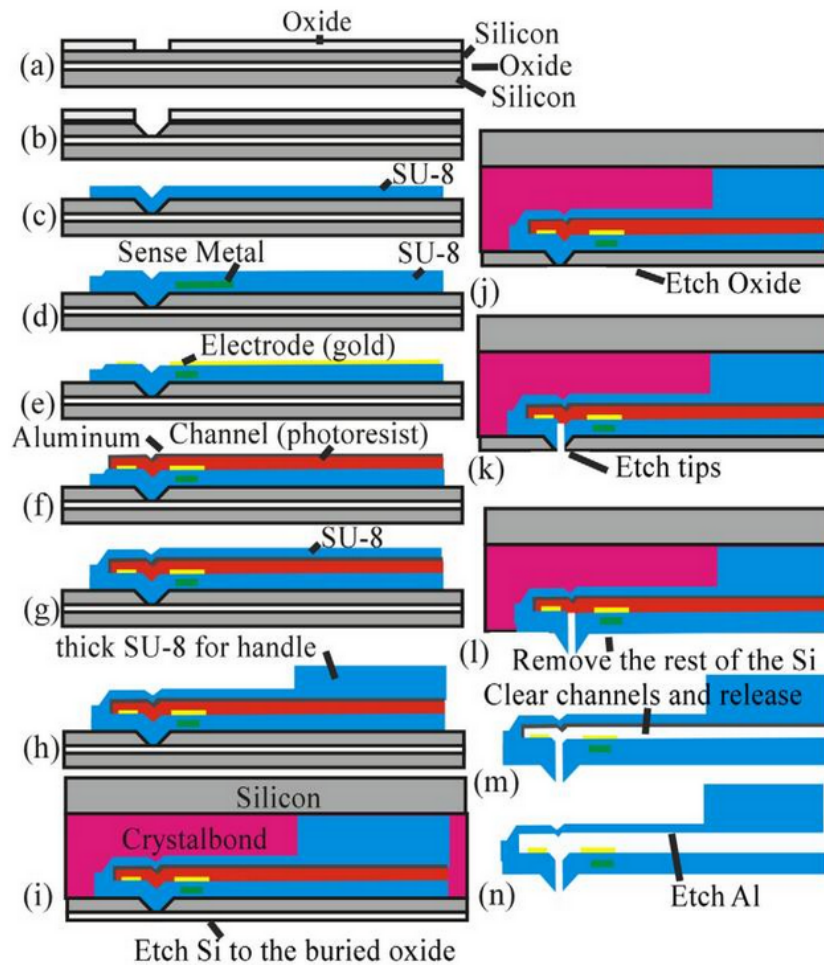


Figure 3.9: SU-8 cantilever probe production process flow chart. The process starts with an oxide mask, formed by thermal oxidation, on a silicon on insulator (SOI) wafer, **A**) the oxide is etched, **B**) The silicon is etched anisotropically (KOH) where it is exposed (no oxide), **C**) SU-8 is spun and patterned onto the device **D**) A deflection sensing element is deposited and patterned, **E**) A gold electrode is evaporated on top, **F**) Photoresist is spun to create a channel, Aluminium is deposited on top, **G,H**) SU-8 is spun on top, **I,J**) a second wafer is attached to the top SU-8 layer the bottom silicon and silicon oxide is removed by dry and wet etching, **K**) O₂ plasma is used to etch through the tip, **L-N**) Sacrificial and support layers are removed leaving a SU-8 cantilever [73].

3.2.7. Polymeric pipettes

There are currently two main production techniques for polymeric pipettes: surface micromachining and 2-photon-polymerization (2PP).

3.2.8. SU-8 micro cantilever pipette

Gaitas et al. [73] have fabricated a microcantilever pipette using SU-8 as the structural material (a biocompatible epoxy-based negative photoresist). A silicon-on-insulator (SOI) wafer was used as a substrate to fabricate the cantilever using surface micromachining techniques. The result can be seen in figure 3.10. An aperture of 10 μm was achieved, but Gaitas et al. suggest that this size can be reduced by changing the masks.

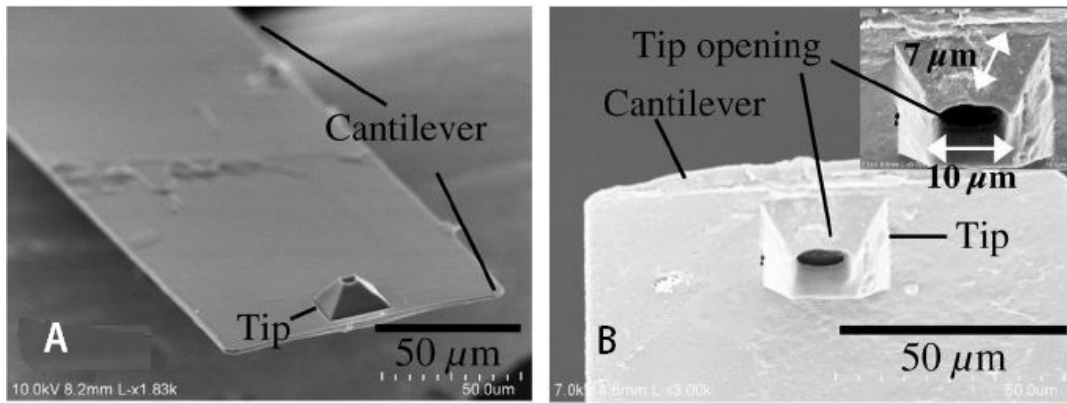


Figure 3.10: SEM image of a SU-8 polymer cantilever with 10 μm aperture. **A)** Overview of SU-8 cantilever pipette, **B)** Close-up of tip of SU-8 pipette [73].

3.2.9. 2PP micro cantilever pipette

Kramer et al. [22] developed cantilevers with a variety of shapes (see figure 3.11), and aperture sizes ranging from 10-20 μm using two-photon polymerization (on top of a 3D print made by digital light processing). The shapes of the pipettes were used for cell penetration, and whole cells were aspirated [22]. The variety of shapes of the pipettes shows the design freedom two-photon polymerization has to offer. Further optimizations can be performed to optimize the printed shapes for different applications.

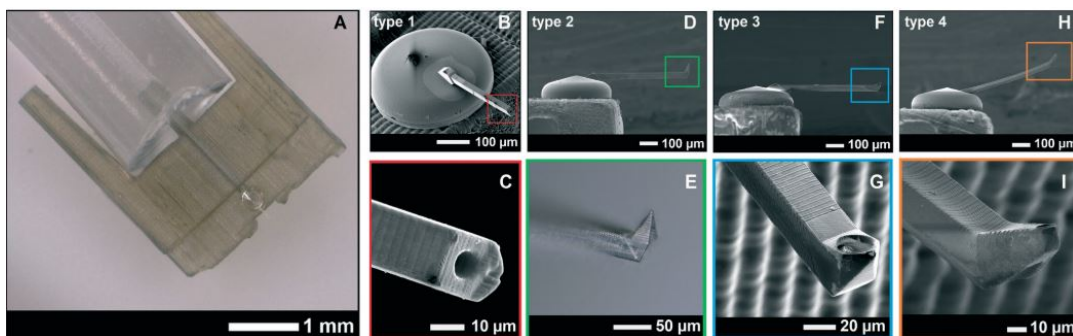


Figure 3.11: Optical microscope and SEM images of various 2PP microfluidic AFM cantilevers with different geometries. **A)** Overview of whole device (multiscale 3D print), **B,D,F,H)** overview of various cantilever geometries, **C,E,G,I)** Show a more detailed image of the cantilever tips from figure B, D, F and H, respectively. For more information, see the original paper [22].

Kramer et al. used a 25x objective with IP-S resin and printed a specially designed structure to capture bubbles while printing at the interface of the substrate. This substrate was also 3D printed using HTM140V2 as a material digital light processing printer). The interface was found manually. A resolution was achieved in the range of single microns. Cicha et al. [74] have printed cantilevers using 2PP to determine the Young's modulus of the material, using nanoindentation equipment. These cantilevers are shown in figure 3.12.

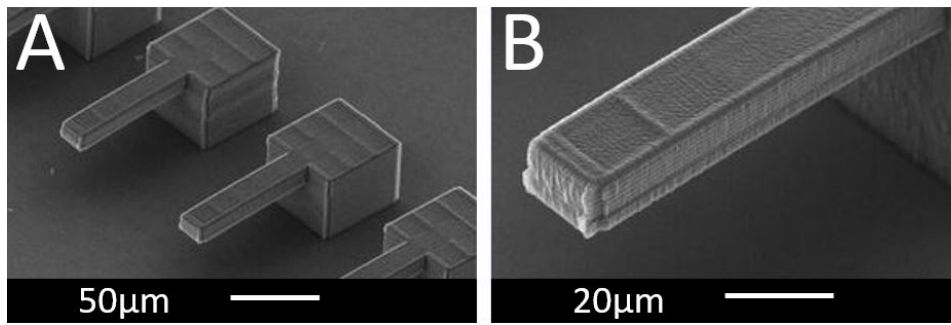


Figure 3.12: SEM images of 2PP printed cantilevers fabricated to determine the Young's modulus of the material. A custom resin was used. Cantilever dimensions: length = $80\ \mu\text{m}$, width of $15\ \mu\text{m}$, a height = $10\ \mu\text{m}$. A) Isometric overview of printed cantilever, B) Close-up of cantilever [74].

A combination of classical micromachining techniques and 2PP printing was performed by Göring et al. [75]. Their results are shown in figure 3.13. This combination is advantageous as it enables the fabrication of tall tips ($h > 100\ \mu\text{m}$) through 2PP and, at the same time get the advantages of silicon cantilevers (e.g. stiffness and Q-factor). A tip radius was achieved of $25\ \text{nm}$ (similar to the curvature of the voxel) [75]. Göring et al. also showed that the cantilever frequency response could be tuned by printing special structures on top of it. This combination of silicon cantilevers with 2PP has not yet been tested for hollow cantilevers.

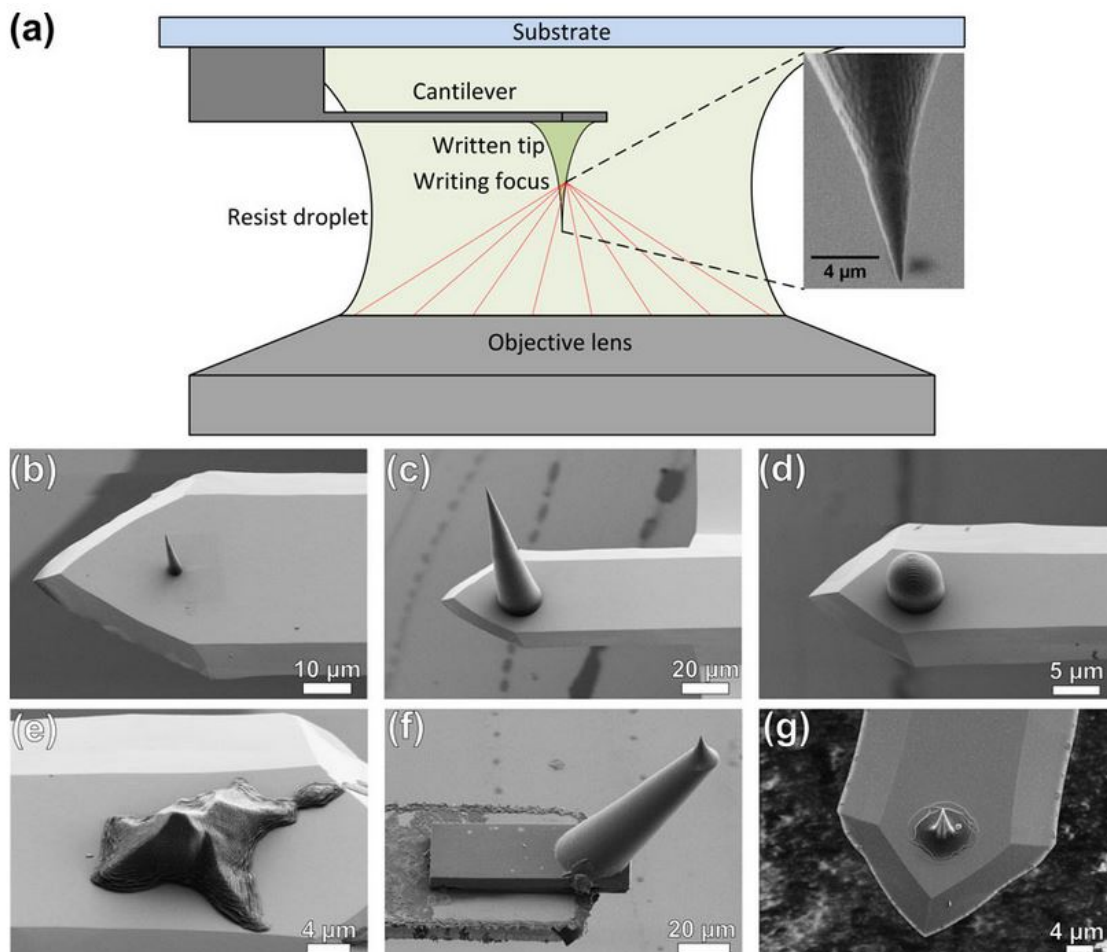


Figure 3.13: SEM image of 2PP tips printed on silicon (nitride) cantilevers. Sharp tips ($r = 25\ \text{nm}$) and very tall tips ($h > 100\ \mu\text{m}$) could be printed. **A)** Schematic print setup used by Göring et al., **B-G)** SEM images of printed tips on top of silicon (nitride) cantilevers [75].

3.2.10. Other pipette types

Chen et al. [76] have developed carbon nanotubes for drug delivery in the cell. These carbon nanotubes act as a needle with a size of 20 to 40nm, to which the drugs can be attached [76]. The application is limited to substances delivery, electrical stimulation and measurements.

3.2.11. Different applications of (hollow) cantilevers

Solid cantilevers in combination with atomic force microscopes (AFM) are typically used to determine surface topologies using the surface-tip force interactions. In section 3.5, the AFM principles will be treated in more detail. Using solid cantilevers, very small masses placed on the top surface of the cantilever can be measured with picogram precision [77].

Suspended microchannel resonators (SMR) were fabricated by Burg et al. [78] to weigh single nanoparticles and single bacterial cells with subfemtogram resolution (with a bandwidth of 1 Hz). Olcum et al., [79], however, were able to achieve a resolution of 27 attograms by vibrating a hollow suspended cantilever (suspended nano channel) and measuring the changes in frequency. Typically, solid AFM cantilevers are used to determine the mechanical properties of a substrate or image the surface of a substrate. Kramer et al. [22] showed that 3D printed polymeric cantilevers can also be used for these AFM measurements.

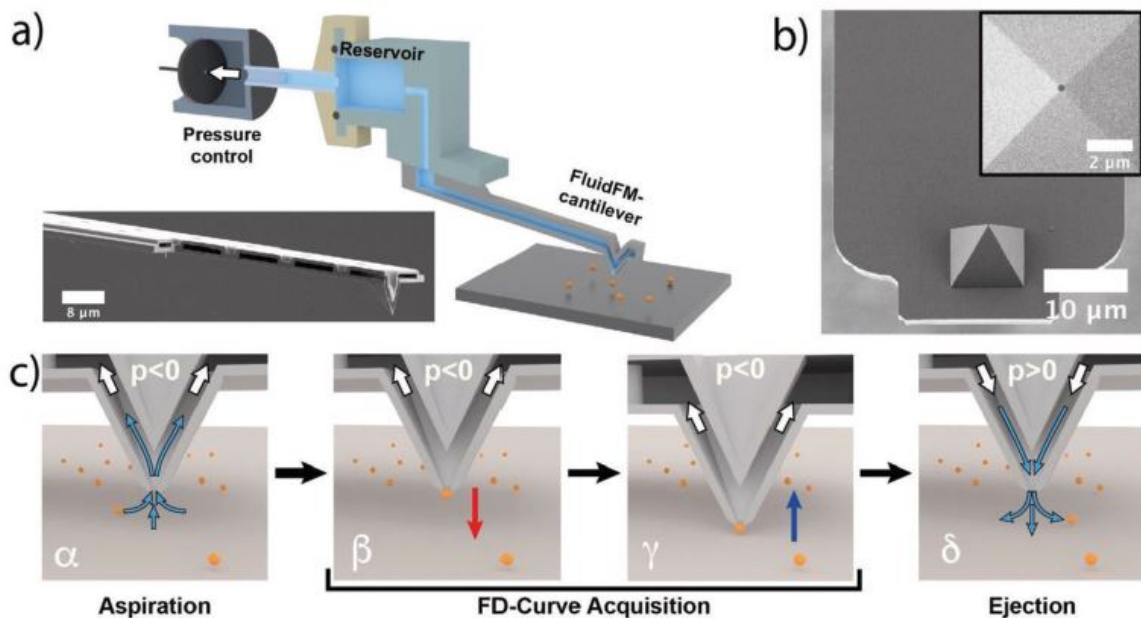


Figure 3.14: Schematics of the pickup of particles using Cytosurge's FluidFM tips. **A)** FluidFM setup overview, **B)** Cytosurge's FluidFM cantilever (SEM image), **C)** Steps to pick up and remove a particle [80].

Aspiration through hollow cantilevers has already been discussed in section 3.1 in which for example Kramer et al. [22], Garza et al. [81], Guillaume-Gentil et al. [41] and Ghatkesar et al. [57] showed the possibilities. A weight measurement of the aspirated components using the AFM is one of the major advantages of this technique. Mark et al. [80] used the Cytosurge's FluidFM cantilever in combination with an AFM system to pick up colloidal particles by applying negative pressure. They showed that the attachment of the particles was reversible, and the immobilization at the aperture is independent of the surface chemistry of the particles (with diameter well below 500 nm) as well as their mechanical properties.

The setup can be seen in figure 3.14. They demonstrated that a particle could be picked up and held at the tip by applying a holding pressure, which can be seen in figure 3.15. Cell manipulation was performed by Martinez et al. [82]. They were able to pattern cells on a substrate with a spatial accuracy of 5 μm . Thus, the microfluidic AFM cantilevers can be used for a wide variety of experiments, including cell manipulation, cell injection and aspiration, dispensing fluids, force sensing, and mass sensing.

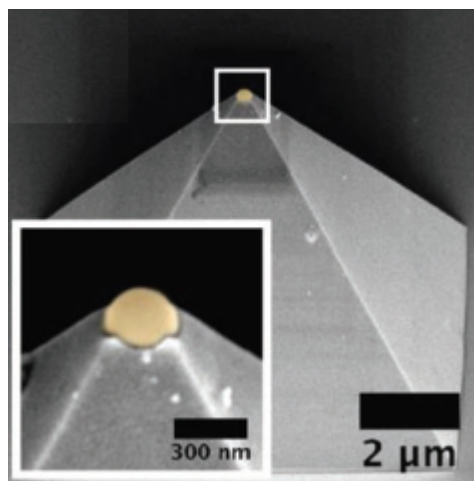


Figure 3.15: False coloured SEM image of particle held by the holding pressure at an aperture of a pyramidal cantilever tip [80].

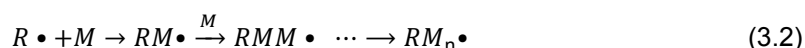
3.3. Two Photon Polymerization

In photopolymerization the polymer reacts to the light only if the energy of the photon is above a certain threshold. To understand two-photon polymerization (2PP), one first needs to understand photopolymerization's basic (chemical) principles. Simply put, photopolymerization is a chain polymerization process initiated by photons (light) [83]. The light causes photo-crosslinking of pre-existing macromolecules by free radicals. This happens in three main processes [84]:

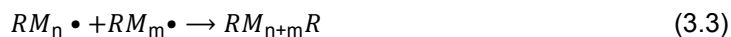
- In the initiation process (eq. 3.1), photoinitiators (PI) are excited by absorption of two photons with frequency ν . This results in a photoinitiator in an excited state (PI^*), which then decomposes into two radicals, which are molecules with at least one unpaired electron (R^\bullet) [84]. h is the Planck constant.



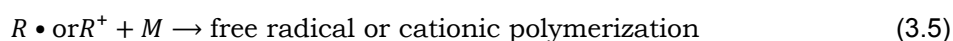
- In the propagation process (eq. 3.2), the radical combines with a monomer (M) in the solution to form a monomer radical (RM^\bullet). This radical can then bind several other monomers to form a large monomer radical (RM_n^\bullet). This only happens if the concentration of radicals is high enough.



- The final step is the termination process. In this step two monomer radicals are combined and the photopolymerization process stops (equation 3.3).



The difference from one photon polymerization (1PP) is that the photoinitiator in 2PP absorbs two photons of a lower energy. For one photon polymerization, the following reactions occur (note R^+ is an ion) [85].



In 1PP, the photoinitiator only absorbs one ultraviolet (UV) photon with a short wavelength (linear absorption [85]). 1PP is used in photolithography (mentioned in section 3.2.1) and direct light processing (discussed in section 3.4). The main disadvantage is that the UV light is absorbed in the first few

micrometers, which only allows a planar process at the surface of the resin [85]. Note that in 1PP also cationic polymerization can occur, which does not occur for 2PP.

In 2PP, near-infrared (NIR) light is used instead of UV. For 2PP $\lambda = 780\text{nm}$, while for digital light processing (a one photon polymerization technique) a wavelength of $\lambda = 385\text{nm}$ is often used (half of that of 2PP). The 2PP photons thus have a larger wavelength and which means a lower energy according to equation 3.6. They are not absorbed directly at the surface, as can be seen in figure 3.16. The photoinitiator absorbs two of these NIR photons, which need to arrive within femtoseconds after each other to cause polymerization by two photons [86].

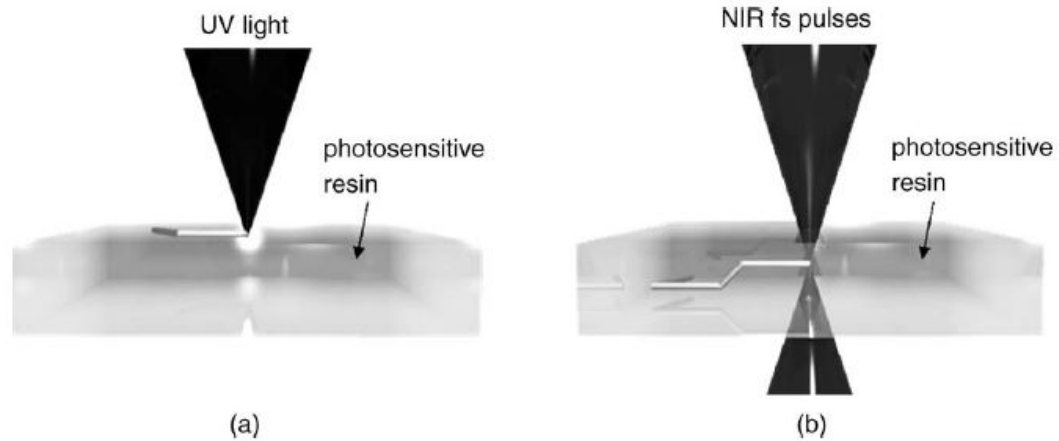


Figure 3.16: **A)** UV light gets absorbed in the first few micrometers of the photosensitive resin, can only be applied for planar structures (2.5D). **B)** NIR light can be focused in the bulk/volume of the photosensitive resin, can be applied for 3D structures inside the bulk of the resin [85].

$$E = \frac{hc}{\lambda} \quad (3.6)$$

But there is a problem: the cross-section for two photon polymerization is orders of magnitude smaller than for one photon absorption (explained later). To create enough radicals (and get high enough density of molecules in the radical state), the intensity of the incident beam should be high (in the order of TerraWatt/cm²) [85]. The absorption of the two photons is a third order nonlinear optical process. The rate of absorption of the photons is given in equation 3.7 [84],

$$\frac{dW}{dt} = \frac{8\pi^2\omega_i}{n^2c^2} I_L^2 \text{Im}(\chi^{(3)}) \quad (3.7)$$

where n is the refractive index, ω_i is the incident light optical frequency, c is the speed of light in vacuum, I is the intensity of the light, and $\text{Im}(\chi^{(3)})$ is the imaginary part of the third order susceptibility (susceptibility is the characteristic constant of a medium, which allows full prediction of the perturbative nonlinear optical effects in a medium caused by the interaction of light with matter [87]). Due to this non-linear light-matter interaction, the excited spot is confined to the focal volume of the laser light, which causes the reduced cross-section mentioned earlier.

From equation 3.7, it can also be seen that the absorption rate for 2 photon absorption is proportional to the square of the light intensity [84]. For 1PP, on the other hand, the absorption is proportional to the intensity. The latter results in larger features, as can be seen in figure 3.17.

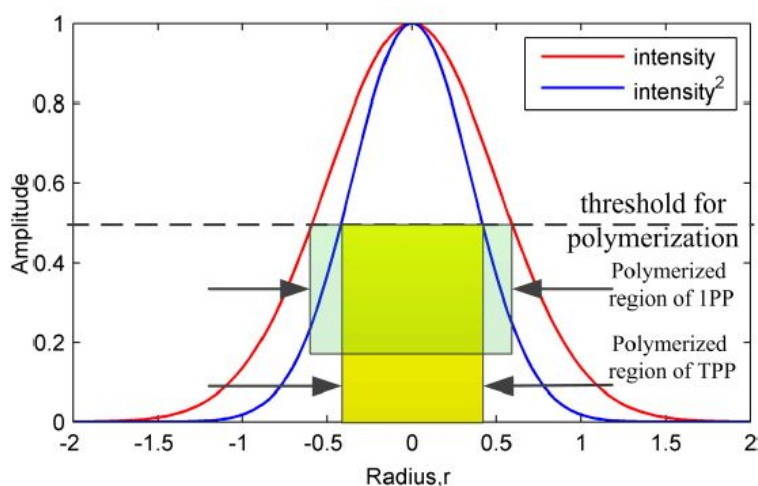


Figure 3.17: Light intensity distribution of a Gaussian beam, intensity (red) and intensity^2 (blue) are shown. 1PP takes place where threshold is reached by intensity, 2PP takes place where threshold is reached by intensity^2 . 2PP has smaller polymerized region [84].

The optical nonlinear absorption and threshold peculiarity contribute to a resolution beyond the diffraction limit for 2PP [84]. The main advantages of 2pp over 1pp are [85]:

- 2PP can be performed in the volume (bulk) instead of on the surface, resulting in 3D structures (instead of 2.5D) and is not influenced by the environment (oxygen on the surface can cause radicals).
- The excited spot is smaller for 2PP, which allows production with lateral resolution of 100nm and axial resolution of 500nm (resolution beyond the diffraction limit is possible). This difference can be seen in figure 3.18.

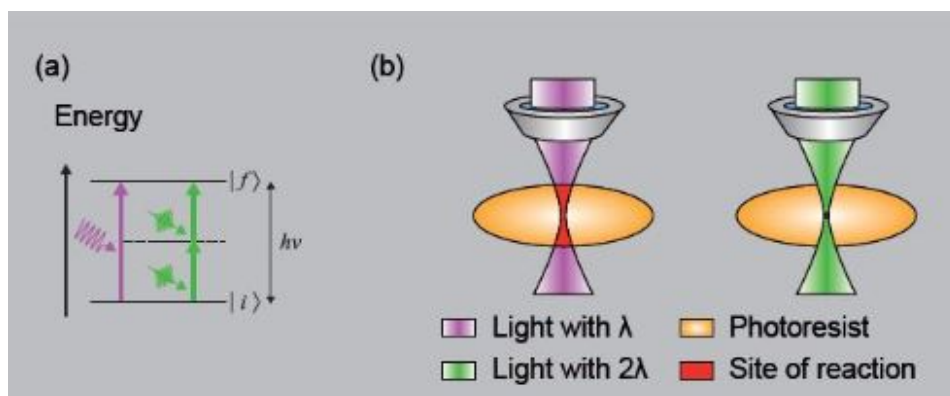


Figure 3.18: **A)** Quantum mechanical scheme of 1PP (magenta) versus 2PP (green), **B)** reaction volumes of 1PP and 2PP with 2PP confining the photoreaction to a tiny focal volume [88].

A disadvantage of 2PP is that it is a serial process (direct laser writing) which increases production time for large-scale production or large features (a voxel scans through the resin in lines instead of layers per layer). To reduce printing time, Accoto et al. [89] suggest printing shells and trapping the resin (unpolymerized) inside a shell. After the printing process, the shell is exposed to a high-intensity UV light, which polymerizes the resin inside the shell. This approach could speed up the process of 2PP production.

For fabrication using 2PP, the setup seen in figure 3.19 can be used. A femtosecond pulsed laser (titanium sapphire laser) is used because it can deliver high peak intensities (which are required for the nonlinear interaction) [85]. The procedure is simple: a photosensitive liquid resin is applied to a substrate. The substrate is then mounted on a 3D piezoelectric scanning stage [85].

This piezo stage, which is mounted on a stepper motor stage for coarse movements, can be programmed to follow a certain path to generate a specific shape. The process is monitored live by a CCD camera.

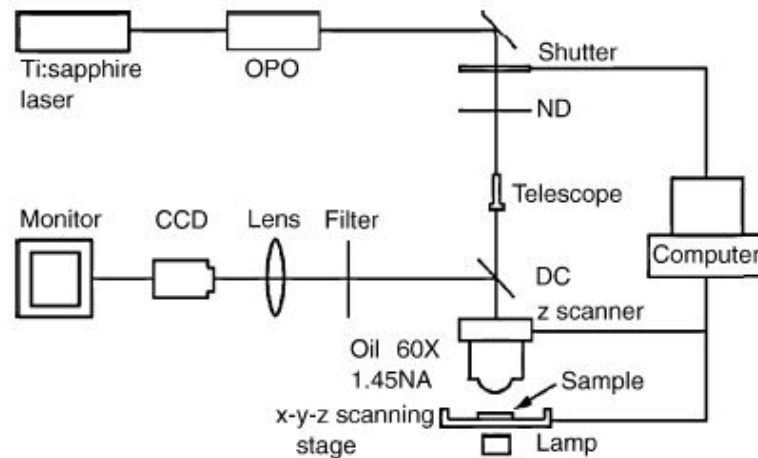


Figure 3.19: Experimental setup for 2PP printing by Wu et al. [85].

The Young's modulus of a 2PP print was found to be dependent on the laser power [90]. Figure 3.20 shows this dependence for multiple materials. This increase in Young's modulus should be taken into account when simulating the behaviour of a 2PP printed structure.

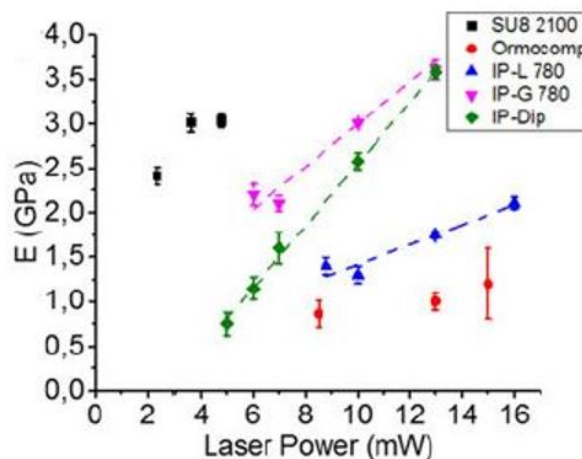


Figure 3.20: Dependence of the Young's modulus to the laser power [90].

3.3.1. 2PP method

Currently, Nanoscribe [91] is one of the few manufacturers of commercial 2PP printing devices. This section lists some essential features of the Nanoscribe to determine the possibilities (essential for the design phase).

With the Nanoscribe, feature sizes of less than 20 nm have been achieved through extreme fine-tuning [92]. However, these are extreme results. Under normal circumstances, feature sizes of 200 nm can be achieved (with maximum sizes of up to 100 μm when stitching is used) [93]. The achievable feature size differs per resin and objective, which should be considered during the design process.

Many different resins are available for 2PP printing using the Nanoscribe. Often used resins are IP-DIP, IP-VISIO and IP-L780. IP-VISIO is non-cytotoxic according to Nanoscribe, and IP-L780 was tested for its cytocompatibility by Nouri-Goushki et al. [48]. A schematic of the Nanoscribe is shown in figure 3.21.

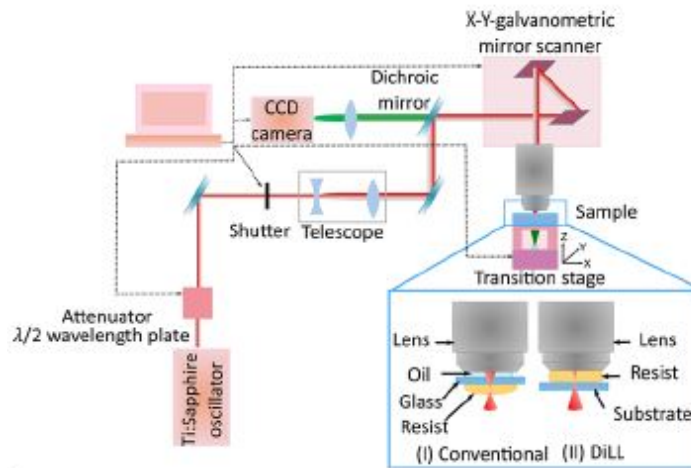


Figure 3.21: Schematic setup of the Nanoscribe Photonic GT2 2PP printer. Further explanation is given in text [48].

The Nanoscribe uses a Titanium Sapphire laser as a light source with a 100 femtosecond pulse duration [48]. This laser has a wavelength of 780nm. A half-wave plate is used together with a cube polarizer to attenuate the laser power when required. The telescope is used to expand the laser beam to match the objective. A dichroic mirror then reflects the laser beam. This mirror is also used to allow a CCD camera to image the substrate before and during the process. A galvo scanner or 3D transition stage can be operated via a computer to position the laser beam into the resin.

Two configurations can be used (see figure 3.21): conventional with oil in between the lens and the glass (I) or a dip-in-laser-lithography (DiLL) configuration (II) with the resist between the lens and the glass. The galvo mode results in lower printing times, but also a lower accuracy than the piezo mode [48]. After the 2PP process is performed, development steps and rinsing are required. Large features (larger than the printing field) can be created by stitching different blocks. This does worsen the achievable resolution and increases the printing time.

3.3.2. Interface Finding

To print on a substrate, the printer must know where the surface of that substrate is located. The Nanoscribe uses the Zeiss Definite 2 module [94] to find the interface between the substrate and the resin. Figure 3.22 shows the basic principle of the Definite Focus (note: it shows the principle for microscopy purposes, but the principle is the same).

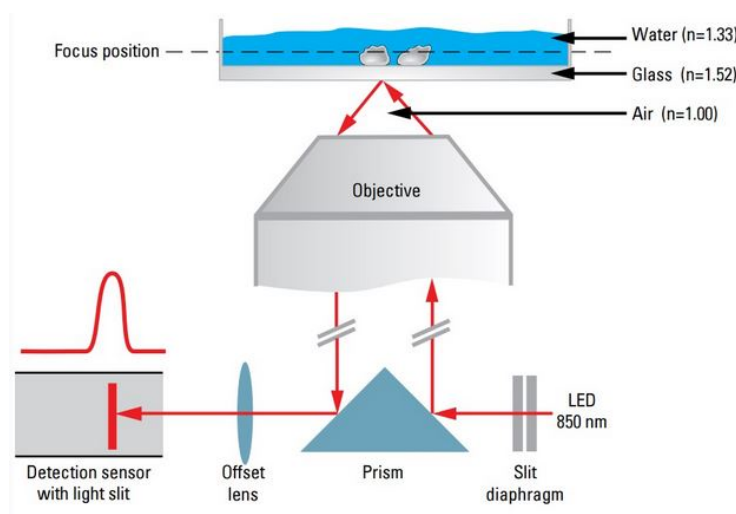


Figure 3.22: Schematic of Zeiss Definite Focus 2 principle (here used for cell visualization, but principle is similar for 2PP printing) [95]

The definite focus principle uses the index of refractive index mismatch between a fluid and a solid. In the case of 2PP, the mismatch between the photoresist and the substrate is used. To find an interface, a LED is used to project a grid through the objective. This grid is located in the focal plane of the objective [94]. The objective approaches the substrate, and at the moment an optical interface is encountered, within the depth of focus of the objective, part of the projected grid will be reflected. This reflection will form an image on the detector of the Definite focus module. Using the data from this reflection, the position of the interface can be determined (when it is in focus). Important is the presence of a reflecting surface for Definite Focus to function correctly.

An index of refraction mismatch between the photoresist and the substrate is required, as the definite focus relies on the reflection of infrared light by the interface. This reflection occurs when light travels into another medium with a different refractive index if the incident angle is large enough (according to Snell's law and the Fresnel equations). With insufficient reflection, no interface will be found. Adding a reflective coating also results in an interface signal.

3.4. Digital Light Processing

Digital Light Processing (DLP) is an additive manufacturing technique in which a 3D shape is created by selectively exposing parts of a photoresist layer. By repeating this step, layer by layer, complex 3D shapes can be formed.

After a layer is exposed, it is covered with new photoresist and the exposure is repeated for the new layer [97, 98]. The new photoresist layer is often applied by lifting the print a few millimetres out of the photoresist pool and then immersing it in the photoresist again (therefore often printing upside down).

The setup of a DLP printer can be seen in figure 3.23. The most important functional component of the DLP printer is the digital micromirror device (DMD or DLP chip). The DMD consists of an array of micromirrors (often millions of mirrors) that can rotate to determine the path of light [98]. Figure 3.24 shows the working principle behind the DMD chip to create the projection that selectively exposes the photoresist layer. The density of the pixels (with pixel spacing from a few to a dozen microns), the lens system and the projection plane determine the print resolution.

The DLP technique can achieve resolutions of up to $6\mu\text{m}$ [98], but commercial printers often have a resolution in the tens of microns range. DLP printing is a relatively fast technique, as it is not based on scanning single voxel lines, but on whole layer illumination. The benefits of the printing technique are that the printing process does not introduce high temperatures, pressures or shear stresses. Currently, DLP printing is applied in many different fields and for various applications. In the medical field, DLP is mostly used for medical models, implants, tissue engineering, drug delivery, etcetera.

To achieve even higher resolution, Saha et al. [99] combined the 2PP process with the DLP approach. They developed a femtosecond projection method (FP-TPL) to focus ultrafast light pulses both spatially and temporally simultaneously. This enables parallel printing of arbitrarily complex 3D structures with submicrometre resolution (and is a layer by layer process) [99].

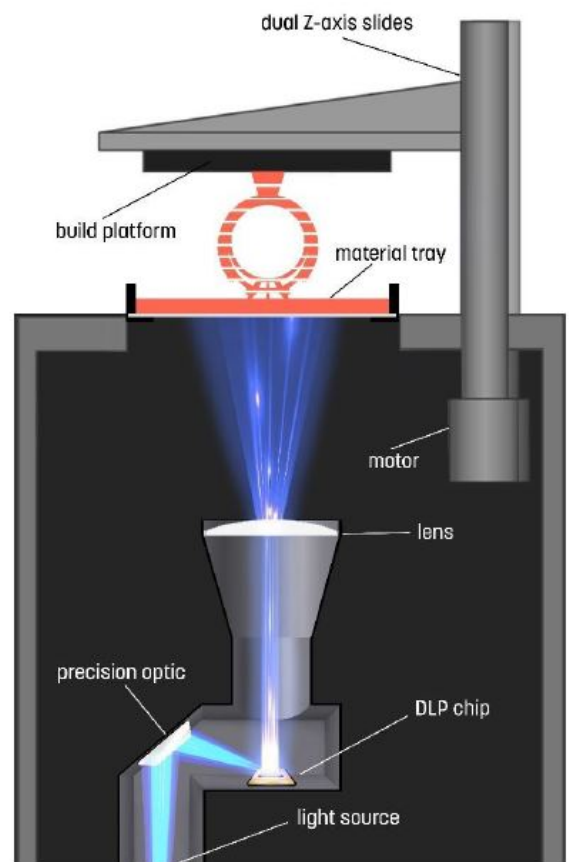


Figure 3.23: Setup of direct light processing system. Printing up-side-down to cover the last printed layer of the print in photoresist (after retracting a couple of millimetres) [96].

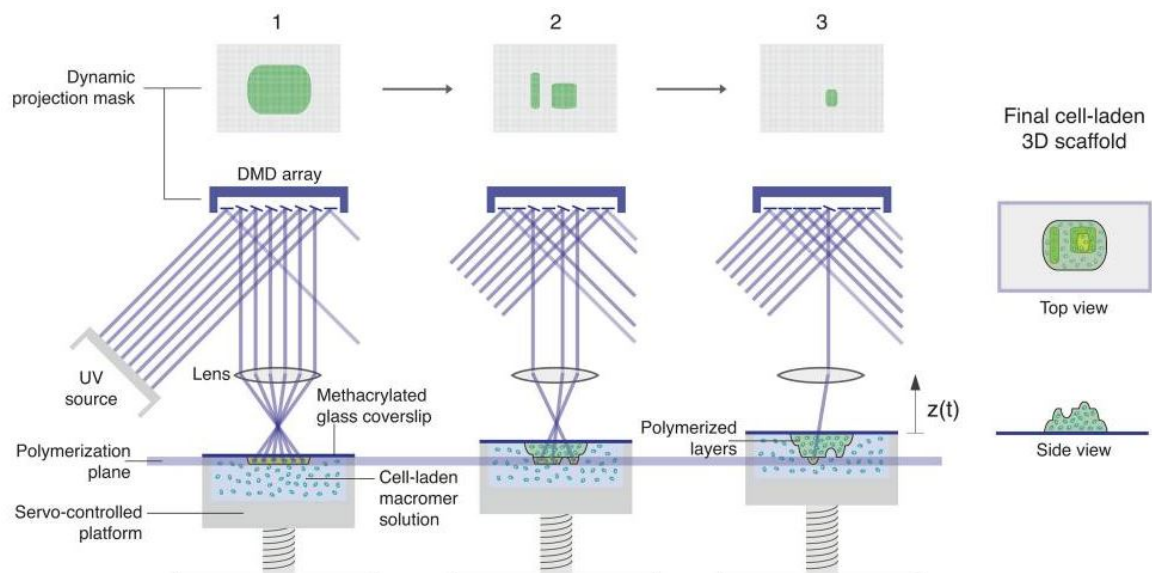


Figure 3.24: Schematic printing principle of the DMD used for DLP printing. Three different layers are shown with different parts of the DMD activated to create a projection [100].

3.4.1. Materials for DLP printing

A variety of materials are available for DLP printers. Most of these materials are based on (acrylated) oligomers and (acrylated) monomers. The oligomers are molecules that consists of repeating units of (similar or identical) monomers. The photoinitiators can either be added separately to the mixture or they can be attached to the polymer subunits (chromophores). Photoinitiators are chemicals that break down into reactive species after exposure to light. These reactive species then activate the functional polymerization groups on the oligomers [101]. UV light is the most commonly used light source as it is highly energetic. Sometimes the resins are doped with additives such as titanium dioxide to increase stiffness or temperature resistance.

An important aspect for the resolution is the printing material. Polyethylene glycol diacrylate (PEGDA) has been used to achieve resolutions as low as $6\mu\text{m}$ while other materials have resulted in resolutions in the range of $20\mu\text{m}$ [98]. Materials have various properties. For example, they can be transparent, coloured or opaque and can be very flexible or stiff. Special materials are on the market for biomedical applications such as implants, medical models, tissues, etc ([98]).

3.4.2. DLP as 2PP substrate

Kramer et al. [22, 49] have shown in their research that it is possible to print 2PP structures on a DLP printed interface. Due to the high surface roughness of the print (because of the layer lines), the automated interface finding property of the 2PP printer (Nanoscribe) could not find the interface between the photoresist and the substrate. This resulted in the formation of bubbles in the 2PP resin and the burning of the substrate, caused by heating due to a too high laser power at the surface of the DLP print. It was observed that small bubbles ($<3\mu\text{m}$) would dissipate, but larger bubbles would persist [49]. To solve this problem, a special structure was developed to minimize the impact of the bubble formation by trapping the bubbles locally [22, 49]. This prevented the bubbles from coalescing into larger bubbles.

In his thesis [49], Kramer concluded that some of the devices, made using the multiscale 3D printing approach (DLP print with special 2PP print on top), were not watertight due to partially connected 2PP bases. No information was given on the success rate of the printing technique. These leakages were caused by uneven or distorted surfaces of the DLP print [49]. Kramer recommends optimizing the DLP print by either precise cutting of the surface, using surface treatment or optimize the printing configuration [49]. Kramer also suggests using other materials between the DLP print and the 2PP print, like for example glass. This would, however, require an assembly and bonding procedure.

3.5. Atomic Force Microscope

The atomic force microscope (AFM) uses cantilevers with sharp tips (with tip radii as small as several nanometres) to sense forces in the range of 10^{-12} to 10^{-8} N between the tip and the substrate [102]. A resolution in the order of fractions of a nanometre have been achieved (more than 1000 times better than the optical diffraction limit). The AFM scans the substrate with the cantilever's sharp tip while measuring the cantilever's deflection to create a surface topology image. This deflection is caused by the interaction between the tip and the substrate [102]. The interaction forces between the substrate and the tip include van der Waals and repulsive electrostatic forces.

A wide variety of substrates, including (non-conductive) solids and (live) cells, can be imaged in air, liquid, and vacuum. The cantilever can also be used to measure the indentation or puncture forces of substrates, which can be used to calculate the Young's modulus of a material. To measure the deflection of the cantilever, a laser is used that is reflected from the back side of the cantilever. The change in the position of the laser on a photodiode array can then be used to determine the deflection of the cantilever [103]. The schematic principle can be seen in figure 3.25.

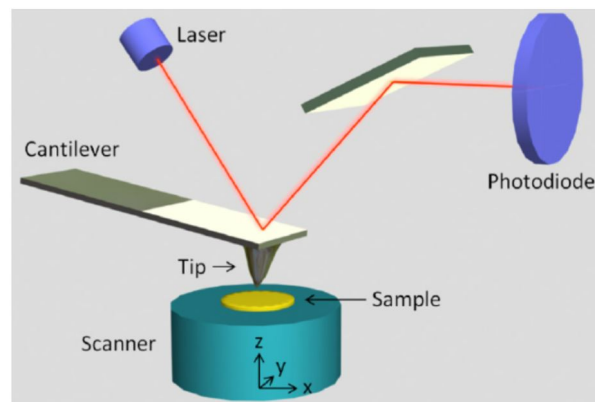


Figure 3.25: Schematic setup of an AFM system. The laser is reflected onto a photodiode by the backside of the cantilever. A deflection causes a change in the position of the laser on the photodiode [103].

The position of the laser on the detector changes when the cantilever is deflected [102, 103]. Force feedback is achieved by measuring the deflection of the cantilever with the laser detector of the AFM, which can be directly linked to the forces at the tip of the cantilever with a known stiffness [34]. Force feedback is of utmost importance in AFM cell experiments because force feedback reduces damage to the cell [34].

3.5.1. AFM modes

The AFM can generally be operated in three modes: contact mode, non-contact mode (also called AC mode) and tapping mode (also called QI mode or intermittent mode). Figure 3.26 shows the modes and their operating region.

The contact mode uses the physical contact between the tip and the substrate. This allows high scan speeds and high resolution, but as it contacts the surfaces, it can damage soft samples and lateral forces can cause artefacts [102, 104].

The non-contact mode excites the cantilever to oscillate at the resonant frequency. The Van Der Waals forces between the substrate and the tip produce a frequency shift in the resonant frequency. One can either keep the frequency constant and use the oscillation amplitude as variable (constant frequency shift image) or use the fluctuations in frequency as a signal (constant height image) [104]. To reduce the effect of the attractive forces, a higher stiffness cantilever is generally used for the non-contact mode than for the contact mode [104].

The intermittent mode is relatively similar to the non-contact mode. However, the tip contacts the substrate very slightly during each oscillation cycle [104]. The single intermittent contact causes a slight loss of energy and the amplitude of vibration changes due to a reduction in the size of the vibrating space. The attractive and repulsive forces affect this mode, but less than in the non-contact mode, resulting in high lateral and vertical resolutions [104].

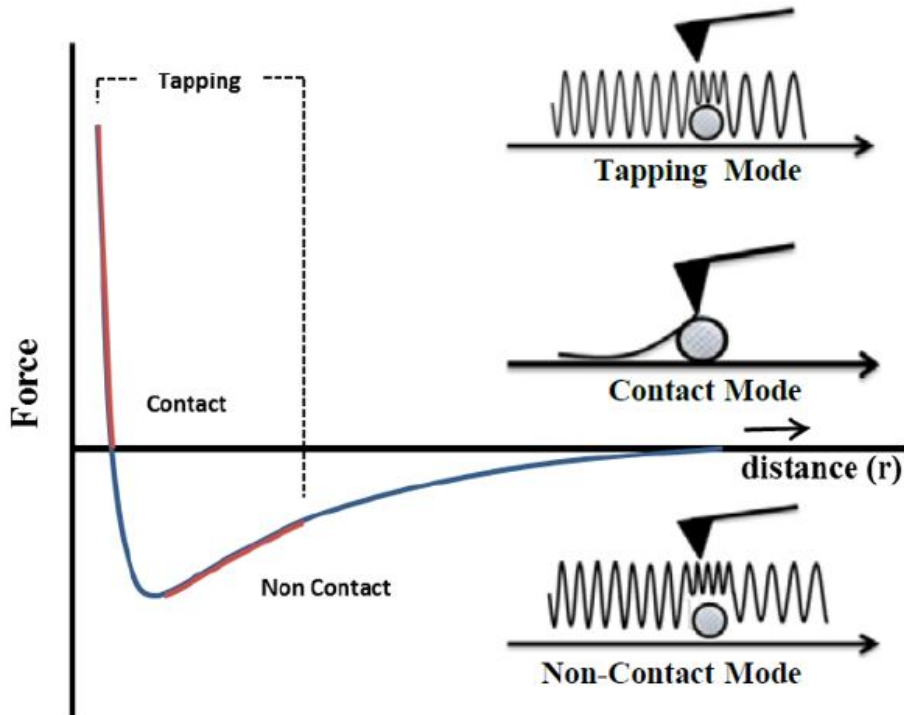


Figure 3.26: AFM modes and the region of the force curve they operate at. In the tapping mode and non-contact mode, the cantilever is excited [104].

Figure 3.27 shows a comparison table from Marrese et al. [104] with the advantages of the various modes. These modes are mainly used for imaging surface topographies. To generate force curves, the cantilever is moved only in the Z direction (not X or Y) and the deflection is measured. The cantilever can be imaged with either a top-view camera or the bottom-view microscope of the AFM. Mirrors are available to image the cantilever from the side. In addition, fluorescence microscopy can be used with the AFM system to visualise specific parts of a substrate.

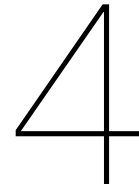
AFM Modes of Operation	Working Principle	Advantage	Disadvantage
Contact Mode	<ul style="list-style-type: none"> Physical contact between the tip and the surface 	<ul style="list-style-type: none"> High scan speeds High resolution 	<ul style="list-style-type: none"> Damage to soft sample Later forces may produce image artefacts
Non-contact Mode	<ul style="list-style-type: none"> No contact between the tip and the sample 	<ul style="list-style-type: none"> Low resolution No damage to sample 	<ul style="list-style-type: none"> Slower scan speed if compared with both contact and tapping mode
Tapping Mode	<ul style="list-style-type: none"> Intermittent and short contact between the sample and the tip 	<ul style="list-style-type: none"> High resolution Minimal damage to sample 	<ul style="list-style-type: none"> Slower scan speed if compared with contact mode

Figure 3.27: Comparison between AFM modes taken from Marrese et al. [104]

3.5.2. AFM actuation

The AFM cantilever holder, for the JPK AFM Nanowizard 4 system, is mounted on a stage, which is supported by a retractable tripod. The tripod is aligned with the substrate using a cone, a groove, and a flat mount. This principle eliminates five degrees of freedom. The translation in the Z direction is not restricted, but the weight of the stage prevents movements in that direction. Stepper motors, can be used to make coarse changes to the Z position of the cantilever.

For much more precise movements, piezo's, near the cantilever mount, are used. For the JPK Nanowizard 4 AFM system, these piezos have a range of 15 μm which can be extended with an additional 100 μm by using the JPK cellhesion module [105]. These piezos provide the movement of the cantilever in the z direction while scanning a substrate. Both the stage and the substrate can be moved independently in the X and Y direction. This can be done with either an automated or manual stage, and can be used to align the cantilever with the viewer and the sample with the cantilever.



Research question

The overarching goal of this research is to fabricate functional microstructures and nanostructures using two-photon polymerization on a 3D printed microfluidic substrate. Although the techniques presented can be applied in a variety of ways, this paper focuses specifically on manufacturing a device for single-cell (surgery) studies. It seeks to optimize and automate multiscale 3D printing in order to produce suspended sharp tip hollow cantilevers with a submicrometre resolution.

In his thesis, ir. Robert Kramer showed the first results on multiscale 3D printing, including features with a resolution of up to one micrometer. Optimization and automation of the printing process opens up many new possibilities and allows easy adaptation for other applications. This research aims to optimize and automate the multiscale printing process to print suspended sharp tip hollow cantilevers with a submicrometre resolution, focussing on ease of handling and fabrication. The combination of the DLP and 2PP printing techniques enable faster production of devices that require production at different scales and resolution.

Cell surgery studies can show the enormous potential of the multiscale 3D printing process. One such study involves the removal of a nucleus from a muscle cell for a disease called facioscapulo-humeral muscular dystrophy (FSHD). Studying the nucleus of a cell provides a lot of information about the regulatory processes in the cell and can help investigate many different diseases.

Currently, the main concerns that prevent researchers from exploring the possibilities of these techniques and conducting experiments with newly designed tools are the inflexibility and cost of current production techniques for making state-of-the-art microfluidic AFM cantilevers. Changing the design of a cantilever currently requires changes throughout the production line (masks, etc.). 3D printing techniques offer greater flexibility in both design and production, which may be beneficial for the faster development of microfluidic AFM cantilevers for single-cell studies.

Thus, the current state-of-the-art in cell manipulation techniques and their applications, combined with our ever-growing understanding of the functioning and behaviour of cells, present several interesting possibilities for future research. This research aims to merge our current knowledge of cells with the advancement of existing micro, and nanotechnology, in search of new applications that can help study diseases on the single-cell level and help towards finding cures.

In conclusion, this research aims to merge our current biological knowledge of cells with the latest micro- and nanotechnology, in order to develop new tools to study diseases on single-cell level. Special focus is set on ease of handling and a lean fabrication process of the newly developed tools.

Two clear knowledge gaps have been identified:

- **Biological gap:** Nucleus extraction (from a multinucleated cell) and the influence on cell viability using other techniques than the manually operated glass pipettes has barely been researched.
- **Technical gap:** Relatively little is known about the use of polymer cantilevers fabricated using 2PP. Only Kramer et al. [22] have shown that polymer probes can be used to aspirate a cell. However, no optimization has been performed for the development of 2PP cantilevers for cellular puncture application or nucleus extraction. The possibilities of “grabbing”, transporting and depositing the nucleus at a desired location using 2PP cantilevers has not been performed. Moreover, the impact on viability of the cells of such a procedure is still unknown and needs to be investigated.

Filling these knowledge gaps may help biomedical researchers find answers to their questions regarding the behaviour of the cell and the possibilities in altering its properties and functioning by swapping, changing or removing the nucleus. Further development of these technologies may eventually lead to finding new cures and to a better understanding of complex diseases such as FSHD.

The identification of the mentioned gaps during this literature research has led to the following main research question:

How to manufacture a sharp tip hollow cantilever with submicron resolution for nucleus extraction using two photon polymerization on top of a 3D printed microfluidic interface?

Using cell studies as target application of multiscale 3D printing yields the following secondary research question:

How to aspirate a nucleus from a multi-nuclear cell without damaging the nucleus, while keeping the cell alive?

To find an answer to this research question, it is important to address these sub-questions:

- How to optimize a microfluidic interface for use with two photon polymerization?
- How to obtain a leak tight 3D printed microfluidic interface that does not require glue to couple tubing?
- How to obtain a leakage free multiscale 3D printed (2PP and DLP) cantilever?
- How to obtain a cantilever, made using two photon polymerization, with a stiffness smaller than 2 N/m?
- What should be the tip geometry that does not result in the destruction of the cell during a puncture procedure?
- Which aperture and channel size is appropriate to aspirate nucleus without damage?
- Do we need surface functionalization while performing the cell biopsy?
- How to dispense an aspirated nucleus at a desired location?

Bibliography

- [1] X. Li and A.P. Lee. Chapter 2 - high-throughput microfluidic single-cell trapping arrays for biomolecular and imaging analysis. In Daniel A. Fletcher, Junsang Doh, and Matthieu Piel, editors, *Microfluidics in Cell Biology Part C: Microfluidics for Cellular and Subcellular Analysis*, volume 148 of *Methods in Cell Biology*, pages 35–50. Academic Press, 2018.
- [2] J.R. Heath, A. Ribas, and P.S. Mischel. Single-cell analysis tools for drug discovery and development. *Nature Reviews Drug Discovery*, 15(3):204–216, 2016.
- [3] Lukelhood. Facioscapulohumeral muscular dystrophy muscular dystrophy muscle diagram. https://commons.wikimedia.org/wiki/File:Facioscapulohumeral_muscular_dystrophy_muscular_dystrophy_muscle_diagram.png, Dec 2020.
- [4] D. Cooper and M. Upadhyaya. *FSHD facioscapulohumeral muscular dystrophy: clinical medicine and molecular cell biology*. FSHD): Clinical Medicine and Molecular Cell Biology. BIOS Scientific Publishers, 1 edition, 2004.
- [5] T. G.J. Loonen, C. G.C. Horlings, S. C.C. Vincenten, C. H.G. Beurskens, S. Knuijt, G. W.A.M. Padberg, J. M. Statland, N. C. Voermans, T. J.J. Maal, B. G.M. van Engelen, and K. Mul. Characterizing the face in facioscapulohumeral muscular dystrophy. *Journal of Neurology*, 268(4):1342–1350, 2020.
- [6] K.R. Wagner. Facioscapulohumeral Muscular Dystrophies. *CONTINUUM Lifelong Learning in Neurology*, 25(6):1662–1681, 2019.
- [7] R Statland, R.; Tawil. Facioscapulohumeral Muscular Dystrophy. *International Neurology: A Clinical Approach*, (December):223–224, 2010.
- [8] R. Statland, J. M., Odrzywolski, K. J., Shah, B., Henderson, D., Fricke, A. F., van der Maarel, S. M., Tapscott, S. J., Tawil. Immunohistochemical Characterization of Facioscapulohumeral Muscular Dystrophy Muscle Biopsies. *Journal of Neuromuscular Diseases*, (2(3)):291–299, 2015.
- [9] L.N. Geng, Z. Yao, L. Snider, A.P. Fong, J.N. Cech, J.M. Young, S.M. Van Der Maarel, W.L. Ruzzo, R.C. Gentleman, and S.J. Tapscott. mediators : Implications for facioscapulohumeral dystrophy. 22(1):38–51, 2013.
- [10] A. M. Rickard, L. M. Petek, and D. G. Miller. Endogenous dux4 expression in fshd myotubes is sufficient to cause cell death and disrupts rna splicing and cell migration pathways. *Human Molecular Genetics*, 24(20):5901–5914, May 2015.
- [11] L. Snider, L.N. Geng, R.J.L.F. Lemmers, M. Kyba, C.B. Ware, A.M. Nelson, R. Tawil, G.N. Filippova, S.M. van der Maarel, S.J. Tapscott, and D.G. Miller. Facioscapulohumeral dystrophy: Incomplete suppression of a retrotransposed gene. *PLOS Genetics*, 6(10):1–14, 10 2010.
- [12] A. Tassin, D. Laoudj-Chenivesse, C. Vanderplanck, M. Barro, S. Charron, E. Anseau, Y. Chen, J. Mercier, F. Coppée, and A. Belayew. Dux4 expression in fshd muscle cells: how could such a rare protein cause a myopathy? *Journal of Cellular and Molecular Medicine*, 17(1):76–89, 2013.
- [13] K.R.Q. Lim and T. Yokota. Genetic approaches for the treatment of facioscapulohumeral muscular dystrophy. *Frontiers in Pharmacology*, 12:281, 2021.
- [14] E.N. Marieb and K. Hoehn. *Human Anatomy & Physiology*. Pearson, 10th edition, 2016.
- [15] G. Karp. *Cell biology*. Wiley, sixth edition, 2010. ISBN: 9780470505762.

- [16] G.J. Tortora and B Derrickson. *Principles of Anatomy & Physiology*. Wiley, 13th, vol. edition, 2011.
- [17] S. Abmayr and G. Pavlath. Myoblast fusion: Lessons from flies and mice. *Development (Cambridge, England)*, 139:641–56, 02 2012.
- [18] E.S. Perillo, M. and Folker. Specialized positioning of myonuclei near cell-cell junctions. *Frontiers in Physiology*, 9(NOV):1–10, 2018.
- [19] L. Slomianka. The muscle. <http://www.lab.anhb.uwa.edu.au/mb140/CorePages/Muscle/Muscle.htm>, 2009.
- [20] A. Manhart, S. Windner, M. Baylies, and A. Mogilner. Mechanical positioning of multiple nuclei in muscle cells. *PLoS Computational Biology*, 14(6):1–25, 2018.
- [21] S. C. Watkins and M. J. C. A quantitative study of myonuclear and satellite cell nuclear size in Duchenne’s muscular dystrophy, polymyositis and normal human skeletal muscle. *The Anatomical Record*, 222(1):6–11, 1988.
- [22] R.C. L. N. Kramer, E. J. Verlinden, L. Angeloni, A. van den Heuvel, L. E. Fratila-Apachitei, Si. M. van der Maarel, and M.K. Ghatkesar. Multiscale 3D-printing of microfluidic AFM cantilevers. *Lab on a Chip*, pages 311–319, 2020.
- [23] B. Alberts, D. Bray, K. Hopkin, A. Johnson, J. Lewis, M. Raff, K. Roberts, and P. Walter. *Essential cell biology*. Garland Science, fourth edition, 2014.
- [24] M. Lucy. *Membrane Structural Biology: with Biochemical and Biophysical Foundations*. Cambridge, 2008.
- [25] V. Idone, C. Tam, J. W. Goss, D. Toomre, M. Pypaert, and N.W. Andrews. Repair of injured plasma membrane by rapid Ca²⁺ dependent endocytosis. *Journal of Cell Biology*, 180(5):905–914, 2008.
- [26] P.L. McNeil and R.A. Steinhardt. Plasma membrane disruption: Repair, prevention, adaptation. *Annual Review of Cell and Developmental Biology*, 19(1):697–731, 2003. PMID: 14570587.
- [27] E. Moeendarbary and A.R. Harris. Cell mechanics: Principles, practices, and prospects. *Wiley Interdisciplinary Reviews: Systems Biology and Medicine*, 6(5):371–388, 2014.
- [28] A.J. Bidhendi and R.K. Korhonen. A Finite Element Study of Micropipette Aspiration of Single Cells : Effect of Compressibility. *Computational and mathematical methods in medicine*, 2012.
- [29] N. Caille, O. Thoumine, Y. Tardy, and J.J. Meister. Contribution of the nucleus to the mechanical properties of endothelial cells. *Journal of Biomechanics*, 35(2):177–187, 2002.
- [30] M. Takaza, K.M. Moerman, J. Gindre, G. Lyons, and C.K. Simms. The anisotropic mechanical behaviour of passive skeletal muscle tissue subjected to large tensile strain. *Journal of the Mechanical Behavior of Biomedical Materials*, 17:209–220, 2013.
- [31] C. Dejous, H. Hallil, V. Raimbault, R. Rukkumani, and J.V. Yakhmi. Chapter 20 - using microsensors to promote the development of innovative therapeutic nanostructures. In D. Fikai and A.M. Grumezescu, editors, *Nanostructures for Novel Therapy*, Micro and Nano Technologies, pages 539 – 566. Elsevier, 2017.
- [32] A.M. Collinsworth, S. Zhang, W.E. Kraus, and G.A. Truskey. Apparent elastic modulus and hysteresis of skeletal muscle cells throughout differentiation. *American Journal of Physiology-Cell Physiology*, 283(4):C1219–C1227, 2002. PMID: 12225985.
- [33] M.R. Angle, A. Wang, A. Thomas, A.T. Schaefer, and N.A. Melosh. Penetration of cell membranes and synthetic lipid bilayers by nanopores. *Biophysical Journal*, 107(9):2091–2100, 2014.

- [34] A. Meister, M. Gabi, P. Behr, P. Studer, J. Vörös, P. Niedermann, J. Bitterli, J. Polesel-Maris, M. Liley, H. Heinzmann, and T. Zambelli. FluidFM: Combining atomic force microscopy and nanofluidics in a universal liquid delivery system for single cell applications and beyond. *Nano Letters*, 9(6):2501–2507, 2009.
- [35] K.P. McCreery, X. Xu, A.K. Scott, A.K. Fajrial, S. Calve, X. Ding, and C.P. Neu. Nuclear Stiffness Decreases with Disruption of the Extracellular Matrix in Living Tissues. *Small*, 17(6):1–11, 2021.
- [36] K. Yum, N. Wang, and M.F. Yu. Nanoneedle: A multifunctional tool for biological studies in living cells. *Nanoscale*, 2(3):363–372, 2010.
- [37] F. Guilak, J.R. Tedrow, and R. Burgkart. Viscoelastic properties of the cell nucleus. *Biochemical and Biophysical Research Communications*, 269(3):781–786, 2000.
- [38] A. C. Rowat, L. J. Foster, M. M. Nielsen, M. Weiss, and J. H. Ipsen. Characterization of the elastic properties of the nuclear envelope. *Journal of the Royal Society Interface*, 2(2):63–69, 2005.
- [39] A. Vaziri and M.R.K. Mofrad. Mechanics and deformation of the nucleus in micropipette aspiration experiment. *Journal of Biomechanics*, 40(9):2053–2062, 2007.
- [40] P.L. McNeil. Repairing a torn cell surface: make way, lysosomes to the rescue. *Journal of Cell Science*, 115(5):873–879, 2002.
- [41] O. Guillaume-Gentil, R. Grindberg, R. Kooger, L. Dorwling-Carter, V. Martinez, D. Ossola, M. Pilhofer, and J.A. Zambelli, T.and Vorholt. Tunable Single-Cell Extraction for Molecular Analyses. *Cell*, 166(2):506–516, 2016.
- [42] R.A. Seger, P. Actis, M. Penfold, C.and Maalouf, B. Vilozny, and N. Pourmand. Voltage controlled nano-injection system for single-cell surgery. *Nanoscale*, 4(19):5843–5846, 2012.
- [43] Cytosurge. single cell injection: Cytosurge. <https://www.cytosurge.com/page/singlecellinjection>, 2019.
- [44] O. Guillaume-Gentil, E. Potthoff, D. Ossola, P. Dörig, T. Zambelli, and J.A. Vorholt. Force-controlled fluidic injection into single cell nuclei. *Small*, 9(11):1904–1907, 2013.
- [45] P. Shende, M. Sardesai, and R. S. Gaud. Micro to nanoneedles: a trend of modernized transepidermal drug delivery system. *Artificial Cells, Nanomedicine, and Biotechnology*, 46(1):19–25, 2018. PMID: 28355887.
- [46] B.P. Nadappuram, P. Cadinu, A. Barik, A.J. Ainscough, M.J. Devine, M. Kang, J. Gonzalez-Garcia, J.T. Kittler, K.R. Willison, R. Vilar, P. Actis, B. Wojciak-Stothard, S.H. Oh, A.P. Ivanov, and J.B. Edel. Nanoscale tweezers for single-cell biopsies. *Nature Nanotechnology*, 14(1):80–88, 2019.
- [47] Cytosurge. Fluidfm nanosyringe. <https://www.cytosurge.com/shop/product/fluidfm-nanosyringe-855>.
- [48] M. Nouri-Goushki, M. J. Mirzaali, L. Angeloni, D. Fan, M. Minneboo, M. K. Ghatkesar, U. Staufer, L. E. Fratila-Apachitei, and A. A. Zadpoor. 3D Printing of Large Areas of Highly Ordered Submicron Patterns for Modulating Cell Behavior. *ACS Applied Materials and Interfaces*, 12(1):200–208, 2020.
- [49] R.C.L.N. Kramer. Multiscale 3d printing of a suspended hollow microfluidic device. *Thesis report*, 2018. <http://resolver.tudelft.nl/uuid:006b4cb6-a490-4160-a6e2-6b74d24248e4>.
- [50] World Precision instruments (WPI). Pre-pulled glass pipettes. <https://www.wpiinc.com/var-3564-pre-pulled-glass-pipettes>, 2019.
- [51] P. Khanna. *Cellular microinjection for therapeutic and research applications*. Woodhead Publishing Limited, 2012.

- [52] K.G. Engstrom and H.J. Meiselman. Fabrication of glass micropipettes: a semi automatic approach for trimming the pipette tip. *Biorheology*, 29(1):499–506, 1993.
- [53] A. Pillariseti, M. Pekarev, A.D. Brooks, and J.P. Desai. Evaluating the effect of force feedback in cell injection. *IEEE Transactions on Automation Science and Engineering*, 4(3):322–331, 2007.
- [54] Y. Zhao, H. Sun, X. Sha, L. Gu, Z. Zhan, and W.J. Li. A Review of Automated Microinjection of Zebrafish Embryos. *Micromachines*, 2018.
- [55] T.S. Hug, T Biss, N.F. de Rooij, and U. Staufer. Generic fabrication technology for transparent and suspended microfluidic and nanofluidic channels. *Transducers '05 conference*, pages 1191–1194, 2005.
- [56] N. Moldovan, K. Kim, and H.D Espinosa. Design and Fabrication of a Novel Microfluidic Nanoprobe. *Journal of microelectromechanical systems*, 15(1):204–213, 2006.
- [57] M.K. Ghatkesar, H.H.P. Garza, and U. Staufer. Hollow AFM cantilever pipette. *MICROELECTRONIC ENGINEERING*, 124:22–25, 2014.
- [58] A. Lewis, Y. Kheifetz, E. Shambrodt, A. Radko, E. Khatchatryan, and C. Sukenik. Fountain pen nanochemistry: Atomic force control of chrome etching. *Applied Physics Letters*, 75(17):2689–2691, 1999.
- [59] K. Kim, N. Moldovan, and H.D. Espinosa. Patterning techniques A Nanofountain Probe with Sub-100 nm Molecular Writing Resolution**. *www.small-journal.com*, 1(6):632–635, 2005.
- [60] Cytosurge. Cytosurge microfluidic probes. <https://www.cytosurge.com/page/probes>, 2019.
- [61] P. Frederix, P. Werten, and D. Yablon. Fluidfm: Precise fluidic positioning and delivery platform with applications in cell biology and soft matter. *Microscopy and Analysis*, 2018.
- [62] Sigma-aldrich. Sigmacote siliconizing reagent for glass and other surfaces: Sigma-aldrich. <https://www.sigmaaldrich.com/NL/en/product/sigma/sl2>, 2021.
- [63] P. Hsu, J. Lin, Y. Wu, W. Hung, and A.G. Cullis. Sensors and Actuators B : Chemical Ultra-sensitive polysilicon wire glucose sensor using a hydrophobic fumed silica nanoparticle mixture as the sensing membrane. *Sensors and Actuators B: Chemical*, 142:273–279, 2009.
- [64] C.M. Glee. Photolithography. <http://en.wikipedia.org/w/index.php?title=Photolithography&oldid=943711334>, 2020.
- [65] P. Rai-Choudhury. *Handbook of microlithography, micromachining, and microfabrication*, volume 2. SPIE Optical Engineering Press, 1997.
- [66] G.T.A. Kovacs, N.I. Maluf, and K.E. Petersen. Bulk micromachining of silicon. *Proceedings of the IEEE*, 86(8):1536–1551, 1998.
- [67] V.R. Mamilla and K.S. Chakradhar. Micro machining for micro electro mechanical systems (mems). *Procedia Materials Science*, 6:1170 – 1177, 2014. 3rd International Conference on Materials Processing and Characterisation (ICMPC 2014).
- [68] J.M Bustillo, Roger T. Howe, R.S. Muller, and L. Fellow. Surface Micromachining for Microelectromechanical Systems. *Proceedings of the IEEE*, 86(8), 1998.
- [69] M. Madou and C. Wang. *Photolithography*, pages 2051–2060. Springer Netherlands, Dordrecht, 2012.
- [70] C. Bastiancich, P. Danhier, V. Préat, and F. Danhier. Anticancer drug-loaded hydrogels as drug delivery systems for the local treatment of glioblastoma. *Journal of Controlled Release*, 243:29 – 42, 2016.

- [71] N. Mojarad, M. Hojeij, L. Wang, J. Gobrecht, and Y. Ekinici. Single-digit-resolution nanopatterning with extreme ultraviolet light for the 2.5 nm technology node and beyond. *Nanoscale*, 7(9):4031–4037, 2015.
- [72] E. B. Brousseau, S. S. Dimov, and D. T. Pham. Some recent advances in multi-material micro- and nano-manufacturing. *International Journal of Advanced Manufacturing Technology*, 47(1–4):161–180, 2010.
- [73] A. Gaitas and R.w. Hower. SU-8 microcantilever with an aperture, fluidic channel, and sensing mechanisms for biological and other applications. *Micro Nanolithography MEMS MOEMS*, 13(3):1–8, 2014.
- [74] K. Cicha, T. Koch, J. Torgersen, Z. Li, R. Liska, and J. Stampfl. Young's modulus measurement of two-photon polymerized micro-cantilevers by using nanoindentation equipment. *Journal of Applied Physics*, 112(9):094906, 2012.
- [75] G. Göring, P.I. Dietrich, M. Blaicher, S. Sharma, J.G. Korvink, T. Schimmel, C. Koos, and H. Hölscher. Tailored probes for atomic force microscopy fabricated by two-photon polymerization. *Applied Physics Letters*, 109(6):063101, 2016.
- [76] X. Chen, A. Kis, A. Zettl, and C.R. Bertozzi. A cell nanoinjector based on carbon nanotubes. *PNAS*, 104(20):8219, 2007.
- [77] M. Mauro, R. Battaglia, G. Ferrini, R. Puglisi, D. Balduzzi, and A. Galli. Single microparticles mass measurement using an AFM cantilever resonator. *arXiv*, pages 1–5, 2014.
- [78] T. Burg, M. Godin, S. Knudsen, W. Shen, G. Carlson, J. Foster, K. Babcock, and S. Manalis. Weighing of biomolecules, single cells and single nanoparticles in fluid. *Nature*, 446:1066–9, 05 2007.
- [79] S. Olcum, N. Cermak, S.C. Wasserman, K.S. Christine, H. Atsumi, K.R. Payer, W. Shen, J. Lee, A.M. Belcher, S.N. Bhatia, and S.R. Manalis. Weighing nanoparticles in solution at the attogram scale. *Proceedings of the National Academy of Sciences of the United States of America*, 111(4):1310–1315, 2014.
- [80] A. Mark, N. Helfricht, A. Rauh, M. Karg, and G. Papastavrou. The Next Generation of Colloidal Probes: A Universal Approach for Soft and Ultra-Small Particles. *Small*, 15(43), 2019.
- [81] H.H.P. Garza, M. Ghatkesar, and U. Staufer. Aspiration through hollow cantilever-based nanopipette by means of evaporation. *Micro and Nano Letters*, 8:p. 758 – 761, 09 2013.
- [82] V. Martinez, F. Stauffer, M. Adagunodo, C. Forro, J. Vörös, and A. Larmagnac. Stretchable silver nanowire–elastomer composite microelectrodes with tailored electrical properties. *ACS applied materials and interfaces*, 7, 06 2015.
- [83] M. Kaur and A. K. Srivastava. Photopolymerization: A review. *Journal of Macromolecular Science - Polymer Reviews*, 42(4):481–512, 2002.
- [84] X. Zhou, Y. Hou, and J. Lin. A review on the processing accuracy of two-photon polymerization. *AIP Advances*, 5(3), 2015.
- [85] S. Wu, J. Serbin, and M. Gu. Two-photon polymerisation for three-dimensional micro-fabrication. *Journal of Photochemistry and Photobiology A: Chemistry*, 181(1):1–11, 2006.
- [86] J.T. Fourkas. Chapter 1.3 - fundamentals of two-photon fabrication. In Tommaso Baldacchini, editor, *Three-Dimensional Microfabrication Using Two-photon Polymerization*, Micro and Nano Technologies, pages 45–61. William Andrew Publishing, Oxford, 2016.
- [87] Y.R. Shen. Nonlinear optical susceptibilities. In K.H.J. Buschow, R.W. Cahn, M.C. Flemings, B. Ilshner, E.J. Kramer, S. Mahajan, and P. Veysseyre, editors, *Encyclopedia of Materials: Science and Technology*, pages 6249 – 6255. Elsevier, Oxford, 2001.

- [88] Fraunhofer ISC. TWO-PHOTON POLYMERIZATION. https://www.isc.fraunhofer.de/content/dam/isc/de/documents/Publikationen/Two_Photon_polymerization_femtosecond_laser_pulses_as_a_tool_for_true_3D_micromachining.pdf, 2019.
- [89] C. Accoto, A. Qualtieri, F. Pisanello, C. Ricciardi, C. F. Pirri, M. D. Vittorio, and F. Rizzi. Two-photon polymerization lithography and laser doppler vibrometry of a su-8-based suspended microchannel resonator. *Journal of Microelectromechanical Systems*, 24(4):1038–1042, 2015.
- [90] E. D. Lemma, F. Rizzi, T. Dattoma, B. Spagnolo, L. Sileo, A. Qualtieri, M. De Vittorio, and F. Pisanello. Mechanical properties tunability of three-dimensional polymeric structures in two-photon lithography. *IEEE Transactions on Nanotechnology*, 16(1):23–31, 2017.
- [91] Nanoscribe GmbH. Nanoscribe. <https://www.nanoscribe.com/en/>, 2020.
- [92] S Wang, Y. Yu, H. Liu, K.T.P. Lim, B.M. Srinivasan, Y.W. Zhang, and J.K.W. Yang. Sub-10-nm suspended nano-web formation by direct laser writing. *Nano Futures*, 2(2):025006, may 2018.
- [93] A.J. Gross and K. Bertoldi. Additive manufacturing of nanostructures that are delicate, complex, and smaller than ever. *Small*, 15(33):1902370, 2019.
- [94] Zeiss. Zeiss axio observer for life science research. <https://www.zeiss.com/microscopy/int/products/light-microscopes/axio-observer-for-biology/definite-focus.html>, 2021.
- [95] C. Júlio. Advanced imaging uic. <http://facilities.igc.gulbenkian.pt/microscopy/microscopy-zeiss-hcs.php>, 2013.
- [96] Envisiontec GMBH. <https://envisiontec.com/wp-content/uploads/2017/04/3sp-white-paper-2017-the-ultimate-guide-to-3d-printing-for-manufacturing-and-production.pdf>, Apr 2017.
- [97] S. Catarino, R. Lima, and G. Minas. *Bioinspired Materials for Medical Applications*. Elsevier Ltd., 2017.
- [98] J. Zhang, Q. Hu, S. Wang, J. Tao, and M. Gou. Digital light processing based three-dimensional printing for medical applications. *International Journal of Bioprinting*, 6(1):12–27, 2020.
- [99] S.K. Saha, D. Wang, V.H. Nguyen, Y. Chang, J.S. Oakdale, and S.C. Chen. Scalable submicrometer additive manufacturing. *Science*, 366(6461):105–109, 2019.
- [100] S. Soman, P., Chung, P. H., Zhang, A. P., & Chen. Digital microfabrication of user-defined 3D microstructures in cell-laden hydrogels. *Biotechnology and bioengineering*, 110(11):3038–3047, 2013.
- [101] J.P. Fouassier and L. Jacques. *Photoinitiators for polymer synthesis: Scope, reactivity and efficiency*. Wiley-VCH, 2012.
- [102] G. Binnig, C. F. Quate, and Ch. Gerber. Atomic force microscope. *Phys. Rev. Lett.*, 56:930–933, Mar 1986.
- [103] G. Zeng, Y. Duan, F. Besenbacher, and M. Dong. *Nanomechanics of Amyloid Materials Studied by Atomic Force Microscopy*. 03 2012.
- [104] M. Marrese, V. Guarino, and L. Ambrosio. Atomic Force Microscopy: A Powerful Tool to Address Scaffold Design in Tissue Engineering. *Journal of Functional Biomaterials*, 8(1):7, 2017.
- [105] JPK Instruments AG. Cellhesion module - jpk bioafm: Bruker. <https://www.jpk.com/products/cell-tissue-mechanics-and-adhesion/cellhesion-module>, 2020.

Part II
Paper

List of figures included in the paper

(1)	DLP microfluidic interface design	54
(2)	2PP print design	55
(3)	Describe block splitting of the 2PP print	56
(4)	Schematic diagram of a nucleus aspiration experiment	59
(5)	DLP printing results	60
(6)	2PP printing results	61
(7)	LDV measurement versus COMSOL simulation	62
(8)	Dispensing a droplet	62
(9)	View of the flow during experiment	62
(10)	QI imaging	63
(11)	Adhesion experiment	63
(12)	Force curve of cell puncture experiment	64
(13)	Aspirating a nucleus	65

Multiscale 3D printing of suspended hollow microfluidic cantilevers for cell nucleus extraction

ABSTRACT - This paper presents a 3D-printed microfluidic atomic force microscope (AFM) cantilever that can puncture a cell membrane with its sharp tip and aspirate the nucleus through a microscale aperture near the tip. The microfluidic AFM cantilever is printed using two-photon polymerization (2PP) onto a microfluidic interface, manufactured using digital light processing (DLP). The microfluidic interface serves as a substrate for the 2PP printing and can also be connected to the microfluidic pressure controller (the connection can withstand up to 6.9 bar without adhesive) and has a tight fit on the AFM cantilever holder. The AFM system allows precise force feedback during experiments, while the microfluidic controller allows precise fluid handling. This research focused on developing a microfluidic AFM cantilever to extract a nucleus from a multinucleated muscle cell to study facioscapulohumeral muscular dystrophy (FSHD). FSHD is a genetic muscle disease that begins in a nucleus and for which there is no cure yet. The state-of-the-art microfluidic AFM cantilevers cannot be used to remove the nucleus from a cell completely. Microfluidic AFM cantilevers with a length of 500 μm , a height of 20 μm and a width of 30 μm were manufactured using 2PP. The cantilevers have an elliptical channel with a height of 15 μm and a width of 25 μm . The stiffness of the cantilevers was 1.84 ± 0.24 N/m. Sharp tips were achieved with a tip radius of 270 nm. An elliptical aperture with a width of 3.1 μm and a height of 3.8 μm , was created adjacent to the apex of the tip. The smallest aperture achieved had a diameter of 1 μm . By optimizing the DLP prints, automated 2PP printing was achieved, allowing rapid prototyping of 3D printed microfluidic AFM cantilevers. Because the 2PP print is designed in independent modules, the fabrication methods can be used for different types of FluidFM research. The modularity allows the geometry to be optimized for different types of single-cell experiments. AFM surface imaging, cell membrane puncture, cell nucleus aspiration, and cell adhesion studies have been successfully demonstrated using 3D printed microfluidic AFM cantilevers. The results prove that this multiscale 3D printing method can be used to fabricate microfluidic probes used for cell experiments and have conventional AFM capabilities. The printing methods can be used to manufacture various types of suspended microfluidic devices to perform a single-cell biopsy and biophysical characterization of single-cells.

1 Introduction

Every cell in the human body is unique in its composition, shape and behaviour. Even if cells in certain tissues are morphologically and genetically identical, the individual cells can behave dramatically differently. These cell-to-cell variations can occur due to differences in cell development and cell cycles, genetic drift, transcription events, and the intrinsic stochastic nature of cellular processes [1]. Heterogeneity between cells can have significant consequences for tissue function and health. It also makes the development of disease models extremely complex [2]. These disease models are needed to understand the mechanisms behind diseases and discover new cures targeting specific cells. Conventional cell experiments do not capture the individual characteristics of cells but rather show the average response of a population of cells [1]. Perturbing, disrupting, altering, and manipulating these individual cells could provide crucial information about their mechanical properties, behaviour, and response to chemical, electrical or mechanical stimuli. These single-cell-level measurements can help researchers characterise healthy and diseased cells by determining their mechanical phenotype. Single-cell anal-

ysis tools are essential to study cells in tissues that are either genetically, functionally, or compositionally heterogeneous [2]. These tools make it possible to study the behaviour of a single cell, which is of paramount importance as a large number of biological and medical questions can be investigated using single-cell analysis [1].

Fluidic force microscopy (FluidFM) is an important technique for research at the single-cell level [3]. FluidFM uses an atomic force microscope (AFM) in combination with hollow (microfluidic) cantilevers to study single-cells. The high-sensitivity AFM apparatus used for FluidFM research not only allows imaging of the sample and positioning of the hollow cantilever but also provides highly sensitive force control through a force feedback loop [3]. The microfluidic AFM cantilevers, consisting of a suspended cantilever with a microchannel combined with a sharp tip with a (sub)micrometre-sized aperture, can be connected to a microfluidic pressure controller. This allows the delivery and aspiration of liquids and small particles [3]. Common types of single-cell experiments using FluidFM are cell manipulation (isolation and displacement of cells), cell injection (injection of compounds into a cell), cell extraction (removal of organelles or fluids from a cell) and cell detachment (measurement of forces between cells and the

substrate or forces between cells). [3–6].

State-of-the-art microchannel AFM cantilevers are typically fabricated using classical microfabrication and nanofabrication techniques that require selective etching of silicon wafers with different masks (photolithographically patterned) and deposited layers (e.g. silicon oxide or silicon nitride). These classical fabrication techniques require expensive and high-maintenance equipment, hazardous chemicals, and repetitive patterning, deposition, and etching. The latter increases the production time for a batch of cantilevers. Other disadvantages of these fabrication techniques include design limitations (depending on wafer thickness, deposited layer thickness and etch properties), the need for new masks for each design change, and mounting the silicon chip with the cantilever on a microfluidic connector, which requires alignment and adhesives. However, the main advantage of the classical technique is that once the design is good, many devices can be manufactured in parallel on one wafer. The classical fabrication techniques have in common that they rely on material removal to obtain the final geometry.

3D printing is a technique that can overcome the limitations of classical manufacturing techniques. 3D printing is based on the principle of adding material to the geometry rather than selectively removing it. 3D printing enables access to the third dimension, which allows greater device complexity and the integration of more functions into a single device [7]. Therefore, 3D printing enables the fabrication of true 3D structures instead of the 2.5D of classical techniques. Submicron resolution is required for the fabrication of microfluidic AFM cantilevers. The only 3D printing technique that has a resolution in this range is two-photon polymerisation (2PP). 2PP printing techniques have been used to print structures less than 100 nm in size and pores as small as 500 nm have been printed [8]. However, the printing process is relatively slow as it scans a single voxel through the photoresist. 2PP printing does not require masks or the deposition of (sacrificial) layers, which means the design can be changed each time it is printed. Another advantage of the 2PP process is that it can be adapted for printing on a wide range of substrates, including polymers.

Kramer et al. [9] have demonstrated the feasibility of 2PP printing for the fabrication of (microfluidic) AFM cantilevers. Using 2PP printing of the (microfluidic) AFM cantilevers, Kramer et al. [9] were able to obtain a variety of geometries for both cantilevers and tips that cannot be fabricated using classical fabrication techniques. Kramer et al. [9] also demonstrated the feasibility of multiscale 3D printing for FluidFM applications.

In this work, the printing process developed by Kramer et al. [9] was optimised in order to achieve a high degree of automation of the printing and to allow a higher printing resolution with more accurate and reproducible results without significantly increasing the printing time.

A similar multiscale 3D printing approach was used to print microfluidic AFM cantilevers onto a microfluidic interface printed using digital light processing (DLP). By printing 2PP structures directly onto a DLP print, the parts that require lower resolution can be printed quickly (DLP), while the other parts can be printed at a high resolution (2PP).

Combining the two printing techniques also eliminates the need for manual bonding or assembly steps.

A high degree of printing automation was achieved by sputtering a gold thin film onto the DLP print. This enabled automatic detection of the interface between the DLP-printed polymer and the 2PP photoresist, eliminating the need for the previously required manual interface search step. This automatic interface finding allowed for leak-tight, reproducible and more accurate 2PP prints. A transparent DLP print material improved the adhesion between the two prints, further enhancing reproducibility. Using the 63x objective and a different photoresist, combined with optimizing the design and print parameters, resulted in higher resolution prints with smaller features. By increasing the galvoacceleration, the increase in printing time was limited to only a few minutes per print, compared to the work of Kramer et al. [9]. The shape of the DLP-printed microfluidic interface was optimized to fit onto an AFM holder and align the cantilever automatically. A special fluidic connector allowed the interface to be connected to a microfluidic controller without adhesive bonding. The latter improved the handling of the devices.

Conventional AFM experiments and FluidFM experiments demonstrated the functionality of the 3D printed microfluidic AFM cantilever. In the conventional AFM experiments, different surface topologies were imaged with the microfluidic AFM cantilever. Furthermore, it was demonstrated that the microfluidic cantilevers could be used to dispense fluids. In the FluidFM experiments, three types of single-cell experiments were performed to demonstrate the wide range of applications and functionalities of the 3D-printed microfluidic AFM cantilevers. The microfluidic AFM cantilevers were used to detach cells from surfaces, puncture cells, and extract a cell nucleus.

The cell detachment experiments demonstrated the capability of the developed devices to potentially be used for measuring cell adhesion forces, which is a fundamental process regulating many cell functions, such as spreading, migration and differentiation.

The cell puncture experiments demonstrated the potential capability of the devices for use as microsyringes for injecting material into living cells or extracting material from them. The latter can be used for non-destructive extraction of cytoplasm for single-cell molecular analysis and single-cell transcriptomics. The response of a cell to an injected drug can be studied without having to consider the transport across the plasma membrane.

Finally, the 3D-printed polymer microfluidic AFM cantilevers were used to extract an entire nucleus from a living multinucleated cell for the first time. The latter paves the way for a new approach for studying the nucleus of a cell. Using the extracted nucleus to perform single nucleus transcriptomics improves the ability to study diseased and healthy nuclei without lysing the cells, thus preserving cell viability. It also has the potential to be used for the exchange of nuclei between cells without affecting the cell's viability. If this proves successful, the nucleus of a mononuclear cell could also be replaced. An application for single nucleus extraction is facioscapulohumeral muscular dystrophy (FSHD). FSHD is a muscle disease in which only a limited number of nuclei of skeletal muscle

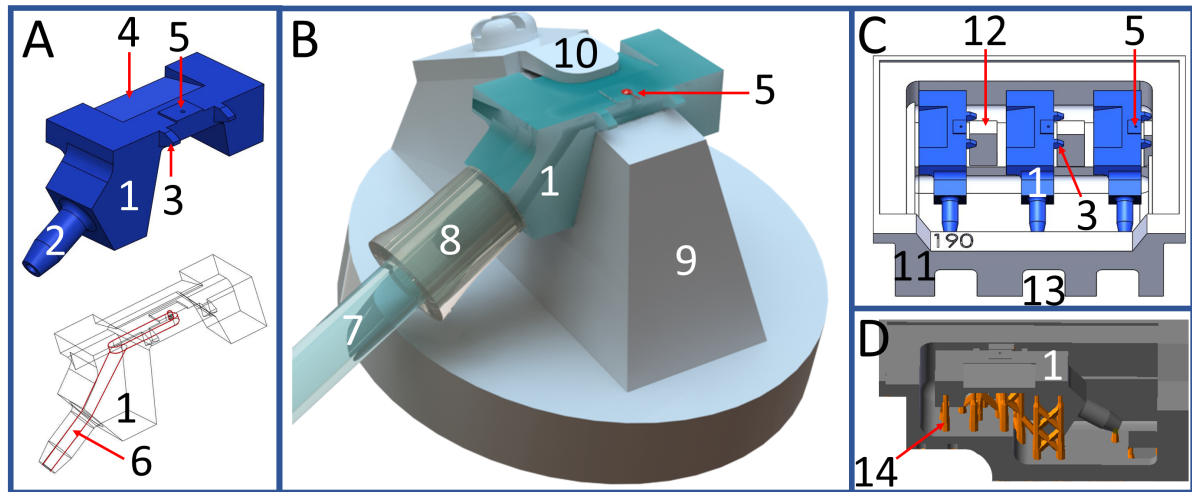


Figure 1: Design of the DLP printed parts, including a render of the assembly on an AFM holder. **A)** CAD design of the microfluidic interface (1). The microfluidic connector (2) allows for connection to the tubing of the microfluidic connector. The cantilever protection (3) prevents damage to the cantilever when handling the interface. The inclined plane (4) is used for the AFM clamp to keep the interface in place. The cantilever base is printed using 2PP around and on top of the aperture (5). The bottom figure shows the internal channel through the microfluidic interface. **B)** Render of the interface connected to the tubing (7), which is slid over the connector and sealed by the securing element (8). A 2PP print is shown at the aperture. The interface mounted on an AFM holder (9) and kept in place by the metal clamp (10). **C)** To mount the interfaces in the Nanoscribe, they were printed inside a sacrificial holder (11). This holder can contain three interfaces and each interface has its own photoresist plateau (12), which ensures enough photoresist remains present when printing the protruding cantilever (explained in appendix A and B). Arches (13) are cut out of the holder to allow access to the connectors during development. **D)** Shows a Perfactory slicer image of the DLP print. The automatically generated support beneath the interface (14) holds the interface in place during the 2PP printing, and is broken when the interfaces with 2PP print are removed.

cells overexpress the DUX4 gene (1/1000 to 1/200 of the nuclei) [10–12]. Removing this DUX4-expressing nucleus, studying its properties, and examining the cell after the nucleus has been removed could help understand the principles behind FSHD and could eventually help find a cure. With these aforementioned experiments, the feasibility of 3D-printed polymer microfluidic AFM cantilevers has been demonstrated, and new functionalities have been developed for FluidFM research.

2 Materials and methods

2.1 Fabrication Methods

The fabrication of a 3D-printed microfluidic AFM cantilever required two consecutive 3D printing steps, both at a different scale. The microfluidic interface, as shown in Figure 1A-D, was printed using digital light processing (DLP) on a commercial desktop DLP printer (EnvisionTEC Micro Plus Hi-Res, EnvisionTEC GmbH.). A commercial 2PP printer (Photonic Professional GT Laser Lithography System, Nanoscribe GmbH) was used to print the microfluidic AFM cantilever on top of the DLP print. The design of the 2PP print is shown in figure 2A-C.

2.1.1. Digital light processing

The computer-aided design (CAD) model of the microfluidic interface is shown in figure 1A. In this CAD model, several features of the interface can be seen, including the ferrule-type microfluidic connector, the channel through the interface and the AFM holder clamping site. The top of this microfluidic interface serves as the substrate for 2PP

printing. A channel runs from the connector to an aperture at the 2PP printing location. The channel transforms from circular (at the connector) to rectangular (below the aperture) with a cross-sectional area of 0.24 mm^2 . The aperture was designed with a diameter of $175 \mu\text{m}$. Two protruding cantilever protection bars protect the cantilever during handling.

The microfluidic interface was designed to fit the BioAFM holder of the JPK BioAFM Nanowizard 4 (JPK Instruments AG). Figure 1B shows a CAD assembly of the interface on the AFM holder, including the tubing that is connected to the microfluidic interface. This connection consists of three parts: the ferrule type connector (attached to the microfluidic interface) that is inserted into the tubing to prevent it from collapsing, the securing element, that prevents the tubing from expanding, and the tubing (Masterflex Transfer Tubing, Tygon® ND -100-80 Microbore, 1 mm ID x 1.8 mm OD) that is connected to the microfluidic pressure controller. The securing element was also printed with the DLP printer. The ferrule type connector was printed at an angle of 30-degrees with respect to the top surface of the microfluidic interface to prevent the tubing from hitting the Petri dish sides during experiments. No adhesive or O-ring was required for the connection between the interface and the tubing.

Three microfluidic interfaces were printed on sacrificial supports in a special holder (figure 1C). The holder is designed to fit into the Nanoscribe sample holder and aligns the microfluidic interfaces with the X, Y and Z axes of the Nanoscribe. It ensures that the top of the interfaces is in the same position as the top of conventional sub-

strates, minimizing the risk of crashing the objective into the substrate. The sacrificial holder contains a photoresist plateau, which is needed to print suspended structures with no substrate underneath.

Figure 1D shows the sacrificial supports in a cross-sectional view. These supports are automatically generated using the Perfactory Slicer (EnvisionTEC GmbH) and can be broken after 2PP printing to remove the interfaces.

DLP print settings and development

A layer height of $50\ \mu\text{m}$ (z-direction) was used to print the microfluidic interfaces using the standard HTM140v2 (EnvisionTEC GmbH) photoresist print recipe. The print is oriented such that the final printed layer of the DLP print is the top surface of the microfluidic interface. This layer is parallel to the build plate and relatively smooth. The smoothness of the last printed layer of the DLP print is required for the 2PP printing.

The DLP printed parts were elevated 1.5 mm above the build plate and supported by external supports to prevent damage to the print when removing it from the build plate. During printing, support structures were illuminated longer than the bulk of the print for easy removal afterwards (default setting). Two interface holders, each with three microfluidic interfaces and six securing elements, fit on one build plate and were printed in parallel.

After printing, the DLP print is removed from the build plate with a sharp razor blade. It is immersed in isopropyl alcohol (IPA, Sigma-Aldrich) and cleaned in an ultrasonic bath for 10 minutes. The channel is then cleaned of resin residues with compressed air (at a pressure of 2 bar). The print is then immersed in fresh IPA, after which it is cleaned in an ultrasonic bath for another 5-10 minutes. Blow-drying

from the side of the aperture results in a print that is free of unpolymerised resin. After the print has been dried, it is placed in a Photopol (A5406, Dentalfarm) curing unit. Two UV sources are used to post-cure the print for 6 minutes. After post-curing, the external support can be removed with a sharp razor blade.

Important factors that should be considered for optimum resolution are humidity, ambient temperature, printer calibration, UV source cycles, print bed alignment, position on the build plate, fluorinated ethylene propylene (FEP) foil quality, photoresist expiration date and separation film quality.

Materials for DLP printing

A methacrylate/acrylate-based photoresist (3DM Tough Clear, ADMAT SASU) was used to print the microfluidic interfaces and the securing element. 3DM Tough Clear is a mixture of acrylic-methacrylic acid esters, acrylate-methacrylate monomers and oligomers, photoinitiators and pigments. The prints were cleaned in IPA (Sigma Aldrich). Further details, explanation of the design and the process are given in the supplementary information in appendix A.

2.1.2. Two photon polymerization

The CAD model of the microfluidic AFM cantilever is shown in figure 2. The 2PP print consists of three modular parts: the dome, the hollow cantilever and the sharp tip with an aperture, as shown in figure 2. The modular design allows for easy customisation of the design. The dome serves as an intermediate structure to connect the microfluidic interface to the cantilever. A cross-section of the dome on a DLP-printed substrate is shown in figure 2A.

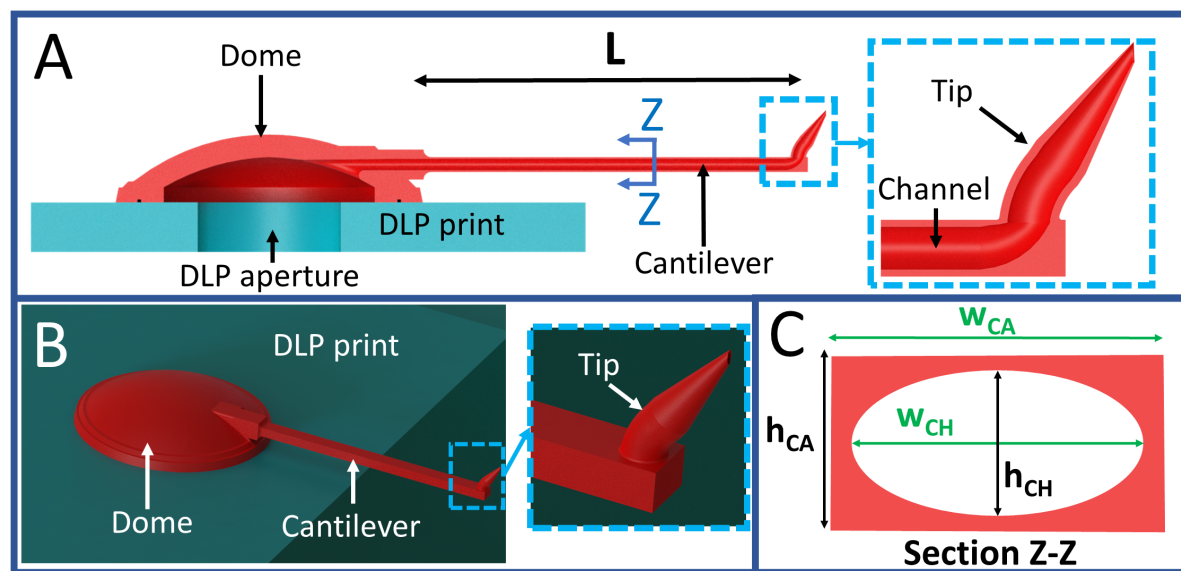


Figure 2: Design of the 2PP printed modular parts which consist of a dome, a cantilever and a sharp tip. **A)** CAD model cross-section of 2PP print on top of the DLP print above the aperture. Z-Z denotes the cross-section visible in figure C. L is the length of the cantilever, which is $500\ \mu\text{m}$. It has a width of $30\ \mu\text{m}$ and a height of $20\ \mu\text{m}$. On the right, a zoom in at the tip with the channel. **B)** Isometric view of the 2PP print on top of the DLP print, with on the right a zoom in on the tip. **C)** Cross-section Z-Z of the cantilever at location marked in figure A. w_{CA} and w_{CH} are the width of the cantilever and channel respectively ($w_{CA} = 30\ \mu\text{m}$ and $w_{CH} = 25\ \mu\text{m}$). h_{CA} and h_{CH} are the height of the cantilever and channel, respectively ($h_{CA} = 20\ \mu\text{m}$ and $h_{CH} = 15\ \mu\text{m}$).

The dome covers the entire aperture and has a wide base to improve adhesion to the substrate. It has a converging channel towards the base of the cantilever to converge the large diameter of the DLP printed aperture to the much smaller diameter of the cantilever. The dome, with an inner diameter of $280\ \mu\text{m}$ and an outer diameter of $408\ \mu\text{m}$ at the base, was sufficiently large to cover the influenced region around the aperture, which had a sub-optimal surface geometry. The height of the dome was $90\ \mu\text{m}$ with a wall thickness of $30\ \mu\text{m}$. The dome has a rectangular protrusion with a 45-degree angle sloped surface, where the converging channel of the dome ends. The sloped surface serves as the foundation for the cantilever.

The cantilever was designed for a stiffness of $1.71\ \text{N/m}$, which was calculated using simple beam equations in Matlab and checked with a linear elastic finite element model (FEM) simulation in COMSOL. For these calculations, the material properties of the polymer (IP-DIP, Nanoscribe) with a Young's modulus of $4.5\ \text{GPa}$, Poisson's ratio of 0.3 and density of $1.170\ \text{g cm}^{-3}$ were used. [13–15]. The stiffness and natural frequency calculations and simulations are discussed in more detail in the supplementary information (appendix B and E). The design resulting from the calculations was a rectangular cantilever with a length of $500\ \mu\text{m}$ (shown in 2A and B) and an elliptical channel. A cross-section of the cantilever is shown in figure 2 C. The cantilever has a width of $30\ \mu\text{m}$ (w_{ca} in figure 2C) and a height of $20\ \mu\text{m}$ (h_{ca}).

The elliptical channel has a width of $25\ \mu\text{m}$ (w_{ch}) and a height of $15\ \mu\text{m}$ (h_{ch}). The elliptical shape of the channel allows for a large cross-sectional area, while the height of the cantilever is kept to a minimum. Flow simulations were used to characterize the flow through the cantilever channel (shown in appendix E). The sharp tip, shown in 2A and B, was printed for AFM imaging and FluidFM cell experiments. The tip has a height of $60\ \mu\text{m}$ and an elliptical aperture with a width of $4\ \mu\text{m}$ and a height of $4.8\ \mu\text{m}$. A converging channel in the tip connects the cantilever channel to the aperture below the apex. The tip is tilted forward, 45 degrees, to be able to see it from above during experiments without the cantilever blocking it. For the adhesion experiments, no tip was printed on the cantilever, resulting in a $7\ \mu\text{m}$ aperture on the top side of the cantilever.

2PP print settings and development

For the 2PP printing, the dip-in-laser-lithography (DiLL) configuration was used with the IP-Dip (Nanoscribe GmbH) photoresist in combination with the 63X objective to achieve optimal feature sizes. The DLP print was taped to the Nanoscribe sample holder, which was then inserted into the Nanoscribe. DiLL requires a droplet of photoresist between the substrate and the objective. This droplet of photoresist was applied the DLP print (microfluidic interface and photoresist plateaus) and to the objective.

The main challenge was to find the interface between the DLP print and the photoresist due to the insufficient refractive index mismatch. This mismatch is used by the Definite Focus module (Zeiss) of the Nanoscribe to detect the surface of the substrate. To circumvent this problem,

the optical properties of the substrate were changed by sputter coating a gold thin film (JEOL JFC-1300 sputter coating system, 5 seconds at $10\ \text{mA}$ with a $20\ \text{mm}$ distance between the target and the substrate, $3\ \text{nm}$ film thickness) on top of the DLP print. This created a reflective film that could be detected by the interface finder. Thicker gold layers resulted in burning of the top layer of the DLP print due to higher absorption (interaction between the gold and the femtosecond laser).

In addition, the interaction between the femtosecond laser and the gold layer caused bubbles to form on the DLP printed surface, even for thin gold coatings. When using the correct gold layer thickness and dose, these bubbles were not a problem, as they were embedded almost immediately in the print.

Since the dome is larger than the print field of the 63x objective, hexagonal stitching was used. The stitching of the dome is shown in figure 3.

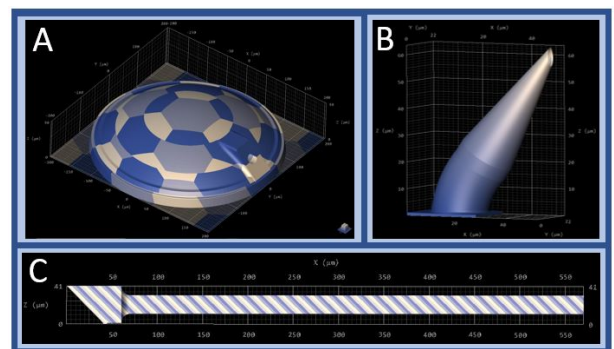


Figure 3: Describe block splitting and slicing of the 2PP print, **A**) Hexagonal block splitting of the dome printed in three block layers. **B**) Slicing of the sharp tip, **C**) Rectangular block splitting of the cantilever with blocks at 45-degree angle.

To print the dome, the interface was detected $200\ \mu\text{m}$ away from the edge of the aperture. Because there may be height differences and tilt of the surface, the initial depth of the print was set to $8\ \mu\text{m}$ below the interface, to ensure that the entire base of the dome was attached to the substrate, properly adhered and leak-tight (prevents leaks caused by tilt or surface imperfection of the DLP print). Since the dome has a relatively large print volume, the galvoacceleration was increased to reduce the print time (galvoacceleration = $6\ \text{V/ms}^2$). The optimization of the print parameters (e.g. laser power, scanning speed, block splitting, etc.) was done separately for each module of the 2PP print.

The tip required no stitching as it was smaller than the printing field of the objective (figure 3B). It is however the part that requires the highest resolution to obtain the smallest possible features (aperture and tip radius). To achieve this, the hatching and slicing parameters were set to a minimum. A contour was added to the print to obtain smooth prints.

The cantilever was printed attached to the dome, with an overlap of $1\ \mu\text{m}$. The cantilever was printed in slabs of $4\ \mu\text{m}$ at 45-degree angle, each overlapping $2\ \mu\text{m}$ with the previous block (by using the block splitting option in Describe) as shown in figure 3C. The angle and overlap of the

blocks prevented delamination problems that occur when printing long, single-layer overhangs (the first layer bends down before the next layer is printed). The parameters for the cantilever (including laser power, scanning speed, slab width, overlap, and slab angle) were optimized by printing batches of cantilevers with different printing parameters. Table 1 shows the most important printing parameters. An extended table, which includes additional parameters, is provided in the supplementary information (appendix B).

Parameter [unit]	Dome	Cantilever	Tip
Laserpower [mW]	31.25	30	25
Laserpower [%]	62.5	60	50
Scanningspeed [mm/s]	60	40	50
Slicing distance [μm]	0.35	0.2	0.05
Hatching distance [μm]	0.25	0.2	0.1
Contour count	3	-	1

Table 1: Important 2PP printing parameters per module. An extended table is provided in the supplementary information (appendix B)

After printing the 2PP structures, the interface holder was immersed in a beaker filled with propylene glycol methyl ether acetate (PGMEA, Sigma-Aldrich) with the cantilever vertically (pointing down). This removed most of the unpolymerized IP-Dip. After one hour, the container was removed from the PGMEA and immersed in a fresh bath of PGMEA for at least 48 hours to allow the PGMEA to rinse the whole internal channel by diffusion. The print was then immersed in IPA to remove the PGMEA. After one hour, it was immersed in fresh IPA for at least 16 hours. Longer times in PGMEA (72+ hours) and IPA can were used for apertures smaller than $3\mu\text{m}$ and longer channels.

After the IPA bath, the specimens were blow-dried and left to dry in air. When resin was observed on the print, additional PGMEA and IPA baths were applied. The total device, DLP print with the 2PP print on top, could be removed from its support using a pair of tweezers, after the development steps. A detailed report of the design, slicing and printing parameters of the 2PP print are given in the supplementary information (Appendix B).

Materials for 2PP printing

For the 2PP printing, the DiLL configuration with the 63X objective and IP-Dip (Nanoscribe GmbH) photoresist were used. According to the safety sheet, IP-Dip contains: Aliphatic alcohol containing acrylate (60-80%), hydrocarbon acrylate (<24%), acrylate and polyether containing alicyclic hydrocarbon and less than 10% other components. The exact composition is classified. The prints were cleaned using PGMEA (Sigma Aldrich) and rinsed in IPA (Sigma Aldrich).

2.2. Device characterization

2.2.1. Optical characterization

After the DLP prints were developed and post cured, all devices were inspected using an optical microscope (Keyence Digital Microscope VHX-6000). The aperture and channel were inspected for blockages and other defects. The surface quality around the aperture was checked for contamination, imperfections and unevenness.

The diameter of the aperture was checked with the microscope's measuring tool. Clogged devices and devices with an aperture greater than $200\mu\text{m}$ were discarded. The microfluidic connector was inspected for defects such as holes, collapse and bending. The 2PP prints were also inspected with the light microscope after development. Defects checked for included delamination (from the DLP print and between blocks), large bubbles, holes in the print, bending of the cantilever and clogging of the channel. Prints with defects were marked and discarded.

2.2.2. Scanning electron microscope characterization

A secondary inspection for defects was carried out using a scanning electron microscope (SEM, Jeol JSM-6010LA). This requires a gold sputter coating of 30 seconds at 20 mA (approximately 16 nm) and a constant sputter-target distance of 20 mm. Devices with defects were rejected. Defects checked for included gaps between the dome and the DLP print, shifted blocks, holes in the print that could cause leakage, bent cantilevers, damaged tips and other defects that affect the stiffness of the cantilever.

2.2.3. Mechanical characterization

A laser Doppler vibrometer (LDV, Polytec MSA400 Micro System Analyser) was used to compare the printed cantilevers with the numerical and analytical results. The LDV measurement was used to obtain the frequency response of the cantilever and to determine the Q-factor and power spectral density of the cantilever, which were used to calculate the stiffness of the cantilever. These measurements can then be compared with the analytical and numerical results.

A thick layer of gold (ranging from 150-315 nm) was sputtered onto the back of the cantilevers using a special 3D-printed holder, holding two interfaces turned upside down (2-5x 120 seconds, 20mA with a sputter-target distance of 25mm). Multiple holders could be placed in the sputter coater, allowing at least 10 cantilevers to be coated at once, ensuring they remained near the centre of the sputter coater. This gold coating forms a reflective layer needed for deflection measurements with a laser.

The microfluidic interface was then mounted upside down on the LDV system (so that the laser is reflected by the gold coating on the bottom side of the cantilever, opposite the tip) on a lead zirconate titanate (PZT) piezoelectric element. The laser of the LDV was focused on the free end of the cantilever, and a grid of measurement points was defined near the tip (where the amplitude of vibration is maximum). To measure the resonant frequencies and the Q-factor of the cantilever, the piezoelectric

element was driven with a pseudo-random signal with an amplitude of 3 volts over a frequency bandwidth from 0Hz to 200kHz. To calculate the stiffness of the cantilever, the power spectral density, the Q-factor and the natural frequency can be used. To measure these variables, the piezo driving signal was turned off and the thermal noise was measured over a frequency range of 500Mhz. From this measurement, the power spectral density (PSD) was recorded. The magnitude of the power spectral density at the resonant frequency (PSD_{peak}), the magnitude of the power spectral density (PSD_{base}) and the Q factor were recorded. The ambient temperature was measured with a thermometer. From the measured data, the stiffness was calculated using [16]:

$$X(\omega) = \frac{\sqrt{4k_b T \frac{\omega_0}{mQ}}}{\sqrt{(\omega_0^2 - \omega^2)^2 + \left(\frac{\omega\omega_0}{Q}\right)^2}} \quad (2.1)$$

with X the auto spectral density, $\omega = \omega_0$ the resonant frequency, Q the damping coefficient, T the ambient temperature, k_b the Boltzmann constant and with the mass (m) equal to:

$$m = \frac{k}{\omega_0} \quad (2.2)$$

with k the cantilever stiffness.

The auto spectral density X can be calculated using:

$$X^2 = \sqrt{PSD_{peak}^2 - PSD_{base}^2} \quad (2.3)$$

The LDV measurements were repeated in a vacuum chamber with a pressure of $9 * 10^{-3}$ mbar.

2.2.4. Pressure and flow tests

A pressure test was performed on the fluidic connector of the microfluidic interface to determine the maximum pressure it can withstand. For this experiment, a connector with a dead end was printed. The tube was filled with water and then connected to the connector of the microfluidic interface. The securing element was slid over the connector-tube combination, after which the tube was connected to the microfluidic pressure controller (Elveflow OB1). The pressure was slowly increased to a maximum pressure of 6.9 bar to test the maximum pressure the connector could withstand. The same experiment was carried out with air-filled tubing with the device immersed in water, applying both positive (6.9 bar) and negative pressures (-1 bar).

The printed 2PP structures were tested for leaks and the minimum dispensing pressure was determined. To test the minimum dispensing pressure, the microfluidic interface was mounted on an optical microscope (MOTIC BA310) with a 40x magnification objective. The Tygon tubing was filled with double-filtered demineralized water (until the water was 10 mm from the end of the tubing) and then connected to the microfluidic interface and to the microfluidic controller. The pressure was increased until

liquid came out of the aperture. To check if the dome was leaking, the pressure was increased to 4 bar.

To predict the fluidic behaviour of the design, a finite volume model was implemented in COMSOL. In this simulation, laminar flow was assumed. The pressure drop and flow velocity were simulated with an imposed inlet pressure of 1000 mbar and an outlet pressure of 0 bar.

2.3. Cell culture

Cell culturing of the myotubes was performed at the Leiden University Medical Center (LUMC) at the department of human genetics. Cultured cells were transported to the Delft University of Technology for the experiments.

Human primary myoblasts were cultured in Ham's F-10 Nutrient Mix (Life technologies), in combination with 20% heat-inactivated Fetal Bovine Serum (FBS, Gibco/Life Technologies), 1% Pen Strep (antibiotic solution of penicillin/streptomycin, Gibco/Life Technologies), 10 ng ml⁻¹ of fibroblast growth factor (rhFGF, Bio-Connect) and 1 μmol dexamethasone (for proliferation, Sigma-Aldrich). The myoblasts were cultured for 3 days in Dulbecco's Modified Eagle Medium (DMEM, Life Technologies) supplemented with 15% Knock-Out Serum Replacer (KOSR, Life Technologies) for the terminal myogenic differentiation, resulting multinucleated myotubes for the puncture experiments. The same protocol was followed as used by Kramer et al. [9].

For the adhesion experiment, mouse preosteoblast (MC3T3-E1, Sigma-Aldrich, passage 11) were used, with the same protocol as Nouri-Goushki et al. [6]. The cells were seeded on a 6-well plate (Greiner Bio-One, Netherlands) with $5.0 * 10^4$ preosteoblast cells per well. The preosteoblasts were incubated in an alpha minimum essential medium (α-MEM, Thermo Fisher) supplemented with 10% fetal bovine serum (Thermo Fisher) and 1% penicillin-streptomycin (Thermo Fisher) at 37 degrees Celsius and with 5% CO₂ (Life Technologies).

2.4. AFM experiments

For the AFM and FluidFM experiments, the JPK BioAFM Nanowizard 4 with an attached inverted microscope (Zeiss Axio Observer 3, Carl Zeiss Microscopy GmbH), with 10x, 40x and 63x objectives, was used.

2.4.1. Cantilever calibration

A schematic overview of the AFM setup can be seen in figure 4A. For the calibration, the cantilever was mounted on the AFM holder without the tubing. After the laser has been aligned with both the cantilever and the detector (by adjusting laser position and adjusting the detector and the mirror to get an optimal signal), a flat substrate was approached (in air). When the cantilever has approached the substrate, the cantilever can be calibrated using the contact-based method. This method uses the slope of the approach force curve (the deflection of the cantilever was measured after a small displacement) to calculate the sensitivity and the thermal noise to determine the stiffness. For measurements in liquid, the sensitivity has to be recalibrated after the cantilever has been immersed. After calibration, experiments can be performed.

2.4.2. AFM imaging

To test the functionality of the cantilever, a force measurement on a hard substrate. This measurement was performed in air and water. AFM imaging studies were performed to determine the imaging functionality of the cantilevers. After the cantilever was mounted (without tubing), the laser was aligned and the substrate was approached. With an approached cantilever, the calibration was performed. Test grids were imaged in quantitative imaging (QI) mode, contact mode and tapping mode. These studies were used to determine if the cantilevers could provide accurate results for AFM imaging. Gratings (with spacings of 3, 10, 20, and, 50 μm) and a grid (with 10 μm holes) both with 100 nm tall ridges, were used as test substrates for the imaging experiments.

2.4.3. Cell adhesion experiment

Additionally, tipless cantilevers were printed with a 7 μm aperture to perform cell adhesion experiments. The mouse preosteoblast cells, used for the adhesion experiment, were cultured at Delft University of technology. The setup of the experiment is similar to the puncture experiment, but the JPK Cellhesion module was used to increase the Z-length to 150 μm . The cells were approached, and then a negative pressure was applied (-500mbar). During retraction, the force curve was monitored for the cell detachment.

2.4.4. Nucleus aspiration experiment

Cell puncture and nucleus extraction experiments were performed on multinucleated myotubes. The experiments were performed at room temperature to avoid thermal drift

of the cantilever signal. A schematic overview of the setup, used for the cell experiments, can be seen in figure 4A. First, a protective silicone ring was mounted on the AFM holder (BioAFM holder, JPK), to prevent damage to the piezos of the AFM by condensation. Then, the microfluidic interface was mounted on the AFM holder using the steel spring and Phillips screw (the shape of the interface guides it into the correct position). After tightening the screw, the stage was placed on the AFM and the laser was aligned to the back side of the cantilever (with the sputtered gold, 2 to 5 times 120s at 20 mA and a 25 mm target-substrate distance, approximately between 150 and 315 nm thickness).

After calibrating the cantilever on a glass slide (contact based method), the piezo stage was removed. The Tygon tubing was filled with double filtered demineralized water and the sleeve was slid over the tubing. The tubing was then pushed onto the microfluidic connector of the interface and the sleeve was slid into position. Using a 2mL syringe, at the other end of the tubing, the fluid was forced through the interface and the cantilever until a drop was visible at the end of the cantilever. After the Petri dish holder with the cells was mounted on the AFM, the piezo stage was put back into place, with the tubing secured to it. The tubing was then connected to the microfluidic pressure controller (Elveflow OB1).

After immersing the cantilever in the cell medium, a new calibration was performed to determine the sensitivity of the cantilever in liquid. The procedure of the experiment is schematically shown in figure 4B1-B5. After approaching the Petri dish, suitable cells were selected for the cell experiments and a nucleus was located. Then the tip was

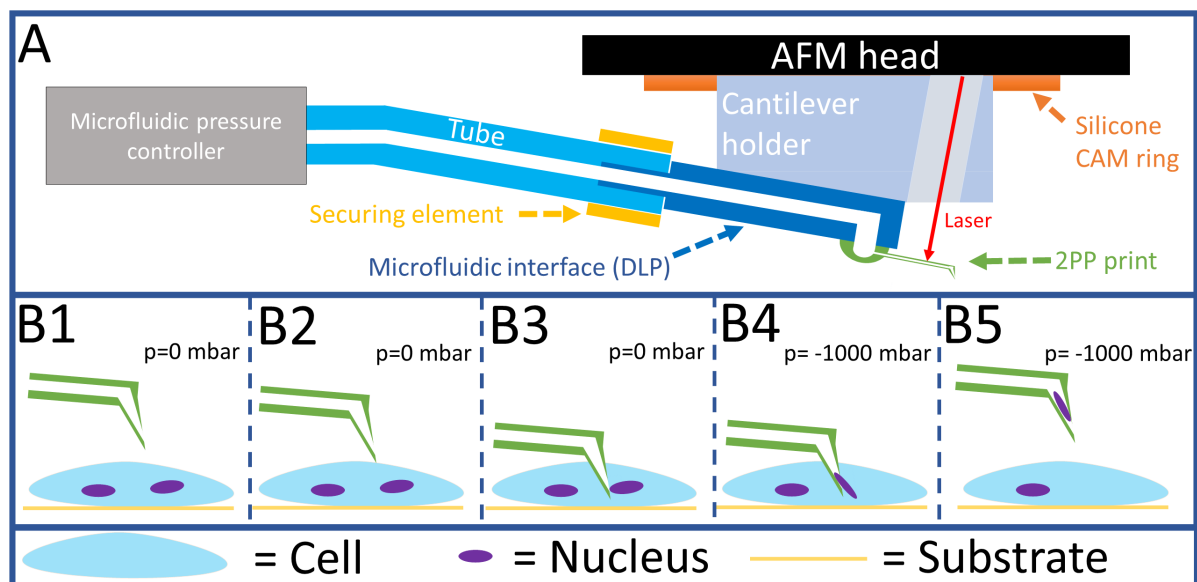


Figure 4: Schematic diagram of the nucleus aspiration experiment (not to scale). **A**) Schematic of the AFM setup with the DLP-printed microfluidic interface mounted on the cantilever holder. The cantilever of the 2PP print, which is printed on the DLP print, reflects the laser. The tubing and securing element connect the DLP print to the microfluidic pressure controller. **B1-5**) Show the procedure for aspirating a cell nucleus. First, the tip is positioned over the cell at the location of the nucleus (B1), then the cell is approached (B2). The piezos are extended until the set point force is reached. In the meantime, the cell is punctured (B3). The microfluidic controller pressure is set to -1000mbar for 30 seconds to aspirate the nucleus (B4). When the entire nucleus is aspirated, the piezos retract the cantilever with the nucleus inside (B5).

moved over the nucleus. The cells were automatically approached with a set point of 10 nN before the experiment. After the approach, an automatic puncture was started. The cells were approached until a set point force of 80 nN was reached with a Z-length of 15 μm and a velocity of 1 $\mu\text{m s}^{-1}$. A minimum set point was determined by a separate cell puncture experiment. To make sure the whole tip was inside the cell, when this set point was reached, a set point was chosen higher than the minimum puncture force.

At the set point a programmed pause of 30 seconds was started, at which a pressure of -1000mbar was applied for aspiration of the nucleus. After the pause, the cantilever was retracted. During the experiments, the force and approach curves were monitored to determine when to apply the negative pressure. For the puncture experiments, used to determine the set point force, the same protocol was used, but no pressure was applied, and no pause was programmed.

3 Results

3.1. Digital light processing

One DLP print, with two interface holders and six securing elements, took approximately 1 hour and 45 minutes. The resulting prints can be seen in figure 5. Figure 5A shows a microfluidic interface in an interface holder. The bottom figure shows the aperture of the microfluidic interface.

The geometry and sizes of the DLP print matched with the design. The largest variation was found for the diameter of the aperture. The average diameter of the aperture was $171 \pm 16 \mu\text{m}$, with an affected area around the aperture with an average diameter of $243 \pm 18 \mu\text{m}$ ($n=12$). The channel through the interface was sufficiently large to allow flushing of the channel during development to remove unpolymerized and partially polymerized photoresist. The "floor" and "ceiling" of the channel were sufficiently thick to withstand the forces of removing the supports from the bottom of the interface and withstand the internal pressure applied by the microfluidic pressure controller.

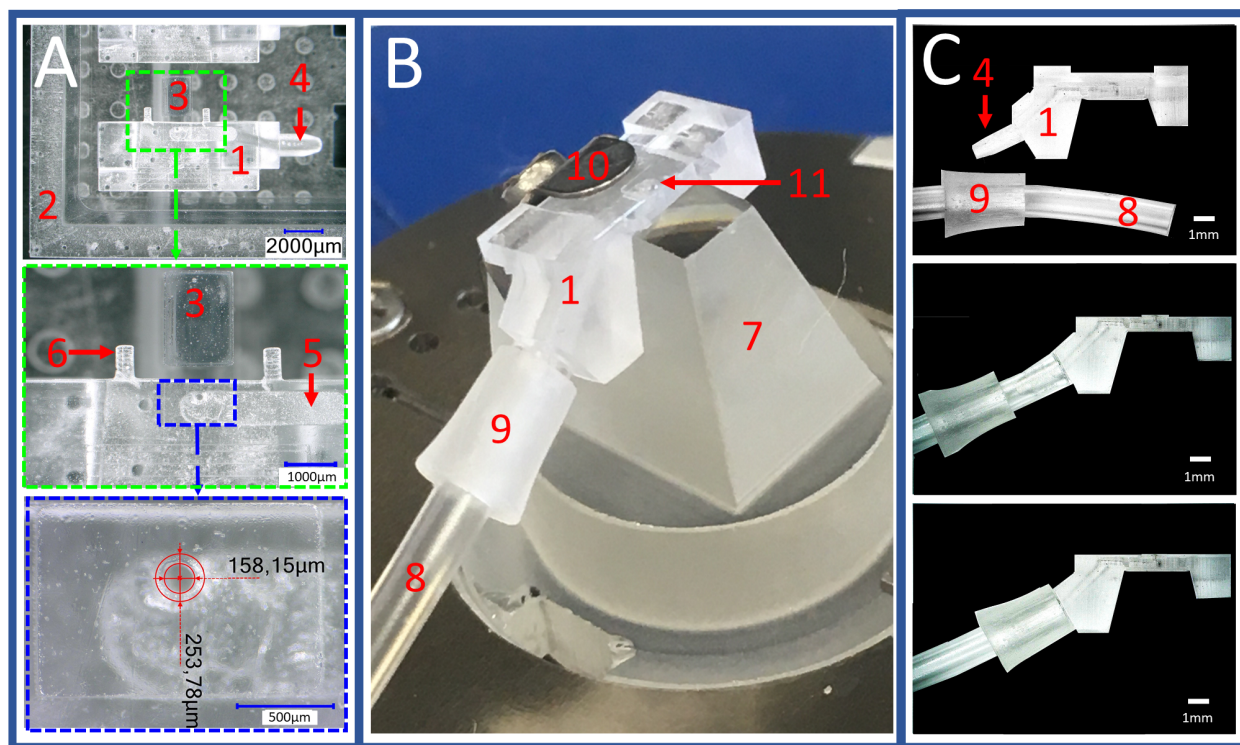


Figure 5: Results of the DLP printing with 3DM Tough Clear **A**) The microfluidic interface (1), which serves as a 2PP substrate, can be mounted on an AFM system and is connected to the microfluidic pressure controller. The microfluidic interface is printed into a sacrificial holder (2) that fits into the Nanoscribe, and holds up to three microfluidic interfaces (part of a second interface is shown at the top of the image). The photoresist plateau (3) provides sufficient resin for suspended cantilever printing. To the right of the interface is the fluidic connector (4). The middle image shows a magnification of the region near the 2PP printing site. The channel (5) through the microfluidic interface runs from the connector to the aperture. The cantilever protection (6) protects the cantilever during handling and mounting of the interface. The bottom image shows a further zoom in on the microfluidic interface at the aperture. The 2PP structure was printed on the surface surrounding the aperture. The inner circle indicates the size of the aperture, and the outer circle indicates the influenced area around the aperture, which has irregularities. The surface is relatively smooth as it is the last layer printed. **B**) Shows the microfluidic interface (1) mounted on the BioAFM holder (7) and held by the metal spring (10). The microfluidic interface is connected to the tubing (8) via the securing element (9). The 2PP printing site is located at the front of the interface (11), **C**) Shows the principle of connecting the microfluidic interface (1) to the tubing (8) using a connector (4) and a securing element (9). Top image: securing element slid over the tubing. Middle image: tubing slid over the connector. Bottom image: Securing element slid over the tubing at the location of the connector.

The interfaces could easily be removed from the holder with tweezers after the 2PP development process.

Figure 5B shows the mounting of the microfluidic interface on the BioAFM holder. The shape of the interface properly aligned it on the holder, and the clamp kept it in place. Figure 5C shows that the microfluidic interface can be connected to the tubing. The connection procedure created a leak-tight connection that could withstand high pressures up to 6.9 bar. As designed, the tubing could not hit the Petri dish during experiments.

3.2. Two Photon Polymerization

The resulting 2PP prints can be seen in figure 6A-I. The average outer diameter of the printed dome was $398\mu\text{m}$, which is a shrinkage of 2.5% with respect to the design. The dome geometry matched the design and did not collapse. The dome was also fully attached to the interface and showed no displaced blocks, as shown in figure 6A, B, D and E. The walls of the dome can be seen in 6E. The effect of the hexagonal block splitting on the surface roughness of the dome can clearly be seen in 6B. Printing one dome took 54 minutes.

The cantilevers were successfully printed with a length of $489\mu\text{m}$ (shrinkage of 2.2%) with an open channel and aperture. The designed length was $500\mu\text{m}$, but shrinkage occurs. The protruding length (the portion of the cantilever that is not on top of the substrate) was $300\mu\text{m}$. The resulting cantilever can be seen in figure 6A, C and D. The exterior and interior of the cantilever are relatively smooth as shown in figure 6C. The geometry of the cantilever and

the channel matched the design. Printing one cantilever took approximately 22 minutes.

Relatively smooth tips were obtained, as shown in figure 6C, F-I. The printed contours, used for printing the tip, reduced the surface roughness of the tip. Shrinkage of $1\mu\text{m}$ was observed for the aperture of the tip. Apertures were printed ranging from circular with a diameter of $1\mu\text{m}$ to elliptical with a height of $3.8\mu\text{m}$ and a width of $3.1\mu\text{m}$. Tip radii of approximately 270nm were obtained, which is similar to the design after slicing. Printing the tip took approximately 15 minutes. The supplementary information (Appendix B) explains in more detail the optimization and achieved results of the 2PP print.

3.3. Mechanical characterization

Table 2 lists the results of the analytical calculations, FEM analysis, LDV measurements and the JPK measurements. The stiffness of the cantilever and the resonant frequency, measured in the LDV experiments, are in the same range as the design. The measurements of the stiffness and the resonant frequency performed on the AFM show a larger variation, with an average slightly larger than the design.

Measuring the cantilever characteristics in vacuum during the LDV experiment increased the Q factor with 4.83 to 23.58. In liquid, the Q factor decreased below 3 due to viscous damping (measured on the AFM). The sensitivity was measured during the JPK measurements. In air, the sensitivity was found to be $97.99 \pm 10.82\text{nm/V}$ ($n=5$). It decreased below 60nm/V when the cantilever

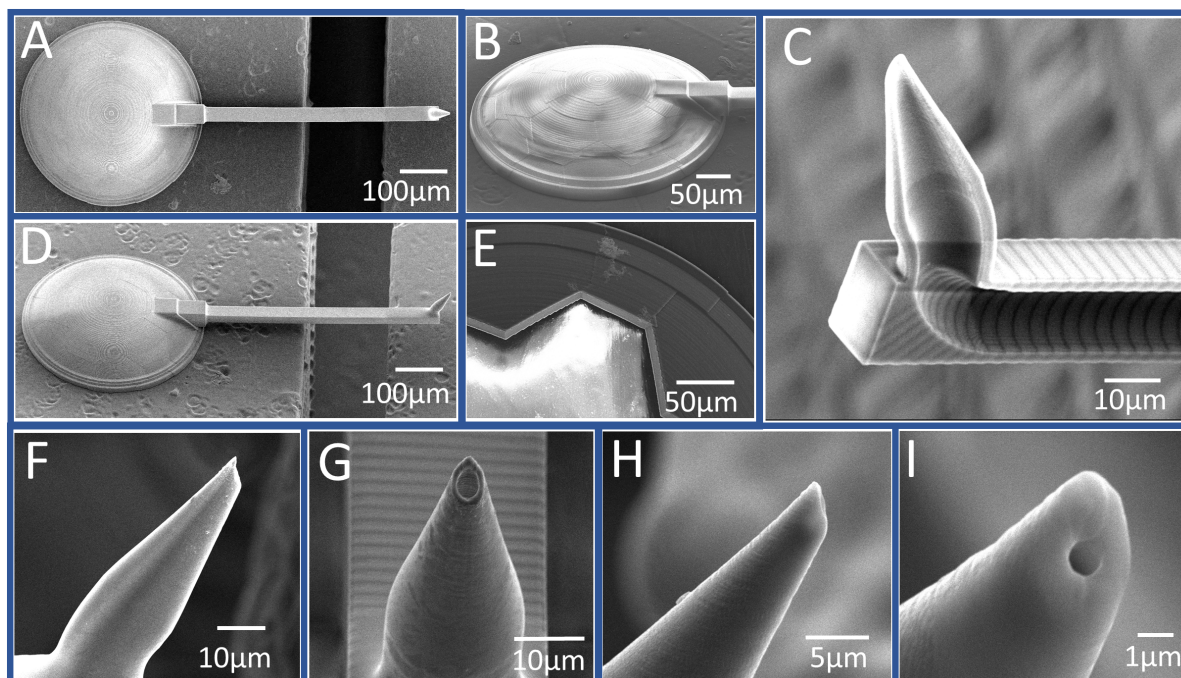


Figure 6: Results of the 2PP print using IP-Dip and the 63x objective (SEM images). **A)** 2PP printed dome with cantilever and sharp tip (top view), **B)** 2PP printed dome (60-degree side view), **C)** Cross-section of 2PP printed tip and cantilever, **D)** 2PP printed dome with cantilever and sharp tip (dimetric view) **E)** 2PP printed aborted dome with walls visible (top view), **F)** 2PP printed tip (type 1, side view), **G)** 2PP printed tip (type 1, front view) with aperture visible, **H)** 2PP printed tip (type 2, side view), **I)** 2PP printed tip (type 2, dimetric view) with aperture visible

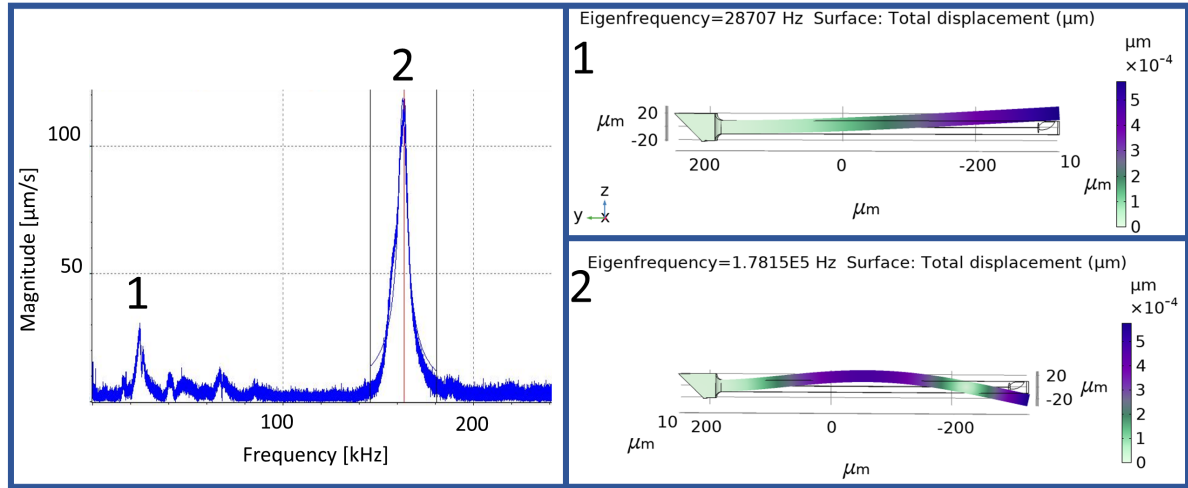


Figure 7: LDV measurement (left) versus COMSOL simulations (right). 1 and 2 indicate the resonant frequencies of the LDV measurement (1 at 25.1 kHz and 2 at 163 kHz) with the corresponding COMSOL simulations.

was immersed in liquid ($n=3$). It is important to note that the cantilever, whose stiffness was measured on the LDV system, was also tested with the AFM system, which resulted in a stiffness of 1.66 N/m, a natural frequency of 25.84kHz and a Q factor of 25.4. The low-quality factors of the cantilever are due to the energy dissipation caused by the viscoelastic properties of the polymer.

Figure 7 shows the frequency spectrum found during the LDV measurement and the corresponding results of the COMSOL simulations, indicating that characteristics of the device are in the same range as the design. The results and plots of this mechanical characterization and the simulations can be found in the supplementary information (appendix B, C, D and E).

3.4. Fluidic characterization

With an imposed inlet pressure of 1000mbar, maximum flow velocities in the cantilever of 0.55 m/s were obtained with a flow rate 0.4 $\mu\text{L}/\text{min}$ and a pressure drop from the inlet to the tip of approximately 940mbar. Details on the fluidic simulations can be found in the supplementary information (appendix E).

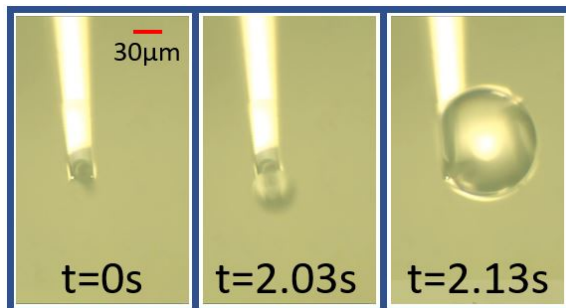


Figure 8: Dispensing a droplet from a sharp tip cantilever (optical microscope). An over pressure of 600mbar was used with a flow rate of 0.26 $\mu\text{L}/\text{min}$. The droplet on the right has a volume of approximately 0.6 nL.

For the sharp tip aperture, droplets became visible at the aperture at a pressure of 600 mbar (see figure 8. For tipless cantilevers, the first droplets appeared at 150mbar. After the first droplets were visible, the pressure to dispense decreased with approximately 100mbar due to the initial wetting of the channel caused by the capillary forces. The results of the dispensing of the droplet can be seen in figure 8.

	f [kHz]	k [N/m]	Q factor (air)
Analytical*	24.71	1.71	-
COMSOL FEM*	28.71	1.60	-
LDV ($n=1$)	25.1	1.64	18.75
AFM ($n=7$)	25.01 ± 1.10	1.84 ± 0.24	24.02 ± 1.17

Table 2: Calculations and measurements of resonant frequency (f), stiffness (k) and Q factor. For the calculations a Young's modulus was used of 4.5 GPa [13–15], a Poisson ratio of 0.3 and a density of 1.170 g cm^{-3}

To test for any leakage at the dome, the pressure was increased to 4 bar, but no leakage was observed. Figure 9 shows the flow from a cantilever on the AFM during an experiment (cantilever submerged in liquid).

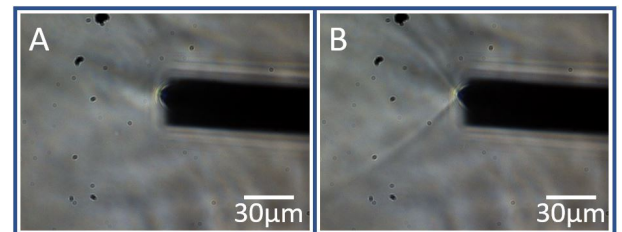


Figure 9: View of the flow near the Petri dish during experiment (optical microscope). **A**) Pressure controller at 0 mbar. **B**) Pressure controller at 1000mbar. Expanding flow clearly visible. Total fluidic resistance of the 3D print (DLP and 2PP) of approximately $2.38 \times 10^{14} \text{ Pa}\cdot\text{s}/\text{m}^3$ from COMSOL simulation.

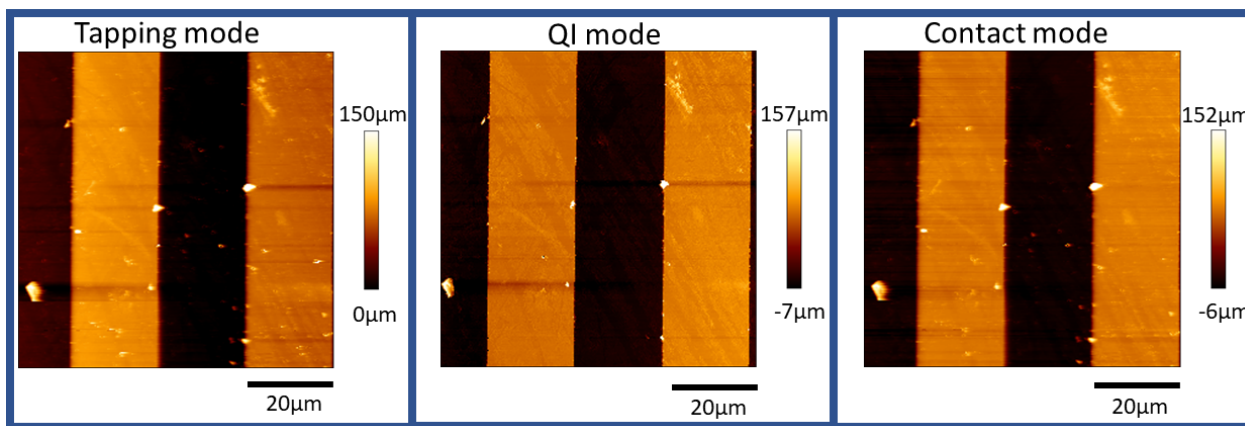


Figure 10: AFM imaging of test grid substrate with 10 μm ridges and 10 μm spacing. The average roughness (R_a) was 34.06 nm and the peak-to-valley roughness(R_t) was 85.8 nm. Images were made using a tip with 270 nm tip radius

3.5. AFM imaging

Successful force measurement was performed on a rigid substrate in air and water. The results of these measurements can be found in the supplementary information (appendix C). The measurement in air clearly shows a jump into contact and adhesion behaviour, both of which are not present when measuring water. This means that the force measuring capability of the cantilever was verified. The test grid and gratings (gratings with spacings of 3, 10, 20, and 50 μm and a grid with 10 μm holes) were all im-

aged successfully in three different imaging modes using a sharp tip cantilever with a tip radius of 270 nm. Figure 10 shows a 20 μm grating imaged in tapping mode, QI mode and contact mode. All three modes worked for imaging the test substrate, with the QI mode giving the best results with the lowest amount of noise. Additional images are given in the supplementary information (appendix C) for the various gratings and the grid.

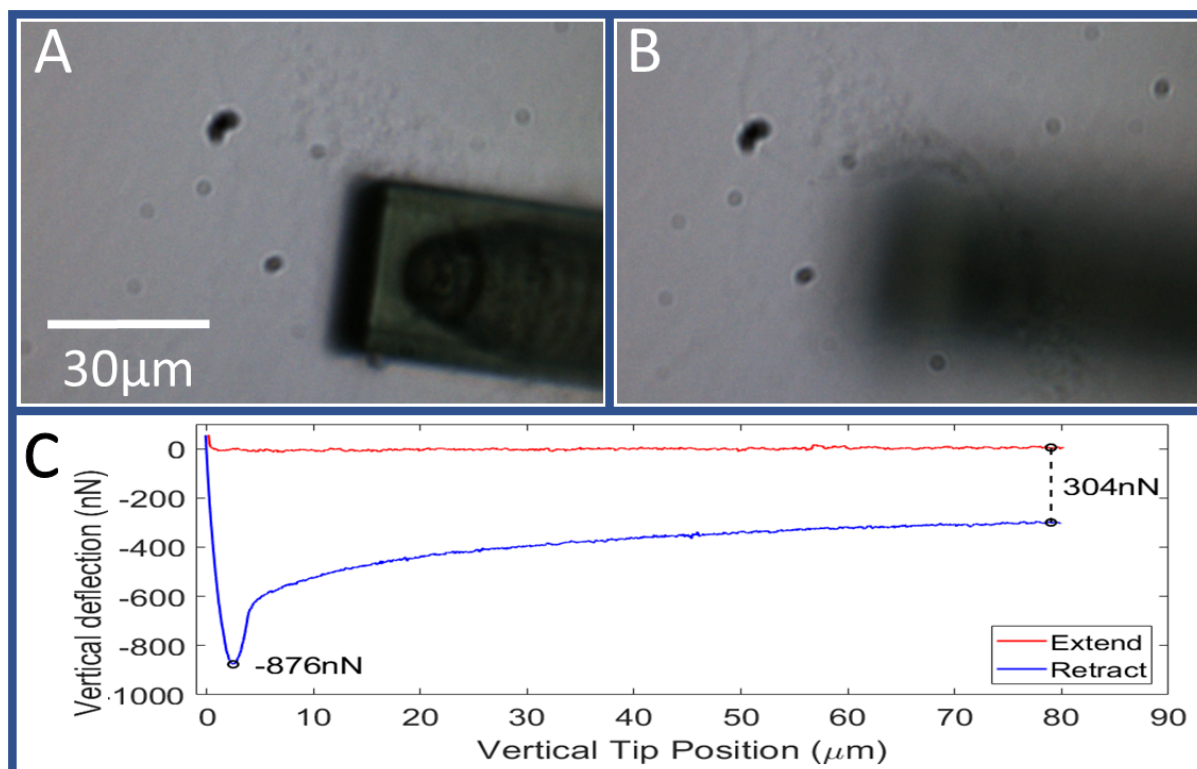


Figure 11: Result of an adhesion experiment. Partial detachment of the cell. **A)** Before aspiration (optical microscope), **B)** during retraction of the cantilever. Partial detachment of the cell as only the centre of the cell is being detached and the rest of the cell remains on the substrate

3.6. Cell experiments

A cell adhesion study was performed using tipless cantilevers. Figure 11A and B shows the cell before and during the experiment and figure 11C shows the resulting force curve of a partially detached cell.

During the cell experiments, cell debris sometimes clogged the aperture. If applying pulsating positive pressure, failed to remove the debris, Terg-a-zyme (Sigma-Aldrich) was used to clean the cantilever (outside the AFM setup). Clogged apertures and cellular debris, at the aperture, were clearly visible on the microscope view. If the flow, as seen in figure 9, was not visible or there was a large amount of debris at the tip, the cantilever was cleaned or replaced.

Before the aspiration experiment could be performed, the puncture force had to be determined. To determine this force, a puncture experiment was performed. One of the resulting force curves, for a puncture on top of the nucleus, can be seen in figure 12. The inset of figure 12 shows three peaks, with one more pronounced than the others. This peak indicates the puncture of the cell. With a set point force of 80 nN, a successful puncture and nucleus aspiration experiment was performed.

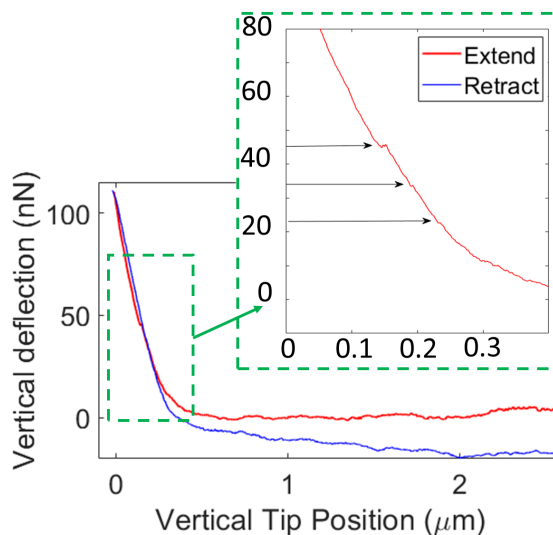


Figure 12: Force curve of cell puncture experiment with tip positioned on top of the nucleus. With zoom in at the puncture region.

At -300mbar pressure and a 10-second pause, only partial aspiration was achieved. Using -1000mbar and a 30-second pause, a full nucleus aspiration was obtained. This can be seen in figure 13. The details on the partial aspiration can be found in the supplementary information (appendix C).

4 Discussion

This study aimed to improve, optimize, and automate multiscale 3D printing for the fabrication of microfluidic AFM cantilevers for cell nucleus aspiration research. While previous researchers were able to obtain 3D printed apertures with sizes in the range of $10\mu\text{m}$ and were able to aspirate whole cells [9], the present study demonstrated

that apertures with sizes as small as $1\mu\text{m}$ can be achieved and can be used for nucleus aspiration. In addition, 3D printed microfluidic AFM cantilevers were fabricated with half the stiffness compared to previous work (1.84 N/m versus 3.7 N/m) [9]. The reduction in feature sizes was obtained without a significant increase in printing time (several minutes).

The Q-factor found (18.75-24.02) in this work is much lower than the Q-factor found by Kramer et al. [9] who found a Q factor of 174, but also compared to the U-shaped SiO_2 hollow cantilevers of Ghatkesar et al. [17] which had a Q-factor for 457 (hollow cantilever with a length of $155\mu\text{m}$, a wall thickness of $1\mu\text{m}$ and a channel size of $3.7\mu\text{m} \times 2.2\mu\text{m}$, with a stiffness of 4.3 N/m). The low Q-factor is attributed to the low Young's modulus (4.5 GPa versus 87 GPa for SiO_2) of the IP-Dip and the viscoelastic behaviour of the polymer.

The results highlight that 3D printed (microfluidic) AFM cantilevers can be used for AFM measurements, AFM imaging and FluidFM experiments, which is in line with the results found by Kramer et al. [9]. The puncture force of 43 nN is in the same range as found by Kramer et al. [9]. The results represent the first direct demonstration of targeted nucleus aspiration from a cell using microfluidic AFM cantilevers.

The nucleus could be aspirated with a pressure of -1000mbar (pressure set on the microfluidic pressure controller), which would result in a pressure at the tip of the cantilever of about -60mbar (according to the COMSOL simulation). This is comparable to the pressures reported by Guilak et al. [18] applied to determine the mechanical properties of cells. The discrepancy between the experimental stiffness and, the analytical and numerical stiffness, are attributed to the fact that the gold coating and the cantilever shrinkage were not considered in the calculations and simulations.

The large range of the measured cantilever stiffness (measured on the AFM) is attributed to differences in cantilever shrinkage, gold coatings and environmental changes that influence the printing and experimental results. A shrinkage of $10\mu\text{m}$ (decrease of cantilever length) would result in a 7% increase in stiffness.

The AFM measurements and the LDV measurements showed comparable results for the same device, except for the measured Q-factor. Further LDV experiments are needed to compare the results from the LDV and AFM experiments. The tape between the microfluidic interface and the piezo element could have caused the Q-factor in the LDV experiments to be lower compared to the AFM measurements.

The developed multiscale printing approach, which includes the DLP printing, changing the optical properties of the DLP print and the 2PP printing, is an effective and highly automated fabrication method. A DLP-printed microfluidic interface was fabricated that could be easily mounted on a JPK AFM system. The design of the DLP print can be changed to fit other AFM systems.

A new microfluidic coupling principle, which does not require any adhesive, was successfully developed. The microfluidic connection, which uses a connector and a securing element, withstood up to 6.9 bar. This fluidic cou-

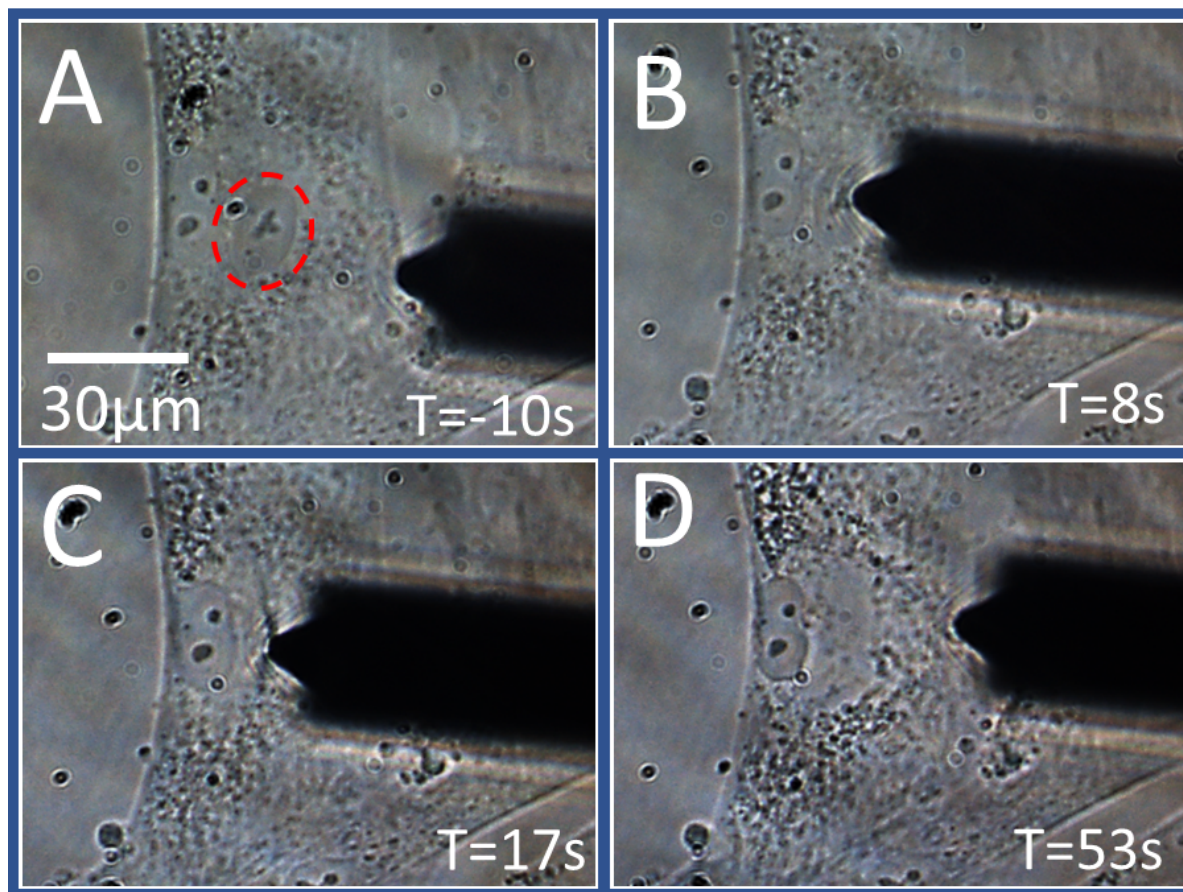


Figure 13: Aspiration of a nucleus in an AFM experiment (optical microscope). Two other nuclei are visible left of the aspirated nucleus. The tip type 1 (shown in figure 6F&G) was used for this experiment. As mentioned, the forward tilt of the tip allows for visualization of both the tip as the nucleus. **A)** Nucleus position before starting the experiment. **B)** After puncture no aspiration yet, **C)** After applying -1000mbar, nucleus almost fully aspirated, pulling on cytoskeleton is visible **D)** Retracted and no pressure applied. The nucleus is fully removed, but the membrane still being aspirated.

pling principle, combined the cantilever protection and the relatively large microfluidic interface, improved the handling of the device and reduced the risk of breaking the cantilever. By changing the optical properties of the DLP surface, automatic interface finding was achieved, resulting in a good connection between the DLP print and the 2PP print. The automation and modularity of the 2PP printing greatly improved the printing process and repeatability. The photoresist plateau increased the printing reliability even further. Measurements of the stiffness of the cantilever confirmed the validity of the COMSOL simulations. The reliability and repeatability of the developed methods are high.

The multiscale 3D printing approach was proven successful. The dome adequately to the DLP print and was able to withstand at least 4 bar. Straight cantilevers with a length of $489\ \mu\text{m}$, a width of $30\ \mu\text{m}$ and height of $20\ \mu\text{m}$ were successfully printed with a stiffness of $1.84 \pm 0.24\ \mu\text{m}$. Various different tip geometries with apertures down to $1\ \mu\text{m}$ in diameter and tip radii of $270\ \text{nm}$ were printed. Although the present results demonstrate that microfluidic AFM cantilevers can be 3D printed, it is appropriate to recognize several potential limitations.

The fabrication approach and design, have significantly improved the resolution and quality of the print without a significant increase in printing time (1h 33 min) compared to the work of Kramer et al.[9], who had a printing time of 1hr 26 min. Apertures were achieved with a diameter between 1 and $3.5\ \mu\text{m}$, which is significantly smaller than the $10\ \mu\text{m}$ aperture used by Kramer et al. [9] to aspirate whole cells. The viability of the cells after puncture and removal of the nucleus could not be determined in the experiments.

There are three main aspects that can reduce the viability of the cell. Firstly, the damage to the membrane that caused by the puncture. Secondly, the disruption of the cell activities that were regulated by the nucleus. Thirdly, the extracted volume could be too large for the cell to restore. The latter is thought to have little effect on cell viability if only the nucleus (volume of less than $1\ \text{pL}$) is removed, as Guillaume-Gentil et al. [19] have shown that only 19% of the cells die when less than $4\ \text{pL}$ is extracted.

The microfluidic interface was designed for use on the BioAFM cantilever holder of the JPK AFM system. A new design is required for another AFM system brand. Another limitation is the aperture size of the DLP-print. The aper-

ture size of the DLP print was relatively large, requiring a larger dome to be printed using 2PP, which increased the 2PP printing time. The printing time, in combination with the development time, significantly reduced the yield.

The tip radius limits AFM applications because it is relatively large compared to commercial cantilevers. Due to the printing resolution, the tip shape does not perfectly match the design, making it more difficult to determine the exact tip geometry required for measuring the Young's modulus of a substrate using the Hertz/Sneddon model.

The main limitation of the present study is the laser signal drift, which was observed during the AFM experiments. A drift in the signal towards negative saturation was observed (cantilever bending downwards to the substrate), when performing measurements in liquid. The drift rate was twice as fast in heated liquid (37 degrees Celsius). After immersing the cantilever in room temperature liquid for approximately 30 minutes, the signal stabilized. The drift resulted in a downward slope of the approach curve (of the baseline), far away from the substrate (instead of a horizontal line). Measurements that were affected by the drift were removed from the results. This drift must be eliminated before a definitive conclusion can be made regarding the applicability of the technique. This requires an investigation into the source of the drift.

The 2PP development process, of 48 hours in PGMEA and 16 hours in IPA, is still a disadvantage. Development optimization steps, e.g. flushing or tilt stirring, can speed up the development process. Using 2PP in combination with DLP enables complex designs that were previously impossible with standard cleanroom techniques. Using the 63x objective allows printing of very small features. The mechanical properties of the polymer introduce some disadvantages, such as a low Q factor and swelling.

The cost of 2PP printing compared to classical lithography methods and the design freedom can be advantageous for (small) batch and prototyping studies. The modular design allows for simple changes to a tip for specific applications. Despite the limitations, this research can be considered a step towards 3D printed microfluidic AFM cantilevers for FluidFM experiments and single-cell nucleus removal.

5 Conclusion

In this work, microfluidic AFM cantilevers were printed in a highly automated manner on a DLP print with a high success rate. A fundamentally new approach for multi-scale 3D printing has been created, that can be applied not only for the fabrication of hollow cantilevers but also for other types of structures.

The 2PP printing process using the 63x objective with IP-Dip photoresist resulted in cantilevers with a stiffness of 1.84 ± 0.24 N/m and apertures at the sharp tip as small as $1 \mu\text{m}$. The features of the final devices are given in table 3. With these cantilevers, AFM surface imaging of test substrates, cell puncture, nucleus aspiration, dispensing, and cell adhesion studies were performed. In a controlled puncture and aspiration experiment, a cell nucleus was successfully extracted from a human-derived myotube.

The results indicate that 3D printed (microfluidic) AFM cantilevers with the required functionalities can be printed and can be used for FluidFM experiments. In particular, it was demonstrated that a specific nucleus can be targeted and aspirated from a cell.

Feature	Dimension
Dome inner diameter	280 μm
Dome outer diameter	400 μm
Dome height	90 μm
Cantilever length	489 μm
Cantilever width	30 μm
Cantilever height	20 μm
Cantilever channel width	25 μm
Cantilever channel height	15 μm
Minimum tip aperture	1 μm
Minimum tip radius	270 nm
Cantilever stiffness	1.84 ± 0.24 N/m
Cantilever natural frequency	25.01 ± 1.10 kHz
Cantilever Q-factor (air)	24.02 ± 1.17 kHz

Table 3: Features and characteristics of final devices

Bibliography

- [1] X. Li and A.P. Lee. Chapter 2 - high-throughput microfluidic single-cell trapping arrays for biomolecular and imaging analysis. In Daniel A. Fletcher, Junsang Doh, and Matthieu Piel, editors, *Microfluidics in Cell Biology Part C: Microfluidics for Cellular and Subcellular Analysis*, volume 148 of *Methods in Cell Biology*, pages 35–50. Academic Press, 2018.
- [2] J.R. Heath, A. Ribas, and P.S. Mischel. Single-cell analysis tools for drug discovery and development. *Nature Reviews Drug Discovery*, 15(3):204–216, 2016.
- [3] A. Meister, M. Gabi, P. Behr, P. Studer, J. Vörös, P. Niedermann, J. Bitterli, J. Polesel-Maris, M. Liley, H. Heinzelmann, and T. Zambelli. FluidFM: Combining atomic force microscopy and nanofluidics in a universal liquid delivery system for single cell applications and beyond. *Nano Letters*, 9(6):2501–2507, 2009.
- [4] P. Saha, T. Duanis-Assaf, and M. Reches. Fundamentals and applications of fluidfm technology in single-cell studies. *Advanced Materials Interfaces*, 7(23):2001115, 2020.
- [5] O. Guillaume-Gentil, E. Potthoff, D. Ossola, P. Dörig, T. Zambelli, and J.A. Vorholt. Force-controlled fluidic injection into single cell nuclei. *Small*, 9(11):1904–1907, 2013.
- [6] M. Nouri-Goushki, L. Angeloni, K. Modaresifar, M. Minneboo, P.E. Boukany, M.J. Mirzaali, M.K. Ghatkesar, L.E. Fratila-Apachitei, and A.A. Zadpoor. 3D-Printed Submicron Patterns Reveal the Interrelation between Cell Adhesion, Cell Mechanics, and Osteogenesis. *ACS Applied Materials & Interfaces*, 13(29):33767–33781, 2021.
- [7] P.J.E.M. Van Der Linden, A.M. Popov, and D. Pontoni. Accurate and rapid 3D printing of microfluidic devices using wavelength selection on a DLP printer. *Lab on a Chip*, 20(22):4128–4140, 2020.
- [8] A.K. Nguyen and R.J. Narayan. Two-photon polymerization for biological applications. *Materials Today*, 20(6):314–322, 2017.
- [9] R.C. L. N. Kramer, E. J. Verlinden, L. Angeloni, A. van den Heuvel, L. E. Fratila-Apachitei, Si. M. van der Maarel, and M.K. Ghatkesar. Multiscale 3D-printing of microfluidic AFM cantilevers. *Lab on a Chip*, pages 311–319, 2020.
- [10] L. Snider, L.N. Geng, R.J.L.F. Lemmers, M. Kyba, C.B. Ware, A.M. Nelson, R. Tawil, G.N. Filippova, S.M. van der Maarel, S.J. Tapscott, and D.G. Miller. Facioscapulohumeral dystrophy: Incomplete suppression of a retrotransposed gene. *PLOS Genetics*, 6(10):1–14, 10 2010.
- [11] A. Tassin, D. Laoudj-Chenivresse, C. Vanderplanck, M. Barro, S. Charron, E. Ansseau, Y. Chen, J. Mercier, F. Coppée, and A. Belayew. Dux4 expression in fshd muscle cells: how could such a rare protein cause a myopathy? *Journal of Cellular and Molecular Medicine*, 17(1):76–89, 2013.
- [12] K.R.Q. Lim and T. Yokota. Genetic approaches for the treatment of facioscapulohumeral muscular dystrophy. *Frontiers in Pharmacology*, 12:281, 2021.
- [13] J. Campbell, N. Petta, O. Stein, Y. Liu, Y. Lu, and L. J. Jiang. Three-dimensional printing and deformation behavior of low-density target structures by two-photon polymerization. page 66, 08 2017.
- [14] E. D. Lemma, F. Rizzi, T. Dattoma, B. Spagnolo, L. Sileo, A. Qualtieri, M. De Vittorio, and F. Pisanello. Mechanical properties tunability of three-dimensional polymeric structures in two-photon lithography. *IEEE Transactions on Nanotechnology*, 16(1):23–31, 2017.
- [15] Y. Liu, J.H. Campbell, O. Stein, L. Jiang, J. Hund, and Y. Lu. Deformation behavior of foam laser targets fabricated by two-photon polymerization. *Nanomaterials*, 8(7):1–20, 2018.

-
- [16] J.M.L. Miller, A. Ansari, D.B. Heinz, Y. Chen, I.B. Flader, D.D. Shin, L. Guillermo Villanueva, and T.W. Kenny. Effective quality factor tuning mechanisms in micromechanical resonators. *Applied Physics Reviews*, 5(4):041307, 2018.
- [17] M.K. Ghatkesar, H.H.P. Garza, and U. Staufer. Hollow AFM cantilever pipette. *MICROELECTRONIC ENGINEERING*, 124:22–25, 2014.
- [18] F. Guilak, J.R. Tedrow, and R. Burgkart. Viscoelastic properties of the cell nucleus. *Biochemical and Biophysical Research Communications*, 269(3):781–786, 2000.
- [19] O. Guillaume-Gentil, R. Grindberg, R. Kooger, L. Dorwling-Carter, V. Martinez, D. Ossola, M. Pilhofer, and J.A Zambelli, T.and Vorholt. Tunable Single-Cell Extraction for Molecular Analyses. *Cell*, 166(2):506–516, 2016.

Thesis conclusion

A literature review was conducted, focusing on the fabrication of microfluidic AFM cantilevers for single-cell analysis. This review examined both the biological aspects (such as the components of the cell, cell mechanics and applications of FluidFM for single-cell analysis) and the technological aspects. The latter covered a variety of topics, such as state-of-the-art manufacturing techniques, atomic force microscopy and 3D printing techniques. In this thesis, the multiscale 3D printing technique of ir. Robert Kramer to a new level by improving the achievable print resolution, increasing the reproducibility and developing a highly automated method for printing 2PP structures on polymer surfaces. The result is a multiscale 3D-printed device that can be easily mounted on an AFM and connected to a microfluidic controller for FluidFM experiments, including total nucleus extraction. The developed microfluidic connection principle can be used for a wide variety of microfluidic devices.

The two main research questions posed at the beginning of this research can now be answered.

How to manufacture a sharp tip hollow cantilever with sub-micron resolution for nucleus extraction using two-photon polymerization on top of a 3D printed microfluidic interface?

Microfluidic AFM cantilevers can be 2PP printed with sub-micron resolution using the 63x objective in combination with IP-Dip photoresist in DiLL mode. The 2PP print was designed in three modules (dome, tip and cantilever), each printed with its own optimal settings and printing strategies. Since the 2PP structure did not fit in the writing field of the objective, block splitting was used for printing large structures.

A new substrate material was used for DLP printing (3DM Tough Clear), which is more compatible with 2PP printing process due to its transparency. The orientation of the DLP print (final surface parallel to the build plate) resulted in flat surfaces that are sufficiently smooth for 2PP printing.

The new printing strategy also involved using of a sacrificial holder to align the microfluidic interfaces in the Nanoscribe system. A thin layer of gold on the microfluidic interfaces enabled precise and automatic interface finding for the 2PP print. By tuning the galvoacceleration and other printing parameters, the increase in printing time was kept to a minimum. This printing strategy resulted in highly autonomous printing with high resolution, high repeatability and good bonding between the prints.

Cantilevers with a length of 500 μm and with an elliptical channel (25x15 μm) were printed with average stiffnesses of 1.84N/m. Tips with radii of 270 nm and apertures as small as 1 micron were achieved. This resolution was achieved by tuning the printing parameters for each module individually. The smallest achieved aperture is ten times smaller compared to previous work.

The gold did increase the amount of bubbles that formed at the surface of the DLP printed during 2PP printing. However, the formation of these bubbles was much less compared to HTM140V2. The bubbles were also trapped in the print without the need for any additional bubble trapping structures.

The design of the microfluidic interfaces made it very easy to mount them on an AFM system and connect them to a microfluidic pressure controller.

How to aspirate/dispense a nucleus from/into a multi-nuclear cell without damaging the nucleus, while keeping the cell alive? To be able to aspirate the nucleus, a sharp tip with an aperture at the front was used.

This aperture was located near the apex of the tip and has an elliptical shape (3.8 μm high and 3.1 μm wide). The tip was at a 45-degree angle to visualise both the tip and the nucleus could during experiments. By puncturing the cell at the location of the nucleus, the aperture was automatically aligned for aspiration. Using a set point force higher than that required for cell puncture ensured that the aperture was inside the cell (as far as possible). The viability of the cell after the puncture could not be determined. The distance from the tip to the farthest point of the aperture should be minimal to ensure that the entire aperture is inside the cell before aspiration begins. The pressure should also be set to zero before removing the tip from the cell. For the cell aspiration a pressure of -1000mbar was applied. With longer aspiration times, lower pressures can be used for the aspiration. Dispensing the entire nucleus could not be demonstrated. It was possible to dispense the aspirated liquids, but the nucleus could not be located afterwards.

Recommendations

The multiscale 3D printing approach, optimized in this work, opens up new possibilities for future research. The modular design of the 2PP print allows for adaptations for various types of single-cell research. Additional improvements are required to use the printing techniques and apply the resulting microfluidic AFM cantilevers in single-cell research. In this section, the recommended improvements are discussed.

DLP print

The current design of the microfluidic interface was optimized for the BioAFM holder (JPK). By altering the design, the microfluidic interface could also fit on other AFM systems. The design can also be altered to glue silicon chips with cantilevers onto the DLP print, making handling and aligning the cantilevers easier.

A different material for the DLP print is required to obtain the following features:

- Higher heat resistance and less swelling for cell studies at elevated temperatures.
- Directly detectable by the 2PP interface finder (without gold-sputtered layer).
- Smaller feature sizes (mainly for the aperture as this would decrease 2PP printing time)

If other materials for DLP printing can not be found, some changes can be implemented for the design and DLP printing approach.

- Various aperture shapes (e.g. oval, rectangular hexagonal, or triangular)
- Microfluidic interfaces can be tilted 90 degrees, meaning the aperture will be on what is currently the side of the microfluidic interface (allows for printing the cantilever vertically without block splitting)
- Other DLP print orientations can be tested to find the minimum aperture size (with 3DM Tough Clear it should be possible to print on top of the ripples caused by the Z layer steps of the DLP print)
- To obtain smaller apertures and channels in the DLP print, wavelength selection could be used. [1]
- A coating or post-processing method could be used to optimize the surface of the DLP print.
- Print a membrane and puncture it to create an aperture.

The invented microfluidic connector principle can be used for other applications, e.g. microfluidic chips, organ on a chip, tubing connectors or tube splitters. This allows for connections to be made in any direction, making it much easier to approach a microfluidic chip with a microscope objective.

Alternatives for DLP printed substrates

Other fabrication techniques could also be used to overcome the limitations of the DLP print, suggested techniques that could be explored are:

- Selective laser etching (SLE) of fused silica could offer new possibilities for (reusable) substrates (instead of DLP printing). These SLE interfaces can be mounted in a 3D-printed holder for Nanoscribe printing.
- Machined PMMA could also be used as a substrate. An option to fabricate PMMA interfaces is selective laser machining [2].
- Use fused silica or silicon chips with an aperture as a substrate, which can then be bonded to a 3D printed microfluidic interface.
- Use another 3D printing technique or printer brand.

2PP printing

The multiscale 3D printing approach could also be applied to fabricate other types of devices. This could be in the fluidics field, which allows the coupling of small channels or nozzles to larger structures and printing membranes, pores, valves, and other volume-limiting structures. The latter could be used to achieve precise dispensing.

The automatic interface finding approach, with gold sputtering, could be used for printing on non-3D printed polymers (e.g. flexible plastics or Petri dishes). To further optimize 2PP printing on a DLP print, other DLP print coatings should be investigated. The gold-sputtered thin film still introduces bubbles during the printing process (due to photon absorption). Even though the bubbles remain embedded in the print, their formation should be prevented. Aluminium and titanium coatings might prove beneficial.

Changing the geometry of the dome (e.g. only printing a flat plate on top of the aperture) could speed up the printing process. Another geometry that should be optimized is that of the cantilever. The cantilever and its behaviour during experiments should be investigated (especially the drift). The roughness (sawtooth) shape on the bottom side of the cantilever could be removed by first double printing the bottom micron of the slab before continuing (only required at the free end of the tip where the laser is reflected). Another solution to decrease

the cantilever roughness is printing the cantilever at an angle or even vertical. This can help to decrease the printing time as larger blocks, and less overlap is required (for vertical printing, no block splitting is needed for the cantilever). The shape of the channel and the dimensions can be changed to create a larger cross-section. The height of the cantilever can be lowered, and the width can be increased. The latter will increase the signal strength, as a larger fraction of the laser will be reflected.

Performing a tip optimization could offer huge benefits for new cell experiments. The height of the aperture should be minimized to ensure the entire aperture is inside the cell. The tip optimization should focus on the geometry, surface alterations (e.g. coatings or silanization) and printing parameter optimizations (smaller tip sizes should be possible with repeated scanning at a lower laser power). Coatings that reduce the interaction of the cantilever with the cell membrane should be investigated in future research (e.g. Sigmacote [3]).

Another opportunity is by printing sharp hollow tips on top of commercial silicon cantilevers. This way, the tip geometry has a large design flexibility while keeping the properties of the silicon cantilever. Printing the sharp tip on an existing cantilever can also improve the signal and decrease the drift. Commercial (Cytosurge) FluidFM cantilevers should be compared with the 3D printed microfluidic AFM cantilevers.

Using 2PP, 25nm tip radii should be possible, but it is challenging. A suggestion is to investigate other methods of fabricating sharp tips. Yum et al. [4] made silicon tips with a diameter less than 30 nm using a focussed ion beam (FIB). Using FIB to sharpen the tips after printing could be investigated. Growing carbon tips on top of the cantilever or use focused electron beam-induced deposition (FEBID) for tips with radii in the range of 10 nm ([5]) could also be investigated if the polymers can withstand the environmental conditions (e.g. elevated temperatures).

A new study could be performed into minimizing the printed volume (e.g. lowering dome wall thickness), increasing the galvoaccelerations and changing other print parameters to decrease the total printing time. Printing the dome with another magnification (e.g. 10X) and then the cantilever and tip with the 63X could decrease printing times while keeping the required resolution at the tip and cantilever.

Coating the back side of the cantilever with aluminium could also improve the signal. The influence of the thickness of this (gold) coating on the stiffness and the signal should be investigated in future research.

The low Q factor of 2PP printed cantilevers can be used for high-speed AFM imaging [6]. Adams et al. [6] used SU-8 cantilevers to prove that the low Q can be beneficial for high-speed imaging. The Young's modulus and density of SU-8 are relatively comparable to that of IP-Dip. This means that similar resonance frequencies should be obtainable. However, to get sharp tips, a method has to be developed to either print or grow sharp tips on top of 3D-printed cantilevers.

Experiments

During the experiments, drift was sometimes observed while performing measurements or when approaching. The drift was in the direction of the substrate (so away from the DLP print). The exact cause of the drift remains unclear, but it is hypothesized that the swelling of the DLP print, buoyancy of the 2PP print, hydrodynamic forces or an interaction between the cantilever and the DLP print might have been involved. Only the swelling explains the stabilization after half an hour. Future research should investigate different cantilever geometries with different stiffness and other substrates to determine the cause of the drift.

Wang et al. [7] state that: "The drift can be caused by the thermal bending of the cantilever (especially due to asymmetry in cantilever dimension), electrical fluctuations, and the thermal drift of the mechanical supporting structures. The drift is associated with the environmental temperature and is time-dependent." The cantilever itself is symmetric, but the cantilever is printed in blocks with an overlap. The dose of the cantilever can thus be asymmetric, which can cause bending due to differences in swelling. Post curing the 2PP print could help prevent this bending.

As only 1/1000 to 1/200 of the nuclei show the DUX4 overexpression [8], it is essential to be able to distinguish that particular nucleus. The nucleus can be distinguished and targeted by adding fluorescent labels and using the fluorescent microscope on the AFM. The fluorescence can also help visualize the nucleus after removal, but the influence of the autofluorescence of the cantilever should be investigated. Using fluorescent or stained nuclei can help develop a method to deposit and store a nucleus in a microwell (e.g. filled with mineral oil). The method for depositing a nucleus in a container to be used for tests still needs to be developed. One suggestion is to print a small well (using 2PP) and add it to the Petri Dish with cells. Injecting fluorescent markers into the cell can help determine if the cell survives punctures and how the membrane restores. During the puncture experiments, no clear holes in the membrane remained, and also the cells seemed to survive (did not detach). However, during the aspiration experiments, the membrane often ruptured as the negative pressure was still being applied. Additional experiments are required in which no pressure is applied when retracting the tip to assess the membrane damage.

The aspiration procedure should be optimized for new tips, as there is a trade-off between the applied pressure and the aspiration time. Smaller under pressures require a longer aspiration time, but might result in a more gentle nucleus extraction (less forceful removal) than larger under pressures. Partial aspiration could also be investigated as a nucleus extraction approach. This would mean that the nucleus is at the tip while being retracted.

Coating the cantilever with, for example, Sigmacote [3] is already performed for classical cantilevers to prevent sticking. It is a siliconizing reagent for glass and other surfaces (also used for some plastics [3]). Sigmacote

forms a microscopically thin covalent film on the surface of the cantilever and tip, which repels water (extremely hydrophobic) and prevents the sticking of other materials to the surface. It might even be used to solve the drift problems.

The viability of the cells after puncture should be investigated by monitoring them over a longer period. This requires the incubator conditions, which could be mimicked using the JPK sample heater, preferably a 5% CO₂ concentration and also a correct humidity. The latter is complex to apply in the AFM system. Furthermore, investigations into transporting the nucleus after removal and the cell viability should be performed. This might require adding an incubator system to the AFM, which allows studying the cells over a longer period.

The puncture forces and the stiffness of the cells which come forth from indenting the cell require more precise studying of the tip radius. This requires several experiments on tests substrates (e.g. PDMS) with both printed as commercial cantilevers.

Future work

This work has paved the way for fast multiscale 3D printing with high resolutions for microfluidic AFM cantilever printing. The simulations show that the behaviour of the cantilever can be captured accurately. In addition to the recommendations, future projects can investigate:

- Combining 2PP printed suspended structures with inkjet printed electrodes (e.g. MEMS devices or for actuation).
- Printing cantilevers with optimized frequency response by using unconventional geometries.
- Printing low stiffness solid cantilevers ($k < 0.06$ N/m) for cell imaging.
- Printing nozzles on DLP prints. The methods can be used to print pick and place nozzles with a very small aperture on top of a DLP print.
- Designing an inexpensive tool that allows the use of the cantilevers without the need of an AFM setup.
- Optimization of the tip shapes for various types of FluidFM experiments, including cell puncture, cell manipulation, cell adhesion and cell indentation.

Part III

Appendices

Contents of the appendices

The following appendices provide more detailed information on the production and experimentation process. They serve as supplementary information to the paper found in the second part of this report. The contents of the appendices are listed below.

Appendix A: EnvisionTEC (DLP) Printing	p. 77
Appendix B: Nanoscribe (2PP) Printing	p. 105
Appendix C: AFM	p. 147
Appendix D: Polytec	p. 159
Appendix E: COMSOL	p. 165

Appendix A: Digital light processing (DLP)

A.1. Introduction

The basic principles of DLP printing were discussed in the chapter “Introduction to the Technological Aspects” (part 1 of the report, section 3.4). The paper (part 2 of the report), summarized the results obtained from DLP printing. However, there were many challenges during the research process, as the designs are close to the limit of the printer. Any DLP print requires a certain degree of optimization to achieve optimal results. There are only a limited number of variables that can be changed on the EnvisionTEC Micro HD printer, which makes the device user-friendly and makes it difficult to push it to extremes.

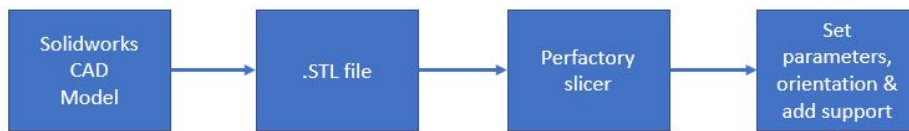
In this appendix, printing with the EnvisionTEC DLP printer will be discussed for future researchers to get a head start. The optimization and design process will be summarized to provide guidance for new projects. The main emphasis will be on the optimization of the print for this research, but the approach can be used for various applications.

It should be noted beforehand that the obtained results depend on the machine, the calibration and the environmental conditions. These will be discussed in this appendix as well.

A.2. Workflow

The first important topic to discuss is the general workflow for the EnvisionTEC Micro HD. The workflow can be divided into three main parts: preparation of the print file, preparation of the printer and development of the print. The workflow is shown schematically in figure A.2.1.

A) Preparing the print file



B) Preparing the printer



C) Developing print

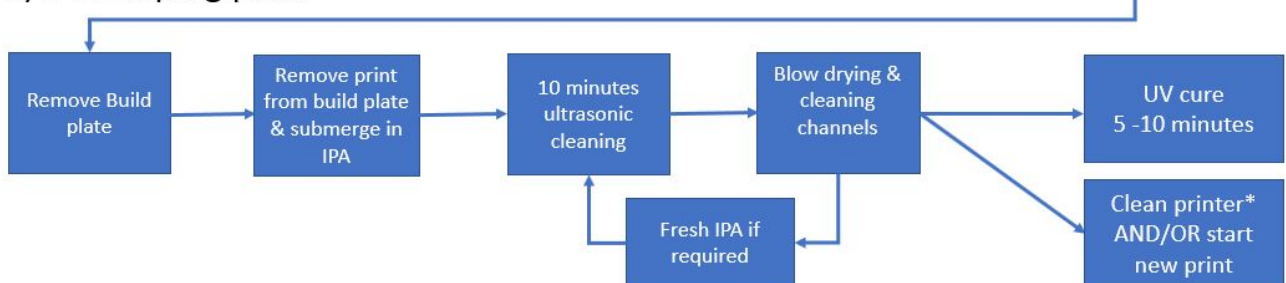


Figure A.2.1: EnvisionTEC workflow used during this research. Three parts are distinguishable, namely preparing the print file, preparing the printer and developing the print. *For the cleaning of the printer, the workflow given during training must always be followed precisely. After failed prints (e.g. only support printed or parts missing) the resin tray should always be cleaned.

As can be seen in figure A.2.1, there are a limited number of steps that the user can take to influence the outcome of the print using the EnvisionTEC printer. The main variables that the user can change are the design of the object, orientation, placement and properties of the support, the choice of material and the development. By tuning these variables, one can print features close to the printer's maximum resolution and meet the requirements. It is important to know that no changes can be made to the exposure time on this machine. The following sections discuss these optimizations, focussing on how they were applied to this research. It should be noted that any change to a design might require a new optimization. So the parameters are not set in stone but should be used as a guideline.

A.3. Materials for DLP printing

There is a vast range of materials available for DLP printing. Each material is optimized for a specific wavelength and a specific application. Some materials can withstand high temperatures, be used for high-resolution printing, remain flexible, or have unique properties. However, the EnvisionTEC Micro HD prevents the use of third party resins by using a special material tag. This material tag stores the amount of resin used and comes with each bottle of resin. The printing recipe is tuned by EnvisionTEC for each material and each layer height. This recipe contains the exposure time per layer. Unfortunately, these parameters cannot be changed by the user. Only a limited number of materials were available in our lab for the EnvisionTEC printer. One of the official materials available for the printer is HTM140V2. This material is designed for high-resolution printing with layer heights as small as 25 μ m. It is mainly used for high-temperature moulding as it has a high-temperature resistance (can withstand up to 140 degrees Celsius). To achieve this high temperature resistance, titanium dioxide (TiO₂) is mixed with the acrylated monomers and oligomers. This addition makes the material relatively brittle after printing. The HTM140v2 prints have an olive green colour and are opaque. The biocompatibility of HTM140V2 was tested by Kramer et al. [9] by investigating the viability of cells after contact with the print. Kramer et al. [9] also printed 2PP structures on this material but with suboptimal results.

For multiscale 3D printing, it was found that the 2PP does not print optimally on the HTM140V2. It is hypothesized that the additives (TiO₂ and colouring), the opaqueness and chemical compatibility caused the suboptimal 2PP printing quality. This will be discussed in more detail in appendix B.

The latter means that a different material had to be found for multiscale 3D printing. Various third-party materials were tested on the EnvisionTEC printer, using the same recipe, settings, and material tag as used for the HTM140v2 (as the recipe itself cannot be changed and no other recipes were available at the time of this research).

The best compatible third-party material was found to be 3DM Tough Clear, a transparent material that can be printed with UV LED light sources with wavelengths ranging from 365 nm to 405 nm [10]. It is therefore compatible with the EnvisionTEC Micro HD. Figure A.3.2 shows two flat prints, one made using HTM140V2 and one using 3DM Tough Clear.



Figure A.3.2: Comparison of HTM140V2 (left) and 3DM Tough Clear (right) by printing flat plates (25 mm x 25 mm x 0.7 mm) that can be used as 2PP substrate for dose tests.

3DM Tough Clear can also be used for medical models and devices, according to the manufacturer [10]. However, the heat resistance of 3DM Tough Clear is suboptimal, as the material becomes more flexible when exposed to elevated temperatures (noticeable from about 35 degrees Celsius). The achievable resolution is also worse compared to HTM140V2 due to the material properties and transparency. The transparency means that stray light can lead to over-polymerization, which can clog channels and apertures. To prevent this, changes have been made to the design to achieve optimal printing results that meet the requirements. An advantage of the transparency is the improved compatibility with 2PP printing, discussed in appendix B. An additional advantage is the price: HTM140V2 is three times as expensive per litre as 3DM Tough Clear. As mentioned in the paper, the experimental results with cells were all achieved using 3DM Tough Clear as a material for the DLP print. For future research, it is recommended to buy additional (official) materials from EnvisionTEC to compare the print results and properties.

A.4. Slicing

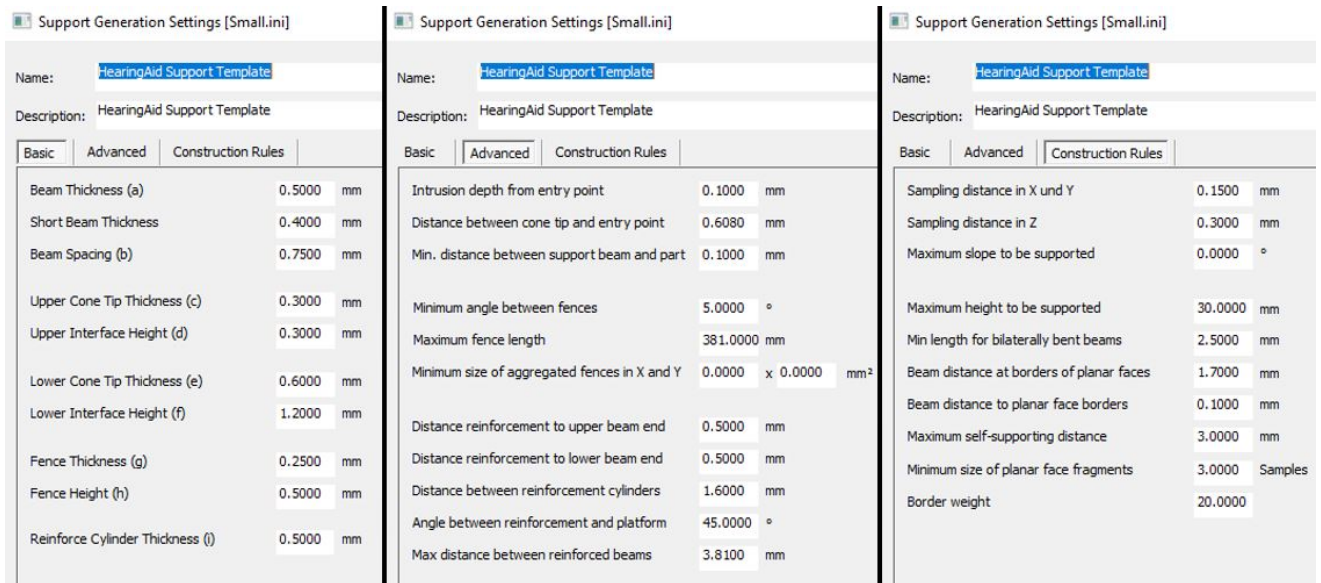


Figure A.4.3: Support settings EnvisionTEC (“small” support based on default hearing aid support template)

The design of both the interface holder and the interface is performed in Solidworks as two separate parts. These parts can then be combined into an assembly, which results in an interface “floating” in the holder. When the CAD assembly is finished, it can be imported into the Perfactory slicer (as an .STL file). Both parts of the assembly are then combined in one .STL file. For every material, the user can select various layer heights in the Perfactory slicer. For the HTM140V2 resin, the layer heights that can be selected are $25\mu\text{m}$, $35\mu\text{m}$ and $50\mu\text{m}$. The greater the layer height, the shorter the printing time. Smaller layer heights, however, often (but not always) result in better resolution. Changing the layer height also influence surface quality.

For this research, the DLP print design was optimized to be used with the $50\mu\text{m}$ layer height. Other layer heights did not significantly change the sizes of features, and the surface quality was even better with greater layer heights. Again, each design may have its optimal setting. Once the layer height has been selected, one can orient the print on the print bed. All prints were elevated from the build plate with 1-1.5 mm to prevent the print from bending during its removal from the build plate. Adding the support to the print job in the slicer is an easy step, but the support sizes and density need to be tuned. By changing various sizes of the support and the support density, one can alter how easy or difficult the print comes off. However, too little support results in failing prints, and too much support require much post-processing. The “small” support settings were used for printing the devices for this research. The used support settings can be seen in figure A.4.3.

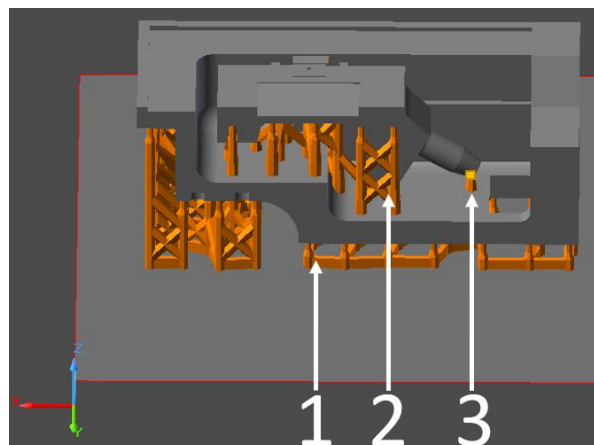


Figure A.4.4: Screenshot of Perfactory slicer after support has been added. 1) Indicates external support that bridges the 1.5 mm elevation from the build plate, 2) Indicates the internal support below the interface, 3) Indicates a manually added support marked by a yellow square.

It was often necessary to manually add or remove supports to the print. The manual removal of the programmed supports was sometimes required for the channels in the print, and the addition was necessary in case a large area lacked supports. Therefore, the print needs to be inspected before generating the build job. Figure A.4.4 shows the supports of a part that is elevated 1.5 mm above the build plate. As indicated in the figure, additional supports were manually added to the print job. The slicer automatically programs a longer exposure time for the supports, making them more brittle and thus easier to remove. A resulting print is shown in figure A.4.5 (before removal from the build plate).

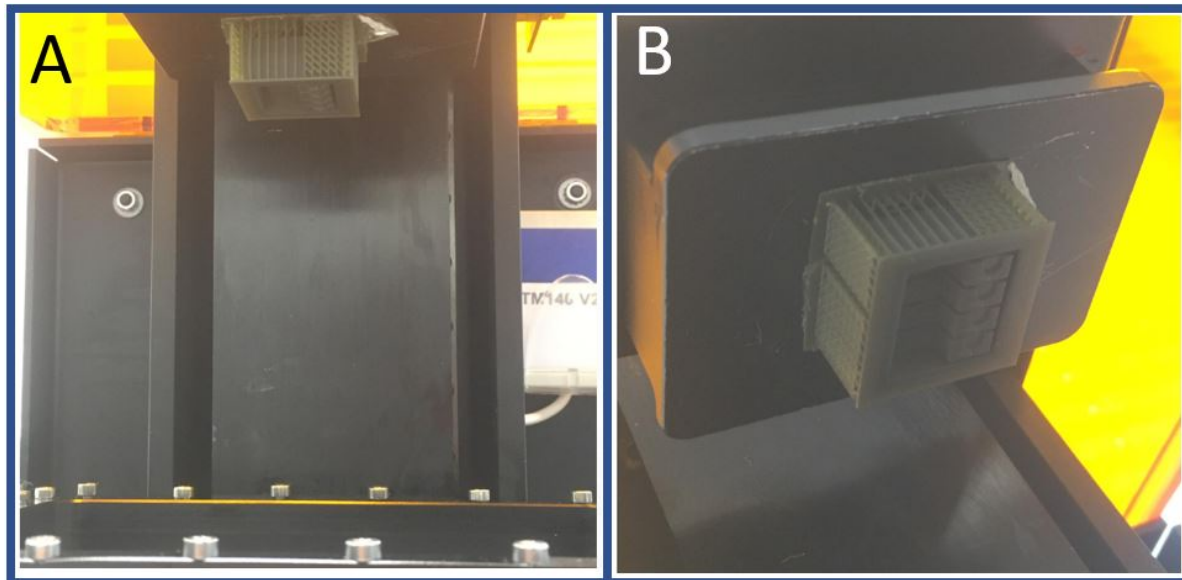


Figure A.4.5: Two different views of a print on the build plate. The print is printed upside down to be able to cover each new layer with resin by withdrawing the print from the resin pool and immersing it again. **A)** Front view **B)** Isometric view

The best results with the Nanoscribe can be obtained on smooth surfaces. Since DLP is a layer-by-layer process, ripples appear on the sides of the print for each layer. However, the final surface is much smoother as it is exposed all at once. The layer ripples and the smooth surface are visible in figure A.4.6. For some printers, the X resolution is better than the Y resolution. However, with the EnvisionTEC this was only visible if it was poorly calibrated, i.e. the rotation (around the Z-axis) of the part should not matter.

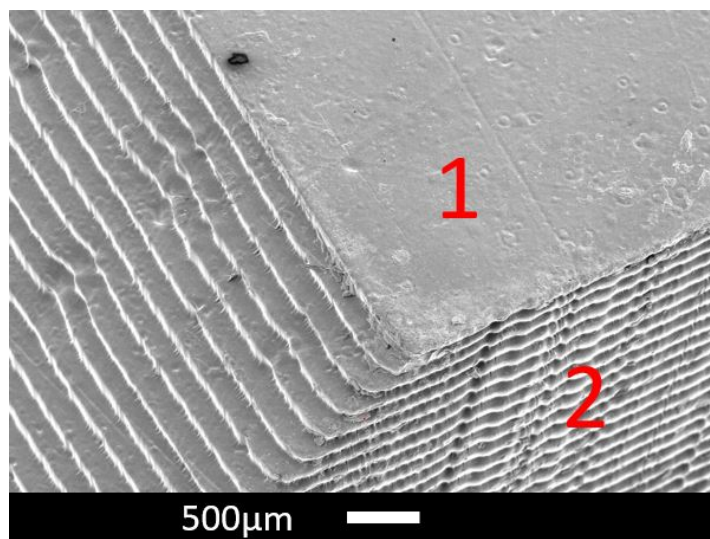


Figure A.4.6: SEM image showing the roughness of the top plane (1 = XY plane) and side plane (2 = XZ plane).

To determine the roughness in the various printing planes, a test cube was printed. Figure A.4.7 shows the results of a printed square XYZ test cube. The X indicates the plane perpendicular to the X-axis (YZ plane), the Y indicates the plane perpendicular to the Y-axis (XZ plane), and the Z indicates the plane perpendicular to the Z-axis (XY plane). One can see that the surface indicated with the Z (final printed surface printed) is much smoother than the other faces. The obtainable feature sizes were also best in this plane, as layer ripples did not influence them.

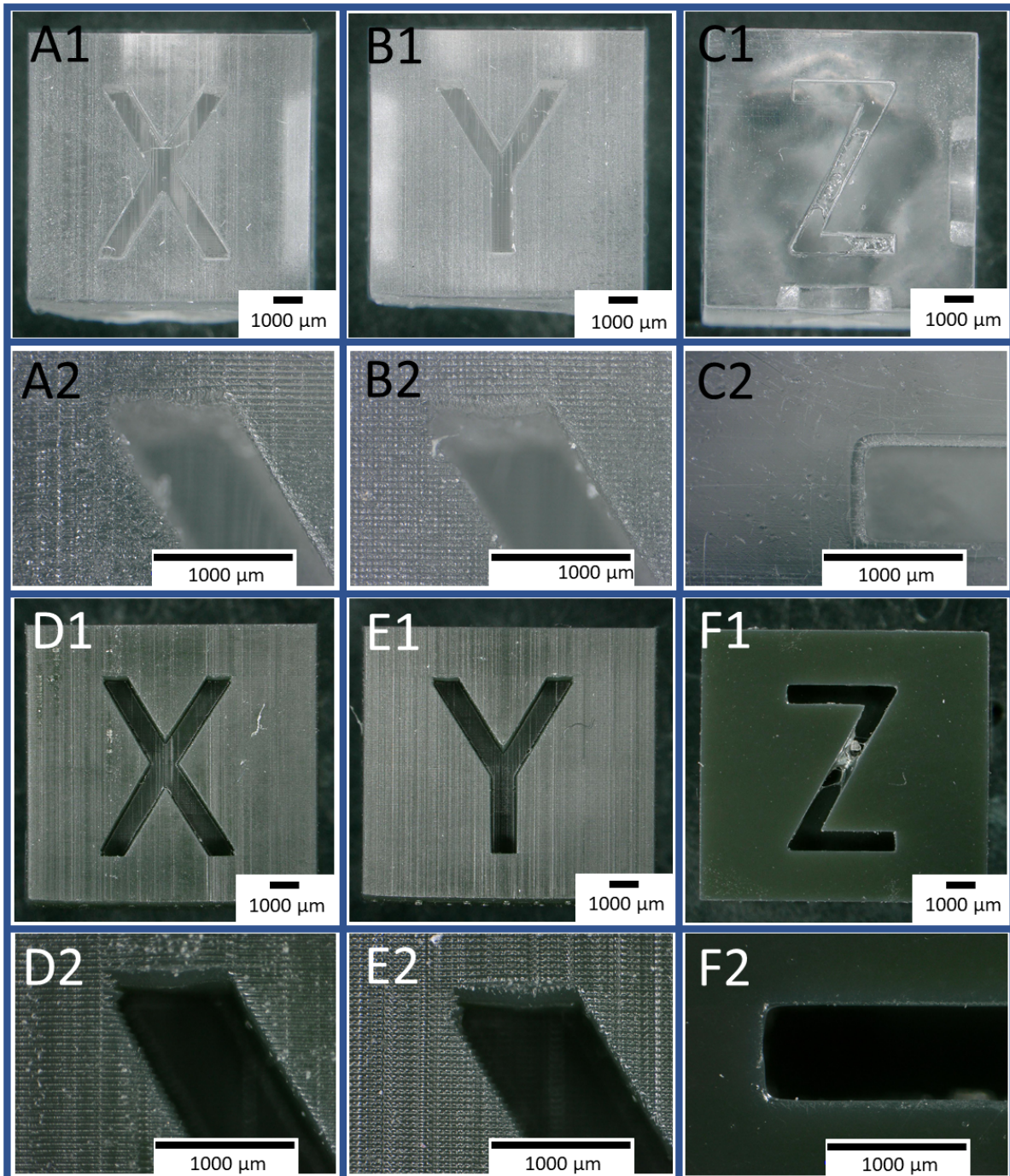


Figure A.4.7: Comparison of various printing surfaces. The X indicates the plane perpendicular to the X axis (YZ plane), the Y indicates the plane perpendicular to the Y axis (XZ plane) and the Z indicates the plane perpendicular to the Z axis (XY plane). The latter is clearly much smoother than the other surfaces. **A-C)** 3DM Tough Clear print with 1 = 20x magnification, 2 = 150x magnification, **D-F)** HTM140v2 print (same magnifications as for A-C)

A.5. Design & print iterations

The design process for DLP printing starts with printing test structures to determine the achievable feature sizes and print quality. The results of these test structures were used to make the first iterations for the functional parts. However, as the print quality depends on the geometry, their results could not be applied directly, and additional iterations were required, which had to be carried out separately for each material. Through continuous iterations, each part of the design was optimized.

There were five parts to be printed using DLP, all of which required a certain degree of optimization. These parts are listed below:

- Microfluidic interface: a substrate for 2PP printing, connects the fluidics of the microfluidic controller to the cantilever and fits the AFM system.
- Securing element: creates a leak-tight connection with the tubing together with the connector of the microfluidic interface.
- Interface holder: holder that fits the Nanoscribe substrate holder & aligns multiple interfaces (printed together and attached to the interfaces using sacrificial supports).
- Flat test substrates for Nanoscribe.
- Sample development holder: to hold substrates while developing 2PP prints.

To optimize the printing of these parts, test structures were printed to vary parameters over an extensive range.

A.5.1. Test structures

To optimize the crucial features of the device, several test structures were designed and printed to find a range for the final design. The most important parts of the DLP print to optimize for this research were the channel through the microfluidic interface and the aperture at the print's surface.

The parameters that can be optimized include:

- Geometry
- Layer height
- Distance to edge of print
- Number of layers above a cavity

An example of geometry optimization is shown in figure A.5.8. The test shows that all the apertures are open, but the smaller the square apertures become, the more they start to become circular due to over polymerization. The underlying channels can also be seen in figure A.5.8A for the top three apertures. No channel is visible for the bottom two apertures, which means that they are clogged due to over polymerization (channel diameter is too small).

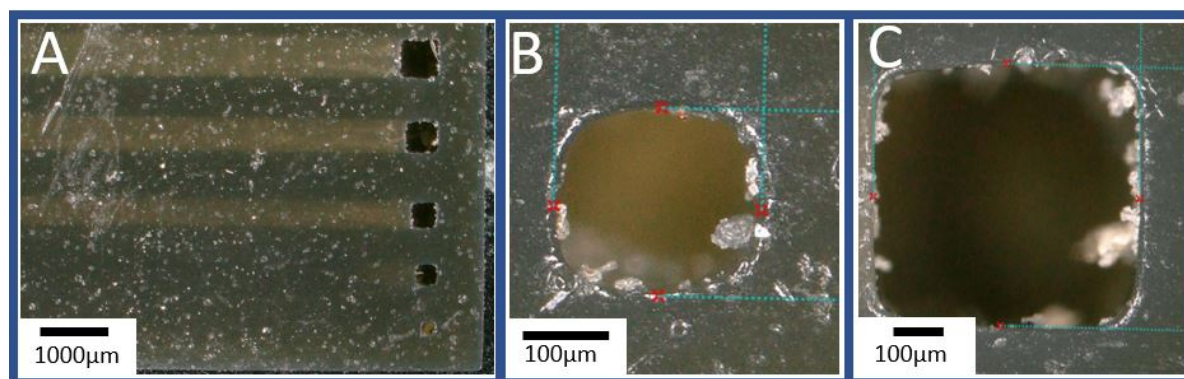


Figure A.5.8: Square hole printing test using HTM140V2, with apertures printed on XY plane of printer. **A)** Overview of a test print with square apertures with sizes ranging from $250\ \mu\text{m}$ (bottom) to $650\ \mu\text{m}$. One can see that the bottom two channels are clogged while the others are open (light coloured horizontal lines) **B)** square hole designed to be $250\ \mu\text{m}$ (printed $228 \times 242\ \mu\text{m}$). starts to become circular, **C)** $550\ \mu\text{m}$ square hole (printed $514 \times 532\ \mu\text{m}$)

A better result was observed for circular apertures (shown in figure A.5.9). During these experiments, it was found that circular apertures of $80\ \mu\text{m}$ in the XY plane are possible to print (note: results with HTM14V2). It is important to note that there is an influenced region around the aperture where the surface is curving into the aperture. This region, indicated in figure A.5.9 approximately has a diameter of $120\ \mu\text{m}$ for an aperture of $80\ \mu\text{m}$.

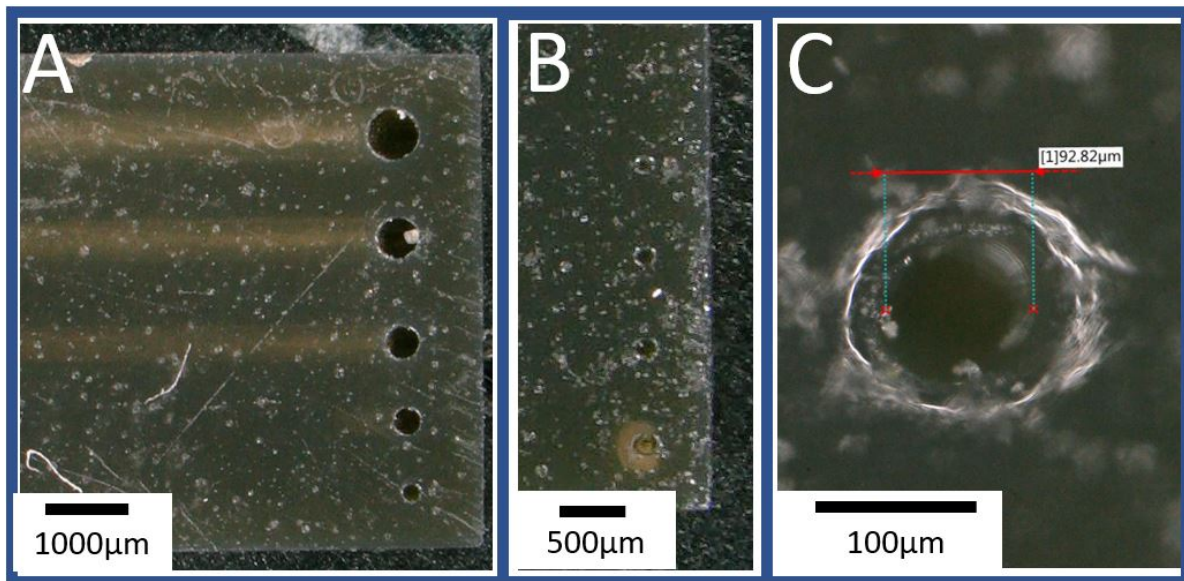


Figure A.5.9: circular hole printing test using HTM140V2, with apertures printed on XY plane of printer. **A)** Overview of a test print with circular apertures with diameters ranging from $250\ \mu\text{m}$ (bottom) to $650\ \mu\text{m}$. One can see that the bottom two channels (same size as the aperture) are again clogged while the others are open (light coloured horizontal lines) **B)** Hole test with apertures ranging from $60\ \mu\text{m}$ (top) to $140\ \mu\text{m}$ with **C)** $80\ \mu\text{m}$ hole with a large influenced area around it.

As can be seen in figure A.5.8 and A.5.9, some of the underlying channels were clogged. Therefore, the dimensions of the channel had to be optimized to prevent this clogging. An example of a test print to find the minimal channel size can be seen in figure A.5.10.

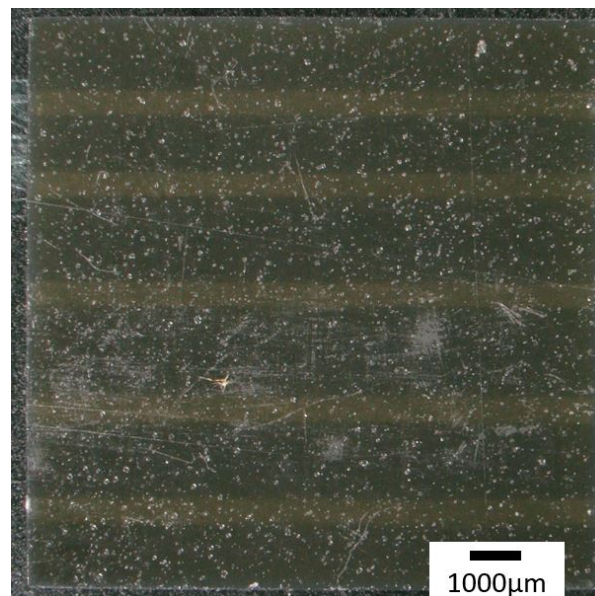


Figure A.5.10: Test print of various channel widths (all properly developed) ranging from $400\ \mu\text{m}$ (top) to $800\ \mu\text{m}$ (bottom) and a channel height of $200\ \mu\text{m}$. Channels run internally through the print from left to right and are the lighter parts of the print.

The required distance between the edge of the print and the aperture was also determined experimentally using a test print with varying edge to aperture distances. The print can be seen in figure A.5.11. No problems occur for distances greater than $110\ \mu\text{m}$ (as long as the channel is equally far from the edge as the aperture).

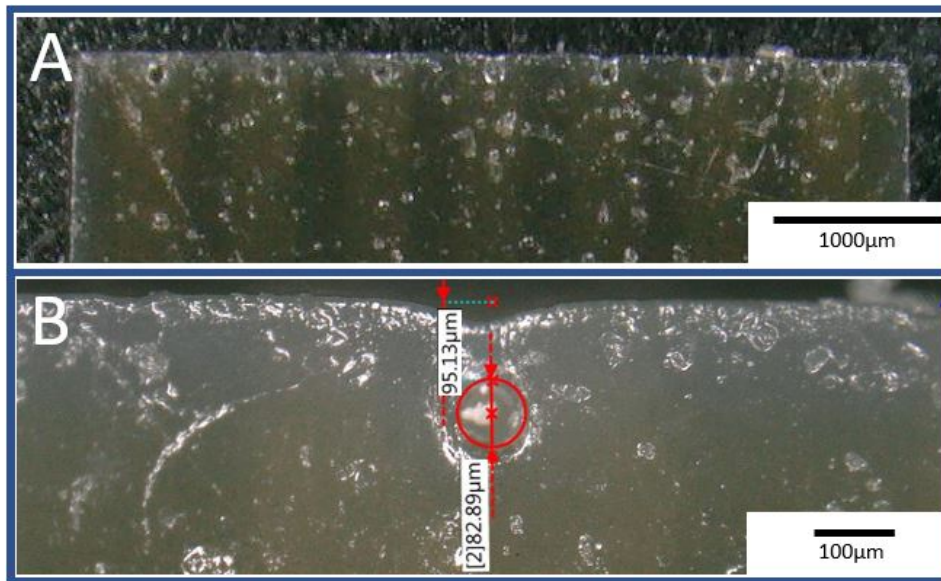


Figure A.5.11: Test print (HTM10v2) of various distances between the aperture and the print edge with constant aperture diameter of $80\ \mu\text{m}$, **A**) Overview of the print with distances ranging from $50\ \mu\text{m}$ (right) to $120\ \mu\text{m}$ (left), **B**) Print of with an edge-aperture distance of $100\ \mu\text{m}$, the influence of the aperture is clearly visible at the edge.

After these first optimization steps, more realistic structures were printed with the simple test structures' parameters. It was found that the parameters were not directly transferable to the final structures. However, they provided an initial range for the first designs. Therefore, the values found in the test prints were used as a starting point to optimizing the final designs. Therefore, test prints with simple structures were kept to a minimum (only performed when changing materials), and instead, arrays of structures resembling the final geometries were printed with varying parameters, as shown in figure A.5.12.

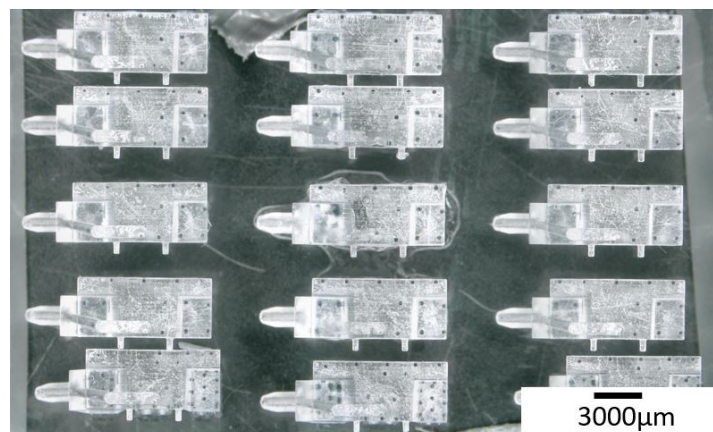


Figure A.5.12: Array of 3DM microfluidic interface printed to determine the minimum aperture diameter. To rule out external factors, prints were repeated with multiple identical prints at various locations on the print bed

The following sections discuss the design and print optimization for several parts of the DLP print (which were optimized by printing large arrays with varying parameters but repeated multiple times to rule out accidental successes).

A.6. Microfluidic interface

The microfluidic interface has four crucial parts: the AFM mounting area, the channel, the aperture, and the surface's quality around the aperture. These are discussed separately in the following subsections.

A.6.1. The AFM mounting

To mount the microfluidic interface on the AFM, the BioAFM holder was used. In figure A.6.13A-D, a CAD model of the holder is shown. This CAD model was used to design the cavity in the microfluidic interface. By subtracting the shape of the holder from a solid interface shape, the exact inverse shape of the holder was mimicked. Figure A.6.13C and D show the spring and screw that hold the interface in place. The interface is secured by tightening the screw. The combination of the shape and the spring clamp determines the position of the interface and automatically aligns it (and thus also the cantilever).

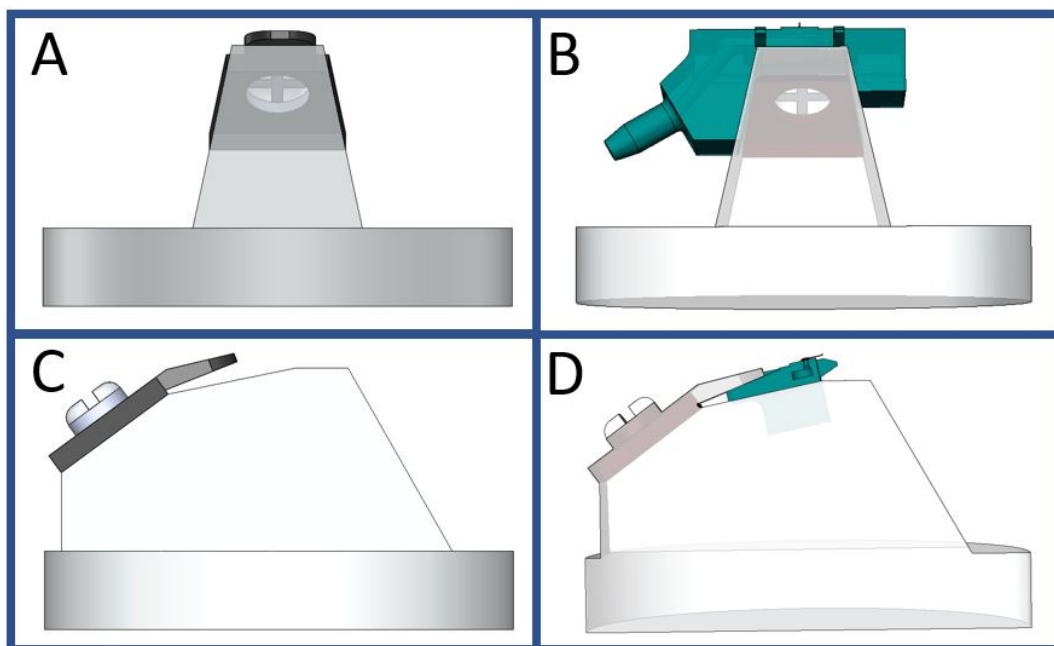


Figure A.6.13: JPK BioAFM holder CAD model and with(out) microfluidic interface. **A)** Front view of BIO AFM holder without microfluidic interface **B)** Front view of BioAFM holder with micro fluidic interface **C)** Side view of BioAFM holder without microfluidic interface, **D)** Side view of cross-section of BioAFM holder with microfluidic interface.

Since the spring clamps the interface at an angle (as seen in A.6.13C), a slope was added to the design of the interface to prevent plastic deformation of the spring. This slope can be seen in figure A.6.14A.

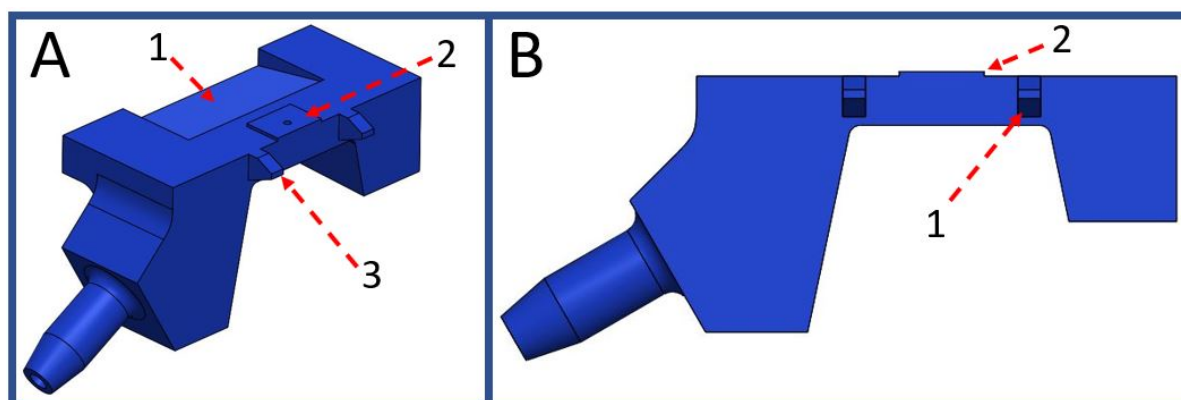


Figure A.6.14: Two different views of the microfluidic interface. **A)** Isometric view of the interface. 1 = The sloped ramp for the AFM holder spring, 2 = Elevated plateau for 2PP print and 3 = The cantilever protection. **B)** Front view of the microfluidic interface, with 1 = The cantilever protection and 2 = The elevated plateau.

During the handling and mounting of the interface, accidents can occur. In particular, tipping over the interface could cause damage to the cantilever. Therefore, the microfluidic interface was provided with cantilever protection bars that prevent the cantilever from breaking when the device tips over. The protection bars were the idea of dr. ir. T. Manzanque Garcia and are shown in figure A.6.14A and B.

Another additional feature of the design is the elevated plateau (see figure A.6.14). The 2PP print is printed on top of this plateau, which ensures that the 2PP printed tip is always the highest point of the device and thus the first to contact the substrate (during AFM experiments).

Several iterations were performed to get a correct fit on the AFM holder. In order to exactly replicate the inverse shape of the AFM holder, the shrinkage of the polymer needs to be taken into account. Through trial and error, the correct dimensions were found. Another crucial dimension is the distance between the raised printing plateau and the AFM holder. For this research, $950\ \mu\text{m}$ was used for this distance, as shown in figure A.6.15. This is because the ceiling and floor of the channel running through the interface should remain thick enough to prevent damage when the interface is removed from its supports.

Reducing the height of the interface and thus bringing the cantilever closer to the AFM holder might improve the cantilever's performance (e.g. signal and drift). The overall size of the interface posed no problems for the experiments (it did not hit any of the AFM parts). The height of the interface was even beneficial for the tubing during the AFM experiments (tubing could not touch the Petri dish).

Figure A.6.15 to figure A.6.19 show the technical drawings with the dimensions of the microfluidic interface from various views. In the next section, a render is shown next to the assembled device (figure A.6.27).

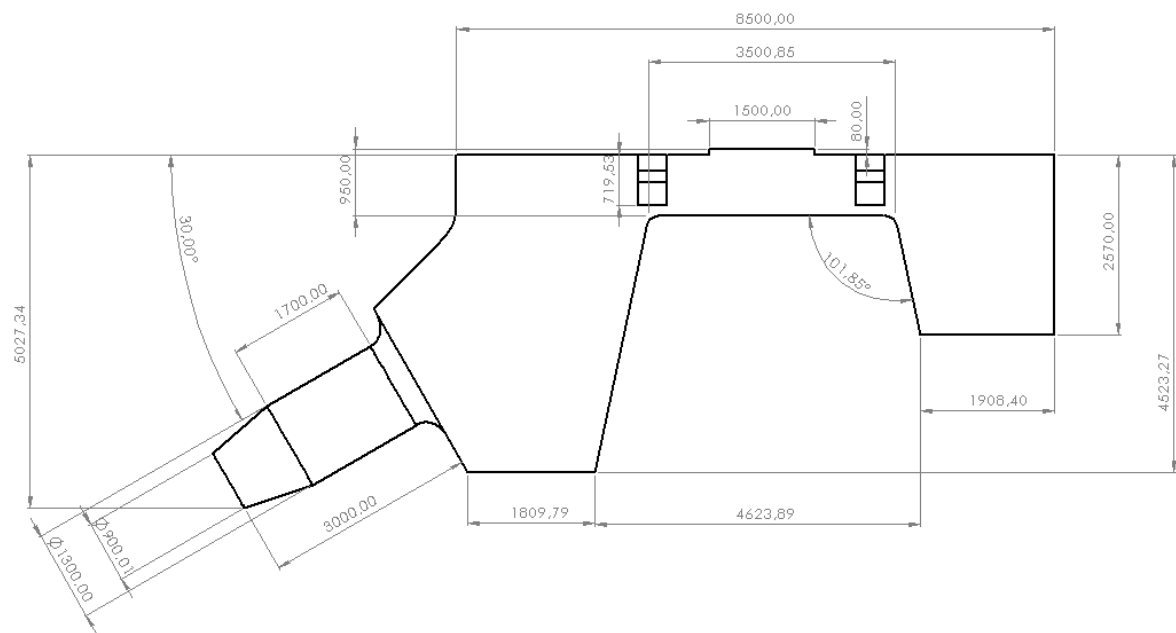


Figure A.6.15: Microfluidic interface drawing front view. Dimensions in micrometres [μm].

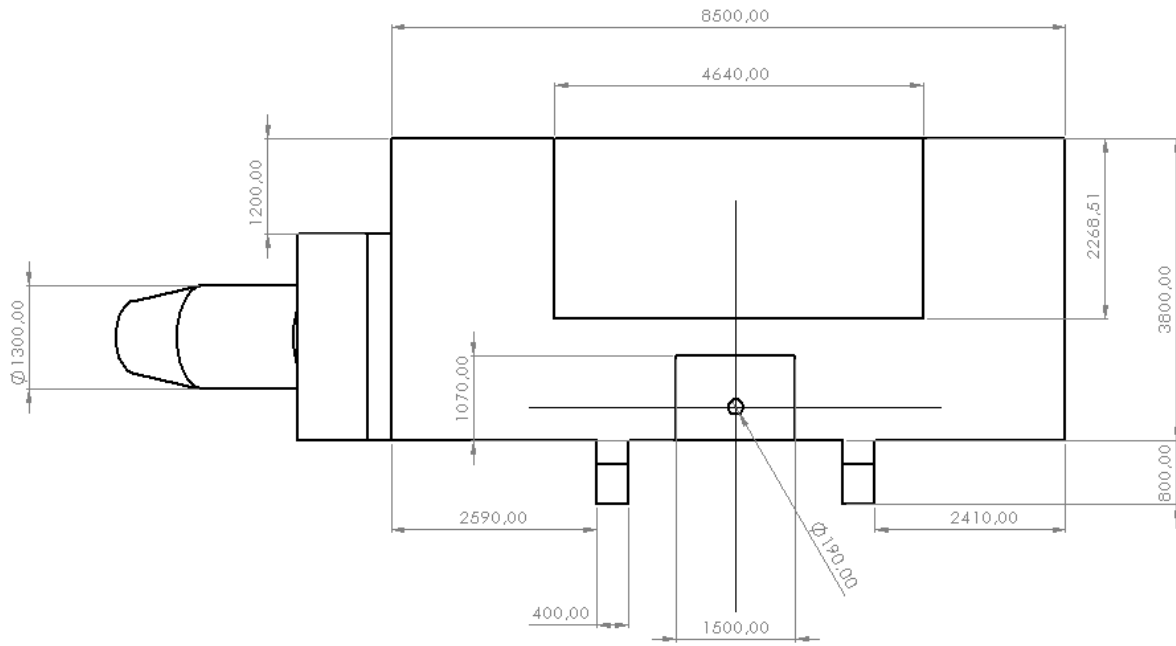


Figure A.6.16: Microfluidic interface drawing top view. Dimensions in micrometres [μm].

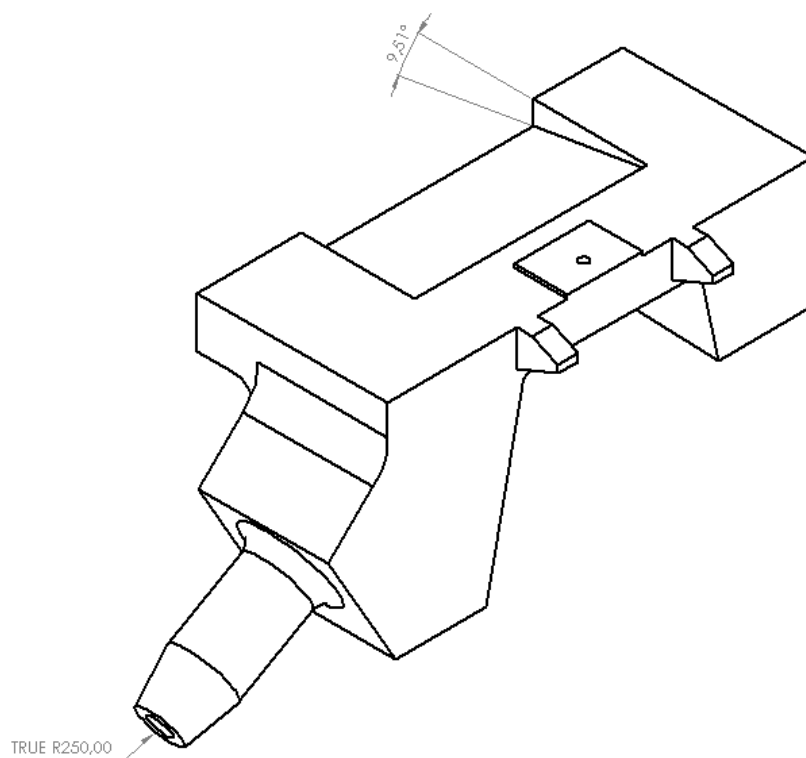


Figure A.6.17: Microfluidic interface drawing isometric view. Dimensions in micrometres [μm].

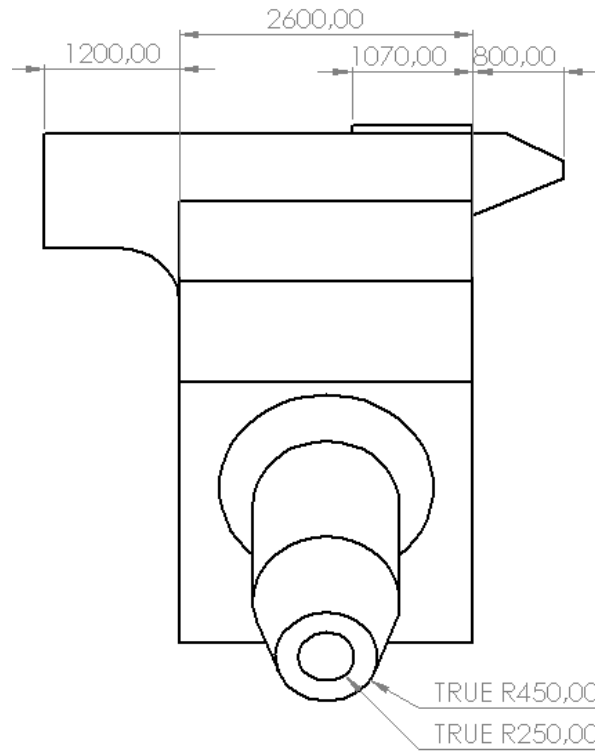


Figure A.6.18: Microfluidic interface drawing, left side view. The top of the device protrudes to the left to prevent the device from hitting the sides of the spring. Dimensions in micrometres [μm].

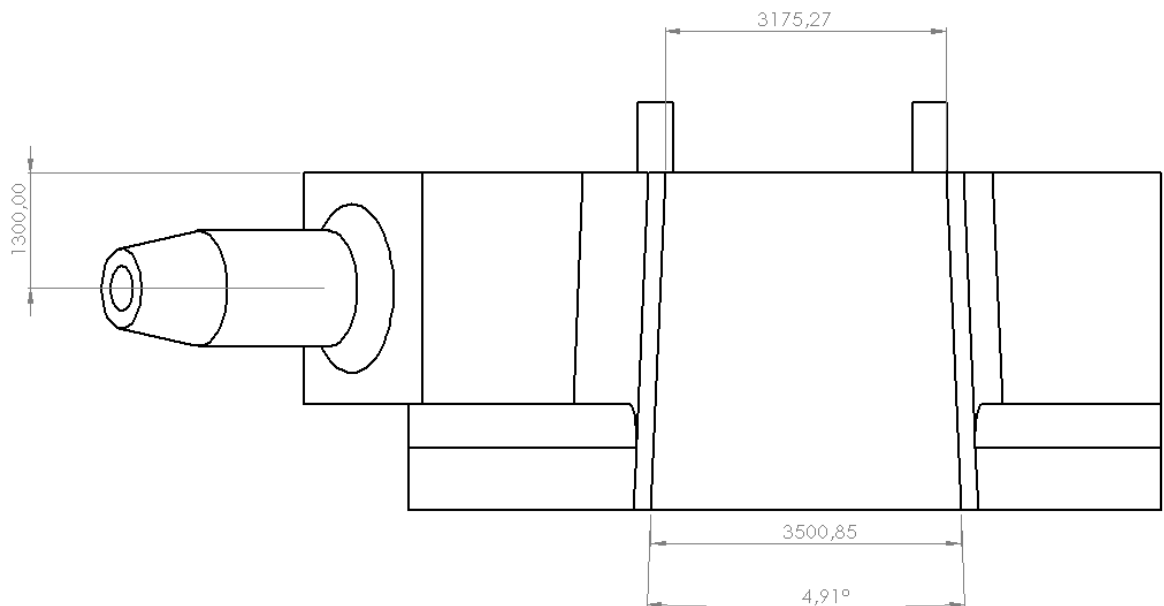


Figure A.6.19: Microfluidic interface drawing, bottom view. Dimensions in micrometres [μm].

A.6.2. Microfluidic channel and aperture

With the basic shape of the interface as a boundary condition, a channel could be designed. Using the test prints, including those in figure A.5.9 and A.5.10, a lower limit was determined for channel size with a minimum of height and width of $200\ \mu\text{m}$. Since the geometry mainly limits the height of the channel, the interface must remain strong enough to remove the supports. The height of the channel was designed to be $300\ \mu\text{m}$ and the width $800\ \mu\text{m}$. A larger cross-sectional area allows for better and faster development of both the DLP and the 2PP print (the height was minimized to keep the interface thin but strong at the top). Figure A.6.20A & B show the 3D path of the channel from the connector to the aperture. At the connector, the channel starts circular with a diameter of $500\ \mu\text{m}$ and converges to rectangular after bending towards the aperture.

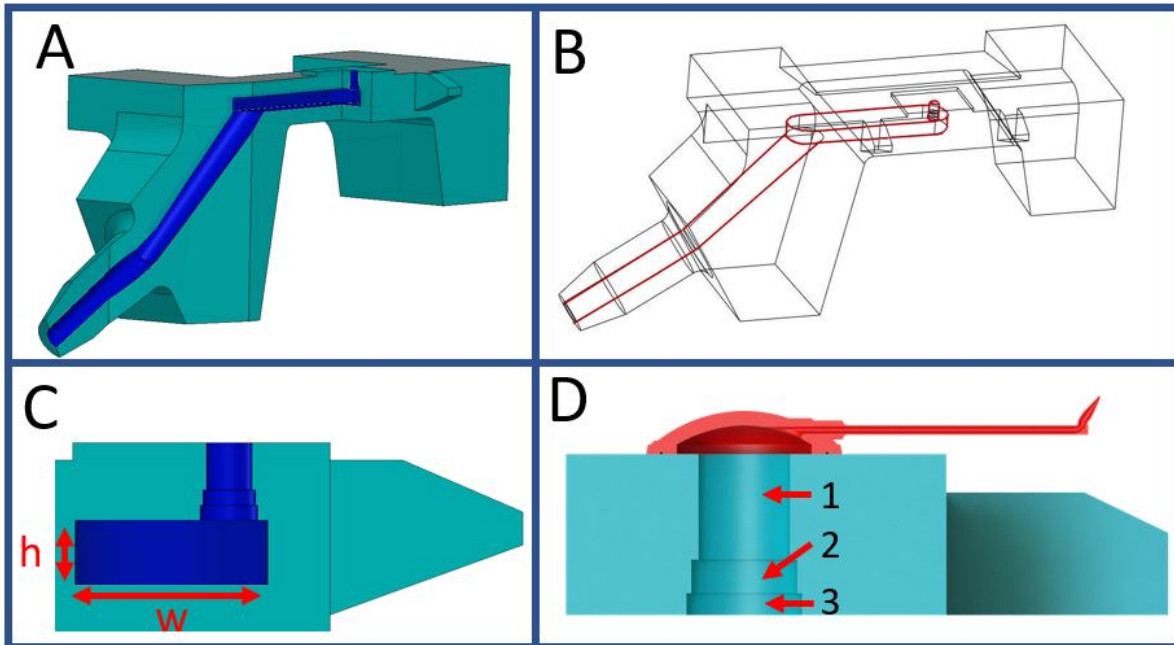


Figure A.6.20: CAD model showing the channel through the microfluidic interface, **A&B**) Show a CAD model with the channel going from the connector to the aperture (figure A has a cut-out to show the channel), **C&D**) Show the step converging towards the aperture (height indicated with 1-3 in D described in the text). Note the off centring of the aperture (figure D has the 2PP print on top of the aperture). w is the width of the channel ($800\ \mu\text{m}$) and h the height of the channel ($300\ \mu\text{m}$).

The aperture is off centre with respect to the channel, as can be seen in A.6.20C. This ensures that the aperture is as close as possible to the edge of the interface, while the channel is as far away as possible. This prevents the edge defects discussed earlier.

An important aspect for the aperture size is the height of the ceiling of the channel at the location of the aperture (so the distance between the top of the channel and the top surface of the interface). The channel below the aperture (vertical channel) connects the aperture to the main channel. The vertical channel is normally as long as the distance from the surface of the interface to the top of the channel (called the ceiling height, as defined in the top right corner of figure A.6.21). It was observed that the ceiling height of the main channel significantly affects the aperture size. This is shown in the test print in figure A.6.21.

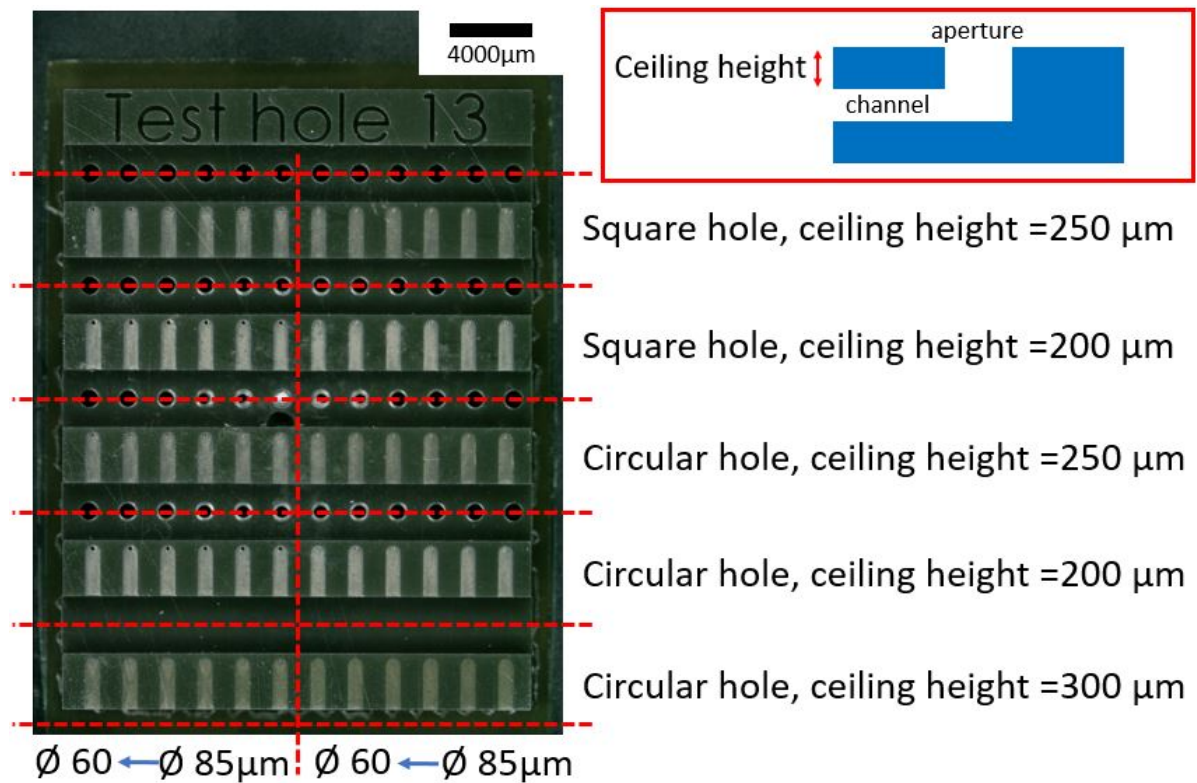


Figure A.6.21: Influence of ceiling height on the aperture for various aperture sizes. Too large ceiling height (here 300 μm) causes clogging. Too small ceiling height (here 200 μm) causes large apertures. Left and right have identical hole sizes, ranging from 60 to 85 μm . Note the position dependence of the aperture (right side is clogged while left side is open) due to bad calibration. Figure on tip right indicates ceiling height definition.

In figure A.6.21 clearly shows that if the ceiling height is too large (bottom row, with a height of 300 μm) it results in clogged apertures. On the other hand, a too-small ceiling height leads to too large apertures (second row from bottom, height of 200 μm), and a good ceiling height (middle row, height of 250 μm) results in accurately sized apertures. However, one wants the channel through the centre of the interface (as it is the strongest).

Using a stepped convergence (seen in figure A.6.20 C and D) from the channel towards the aperture has experimentally demonstrated to solve this problem. It allows for a long and slender upward channel with a lower probability of clogging and the smallest possible aperture (less over polymerization). For the 3DM Tough Clear prints, the smallest aperture had a diameter of 160 μm with a height of 220 μm (1 in figure A.6.20D). The diameters of steps 2 and 3 in figure A.6.20 were 220 and 240 μm respectively, both with a height of 70 μm . However, designing the aperture larger allowed for better repeatability (design of 175-200 μm).

The influenced area around the aperture remained relatively unchanged when the size of the aperture was changed (often adding 20-50 μm to the radius of the aperture). The aperture, achieved by trial and error by printing arrays of microfluidic interfaces, can be seen in figure A.6.22.

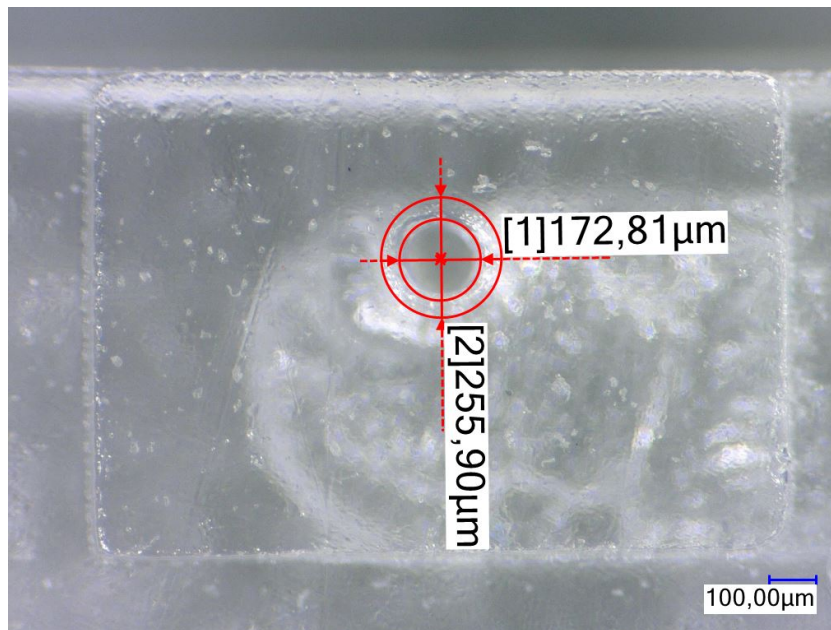


Figure A.6.22: Close up of aperture. Inner circle indicating the aperture size, outer circle indication the influenced area

The absolute smallest aperture achieved with 3DM Tough Clear had a diameter of $120\ \mu\text{m}$, but this was only achieved a couple of times ($35\ \mu\text{m}$ layer height). With the same print file, other prints failed to print and develop an aperture. Apertures with a diameter of $160\ \mu\text{m}$ were printed more successful, but, as can be seen in figure A.6.23, sometimes they are still clogged for no apparent reason. For future research, it could be interesting to print a membrane and puncture it to create an aperture.

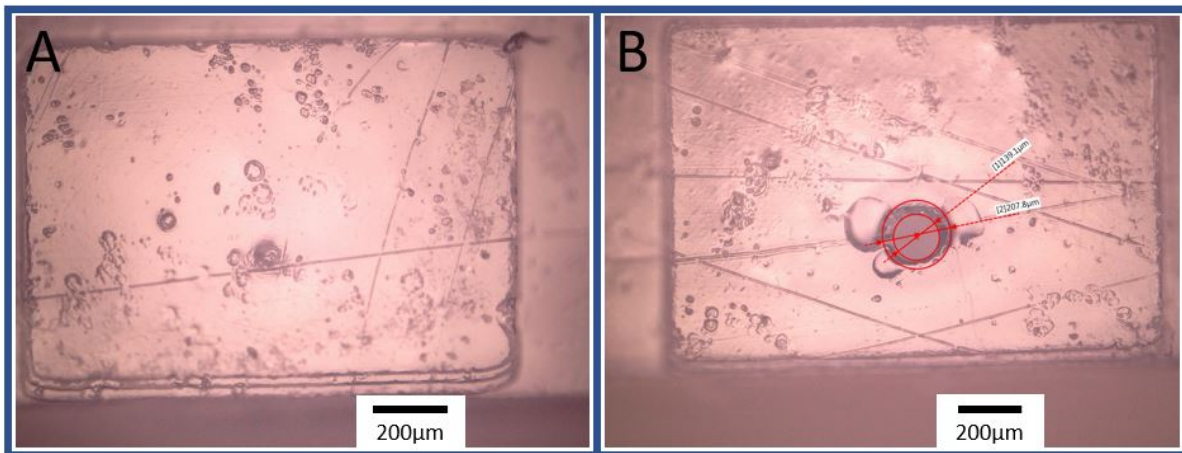


Figure A.6.23: Close up of two apertures printed with the similar sizing (aperture diameter in design = $160\ \mu\text{m}$). **A)** Clogged aperture, **B)** Open aperture, Inner circle indicating the aperture size (diameter= $139\ \mu\text{m}$), outer circle indication the influenced area (diameter= $207\ \mu\text{m}$)

It was decided to print two different aperture sizes in one print job. As two sets of three interfaces (inside their holder) fit on the build plate of the EnvisionTEC, it was chosen to print one set of three interfaces with apertures having a diameter of $160\ \mu\text{m}$ and one set with diameters of $175\ \mu\text{m}$. This was necessary because the poor LED calibration of the printer caused differences in the UV intensity on the print bed. There was a visible gradient in the UV intensity, which resulted in varying quality of the prints depending on their location on the print bed. Therefore, two different aperture sizes (smaller apertures at a location with lower UV intensity) were printed to achieve high throughput with a low failure rate (clogged devices). The influence of calibration is discussed in the last section of this appendix.

A.6.3. Microfluidic coupling

As part of this research, a variety of microfluidic coupling mechanisms were investigated to connect the channel of the microfluidic interface to the microfluidic pressure controller. In this section, some of the designs are briefly discussed, and at the end, the final design will be shown, which was used for the experiments and successfully tested.

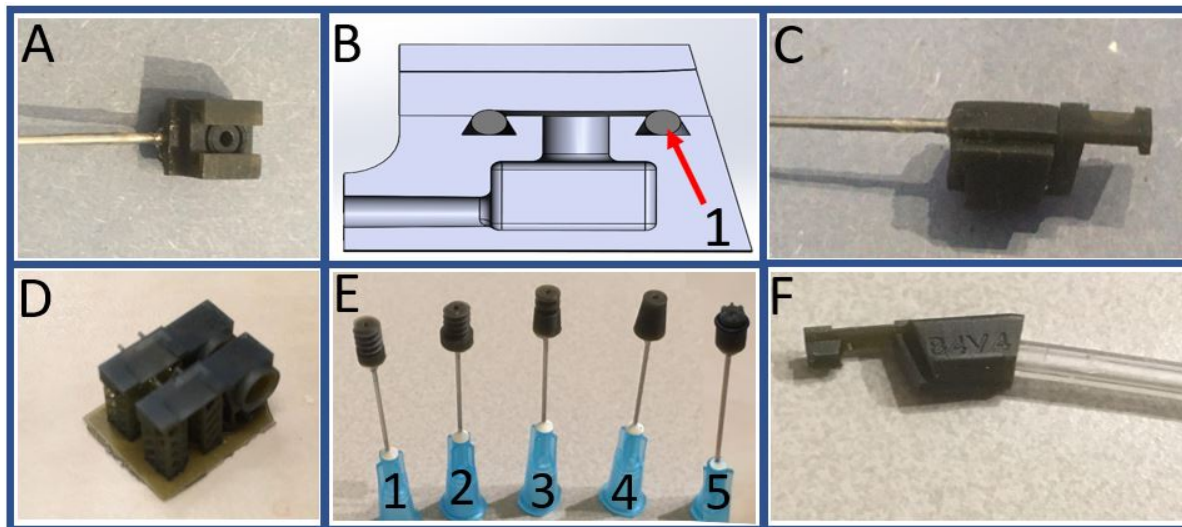


Figure A.6.24: Various designs for microfluidic couplers. **A, B, C**) Microfluidic coupling based on an O-ring in a dovetail groove. The needle is glued to the connector and connects to the tubing. the interface slides over the O-ring. **D**) Interface that can be adapted to be used with the connectors in figure E, it contains an opening which is either smooth (press fit) and conical or threaded (screw connection). **E**) Various types of connectors to be used with the interface in figure D. 1&2= threaded connector (2 in combination with O-ring), 3= double O-ring connector (axial press fit), 4 = conical connector without O-ring (press fit) and 5 = single O-ring connector. **F**) Connector that has an internal conical taper, the tube is press fitted into the cavity.

The connectors, shown in figure A.6.24, were developed to connect the tubing to the interface. Various principles were tested, ranging from O-ring designs to threaded designs. All of these designs have disadvantages that make them undesirable for this research. All the connectors in figure A.6.24A-F either leaked (under positive and/or negative pressure), had much friction or caused debris. This debris could then clog the cantilever. The re-usability of the connectors was also very low. Figure A.6.24F showed promising results, but for negative pressures, the tubing collapsed. However, this coupling mechanism was the only one that did not require any adhesives to attach the tubing to the interface. The adhesive used for the other connectors could also clog the channel. Additional designs were made that used a press-fit from the inside of the tubing (tube slid over a tapered ferrule). With high pressures (2 bar), this did cause leakages, but for negative pressures no leaks were observed (as the tube could not collapse due to the ferrule). By combining this design with the design seen in figure A.6.24F, a new design was made. This design introduces the concept of both internal expansion and external compression using only three main parts, and no adhesive is required. The principle behind the design was already treated in the paper (part 2). However, it is essential to elaborate more on it. The design and the principle behind it can be seen in figure A.6.25. Figure A.6.25 shows the three components of the fluidic connection: the tubing, the connector, which prevents collapse of the tubing and is attached to the microfluidic interface and the securing element, which prevents expansion of the tubing. The figure also shows the steps to create the connection. Key to the connection design is the ratios between the three elements:

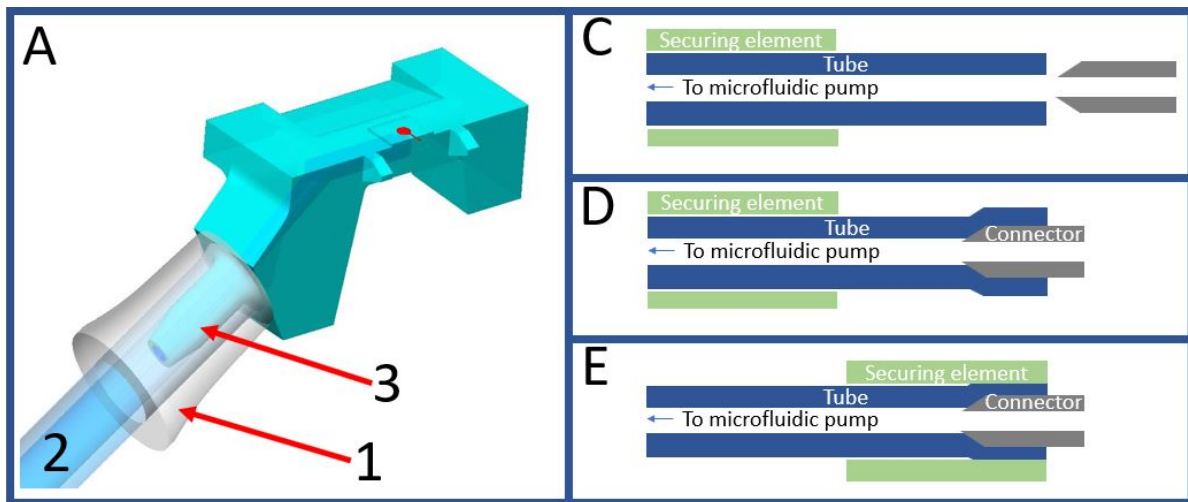


Figure A.6.25: Design principle of the microfluidic connector, **A)** Render of the assembled microfluidic connector with 1 = The securing element, 2 = The flexible tubing, 3 = The ferrule type connector. **B)** Securing element slid over the tubing, **C)** Ferrule type connector inserted into the tubing, **D)** Securing element slid over the tubing at the ferrule type connector.

Initially (before assembly):

$$ID_{tube} \leq OD_{ferrule} \leq ID_{securingElement} \quad (A.4)$$

$$OD_{tube} \leq ID_{securingElement} \quad (A.5)$$

with ID the inner diameter and OD the outer diameter of the respective element.

During assembly (step seen in figure A.6.25D)

$$ID_{tube} \geq OD_{ferrule} \quad (A.6)$$

$$OD_{tube} \geq ID_{securingElement} \quad (A.7)$$

After assembly (step seen in figure A.6.25A and E)

$$ID_{tube} \geq OD_{ferrule} \quad (A.8)$$

$$OD_{tube} \leq ID_{securingElement} \quad (A.9)$$

The dimensions chosen for this research fit the 1.016mmID x 1.778 mm OD tygon tubing (Masterflex Transfer Tubing, Tygon® ND-100-80 Microbore, 0.040" ID x 0.070" OD). The dimensions used for the final design can be seen in figure A.6.26.

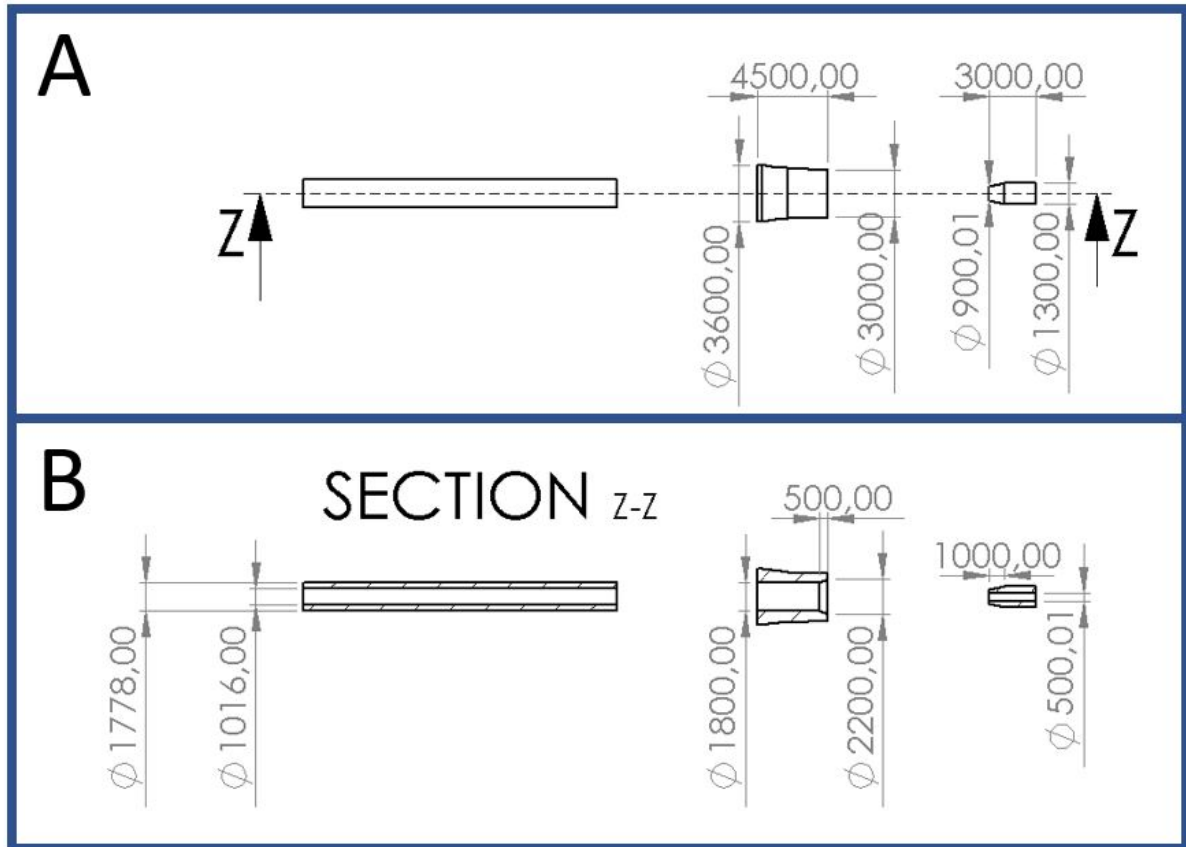


Figure A.6.26: Drawing of the microfluidic connector principle of the microfluidic connector. Dimensions in μm , **A)** Top view, **B)** Section view Z-Z

The expansion of the tube by the ferrule shaped connector, and the compression of the tube, by the securing element result in an optimal fluidic connection. It prevents expansion of the tube when positive pressure is applied, but it also prevents the tube from collapsing when negative pressures are applied. This configuration was tested with the Elveflow pressure controller up to a pressure of 6.9 bar without leaking (6.9 bar could not be exceeded due to insufficient air pressure from the wall outlet). Problems also occurred at the other end of the tube (where the tube popped off the stainless steel tipless needle), showing the efficiency of the developed fluidic connection. The microfluidic connector principle could be used for other applications such as microfluidic chips, for other fluidic applications and at different scales.

The CAD assembly of the DLP prints with the tubing and AFM holder is shown in figure A.6.27A. The assembly with the printed parts and the tubing can be seen in figure A.6.27B. The figures show the resemblance between the design and the print and show that the microfluidic coupling requirement and the microfluidic interface's requirement to fit the AFM holder are met.

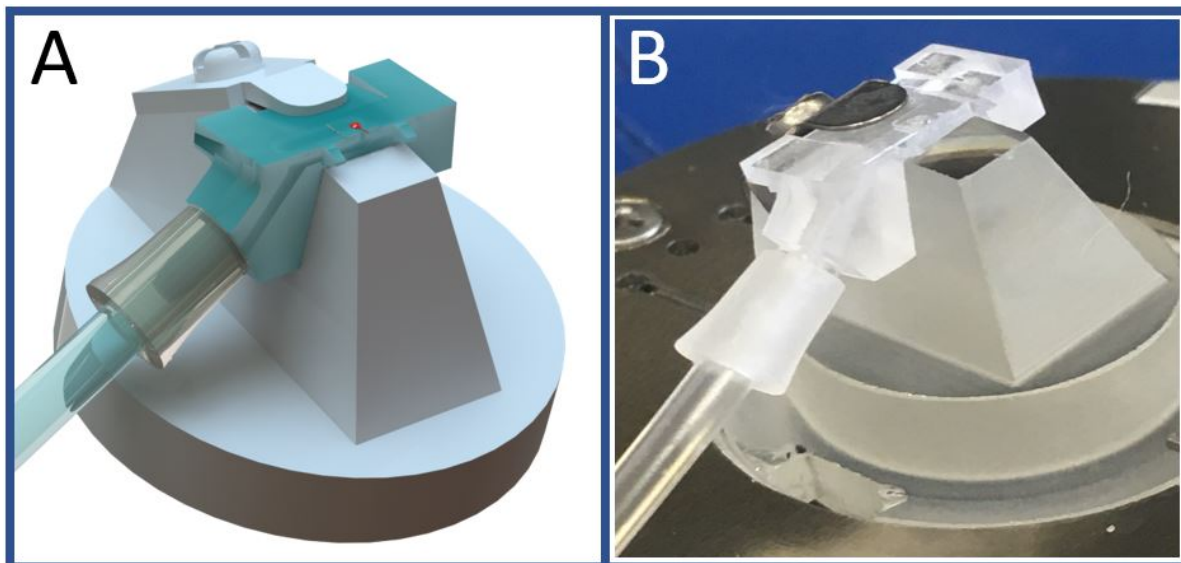


Figure A.6.27: CAD render of DLP print assembly and real assembly. Shows an assembly of the tubing, securing element, microfluidic interface and AFM holder. **A)** Render made in Solidworks, **B)** Printed microfluidic interface assembled on AFM holder connected to tubing.

A.6.4. Interface holder

Three microfluidic interfaces were printed into a square interface holder (container) that fits into the Nanoscribe sample holder. This interface holder mimics the 700 μm fused silica substrates commonly used for 2PP printing. Using this container, the printing surfaces of the microfluidic interfaces are instantly aligned with the substrate holder of the Nanoscribe. This minimizes the risk of the objective crashing into the substrate, as the lens maintains a safe distance from the substrate (that is calibrated for the fused silica substrate thickness). A comparison by the typical Dill printing approach and the approach with the 3D printed holder can be seen in figure A.6.28. Figure A.6.29 shows the reality with an interface taped to the Nanoscribe holder.

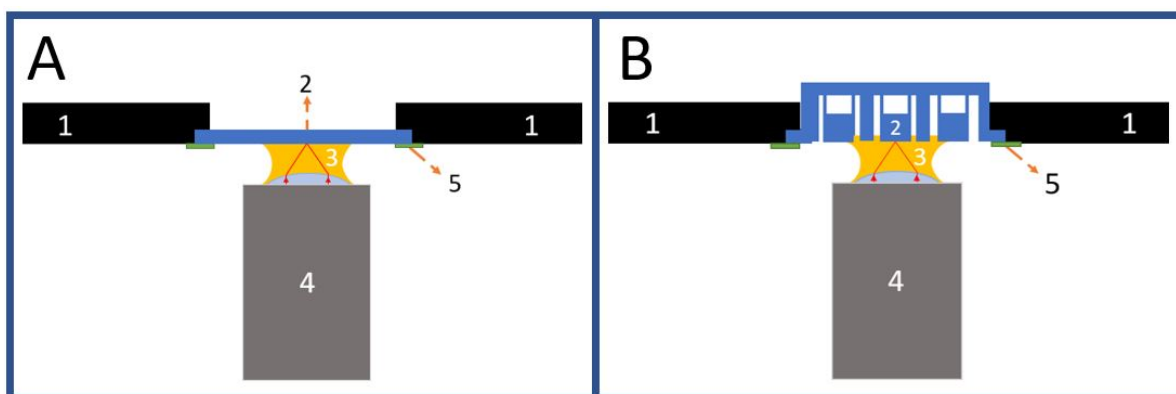


Figure A.6.28: Schematic drawing of substrates in Nanoscribe holder. **A)** The typical DiLL printing approach with 1 = The Nanoscribe holder, 2 = A fused silica substrate, 3 = 2PP photoresist, 4 = The objective, 5 = Green substrate tape. **B)** Nanoscribe holder with 3D-printed interface holder (including interfaces), with 1 = The Nanoscribe holder, 2 = 3D printed microfluidic interface holder, 3 = 2PP photoresist, 4 = The objective, 5 = Green substrate tape.

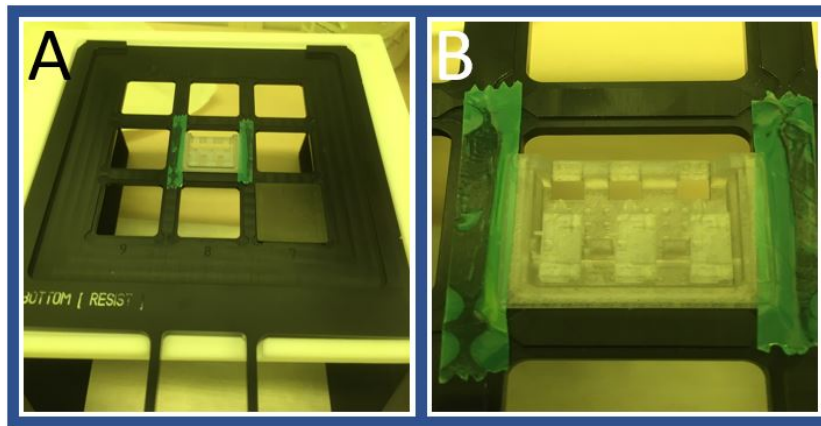


Figure A.6.29: DLP print taped to the Nanoscribe holder. **A)** Overview with in the bottom right a flat substrate, **B)** Zoom in on interface.

The interfaces are connected to the interface holder by the small EnvisionTEC support structures (see figure A.4.3), which are automatically generated by the Perfactory slicing software (as was already discussed earlier). The current interface holder can accommodate up to three microfluidic interfaces. The internal supports (between the interface and the holder), as shown in figure A.4.4, allow the interfaces to be removed after printing and developing the 2PP print. The supports serve as a “break out” mechanism. The supports are also visible in figure A.4.5 and figure A.6.30.

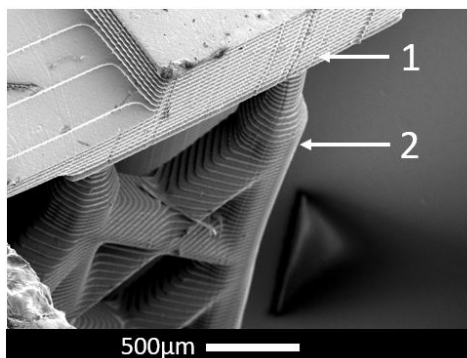


Figure A.6.30: SEM image of the internal supports below the interface. 1 = Microfluidic interface, 2= Supports

An array of holes has been added to the bottom of the holder (closest and parallel to the build plate) to prevent the print from being pulled off the supports. Large flat areas, printed directly on the supports, tend to be pulled off the support due to the adhesion forces with the resin tray. The holes decrease the pulling forces as the surface area is decreased. The bottom surface of the print will, however, never be flat and smooth, even with the addition of the holes. These holes can be seen in figure A.6.31.

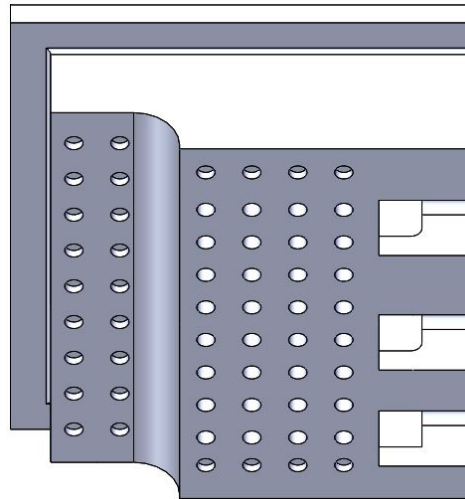


Figure A.6.31: Holes have been added to the bottom surface of the design to prevent the print from being pulled off the supports during the first layers. The indentation on the left side prevents the substrates from hitting the back side illumination mount off the Nanoscribe

The advantages of the holder do not stop at the prevention of the objective crashing. There are two more main benefits. First of all, the interfaces are directly aligned with the X and Y-axis of the Nanoscribe. This means that the interfaces will be oriented correctly when the 2PP print starts. The cantilever can then be easily printed in the direction of the positive X-axis.

The last main advantage of the holder is batch printing. The holder aligns three interfaces per sample position, which means that in theory, 27 cantilevers can be printed per job. Therefore, the Nanoscribe can go to the programmed location for each interface and start the print autonomously (will be discussed in appendix B).

The resin plateau is a key element of the holder design, which has not been discussed in a lot of detail in the paper. It is a flat tower attached to the interface holder that is printed opposite to the aperture and is $100\ \mu\text{m}$ lower than the surface of the aperture.

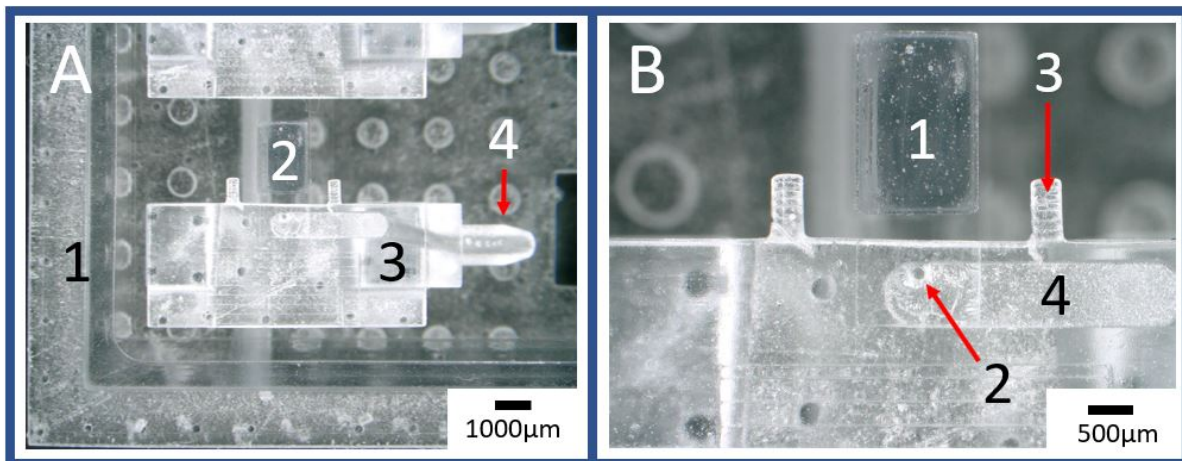


Figure A.6.32: Interface in holder with the resin plateau. **A)** Overview of holder and interface (two out of 3 interfaces visible) with 1 = The holder, 2 = The resin plateau, 3 = The microfluidic interface, 4=The microfluidic connector, **B)**Zoom in on the aperture and resin plateau, 1= Resin plateau, 2 = Aperture, 3 = Cantilever protection, 4 = The channel

This plateau, as seen in the paper and again in figure A.6.32, enables the printing of long suspended cantilevers. The hydrophilic nature of the 3DM Tough Clear, causes the 2PP resin to flow all over the interface, resulting in a shortage of resin when printing the cantilever. The plateau enables the formation of a meniscus of photoresist between the interface, the plateau, and the objective. This method allows long cantilevers (up to $900\ \mu\text{m}$ was tested) to be printed without a local shortage of photoresist. The working principle of the plateau is schematically explained in figure A.6.33.

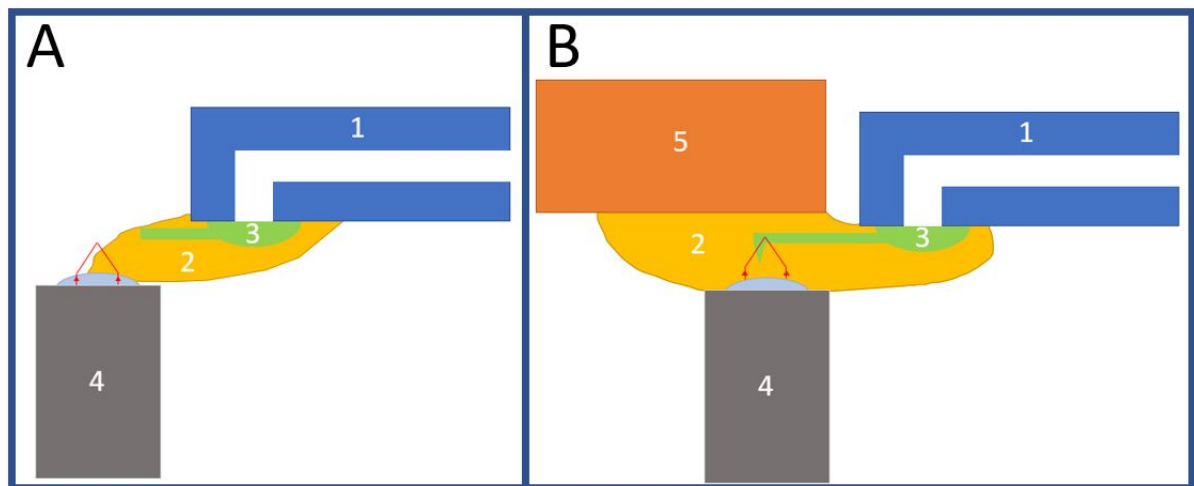


Figure A.6.33: Schematic explanation of the working principle of the resin plateau. **A)** Schematics of print without the resin plateau. A resin shortage occurs when printing the cantilever (far away from the edge). Cantilever print is not successful. 1 = Microfluidic interface with channel, 2 = Photoresist, 3 = 2PP print on top of aperture including cantilever, and 4 = The objective. **B)** Schematics of print with the resin plateau. A meniscus of resin is formed between the objective, the microfluidic interface and the resin plateau. 1 = The microfluidic interface with channel, 2 = Photoresist, 3 = 2PP print on top of aperture including cantilever, 4 = The objective, and 5 = the resin plateau.

A final feature of the interface holder that needs to be mentioned is the arch cutaways. The arches can be seen in figure A.6.34. They give easy access to the connectors of the microfluidic interface for blow-drying or flushing of the channel during and after the development stage. They were used to force PGMEA, IPA and air through the channel to reduce the development time.

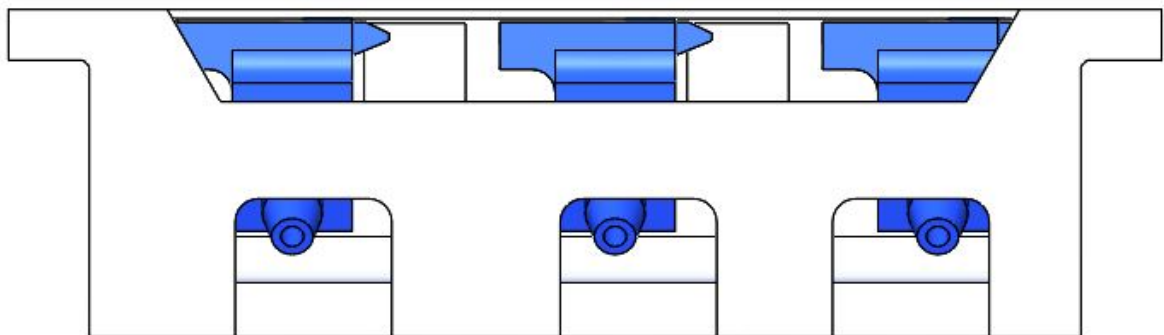


Figure A.6.34: Side view of the interface holder with the arch cutaways visible. These arches allow for blow-drying and connection of the tubing with the interfaces in the holder

A suggestion is to print the aperture on the side of the microfluidic interface and mount them 90 degrees rotated (so the side of the interface is facing up in the holder). This enables printing of the cantilever in a vertical position, of which the benefits will be discussed in appendix B. However, one should note that the tip of the cantilever should be higher than the rest of the print when mounted on the AFM.

A.6.5. Nanoscribe test substrates

Large arrays needed to be printed on the substrate for the initial Nanoscribe tests (dose test, interface finding tests, etc.). Flat 3D-printed substrates are ideal for these dose tests, as they mimic the typical Nanoscribe substrates. These flat substrates were already shown in figure A.3.2. In order to test the printing of suspended cantilever structures in large quantities, flat plates with slits were printed. In this way, more cantilevers could be printed on a substrate to perform a cantilever parameter sweep print (which is explained in appendix B). A substrate with slits can be seen in figure A.6.35.

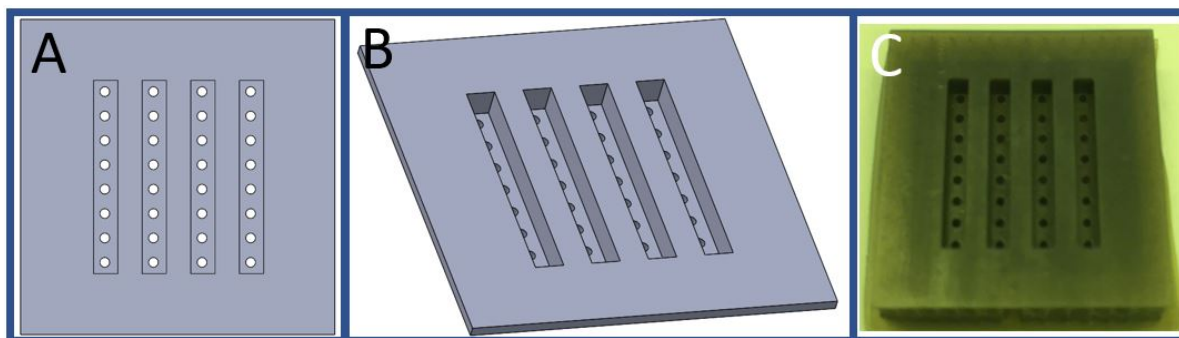


Figure A.6.35: Various views of a slitted flat substrate for cantilever parameter testing. **A&B)** CAD models top and isometric view respectively, **C)** Printed substrate with slits (HTM140V2).

A.6.6. Sample development holder

To develop the prints after 2PP printing, two sample holders were printed on the EnvisionTEC and Prusa SL1 (Stereo lithography apparatus, SLA printer). These sample holders can either hold one or three samples (see figure A.6.36). This way, multiple prints can be developed in the same PGMEA and IPA bath, saving a lot of PGMEA. In addition, it also allowed the cantilevers to be developed vertically, which speeds up development and prevents any unexpected deformations. Handling and transfer of the interfaces to various chemical baths were much easier with these sample holders.

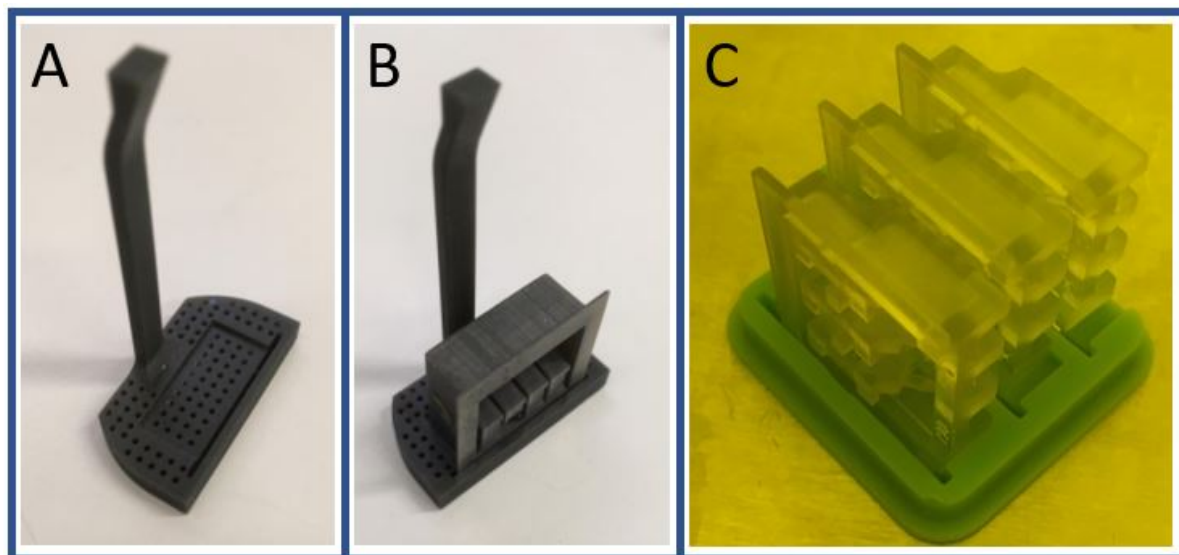


Figure A.6.36: **A&B)** Sample holders printed using the EnvisionTEC (HTM140V2), without and with interface holder respectively. The vertical bar is for easy handling manual handling, **C)** Sample holder with three interface holders next to each other, which can be developed in the same PGMEA bath. Printed on the Prusa SL1 using Prusa Tough Azure Blue resin

A.7. Developing

The development of the DLP print was already shortly discussed in the paper. In this section, the steps will be discussed and illustrated.

After removing the print from the build plate with a sharp razor blade, the entire print should be immersed in IPA in a beaker. To minimize the amount of IPA used, the first cleaning cycle was done with “recycled” IPA from the second cleaning cycle of the previous print (same material print only!). The beaker was covered with a Petri dish lid and put in the ultrasonic cleaner for 5-10 minutes. Fragile structures may require a more gentle approach. After ultrasonic cleaning, a blow-dryer (air pressure = 2 bar) was used to clean the aperture and the channel. IPA can be applied to the print in combination with the blow-drying flush away any resin on the print or in the channel. The print was then immersed in fresh IPA, and the old IPA was disposed of in a chemical waste bottle. Again, an ultrasonic cleaning cycle of 5-10 minutes was started, followed by blow-drying. It should be noted that the water in the ultrasonic cleaner does become warm and should be at the correct level (indicated by the manufacturer).

Too much heat can deform the prints. If required, one can force IPA through the interface using a syringe, but it will not open a clogged aperture or channel. It was observed that if both the aperture and channel are open, the development steps suffice.

If no resin was observed on the print or in the channel, and all the IPA had evaporated (after blow-drying, especially from the aperture side to prevent resin residue around it), the prints were placed in the Photopol A5406 UV curing furnace (see fig. A.7.37) for 5-10 minutes using both light sources (cold light lamps and high-intensity spotlights both with $\lambda=320-550$ nm). It was observed that longer UV exposure leads to better polymerization, limiting swelling of the print in other chemicals. After post-curing, the external support was removed using a sharp razor blade. No support can remain on the holder as it causes a tilt of the substrate in the Nanoscribe.

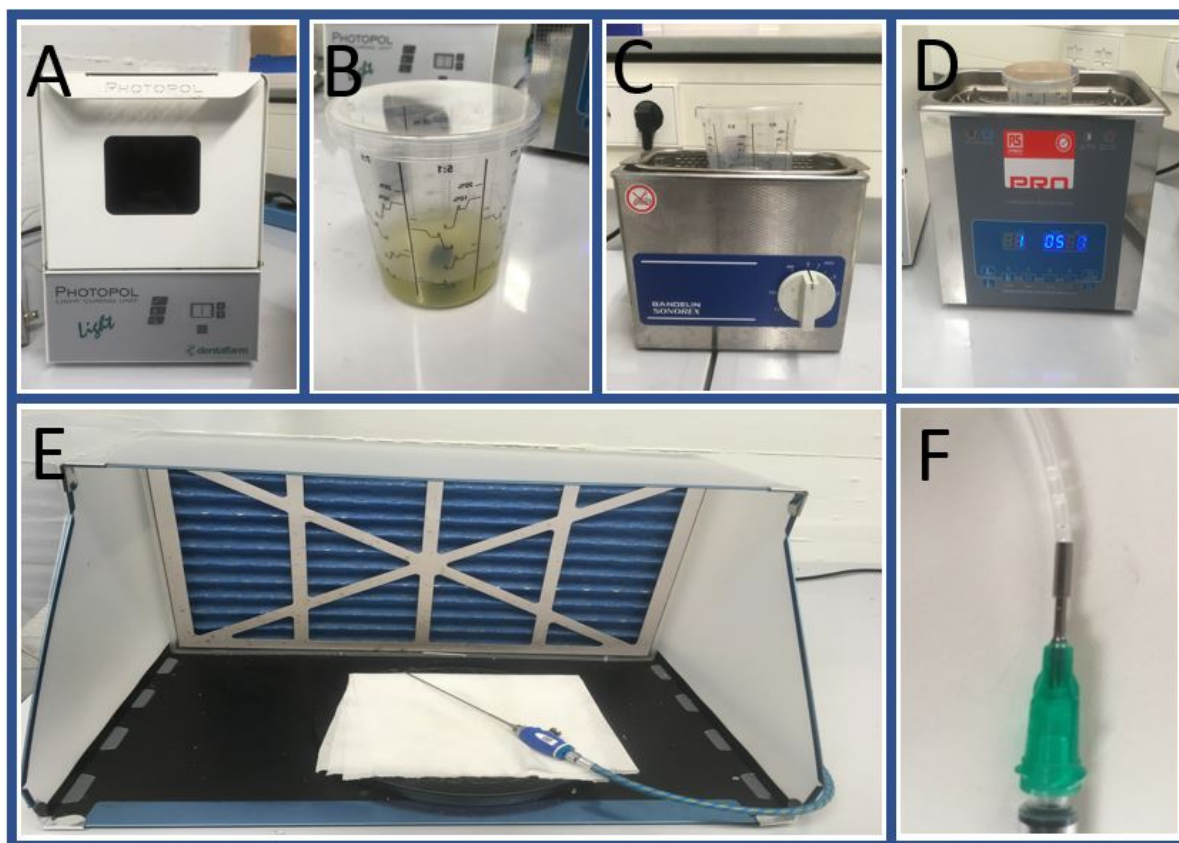


Figure A.7.37: Equipment used for DLP print development. **A)** Photopol A5406 curing furnace, **B)** Development beaker with IPA and HTM140V2 print, **C)** Ultrasonic cleaner (gentle, Bandelin Sonorex), **C)** Ultrasonic cleaner (Harsh, RS Pro) **E)** Blow drying chamber, **F)** Syringe to tube connection,

To reduce the surface roughness of the DLP print, an experiment was conducted where the print was wiped with a cotton swab (before post-curing). With the HTM140V2 prints, this procedure seemed to make the surface smoother, but for 3DM Tough Clear it was not required as the smoothness did not affect the 2PP print.

A.8. Parameters affecting the print

Many variables can affect the DLP print result. Some of them have only a little influence, such as environmental temperature and humidity. At higher ambient temperatures, the apertures will print better (smaller diameters possible). It is suspected that the resin polymerizes less at slightly higher temperatures. This is confirmed by Steyrer et al. [11], who state that less over polymerization occurs at elevated temperatures, which explains the ability to print the smaller aperture sizes. The heating caused by the ultrasonic cleaner could induce bending of the print. To avoid this, long sessions in the ultrasonic cleaner should be avoided. The effects of the humidity were not visible in the quality of the prints.

Another factor to consider is the age of the resin. Older resins may behave differently, and the composition of different batches may also vary. The resins consist of various mixtures of acrylated monomers and acrylated oligomers. To get a constant mixture, it is essential to give the resin a gentle stir before putting it in the machine to mix the compounds properly.

The aforementioned aspects are difficult to control. It is best to try to keep everything stable to achieve repeatable results. Three aspects that can quickly be resolved are LED calibration, platform calibration and the fluorinated ethylene propylene (FEP) foil quality.

The LED calibration needs to be done approximately once every 500-1000 printing hours (depending on print quality). As the optical system can drift over time, and the LED can deteriorate, which influences the print quality. This can lead to a gradient of the UV intensity over the build plate, with areas being exposed more than others. This gradient can be directly linked to the print quality. Prints on the left side of the build plate, where there was a lower light intensity, could be printed with much smaller apertures than those on the right, where there was a higher light intensity (lower intensity = less over polymerization) for a poorly calibrated light source. The calibration reduced the position dependence. The result of the proper calibrated LED system is shown in figure A.8.38.

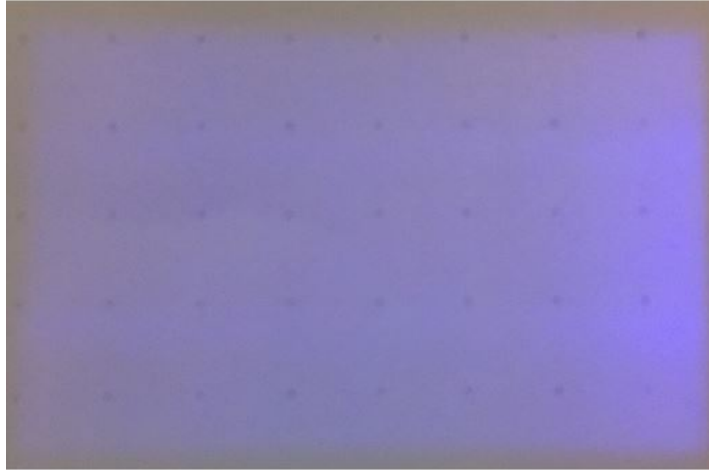


Figure A.8.38: Proper UV calibration of the EnvisionTEC. No significant gradient is visible

Calibrating the build platform eliminates any tilt of the platform and ensures the home position is at the correct distance from the FEP foil. The calibration of the tilt does not have to be performed often, the calibration of the home location is, however, required every time the FEP or separation foil has been replaced.

Properly homing the build plate and removing the tilt results in smoother printed surfaces and better overall prints. The effect on the printed surface by the calibration can be seen in figure A.8.39.

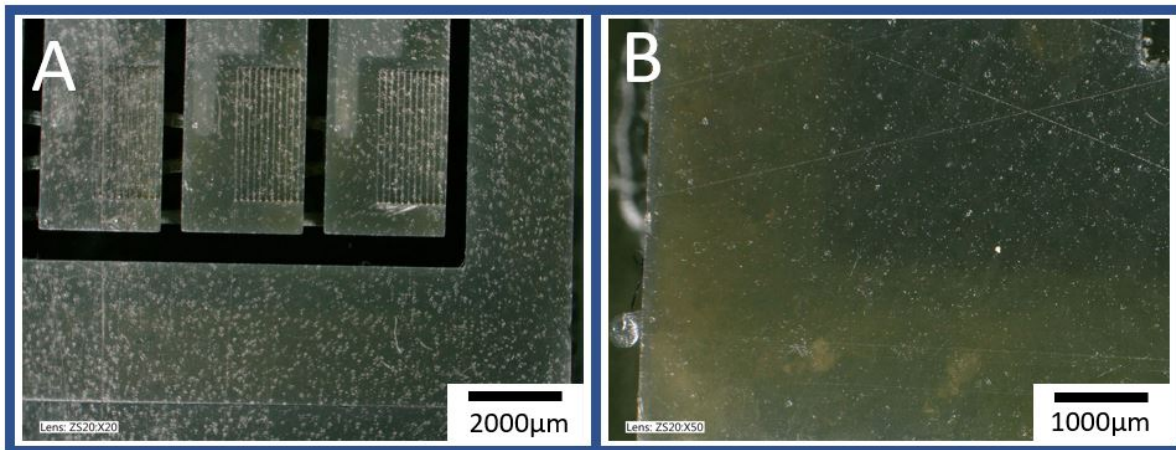


Figure A.8.39: Surface quality before and after calibrating EnvisionTEC **A)** Before tilt and home calibration many large spots visible, **B)** After home calibration, only small spots visible even with larger magnification

A key aspect for the printing results is the quality of the FEP foil and the separation foil. These make sure the print does not stick to the resin tray. However, these foils have a limited lifetime. Either they become less transparent (milky white colour, which prevents proper polymerization and fine details of the print become worse), or dents start to appear in the foils (due to failed prints or debris in the resin, causing artefacts in the print). Both

cases result in a deterioration of the print quality. The FEP and separation foil should therefore be replaced when such defects are found. Figure A.8.40 shows both damaged and proper FEP foil.

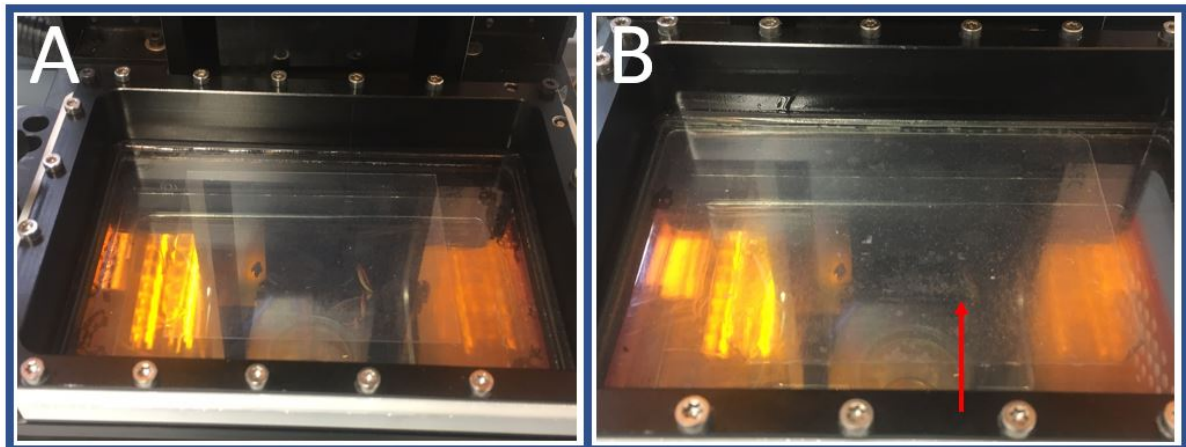


Figure A.8.40: FEP foil in the resin tray **A)** Good FEP foil, clear and no scratches or dents **B)** Damaged FEP foil indicated by arrow. Other parts of the foil are still OK

Not only physical defects can cause printing errors. Improper slicing can also cause defects. As the printer projects images by turning on specific pixels, the slicer must create images. Around the apertures, a particular greyscale occurs in the sliced images, as is shown in figure A.8.41. If the edge of the aperture is in between pixels, it can turn them either on or off. This could lead to clogged apertures. Therefore, one needs to check the images outputted by the slicer, especially around the aperture. The pixel size sets the theoretical minimum size of the aperture ($30 \times 30 \mu\text{m}$), but stray light causes those apertures to clog. Therefore, the size of the aperture has to be designed larger than the resolution of the printer.

An example of a sliced image is shown in figure A.8.41. The sliced image and the zoomed image show the greyscale problem. It is not clear if the grey pixels polymerize the resin. By changing the pixel colour to black (manually or via a Matlab script), one could, in theory, alter the aperture size.

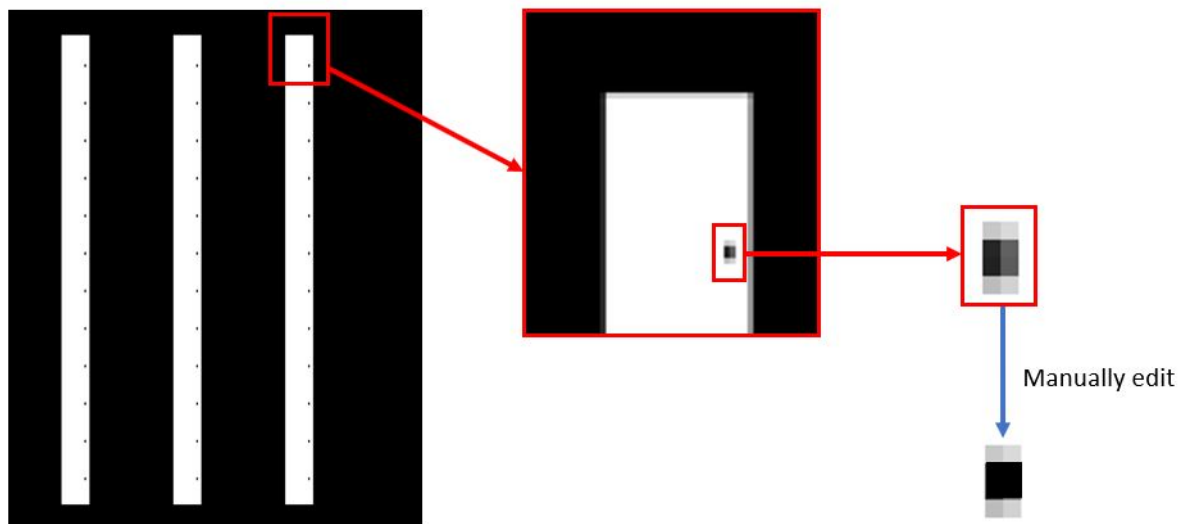


Figure A.8.41: Sliced image of a test print. Two zoom ins are shown at the aperture. By changing the pixel colour manually to black (or via a Matlab script), one can decrease the aperture size

Another aspect that does not apply to the EnvisionTEC is the pixelation of the prints. This occurs with prints made with the Prusa SL1. The Prusa SL1 uses a liquid crystal display (LCD) to project the images directly on the build plate (no lens system used). The EnvisionTEC uses micro-electro-mechanical mirrors and a lens system to project the image. The LCD screen has a significant impact on print quality. Figure A.8.42 shows that the pixels of the LCD are also visible on the top surface of the print.

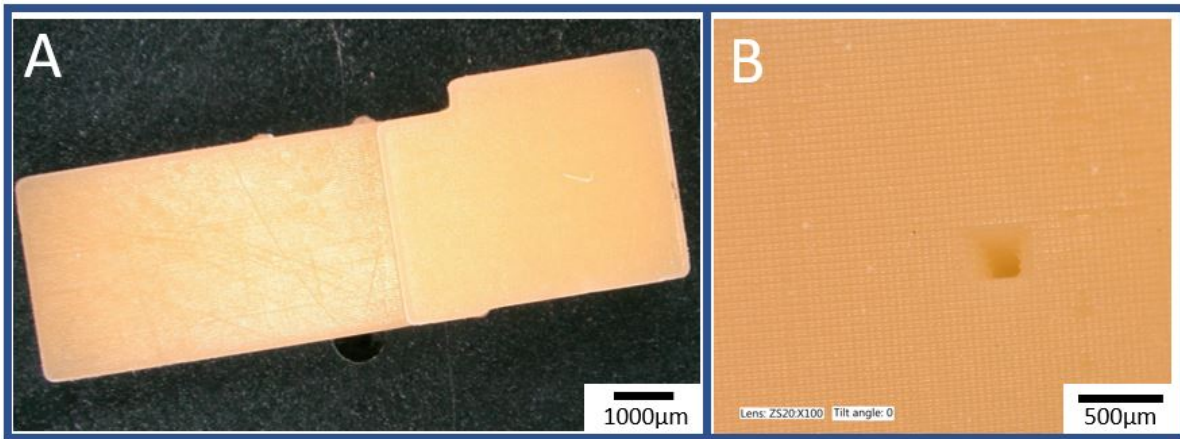


Figure A.8.42: Prusa SL1 print using Prusa Tough Orange resin. **A)** Overview of print, **B)** Zoom-in at surface of print with pixels clearly visible as squares

It is recommended to test printing the interface holder vertical instead of horizontal. This might lead to smaller apertures (sizes slightly bigger than the layer height should be achievable). Selective laser etching of fused silica and selective laser machining of PMMA should be investigated to fabricate microfluidic interfaces. These could make sputter coating of gold superfluous.

Appendix B: Two photon polymerization (2PP)

B.1. Introduction

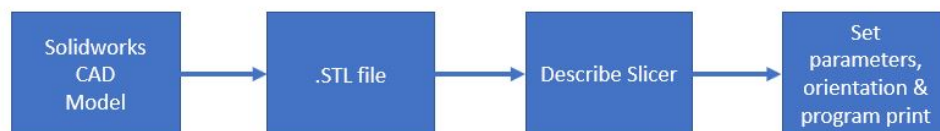
The limited resolution of the DLP printing technology makes it impossible to print cantilevers for nucleus aspiration using only DLP. On the other hand, two-photon polymerisation has a much higher resolution (250 nm), which surpasses the diffraction limit. For this research, the Nanoscribe Photonic Professional GT was used. Because 2PP is a direct laser writing process (voxel scans through the photoresist), it is much slower than DLP. 2PP relies on the absorption of two photons which collectively have an energy that matches the bandgap between two electronic states of the photoinitiator, using nonlinear absorption [12]. This means that only the summed energy of the two photons is sufficient to activate a photoinitiator molecule. To achieve this, a second photon must arrive at the location of the first photon within 1 fs, which then leads to localized polymerization of the resin. The probability of the absorption of two photons by a photoinitiator molecule is nonlinear and decreases with increasing distance from the focal spot [12].

This appendix discusses the steps taken to achieve good 2PP prints on a DLP-printed substrate. It covers the optimization of the printing parameters, the design of the 2PP modules and highlights the problems encountered and their solutions.

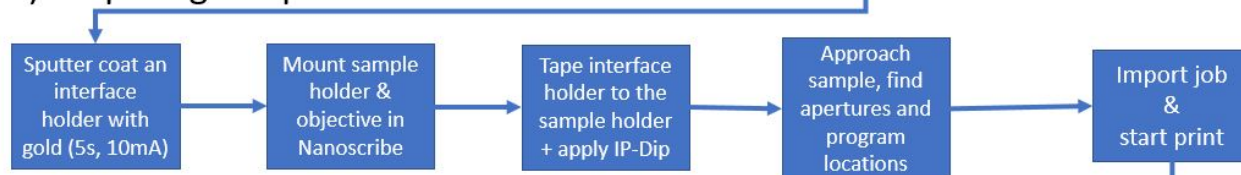
B.2. Workflow

The general workflow for the Nanoscribe printing is quite similar to the DLP workflow in appendix A. The process can be divided into three sections: Preparation of the print file, Preparation of the printer and Development of the print. The workflow can be seen in figure B.2.1.

A) Preparing the print file



B) Preparing the printer



C) Developing print

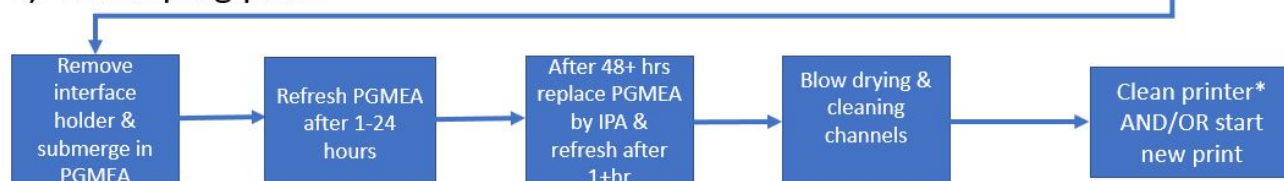


Figure B.2.1: Nanoscribe workflow. If multiple .STL files need to be combined, one should slice them separately and then combine them in the programmed print. The times and cycles in the development steps could be elongated or increased respectively for better development. *For the cleaning of the printer, the workflow given during training should be followed precisely.

Although there are similarities between the EnvisionTEC workflow and the Nanoscribe workflow, the user can change many more variables for 2PP printing. These parameters can be set either in the slicing phase or in the print programming phase. There is also a wide range of photoresists and various objectives, which can achieve

different feature sizes and can be used for different applications. This is all discussed in this appendix. Again, for the Nanoscribe prints, the optimal parameters found during this research are not set in stone and may change with time, geometry and can be influenced by other factors. Any change could require dose testing or other optimizations. However, the found parameters can serve as a starting point for future research.

B.3. Materials and substrates for 2PP printing

For 2PP printing, one first has to select an objective, a photoresist and a substrate. This choice is based on the required resolution, minimum feature sizes, size of the print and the required material properties (e.g. biocompatible, Young's modulus, autofluorescence etc.). After selecting these, one can tune the slicing and printing parameters accordingly. The choice of objective and photoresist determines the minimum feature size and resolution that can be achieved. However, higher resolution comes at the cost of longer print time. The available objectives for 2PP printing are 10x, 25x and 63x. With the 63x objective, one can achieve the highest resolution and the smallest feature sizes. A comparison table can be seen in figure B.3.2. The 63x objective was used for this research because the sharp tip and the cantilever require small feature sizes. The achievable resolution also depends on the photoresist used. Each photoresist has its advantages and is often optimized for a specific objective. IP-Visio, for example, is biocompatible and cytocompatible. However, the minimum feature sizes are relatively big. On the other hand, IP-Dip can achieve the smallest features (along with IP-Dip2) but has a high autofluorescence. Autofluorescence was not a problem in this study. The mechanical properties of the photopolymers also differ. IP-Dip has a relatively low Young's modulus (4.5 GPa [13–15]) compared to other photoresists. This relatively low Young's modulus is advantageous for printing cantilevers with a stiffness that is less than 2 N/m.

Typically, fused silica, silicon, or indium tin oxide (ITO) substrates are used for 2PP printing. For this research, the aforementioned DLP printed substrates are used. Gold was sputtered on top of the DLP printed interfaces to obtain a high degree of automation for the 2PP printing (Sputter Coater JEOL JFC-1300, 5 seconds at 10mA, about 3 nm). The reason for gold sputtering is explained in a later section of this appendix.

Summarized, the 63x objective was used in combination with IP-Dip was used to print 2PP structures on gold coated-DLP prints. In the sections that follow, more attention is given to the materials used.




	10x lens	25x lens	63x lens
Voxel illustration			
Lateral resolution (a_{xy})	1.6 μm	595 nm	340 nm
Axial resolution (a_z)	25.4 μm	3.1 μm	826 nm
Typical print speed	6.8 mm^3/h	0.8 mm^3/h	0.4 mm^3/h
Typical slicing distance	5 μm	1 μm	0.3 μm
Typical hatching distance	1 μm	0.5 μm	0.2 μm

Figure B.3.2: Table with typical parameters and settings per objective for the Nanoscribe with the voxel size illustrated (scaled with 10^3) [16]

B.4. Slicing

Before discussing the design phase, it is essential to understand the slicing steps used to prepare the model for printing. The design should be compatible with this slicing. Therefore, the slicing phase is discussed first. The STL file can be imported into Describe (Nanoscribe slicing software) when the CAD model is finished. The STL file must be of high quality. Designing the model in millimetres will give better quality .STL files with smaller size (quality is dependent on the number of triangles in the file, more triangles follow the designed shape better). After importing the .STL file into Describe, the slicing wizard opens.

The first step is to select a recipe. One can either import a previous recipe (which will change all the settings in the wizard to that recipe) or use a default recipe. The next step is to change the orientation of the model and scale it. In this study, the cantilever was printed in the positive X direction. If the CAD model is drawn with the correct orientation with respect to the origin, the orientation in the slicer will be the same. One can either align the origin of the print with a corner of the model or with the centre of the model. This last option was used for printing the dome, as this aligns the centre of the aperture (of the DLP print) with the centre of the print. Then it is time to slice and hatch the model. Slicing means cutting the STL into horizontal planes (slices) as shown in figure B.4.3A.

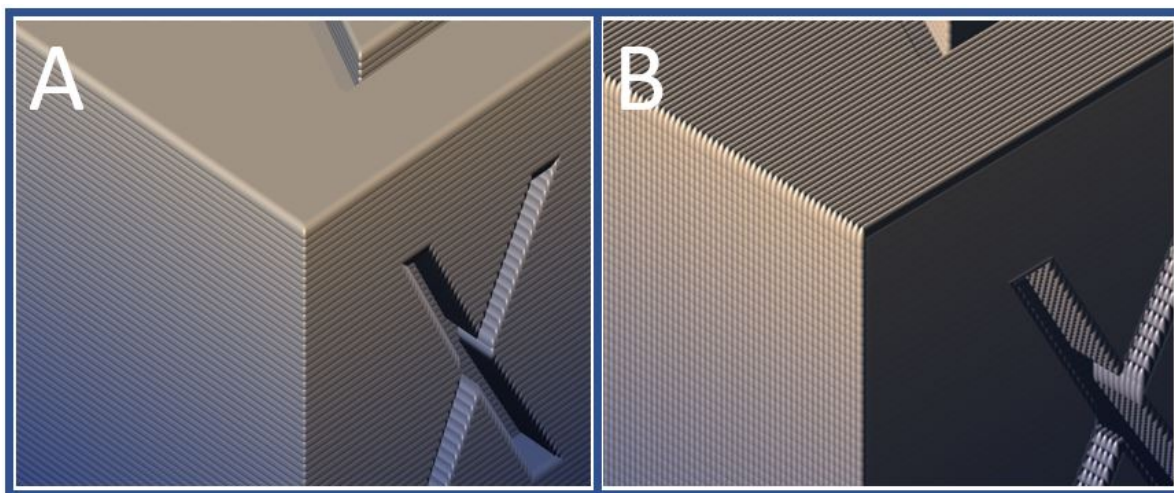


Figure B.4.3: Slicing and hatching in Describe. **A**) Slicing (horizontal planes), **B**) Hatching (splitting the slices into hatch lines that the laser voxel will trace).

By changing the slicing distance, one sets the distance between two printed planes (parallel to the substrate). A larger slicing distance results in a coarser but faster print. Hatching, on the other hand, cuts these planes into voxel lines. The laser scans these lines during printing. The hatching can be seen in figure B.4.3B. Setting the hatching distance defines the distance between these voxel lines (not the voxel width itself). For the hatching, one can set various parameters. For example, one can set a number of contours, which adds hatch lines that trace the outside of the print and result in a smoother print finish. Adding a base slice count defines a certain number of layers as the “base”. The print parameters can be changed for this base, which can improve the adhesion to the substrate (e.g. lower the laser power for those layers). The hatch angle defines the direction of the hatch lines (e.g. laser scans in the direction of the positive X-axis or at a 45-degree angle). By adding a hatch angle offset, the direction of the hatching lines is changed for every layer (slice).

In the last step of the wizard, one should select galvo mode as the scan mode for large structures, with the Z-axis operating in piezo mode. This will yield the best results with short print times compared to the other options. The direction of two neighbouring hatch lines can be set in this last step. This means that the laser either only scans in one direction (e.g. up) or alternating in both directions (e.g. up and down alternating). Setting this to alternating can help to avoid structural deformations in the direction of the scanning line. Setting the exposure to variable allows one to vary the printing parameters in the programming phase (e.g. change base laser power etc.).

The final and most crucial slicing step for large structures is the block spitting step. Since the print field is limited to a 200 μm diameter circle, large structures cannot be printed in one go. Splitting the structure into small parts that are printed one after the other allows one to print these large structures. One can split the structure into either rectangular or hexagonal blocks with user-defined sizes in the X, Y and Z directions. This can be seen in figure B.4.4. One can also specify the shear angle at which the blocks meet and set the overlap between the block. For this research, the splitting of the blocks needed to be just right. This will be discussed in the following sections.

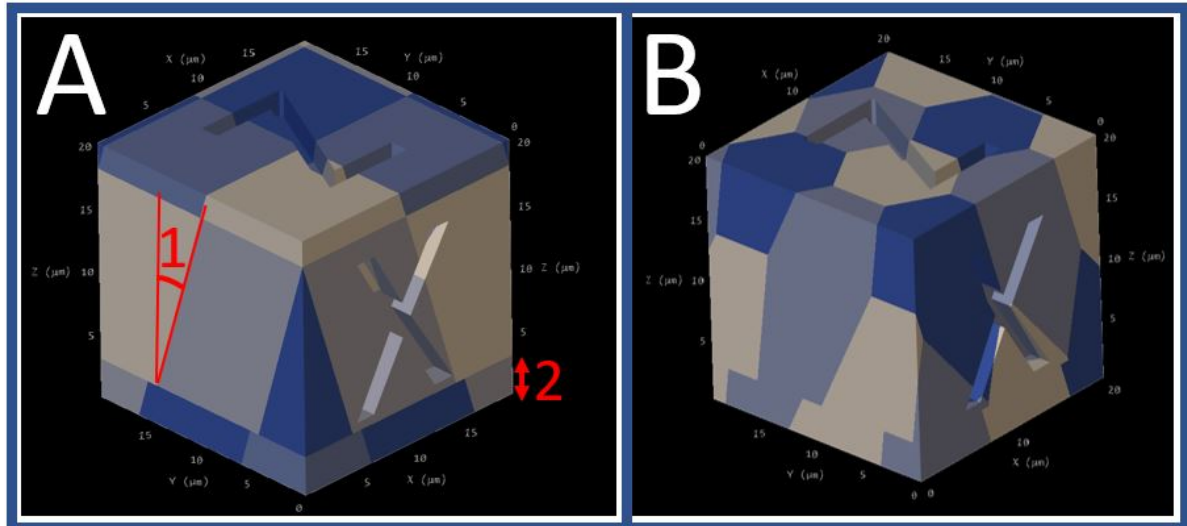


Figure B.4.4: Block splitting in Describe. **A)** Rectangular splitting, 1 = Indicates the shear angle between blocks, 2 = Offset in Z direction. Block sizes in XYZ direction can also be defined by user. **B)** Hexagonal block splitting.

B.5. Design and print approach

Now that the various standard terms for Nanoscribe printing have been explained, the design process and test printing can be discussed. The 2PP print was designed in three modules. This modularity has three main advantages: First, the designs can be easily changed without affecting the other parts. This means that geometry optimizations are easier to perform and allows changing the design for various applications. Second, the 2PP print parameters can be different for each module. Large parts that require less precision can be printed with greater slicing and hatching distance, while small parts can be printed with high precision. The result is faster printing. Thirdly, modularity allows parameters to be optimized in separate prints. This means that the test prints require less printing time, as, for example, only one dome needs to be printed instead of the entire structure.

In the following sections, the design and print optimizations for all modules are discussed separately. These modules are a dome, a cantilever and a sharp tip. Before we turn to these modules, it is important to pay attention to some parameters that can be set by the user during the programming phase (see table B.1). The programming will be covered in a later section, but it is essential to understand the terms as they will be used throughout the text.

AddZDrivePosition	Moves the objective to or away from the substrate, thus changes printing position in Z direction.
FindInterfaceAt	Command that initiates the interface finding. After finding the interface, the objective moves towards the substrate with the value set by InterfacePos.
GalvoAcceleration	Acceleration of the galvo mirror between printing at end and beginning of hatching lines [$Vm^{-1}s^{-2}$].
InterfacePos	Depth into the substrate at which the print starts [μm].
LaserPower	Laserpower (%) of the 50mW laser. Can be set for contour, base and solid parts of the print (e.g. ContourLaserPower)
MoveStageX	Moves the stage in X direction by a set amount (same for Y) [μm]
ScanSpeed	Scanning speed of the laser [$\mu m s^{-1}$]. Can be set for the contour, base and solid parts of the print (e.g. ContourScanningSpeed)
StageGoToX	Moves the stage to a set X coordinate (same for Y).
StageVelocity	Travel velocity of the stage.

Table B.1: Important program commands for Nanoscribe printing.

B.6. Printing on top of a 3D printed substrate

To print 2PP structures on DLP-printed substrates, several problems must be solved. In this section, these problems are discussed, and the found solutions are given. The two main problems are: interface finding and chemical compatibility.

B.6.1. Interface finding

To print on a substrate, the interface between the photoresists and the substrate must be found. The Nanoscribe uses the Definite Focus module from Zeiss to find this interface. The principle of the interface search is based on the refractive index mismatch. This mismatch should be greater than or equal to 0.04 as defined in equation B.10.

$$|n_1 - n_2| \geq 0.04 \quad (\text{B.10})$$

But for the DLP substrates, this mismatch is not large enough. Since HTM140V2 is opaque, it also has an imaginary refractive index. The too-small mismatch results in failure to find the interface automatically. In this case, there are two options: manually searching for the interface or changing the optical properties of the substrate to make the automatic interface search work. The manual interface search is based on printing test blocks on the substrate at different heights. If the blocks remain on the surface during printing, the interface is found. However, this is a labour-intensive approach and prevents the automation of the printing process. Changing the optical properties of the substrate can enable automatic detection of the interface. A simple solution is to coat the substrate with a thin layer of a reflective coating. Sputtering gold is one of the possibilities to change the optical properties. Other materials can be used, but only gold was used for this research since the DLP print material is a polymer, which is not allowed in all sputtering machines.

Various film thicknesses of gold were tried, and it was found that 5 seconds (or less) at 10mA in the sputter coater resulted in good interface finding and good prints (about 3 nm, determined in appendix C). (Much) thicker coatings of gold films resulted in an interesting phenomenon: burning of the surface, as shown in figure B.6.5.

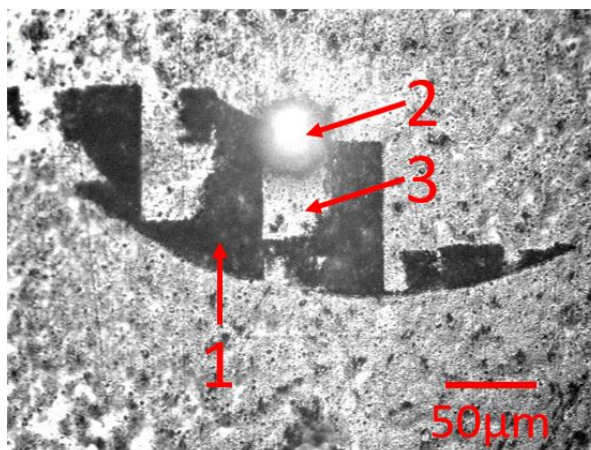


Figure B.6.5: Burning of the surface by the Nanoscribe, caused by a too thick gold coating (burning caused by high energy released after absorption of the photons). View during printing recorded by Nanoscribe camera. 1 = Burnt surface, 2 = Gas bubble due to micro-explosions in the resin at the surface of the substrate, 3 = Part of surface not exposed to the laser due to the bubble blocking the laser.

This burning of the substrate can be explained by looking at the interaction between the femtosecond laser and the gold thin film. Figure B.6.6 shows the absorption for various thin film thicknesses and wavelengths.

Since the Nanoscribe uses a femtosecond laser with a wavelength of 780 nm, the absorption intensity is high and increases for thicker gold films (see figure B.6.6). The photons are absorbed by free electrons of the gold and excite them to a higher energy state. The absorbed energy is converted into lattice energy, which cannot be readily conducted into the DLP print, causing the thin film to heat up and scorch the substrate [17].

Reducing the gold film thickness to a minimum, thereby reducing absorption and heating, improves the 2PP print quality on the DLP substrate significantly. Thinner coatings lead to better printing results, as long as the interface signal is sufficient for automatic detection.

A tilt of the substrate can be detected by using the automatic interface finding for at least three points, but the data is challenging to read automatically from the Nanoscribe (requires python programming). Therefore, printing (deep) inside the surface (using the commands "FindInterfaceAt" and "InterfacePos") helps to reduce the influence of a tilt of the substrate. This procedure "embeds" the print deeper into the substrate. This was used for this research for the 3DM Tough Clear prints as the transparency allows for a deep print (used 8 μm into the substrate but tested up to 15 μm) With the HTM140V2, deeper printing resulted in poor print quality.

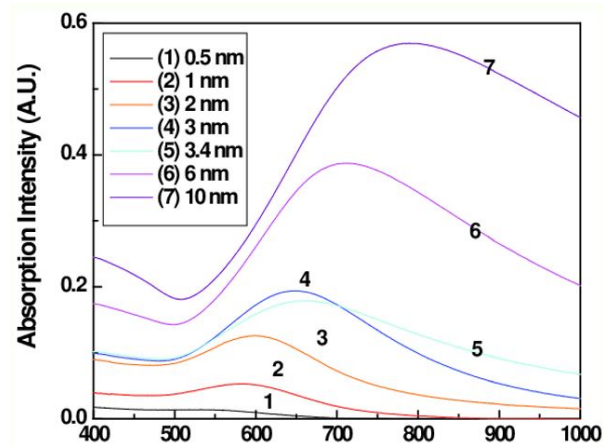


Figure B.6.6: Absorption intensity for various gold layer thicknesses. Thickness of the coating used for this research is about 3 nm [18].

B.6.2. Printing at the interface: parameter sweep

To be able to print on the DLP print, a parameter sweep was performed. This means that several arrays were printed with different printing parameters. These parameters include the printing depth, laser power and scanning speed. To determine the influence of the DLP substrate and the gold layer, a dose test was performed with four different substrates: untreated fused silica, gold-coated fused silica, gold-coated 3DM Tough Clear and gold-coated HTM140V2. The results are shown in figure B.6.7 to B.6.11.

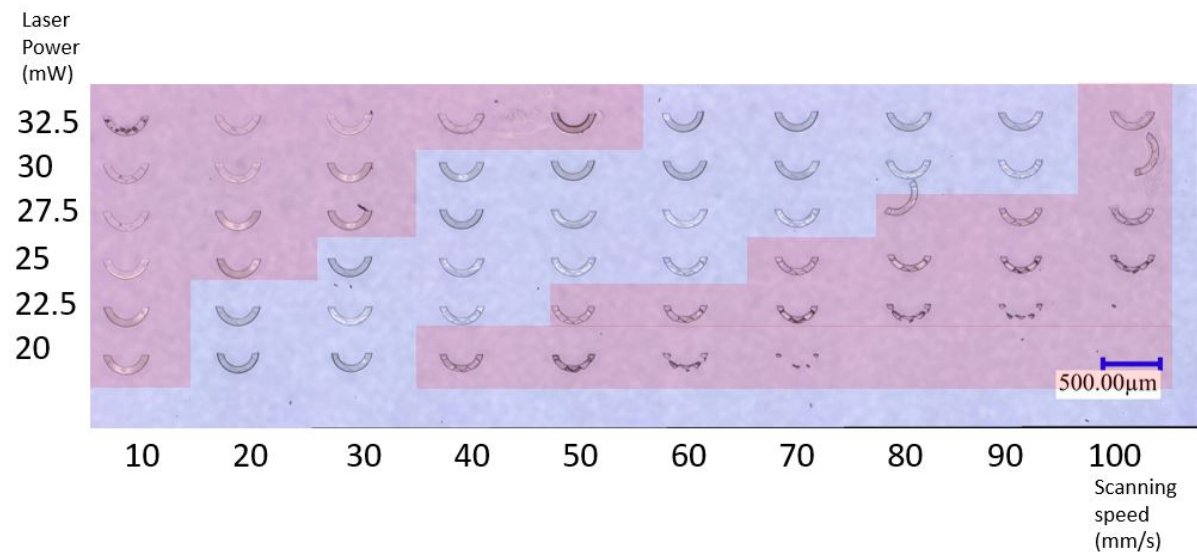


Figure B.6.7: 2PP dose test on fused silica with varying laser power and scanning speed. Red areas indicate bad quality prints.

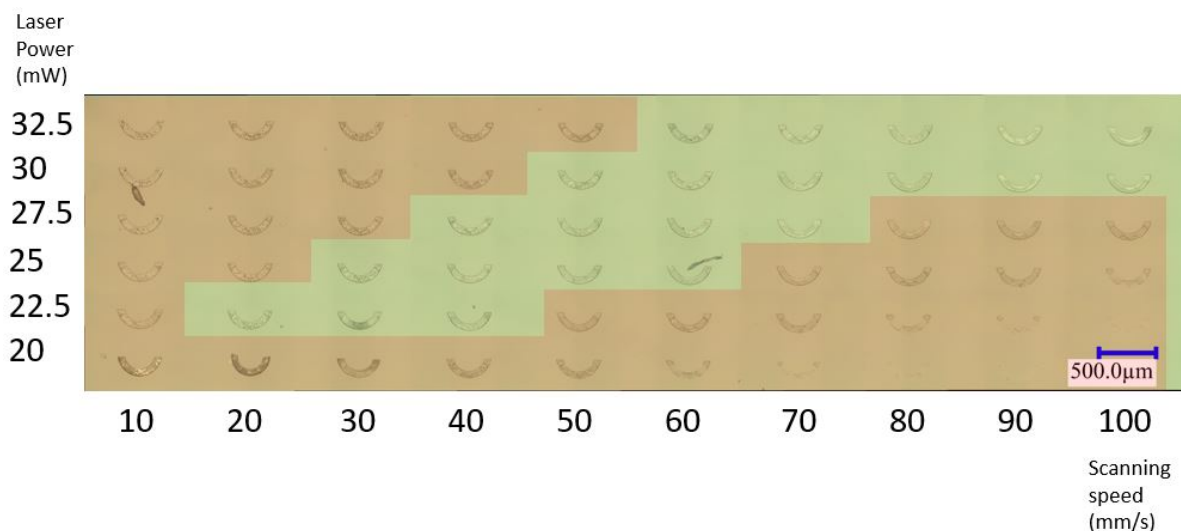


Figure B.6.8: 2PP dose test on gold coated fused silica with varying laser power and scanning speed. Red areas indicate bad quality prints. Bubble formation is hugely increased by gold layer compared to fused silica. However, there seem to be less adhesion problems compared to the bare fused silica.

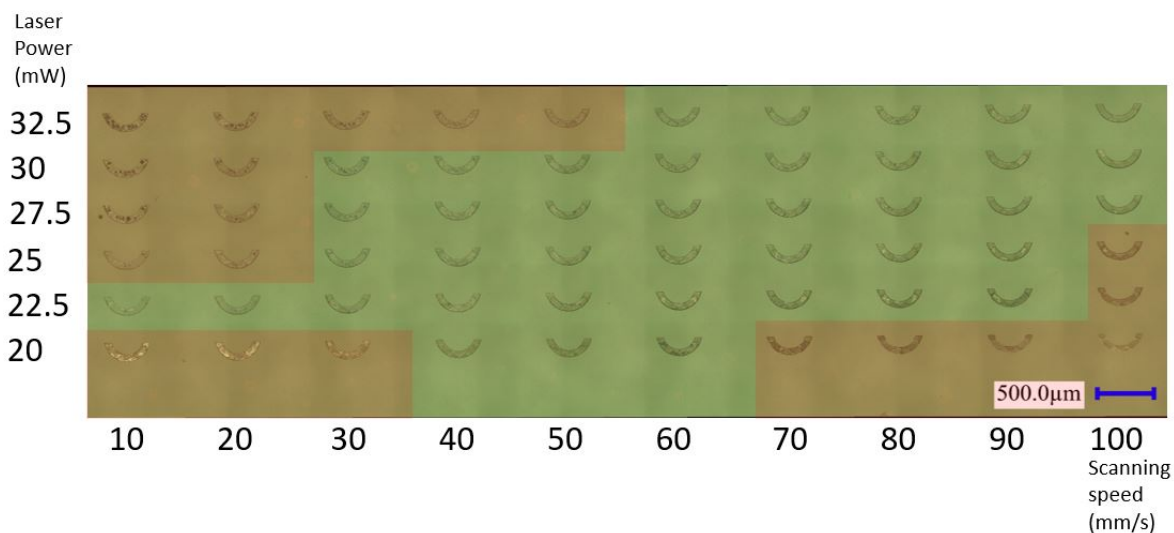


Figure B.6.9: 2PP dose test on gold coated fused silica after plasma cleaning for 30 seconds with varying laser power and scanning speed. Red areas indicate bad quality prints. Bubble formation is hugely increased by gold layer compared to fused silica. However, there seem to be less adhesion problems compared to the bare fused silica. Overall print quality better than without plasma cleaning

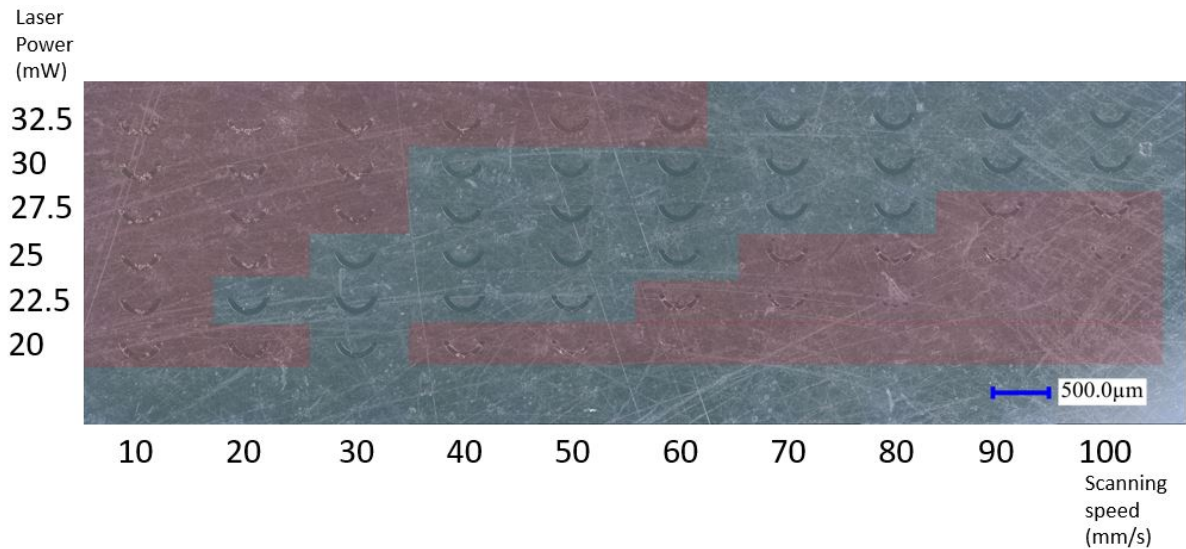


Figure B.6.10: 2PP dose test on 3DM Tough Clear with varying laser power and scanning speed. Red areas indicate bad quality prints

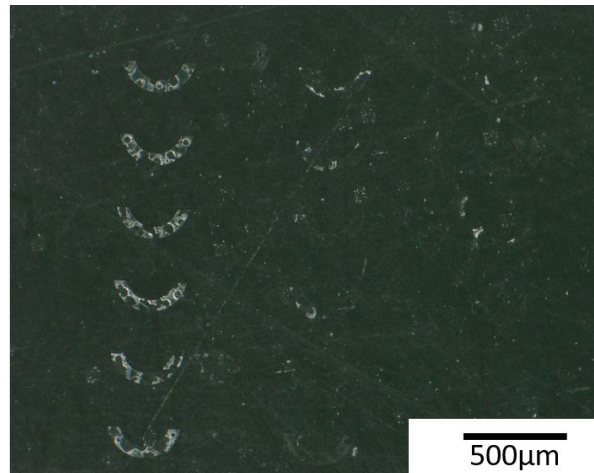


Figure B.6.11: Only remnants of 2PP dose test on HTM140V2 with varying laser power and scanning speed. Other prints did not stick to the surface.

From figure B.6.7 to B.6.11 it can be concluded that although the gold layer introduces bubbles into the print, they are embedded in the print. No alternative structures are required to trap the bubbles. A clear diagonal line of good prints can be seen in the first three dose tests (fused silica with and without gold and the gold-coated 3DM print). It proves that printing on a DLP print and on a gold film is possible, but the gold coating affects the print quality (as the fused silica print without gold does not have bubbles in the good prints). Plasma cleaned gold-coated fused silica shows the most adhered structures and better print quality compared to gold-coated fused silica that has not been plasma cleaned. This indicates that plasma cleaning improves both the adhesion and the printing quality (possibly a small amount of gold is removed during the plasma cleaning). Four ways to improve printing on the DLP surface have been identified. The first is to use a different material for DLP printing with sufficient refractive index mismatch (no gold is required in that case). The second option is to use a different material for the interface coating (or to use a thermally conductive layer underneath, e.g. chromium). Titanium or aluminium could give better printing results than gold, as the interaction with the laser could be less. The third option is to reduce the layer thickness of the gold film even further. The last option, which is the simplest, is plasma cleaning. It has been observed that a short oxygen plasma cleaning cycle (30 seconds) reduces the gold film thickness or changes the properties of the thin film. Widdascheck et al. [19] report the formation of gold oxides by the oxygen plasma. This could improve the print quality and the adhesion of the print to the substrate. Figure B.6.9 shows the results of a dose test on plasma cleaned gold-coated fused silica. More prints appear to have been printed properly, and more prints are on the substrate, which means that better adhesion is achieved. Comparable dose

tests were carried out as part of this research. Often a dose test was carried out with small structures first (e.g. small cubes, see fig. B.6.12A1/A2), then with parts of the final design (e.g. semicircle or half of the base of the dome, see fig. B.6.10) and then with complete structures (e.g. full domes, see fig. B.6.12B1/B2), continuously narrowing down the optimum parameters. Starting with a small structure for the dose test arrays allows varying the parameters over a larger range and narrowing down the parameters for increasingly large structures.

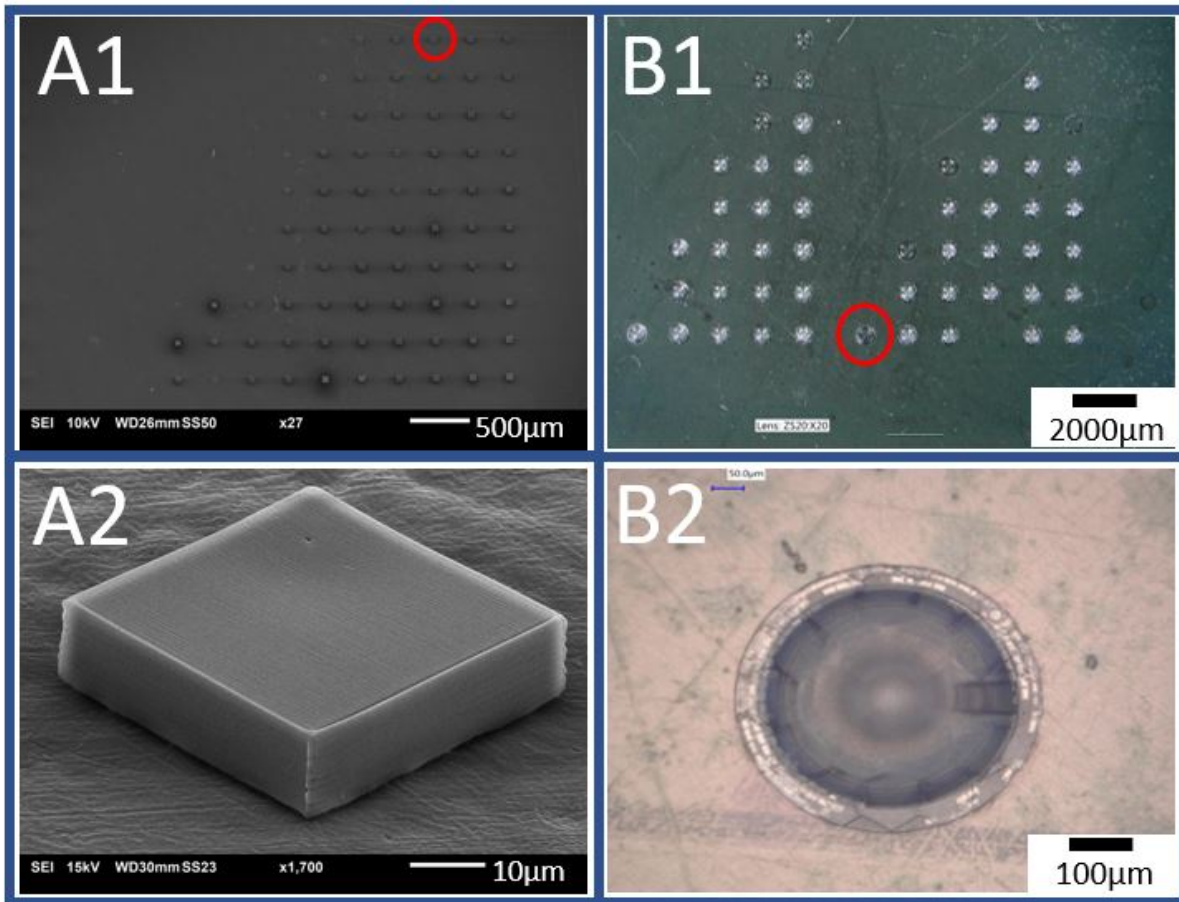


Figure B.6.12: 2PP dose test on HTM140V2 with blocks and domes. **A1&A2** Dose test of simple squares to get a rough dose estimate (SEM image, note: many more structures attached compared to figure B.6.11). **B1&B2** Narrowed down dose test of full domes (sealed) with doses in a range $\pm 10\%$ found by other dose tests.

Because performing dose tests is one of the main tasks during the optimization phase of the 2PP printing parameters, it is recommended to save the data of the individual dose tests in Excel. This way, one can determine which parameters lead to repeatable results. An example of such a file is shown in figure B.6.13, where the data of the dose test of figure B.6.10 is stored.

Laserpower (mW)	10	20	30	40	50	60	70	80	90	100	Scanningspeed (mm/s)
32.5	Red	Red	Red	Red	Red	Orange	Green	Green	Green	Orange	
30	Red	Red	Red	Red	Green	Green	Green	Green	Green	Orange	
27.5	Red	Red	Red	Green	Green	Green	Green	Green	Green	Red	
25	Red	Red	Red	Green	Green	Green	Green	Green	Green	Red	
22.5	Red	Orange	Orange	Green	Green	Green	Green	Green	Green	Red	
20	Red	Red	Red	Red	Red	Red	Red	Red	Red	Red	

Figure B.6.13: A method to record and store dose test data. red indicates absent or bad prints. Orange indicates prints that are almost acceptable and green indicate prints that are acceptable. The print of fig. B.6.10 was used for this figure

B.6.3. Chemical compatibility

The poor print quality of HTM140V2 can be explained by the interaction of one of the photoresist components. HTM140V2 contains titanium dioxide, which can interact with the femtosecond laser and cause micro-explosions in the resin. The resulting gas bubbles can coalesce and ruin the print. The additives to the HTM140V2 resin also prevent printing deep into the substrate, which is possible with 3DM Clear Tough. The chemical compatibility between the 3DM Clear Tough and the IP-Dip seems much better than the HTM140V2.

B.7. Dome

To connect the DLP print to the 2PP print and connect the microfluidic channel of the cantilever to the channel of the microfluidic interface, a transition structure is required. In principle, this structure can have any shape. In this research, various shapes were printed, from hollow cubes to domes. Domes with large baseplates were also tested. These tests were mainly done with HTM140V2 as a substrate, which later turned out to be a suboptimal substrate material. Figure B.7.14 shows a dome on a baseplate. The main advantage of the baseplate is the large surface area, which reduces the probability of leakage. The baseplate does increase the printing time significantly.

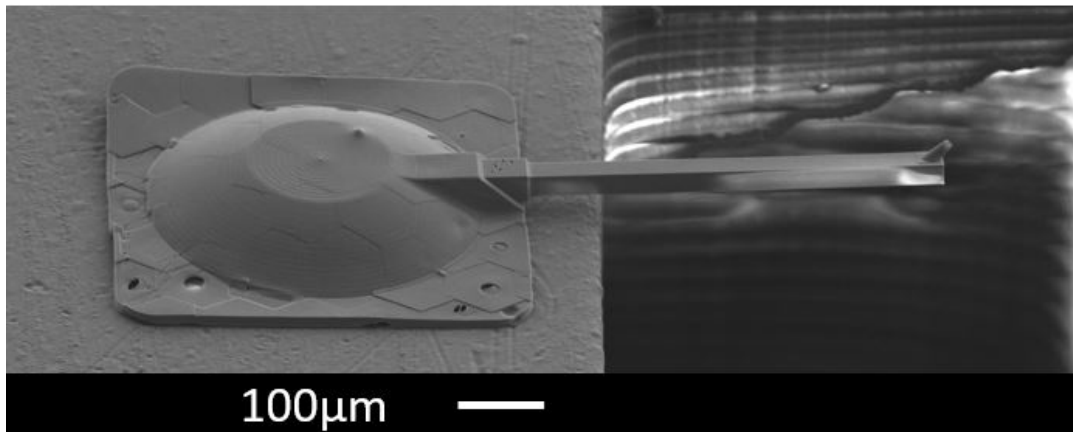


Figure B.7.14: SEM image of a dome with a baseplate printed on HTM140V2. Bad quality print due to delamination and bubble formation, resulting in badly adhered and leaking print.

Various structures were printed with cavities in the base structure, which reduced the printing time, but adhesion to 3DM substrates should be investigated. Hollow walls of the structure can be printed using the scaffold mode of Describe, but stitching can cause problems (scaffolding makes cavities in the structure, which trap resin and should be post-cured). After 3DM Tough Clear was found to be a good substitute for HTM140V2, further progress was made. It was found that 2PP prints on 3DM Tough Clear do not require bubble trapping geometries that Kramer et al. used [9], as the bubbles get trapped by the print itself. This means that a solid dome could be printed without the bubbles forming on the substrate being a problem (as they get trapped in the first layers of the print). The dome shape forms a robust structure with minimal volume. The minimum dimensions of the dome are determined by the size of the aperture and partly by the required distance between the cantilever and the surface of the DLP print.

For best printing results, the entire base of the dome must be on the surface of the DLP print. This means the base of the dome should not be printed on the influenced region (the part where the surface curves into the aperture, as defined in figure B.7.15). Printing in that region could cause leakage due to height differences.

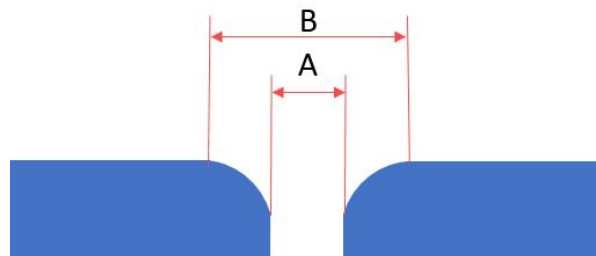


Figure B.7.15: Schematic aperture and influenced area. A = Indicates the aperture diameter, B = Indicates the influenced area diameter.

The minimum inner diameter of the dome is therefore equal to the influenced area. Since there is some variability in the influenced area, an inner diameter of $280\ \mu\text{m}$ was chosen. A too-large inner diameter would result in longer print times. The outer diameter was set at $408\ \mu\text{m}$. Figure B.7.16 shows a printed ring around an aperture. Some deformation can be seen on the ring's inner edge, but this is not a problem as there is a second block on the outer edge. At the beginning of the print, the interface is searched approximately $200\ \mu\text{m}$ away from the aperture. This location is marked in figure B.7.16 and is outside the influenced region.

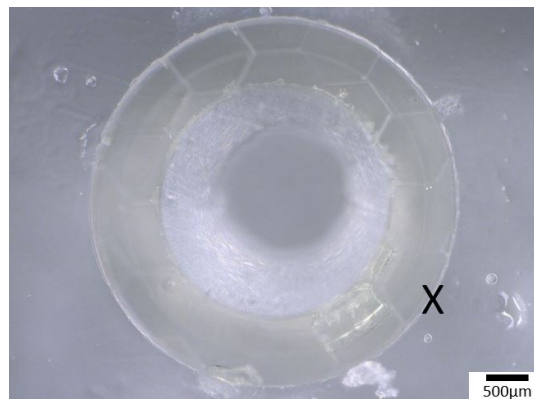


Figure B.7.16: Ring printed around an aperture (3DM) with inner diameter of the ring equal to $280\ \mu\text{m}$. The X indicates the approximate position where the 'FindInterfaceAt' command searches for the interface position.

As can be seen in figure B.7.16, the ring can be nicely printed around the aperture. This ring is part of the dome design and is printed first before the rest of the dome is printed. The centre of the ring should be approximately the same as the centre of the influenced area. Therefore, it may not be perfectly aligned with the aperture. To avoid tilt effects or unevenness, the printing starts $8\ \mu\text{m}$ below the surface found at the location marked with the X. The ring has a height of $21\ \mu\text{m}$. The reason for printing this first layer of blocks separately is so that any bubbles that may appear can dissipate before the next layer of blocks is printed. This second layer of blocks, which form the dome, is programmed to print one to two microns deep into the first ring. As a result, gaps that gas bubbles could create are sealed by this layer. Once the print is past the surface, no more bubbles appear and printing continues as normal. The dome has a wall thickness of $30\ \mu\text{m}$, but domes with thinner walls have also been printed (down to $20\ \mu\text{m}$). A CAD drawing of the dome and its cross-section can be seen in figure B.7.17.

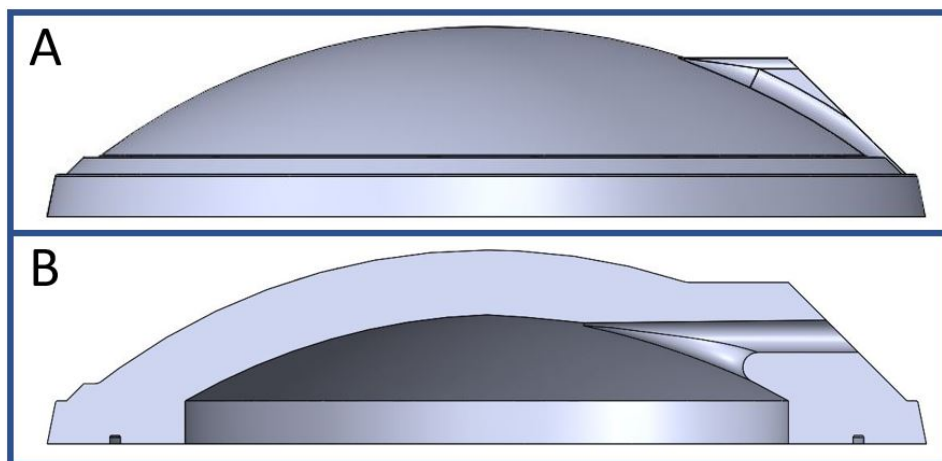


Figure B.7.17: CAD drawings of the dome. **A)** Side view of the dome, with the part where the cantilever attaches on the right side (45-degree angle). **B)** Side view of cross-section of the dome. The channel towards the cantilever is clearly visible. Dimensions given in figure B.7.18-B.7.21.

On the right side of the dome, the foundation for the cantilever is attached to it. The foundation has a surface that is at a 45-degree angle with respect to the DLP surface. On this sloped surface, the cantilever will be printed. The 45-degree angle prevents shadowing by the dome when the cantilever is printed. The channel running towards the cantilever can be seen in figure B.7.17B. This channel is at a $42.5\ \mu\text{m}$ distance from the surface of the DLP print (so the cantilever cannot touch the DLP print). The important dimensions of the dome are shown in figure B.7.18 to figure B.7.21.

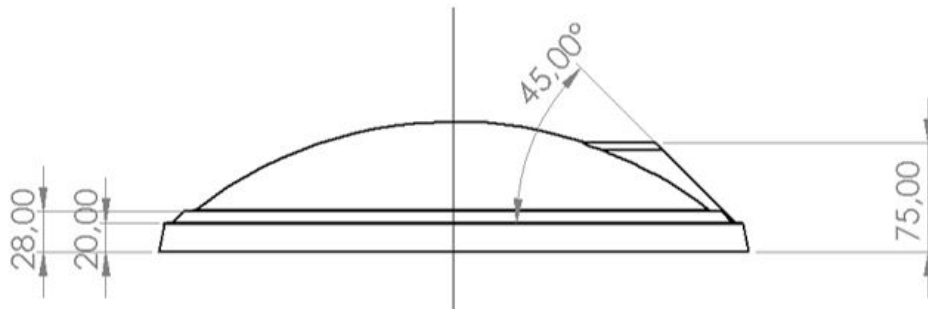


Figure B.7.18: Side view drawings of the dome design. Dimensions in micrometres [μm].

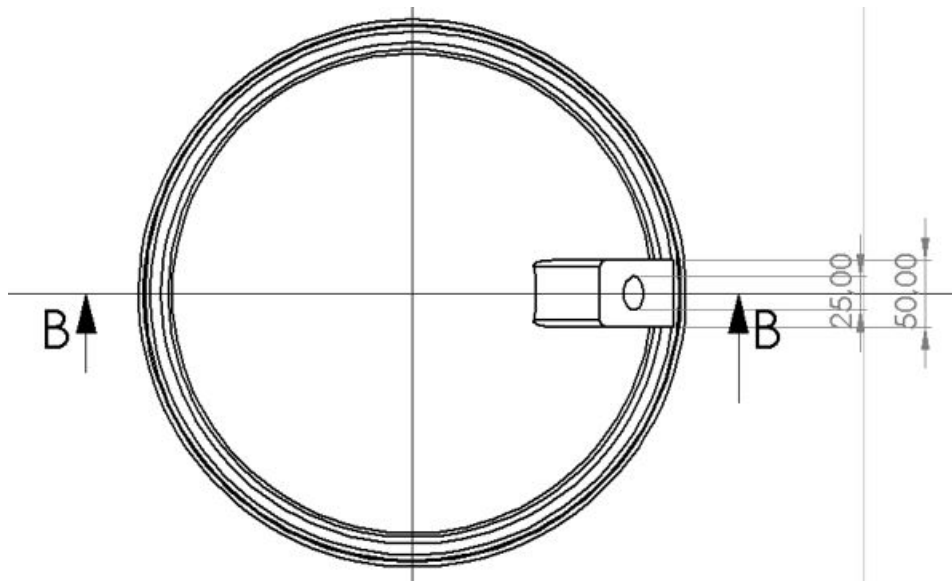


Figure B.7.19: Top view drawings of the dome design. With cross-section BB in figure B.7.20. Dimensions in micrometres [μm].

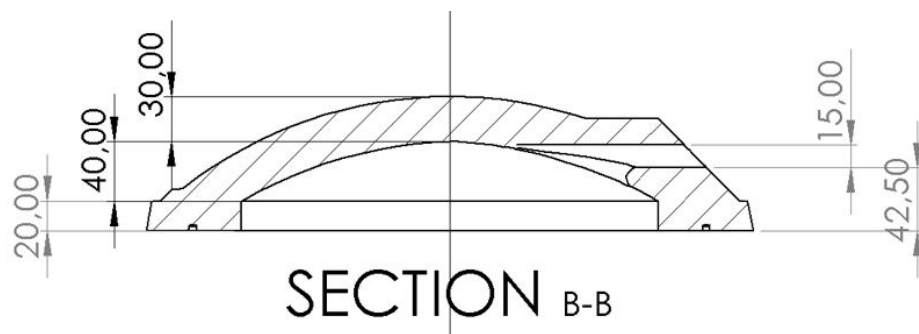


Figure B.7.20: Cross-section view drawings of the dome design (cross-section BB of figure B.7.19). Dimensions in micrometres [μm].

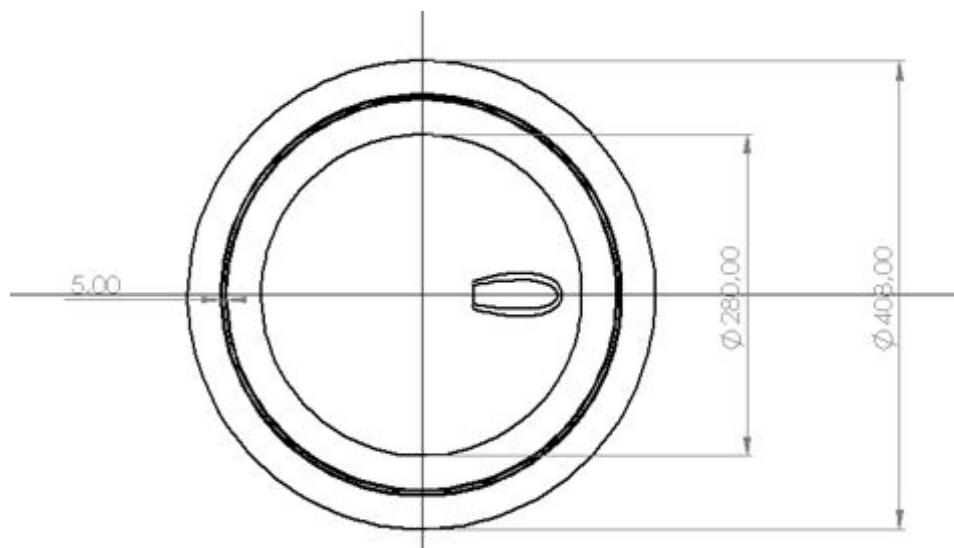


Figure B.7.21: Bottom view drawings of the dome design. Dimensions in micrometres [μm].

To reduce the total printing time, one should try to reduce the print volume of the dome or print it with coarser print settings (e.g. larger hatching or slicing values).

Various structures were printed with cavities in the base structure, which reduced the print time, but adhesion should be investigated for 3DM Tough Clear. Cavities in the walls of the dome can be printed, but stitching can cause problems. For future research, other geometries and different dome dimensions (e.g. wall thickness) should be investigated. It may even make sense to print a flat plate over the aperture instead of a dome, but this needs to be explored.

The bottleneck remains the size of the aperture of the DLP print. Reducing the size of the aperture will reduce the print volume and thus reduce the print time, which should be a priority in future research. Other techniques, such as selective laser etching of fused silica, could help reduce the aperture size, and this also solves the problem of finding the interface.

B.7.1. Unique print parameters for the dome

The main unique feature of the dome in terms of 2PP printing parameters is the block splitting. The block splitting is necessary because the dome is larger than the print field of the objective. To print the dome, hexagonal block splitting was used. The most significant advantage of the hexagonal blocks is the angle between the contact surfaces of adjacent blocks. The combination of the shear angle of the blocks and the angle defined by the hexagonal shape results in stronger structures than with the rectangular splitting. Figure B.7.22 shows the splitting of the dome in Describe.

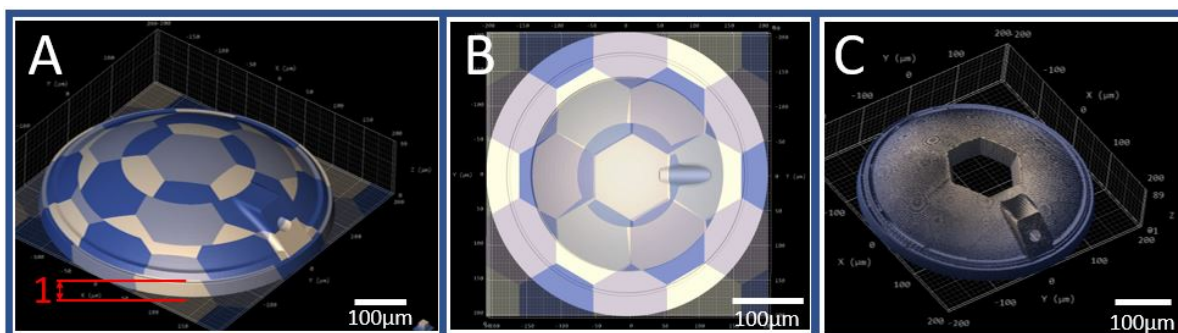


Figure B.7.22: Block splitting of the dome in Describe. **A)** Isometric view of dome split in hexagonal blocks in Describe. 1 = Indicates the first printed ring due to z offset (as seen in figure B.7.16). **B)** Bottom view of the hexagonal block splitting. **C)** Print render with last block removed. The side surfaces of the block are at an angle, increasing the strength of the dome.

The hexagonal splitting also gives better shape results compared to the rectangular splitting. Figure B.7.23 shows the result for the rectangular and hexagonal splitting. Especially at the interface between two blocks, the hexagonal splitting seems to outperform the rectangular splitting because the overhang of the blocks is smaller.

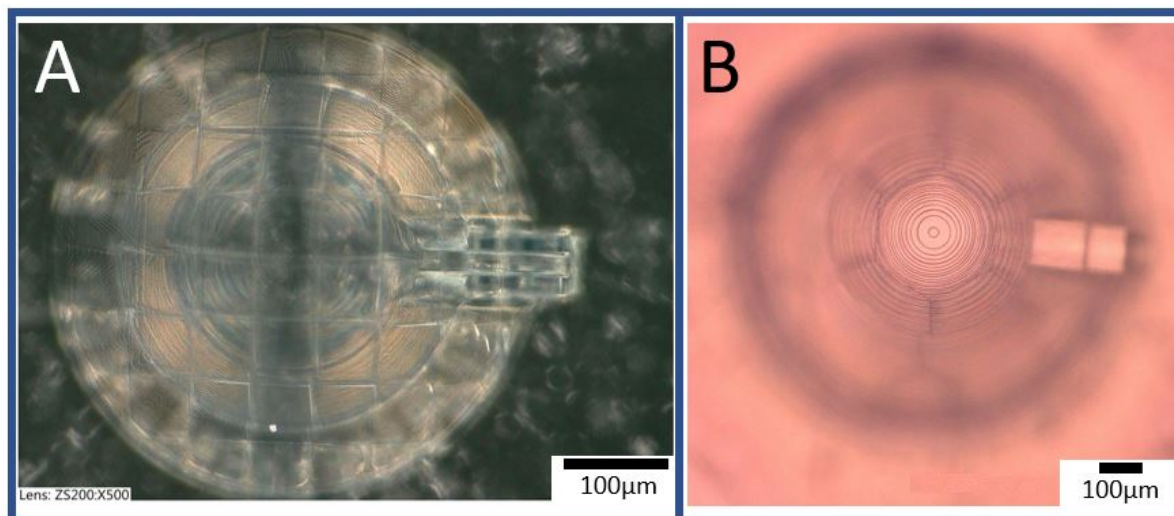


Figure B.7.23: Dome block splitting rectangular versus hexagonal **A)** Rectangular block splitting results in an uneven dome shape (blocks not properly aligned), **B)** Hexagonal block splitting, results in a good dome shape (blocks nicely aligned).

B.7.2. Alignment of dome on aperture

To align the dome with the aperture, the position of the aperture must be programmed in Describe. As the interface holder aligns the interfaces, the position of the aperture can be found within a certain range of the previously found position. By using “StageGoToX” and “StageGoToY” command (and setting the piezo position to a value of 300), one can navigate to this position and search for the aperture. With the same sample position in the Nanoscribe holder, the position of the aperture is often within 100 μm of the previous coordinates (from a previous print).

The aperture, as seen in the Nanoscribe viewer, is shown in figure B.7.24. Note that the centre of the print is not exactly in the centre of the camera view. Test printing a cross at a random location will help determine the exact centre. However, since the dome is printed larger than the aperture, this is not necessary, and it is sufficient to align the aperture in the centre of the viewer (as done in figure B.7.24A). The X and Y positions can be programmed into the code and are used to print at the correct position automatically. (NOTE: the piezo goes from 0 to -300 if a print is started after the Nanowrite software has been closed. This would result in an offset of 300 μm . Make sure the piezo is at -300 before programming the coordinates).

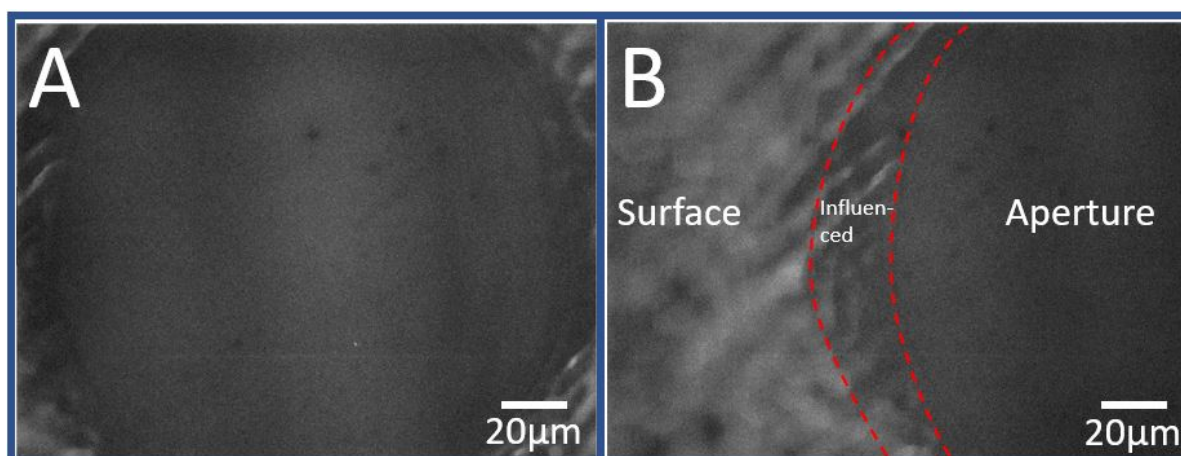


Figure B.7.24: Alignment of the dome with the (Nanoscribe viewer). **A)** Shows the centred aperture **B)** Indicates the difference between the surface, the influenced region and the aperture.

B.7.3. Print results

The dome was successfully printed with no leaks or blockages. The exact printing parameters are listed at the end of this appendix. More important, however, are the results of the prints. Figure B.7.25 shows the dome from different angles using a scanning electron microscope (SEM).

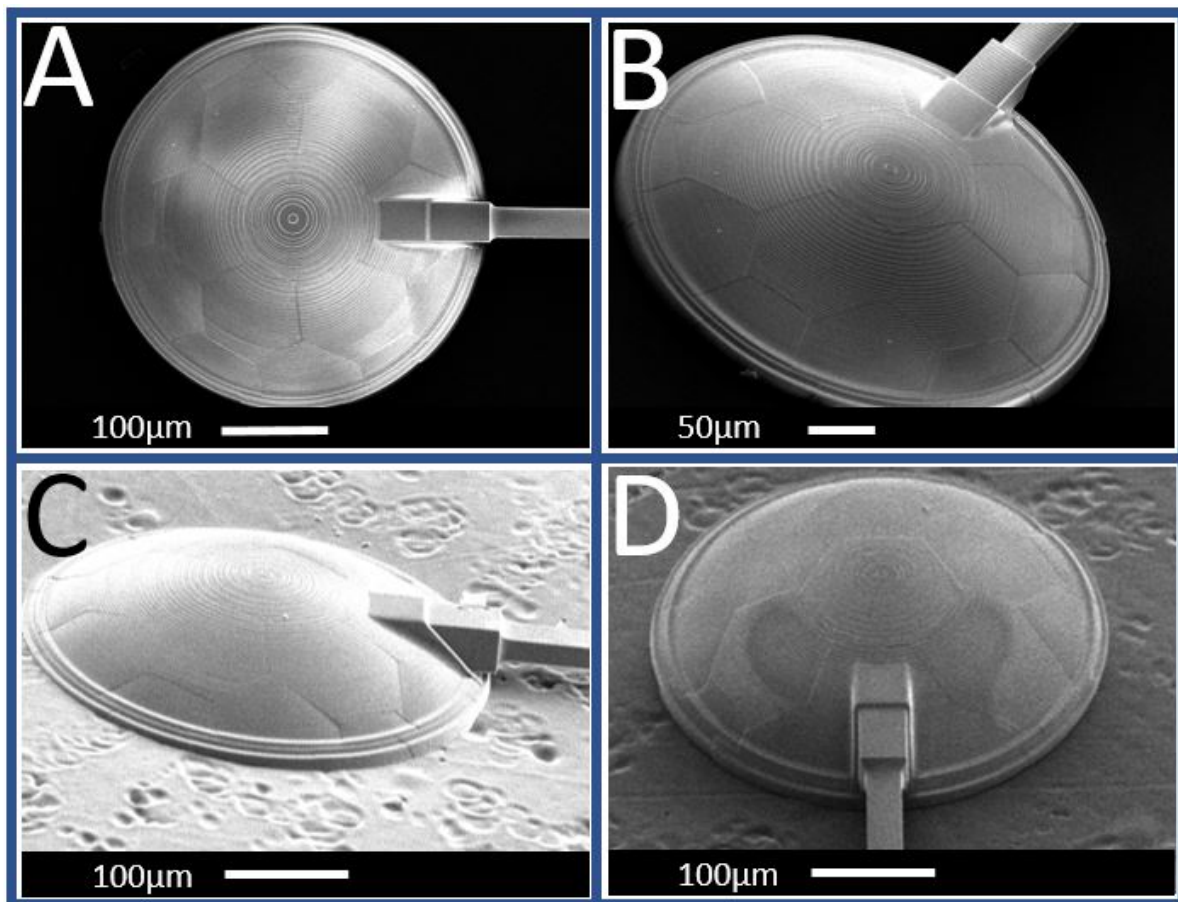


Figure B.7.25: SEM images of the dome from various viewing positions. **A)** Top view, **B)** Isometric back view. **C)** Side view (60-degree tilt), tilt of substrate can clearly be seen as the dome is printed deeper into the substrate on the left. **D)** Front view (60-degree tilt)

Half of the dome was printed to assess the quality of the interior and positioning of the dome. Figure B.7.26 shows SEM images of half a print. Unfortunately, the dome is less stable when cut in half, and the block layout is suboptimal, leading to defects.

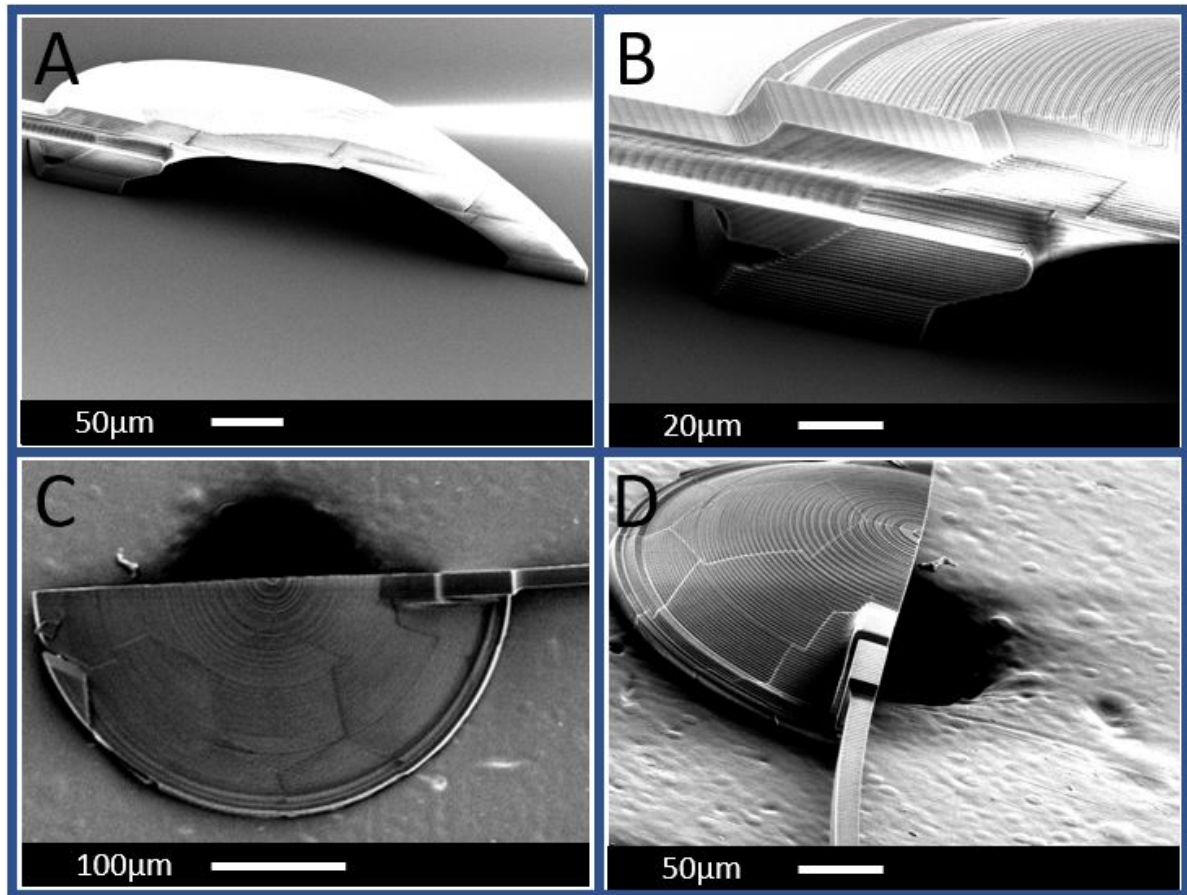


Figure B.7.26: SEM images of cross-section of the dome. **A)** Side view of half a dome **B)** Zoom in on the channel of half the dome **C)** Top view of the half dome with the aperture of the DLP print visible. **D)** Front view of half a dome with aperture of the DLP print visible.

The dome can also be seen under the optical microscope. Figure B.7.27 shows the dome with two different focal points.

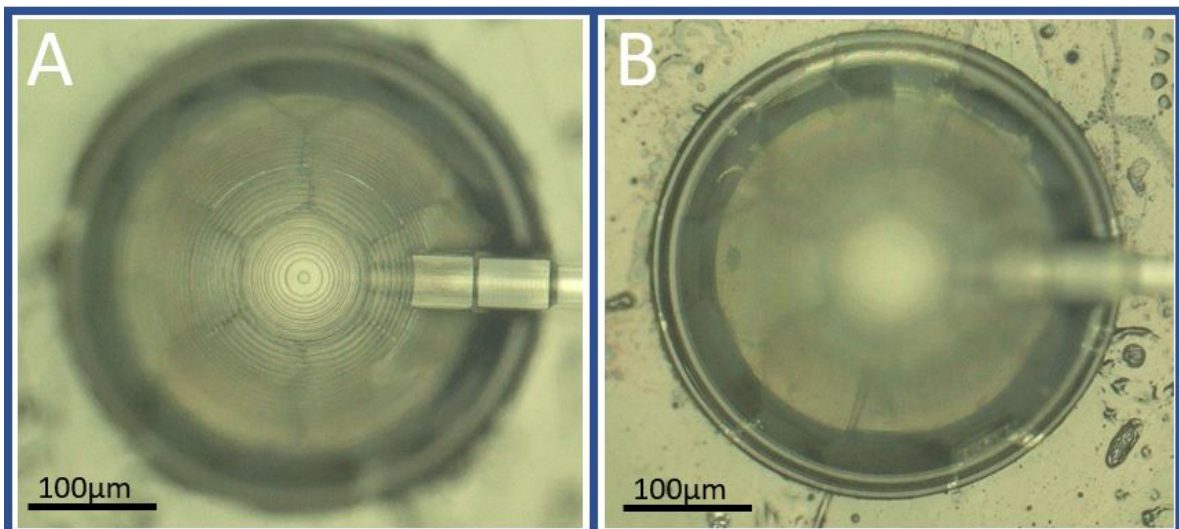


Figure B.7.27: Optical microscope images of the dome. **A)** Focus on the top of the dome with stitching visible. **B)** Focus on the bottom of the dome at interface level.

B.8. Cantilever

Commercial cantilevers for cell puncture often have a stiffness of about 2 N/m [20]. This research aimed to achieve a comparable stiffness. Since a lower stiffness is more challenging to achieve than a higher one, a stiffness of 1.7 N/m was aimed for.

Using simplified beam equations, the dimensions for the cantilever were calculated with MATLAB.

$$I_{total} = I_{rectangle} - I_{ellipse} = \left(\frac{w * h^3}{12} \right)_{rectangle} - \left(\frac{\pi h^3 w}{64} \right)_{ellipse} \quad (B.11)$$

With I the respective moment of inertia, h the respective height of the element and w the respective width of the element. The stiffness can then be calculated using:

$$k = \frac{3EI_{total}}{L^3} \quad (B.12)$$

with k the stiffness, E the Young's modulus and L the length of the cantilever.

Since the stiffness of the cantilever is proportional to the cube of the height of the cantilever, as can be seen from the equations B.11 and B.12, minimizing the height will result in a lower stiffness. However, one would like the channel to have a cross-section as large as possible (for faster development after printing). To minimize the height of the cantilever, while maximizing the cross-section of the channel, an elliptical cross-section was chosen. This allows for a wide channel while keeping the height to a minimum. It also allows the walls to have sufficient thickness. The elliptical shape prevents the channel from collapsing, which can occur with rectangular channels. The ellipse prevents this collapse because the arch supports the top of the channel. In addition, when the ellipse is printed, there is a large overlap between the layers, which prevents large overhangs and thus prevents collapse and indentation of the channel during printing. The calculations, using simple beam equations, resulted in the initial dimensions for the cantilever, which are shown in the technical drawings in figures B.8.28 to B.8.31.

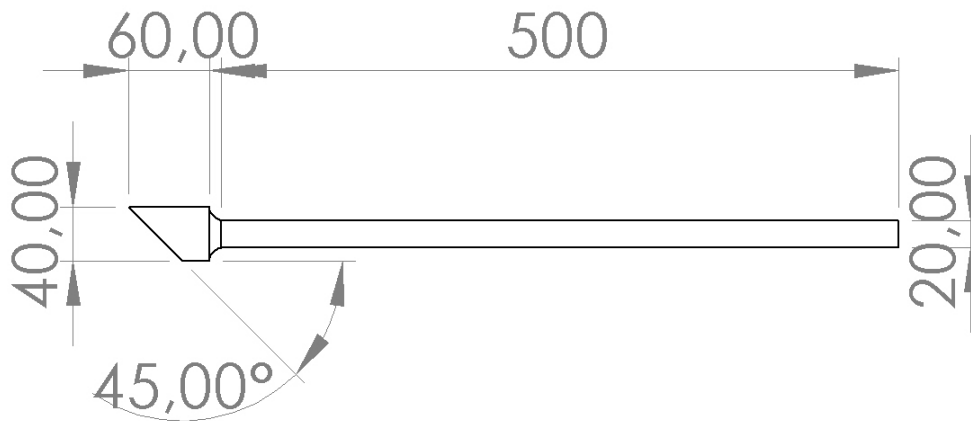


Figure B.8.28: Cantilever drawing, side view. Dimensions in micrometres [μm].



Figure B.8.29: Cantilever drawing, top view. Dimensions in micrometres [μm].

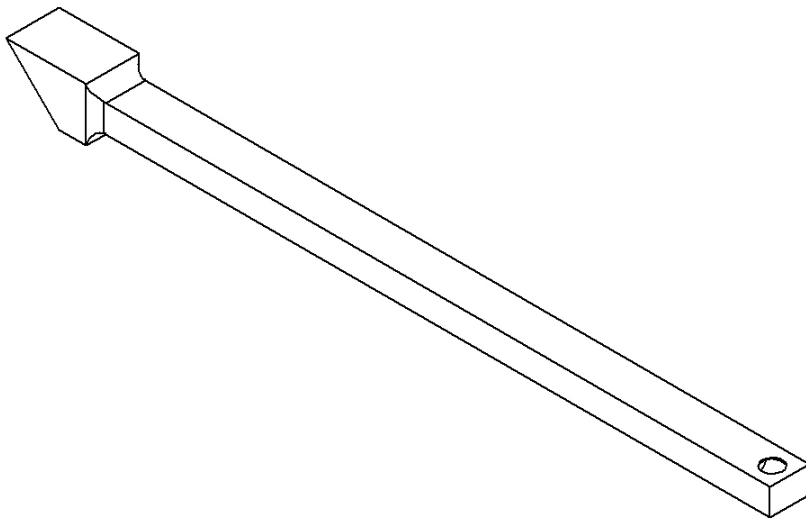


Figure B.8.30: Cantilever drawing, isometric view. Dimensions in micrometres [μm].

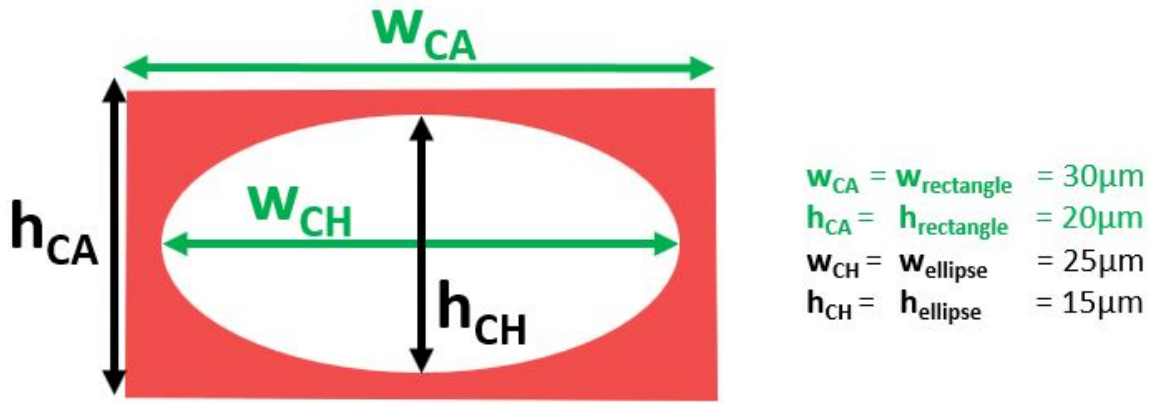


Figure B.8.31: Cantilever cross-section view showing the internal elliptical channel.

The CAD model was used to run a FEM simulation in COMSOL. These simulations were used to determine if the simple beam calculations were in the correct range. The stiffness and resonant frequency results from the simulations were used to verify these calculations. The COMSOL simulations are discussed in Appendix E.

In MATLAB, the resonant frequency of the cantilever was calculated using the following equations [21]:

$$f_0 = \frac{1}{2\pi} * \sqrt{\frac{k_{eff}}{m_{eff}}} \quad (B.13)$$

with f_0 the resonant frequency, $k_{eff} = k$ (eq. B.12) the effective stiffness and m_{eff} the effective mass.

The effective mass is defined as [21]:

$$m_{eff} = \frac{33}{140} m_0 \quad (B.14)$$

with m_0 the mass of the cantilever. This mass can be determined using either Solidworks or by calculating it using equation B.15.

$$m_0 = \rho * V \quad (B.15)$$

with ρ the density of the polymer and V the volume of the cantilever. The volume of the cantilever can be calculated by subtracting the area of the ellipse from the area of the rectangle and multiplying it with the length of the cantilever:

$$V = V_{rectangle} - V_{ellipse} = (A_{rectangle} - A_{ellipse})L = \left((hb)_{rectangle} - \pi * \left(\frac{hb}{2} \right)_{ellipse} \right) L \quad (B.16)$$

For the calculations, a Young's modulus (E) of 4.5GPa was used for the IP-Dip with a density ρ of 1170 kg m⁻³ [16].

B.8.1. Unique print parameters for the cantilever

Once the cantilever design was ready, the printing parameters had to be optimized to obtain good cantilevers. This optimization required a visual inspection to assess the cantilevers after printing.

When large overhangs are printed without a supporting layer under it, the layers tend to bend upwards (due to internal stresses) before the next layer is printed. By splitting the cantilever into blocks, the overhang can be reduced. Fine-tuning the block size and the overlap between the blocks was necessary to achieve cantilevers with high quality. The overlap and block size affected the straightness and surface quality of the cantilever.

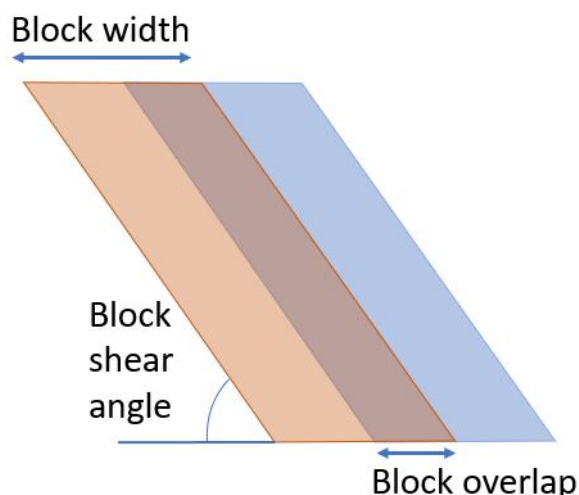


Figure B.8.32: Schematic view of two blocks for block splitting the cantilever. The two blocks overlap to improve printing results.

Figure B.8.32 shows a schematic visualization of two adjacent blocks for the cantilever print. The dose, block width, overlap and shear angle have been optimized to obtain straight cantilevers.

The width and the overlap of the blocks affect both the bending and the surface quality of the cantilever. The underside of the cantilever, which will reflect the laser of the AFM and vibrometer, shows a large roughness if the blocks are too large. Figure B.8.33A shows this sawtooth-like pattern. This pattern is caused by the first printed layers of each block. These layers tend to bend upwards due to internal stresses after polymerization, causing the end of the layer to be higher than the beginning. Reducing the block size helps to minimize this problem. The sawtooth also means that the cantilever is not symmetrical, which leads to more bending of the cantilever after development.

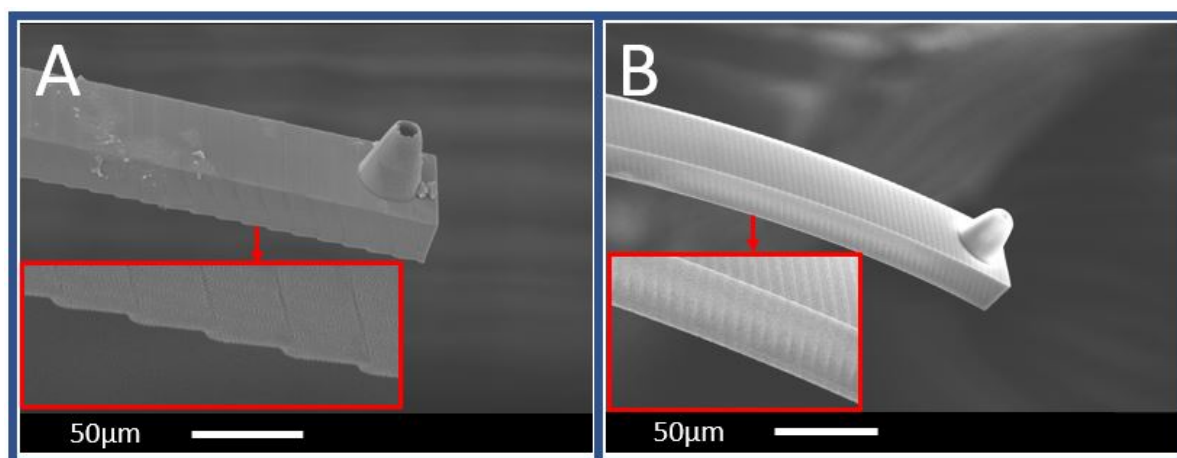


Figure B.8.33: SEM image of cantilevers printed with various block sizes. **A)** $10\ \mu\text{m}$ block width and $2\ \mu\text{m}$ overlap. Sawtooth on the bottom of the cantilever is clearly visible. **B)** $4\ \mu\text{m}$ block width and $2\ \mu\text{m}$ overlap. No clear sawtooth.

The following parameter to optimize is the angle between the blocks. This angle influences the sawtooth and the bending of the cantilever. To test this, arrays of cantilevers were printed with various angles and settings. Test structures were printed with up to five cantilevers. This allowed for easy comparison between parameters. These arrays can be seen in figure B.8.34.

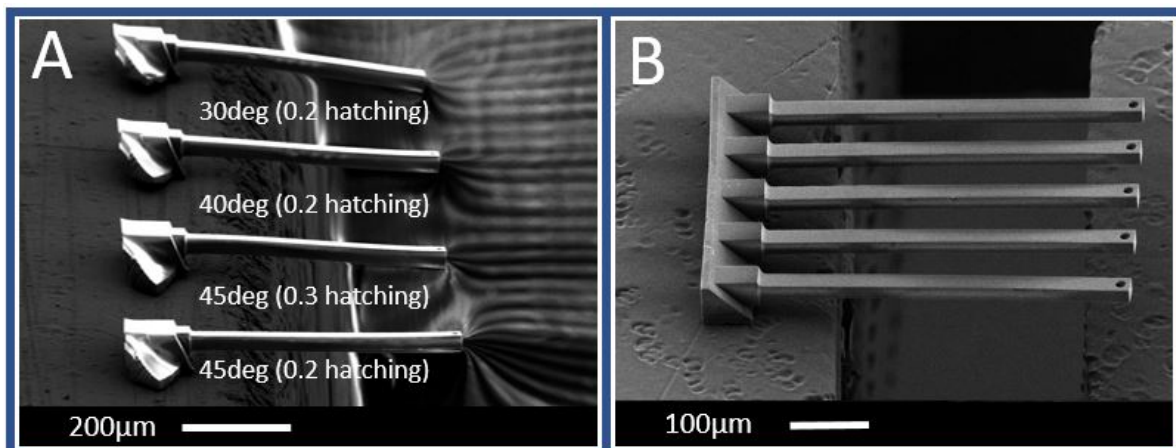


Figure B.8.34: SEM image of cantilever block splitting angle test print. **A)** Cantilevers printed with various block shear angles. The cantilever with 45-degree angle with $0.2 \mu\text{m}$ hatching was assessed as the straightest. **B)** Repetition print of five cantilevers with 45-degree angle with $0.2 \mu\text{m}$ with optimized dosage. All cantilevers are straight.

Larger shear angles have not been tested, but they might give different results. To create a smoother surface of the cantilever, one can print the bottom part of the block first and then print the same part again, overlapping with the first print before continuing with the rest of the block. This results in a smoother bottom of the cantilever, as it cannot bend upwards.

With a constant block splitting, cantilevers were printed with different doses (block angle of 35 degrees, as the dose and angle optimization was done in parallel on the same substrate). Too low a dose resulted in more bending of the cantilever after development (swelling). Too high a dose, on the other hand, resulted in bubble formation in the cantilever, sometimes even preventing printing. Figure B.8.35 shows the effect of too low a dose on the left and a better dose on the right. Note that for these cantilevers, the block dimensions were not yet optimized.

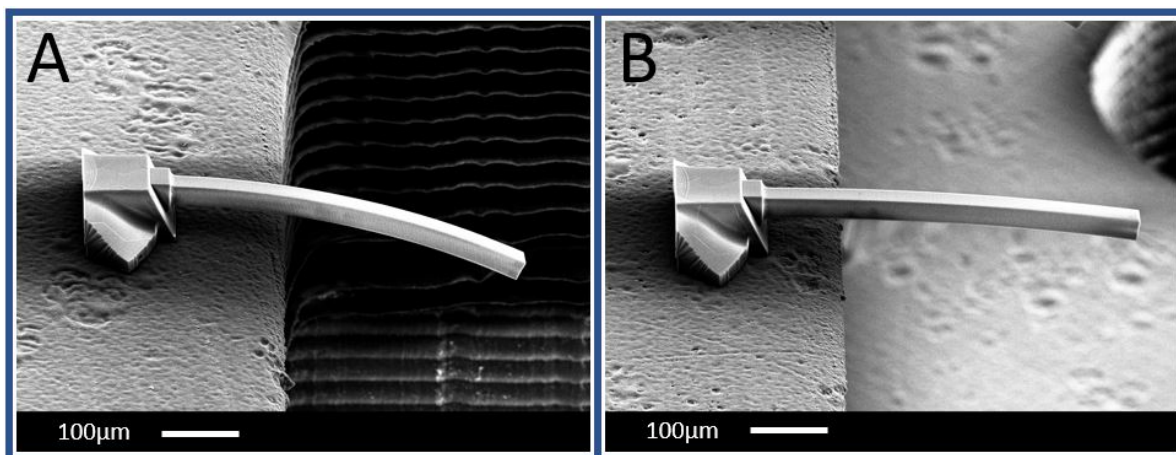


Figure B.8.35: SEM image of cantilever dose test. **A)** Cantilever printed with 32.5mW laser power (65%) and 60 mm/s scanning speed. **B)** Cantilever printed with 32.5mW laser power (65%) and 40 mm/s scanning speed. Straighter than figure A.

As mentioned earlier, too high a dose can result in poor print quality. An example of printing with too high a dose can be seen in figure B.8.36. The bubbles and holes would lead to leaks of the print.

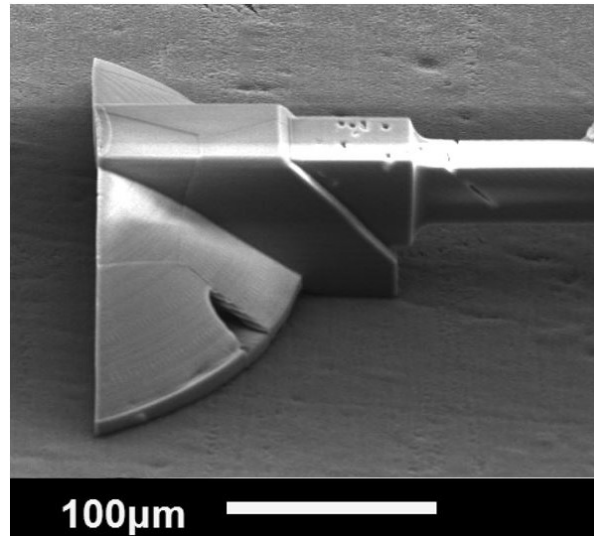


Figure B.8.36: SEM image of a cantilever printed with a too high cantilever dose, resulting in bubble formation and holes in the print.

In the case of cantilevers that were printed with the laser only scanning upwards, a lateral deflection of the cantilever was visible in some prints (bending in the scanning direction). This was prevented by printing upwards and downwards (alternating). This can be corrected by the hatching offset or changing the scanning direction into alternating mode in Describe.

B.8.2. 2PP print results

The final printing results of the cantilever with optimized parameters resulted in straight cantilevers with sufficient surface quality for the reflection of the AFM laser (after coating with gold). Figure B.8.37 shows that the cantilevers can be printed successfully.

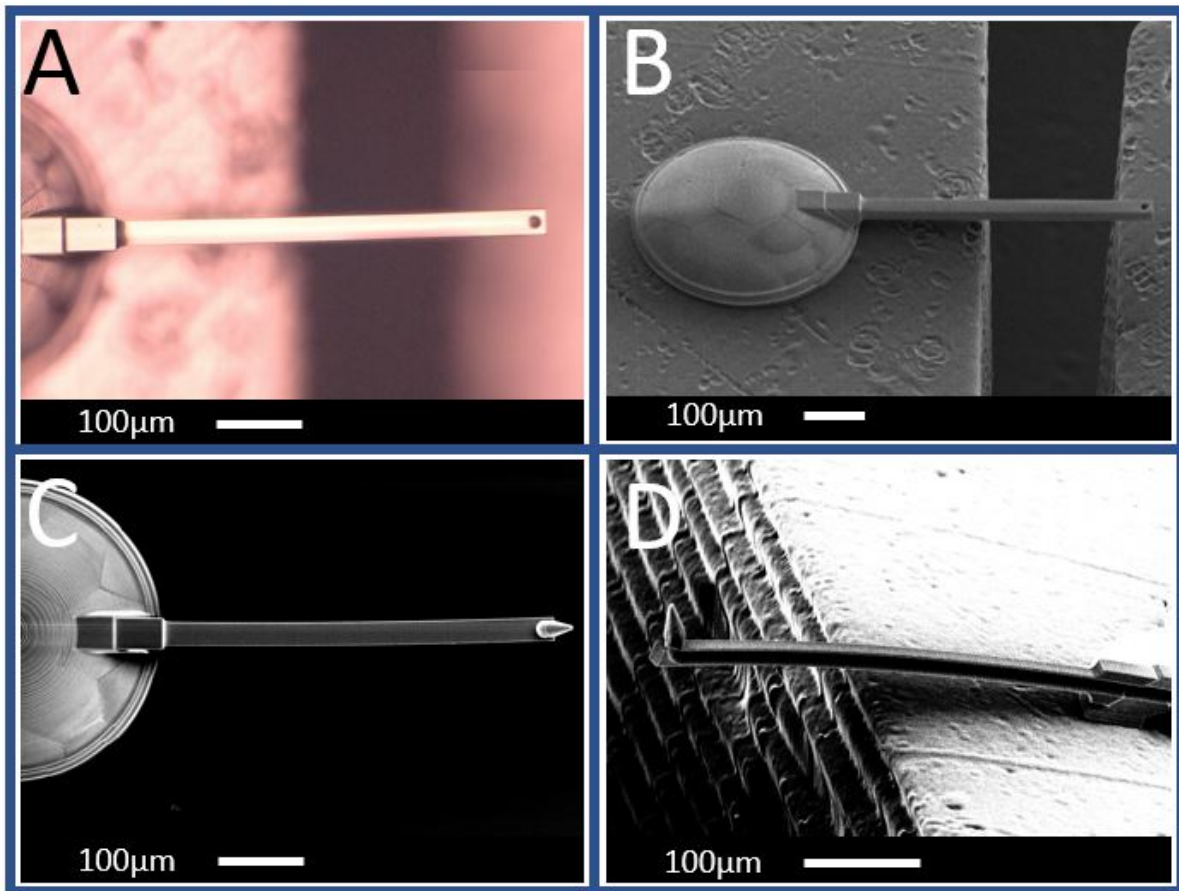


Figure B.8.37: Cantilever printing results from various views. **A)** Microscope image of tipless cantilever, **B)** SEM image of tipless cantilever, **C)** SEM image of top view of sharp-tipped cantilever **D)** Cantilever cut in half, SEM image showing the channel

Figure B.8.38 shows the channel in the cantilever (cross-section).

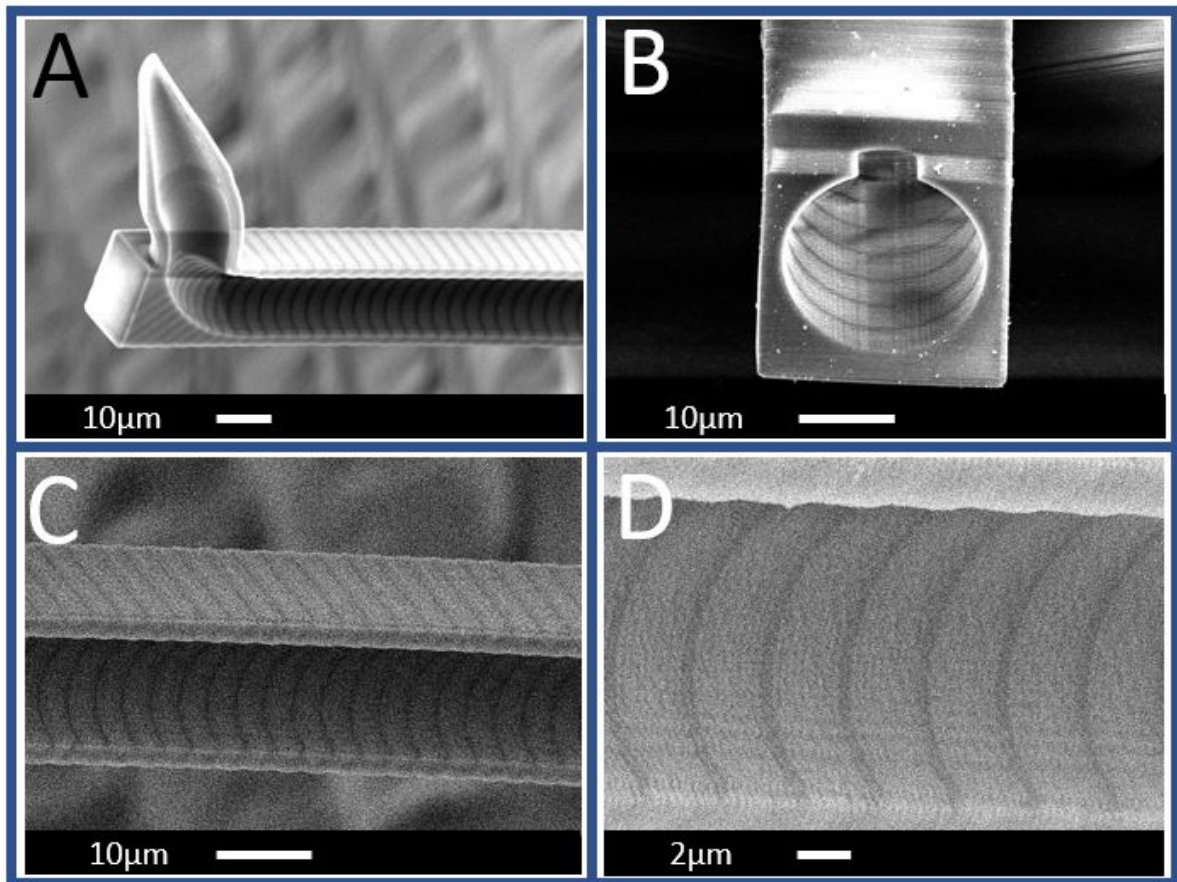


Figure B.8.38: Various views of cantilever, of which only one half was printed. **A)** SEM image of half a cantilever at tip region (side view at an angle), **B)** SEM image of half a cantilever front view (aborted during print), **C)** SEM image of half a cantilever at the middle of the cantilever (side view), **D)** Same region as C but larger zoom.

Figure B.8.39 shows that the length of the cantilever is slightly affected by shrinkage (2.2%). This shrinkage would result in a stiffness of 1.83 N/m instead of the 1.71 N/m, which is closer to the experimental results.

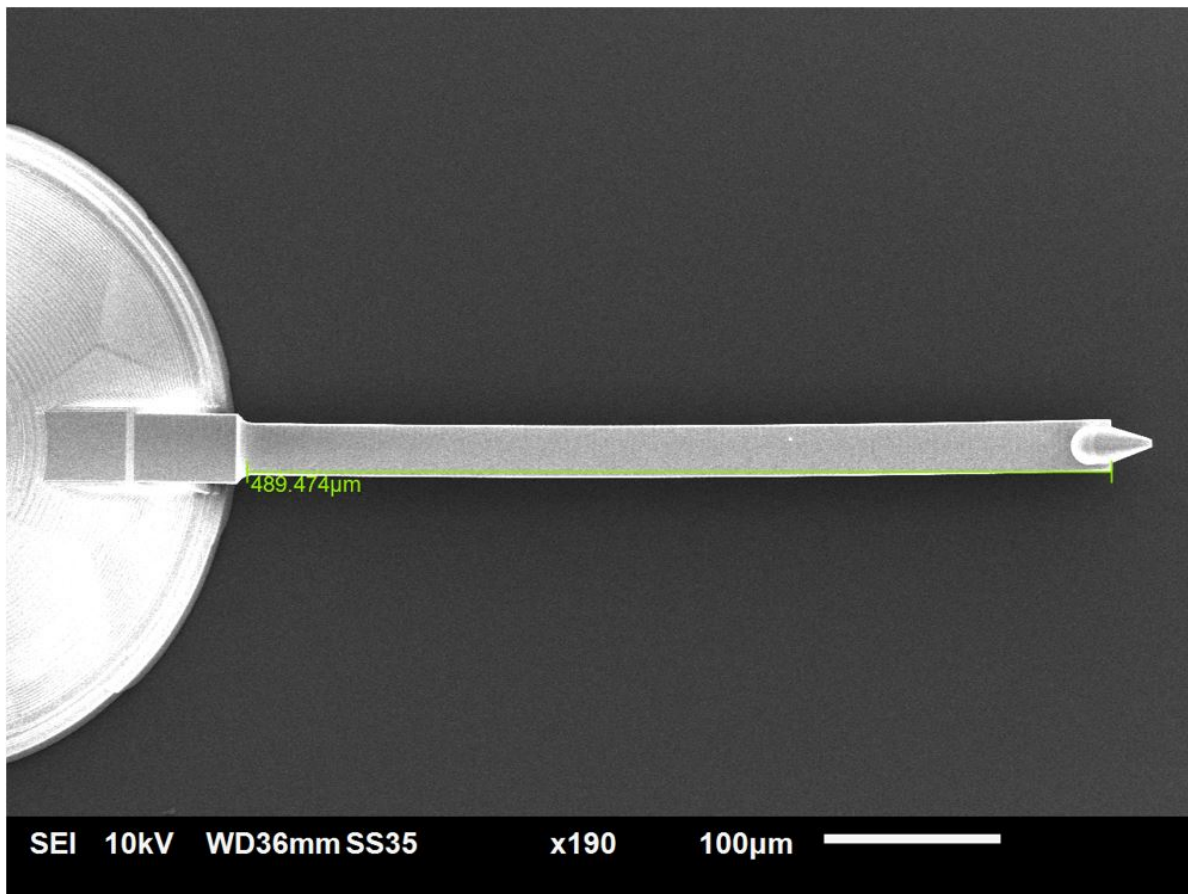


Figure B.8.39: Measured length of cantilever, influenced slightly by shrinkage (SEM image).

Cantilevers with a longer base were printed, as shown in figure B.8.40. The total length of the base and cantilever was 950 μm, which resulted in the effective part of the cantilever (500 μm long) not being above the substrate at all. For future research, printing cantilevers at an angle can be investigated.

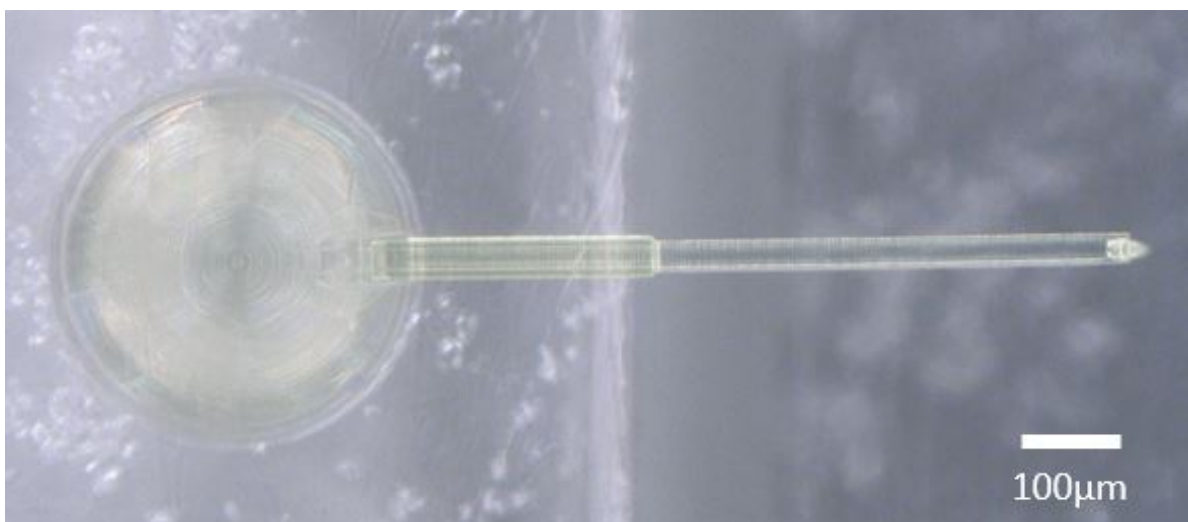


Figure B.8.40: Cantilever with longer base, Fun cantilever protrudes from substrate (total length including base = 950 μm).

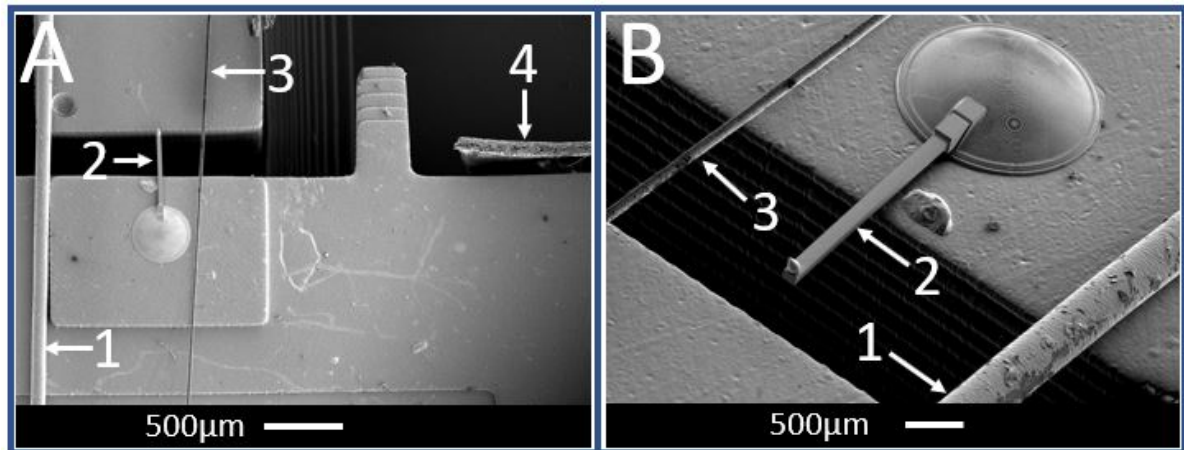


Figure B.8.41: SEM image of 2PP cantilever with two canine hairs and side view of an A4 sheet of paper. **A)** Top view, 1 = Canine hair with $89\mu\text{m}$ diameter (Friesian Stabyhoun, Puck), 2= Cantilever, 3 = Canine hair with $20\mu\text{m}$ diameter (medium poodle, Loeki), 4 = Edge of a sheet of A4 paper (80 g/m^2 , $90\mu\text{m}$ thick), **B)** Isometric view

B.9. Tip

Optimizing the tip geometry for different types of cell research could be a thesis on its own. Unlike the dome and the cantilever, the printing of the tip did not require block splitting, as the dimensions remain within the printing field of the objective. However, the tip has the smallest features of the entire 2PP print. To obtain the smallest possible features and create a smooth outer surface for the tip, the main optimization was done in Describe by altering the hatching and slicing distance. The dose also affected the quality of the print (feature size and bubble formation). In this section, the main focus will be on the Describe settings and dose tests for the tip.

B.9.1. Design

The design of the tip depends entirely on the approach chosen to remove the nucleus. This approach determines the tip geometry and position of the aperture on the tip (at the apex, next to the apex, at the front of the tip, etc.). For this research, a tip was designed with the aperture at the front of the tip so that one can move the tip towards the nucleus and start aspirating. Tilting the tip forward in the design makes it visible from above (instead of being hidden behind the cantilever). This allows for visualization of the tip and the nucleus at the same time during experiments. Figure B.9.42 shows a schematic top view of the tip with the aperture and the nucleus. By moving the tip towards the nucleus, the aperture can be aligned with it.

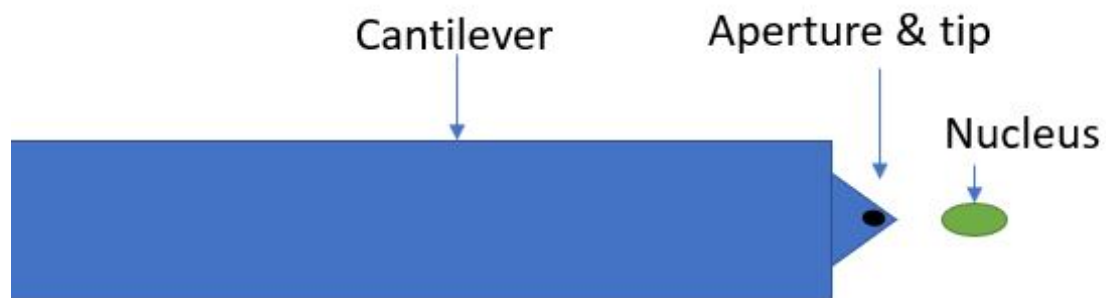


Figure B.9.42: Schematic top view of a tip on a cantilever. As the tip is at an angle compared to the cantilever, it protrudes and is visible from the top during experiments.

For the puncture, one wants the tip to be as sharp as possible (lower puncture force). But the aperture must be close to the tip, as the cell's height is limited (the aperture must preferably be entirely inside the cell). Different tips were designed in the course of this work. The tip used to remove the nucleus is mainly discussed in this appendix. Figure B.9.43 shows different views of the CAD model of that tip.

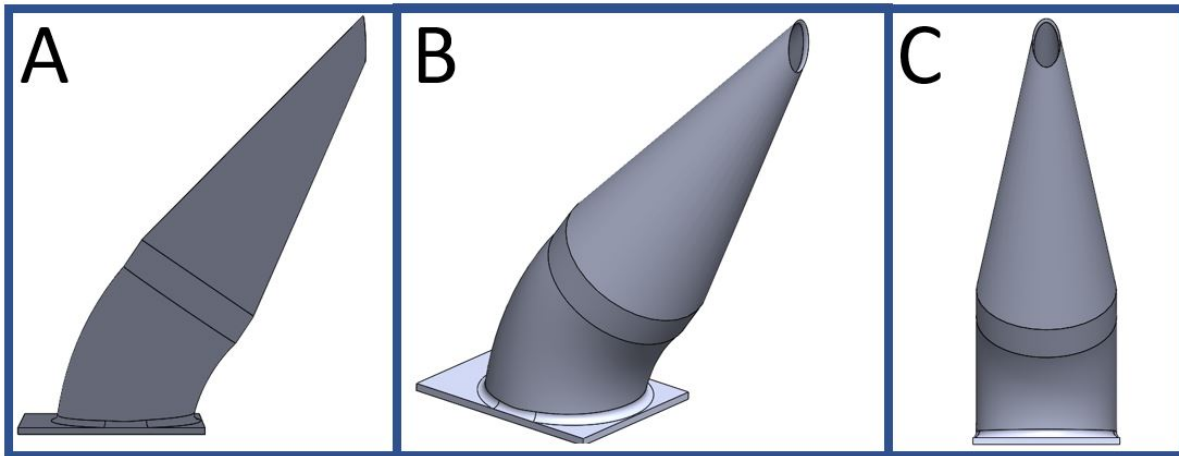


Figure B.9.43: CAD drawing of tip used for nucleus removal. **A)** Side view of tip, **B)** Isometric view of tip, **C)** Front view of tip.

Figure B.9.44 to B.9.47 show the drawings and dimensions of the tip. In these figures and in the CAD drawings in figure B.9.43 a baseplate for the tip can be seen. This baseplate is printed inside the top layer of the cantilever to ensure a good connexion.

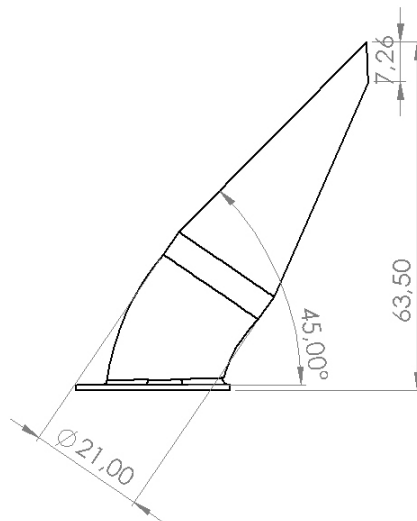


Figure B.9.44: Side view drawing of the tip. Dimensions in micrometres [μm].

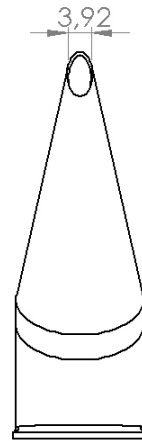


Figure B.9.45: Front view drawing of the tip. Dimensions in micrometres [μm].

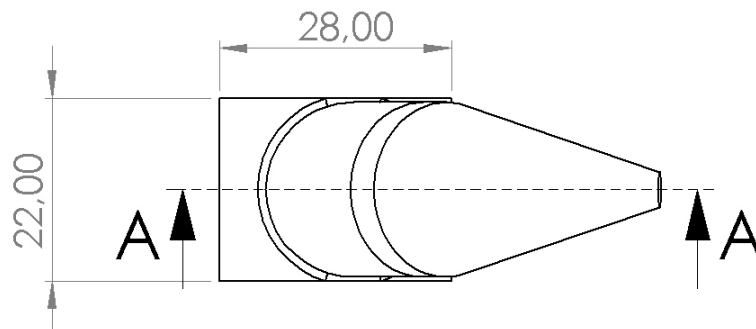
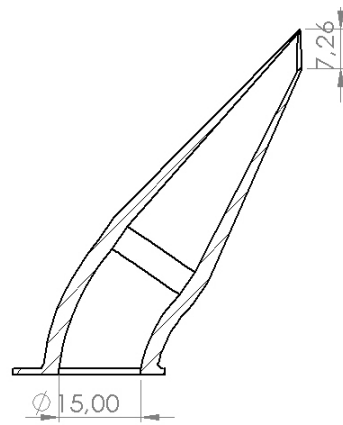


Figure B.9.46: Top view drawing of the tip. Dimensions in micrometres [μm]. Cross-section A-A in figure B.9.47



SECTION A-A

Figure B.9.47: Cross-section drawing of the tip. Dimensions in micrometres [μm]. Cross-section A-A as indicated in figure B.9.46

B.9.2. Describe for the tip

The tip was designed in Solidworks to be infinitely sharp. However, Describe slices the tip into layers. By reducing the size of these layers, the tip will have a better resemblance to the design. By adding a single contour to the print, one can reduce the surface roughness.

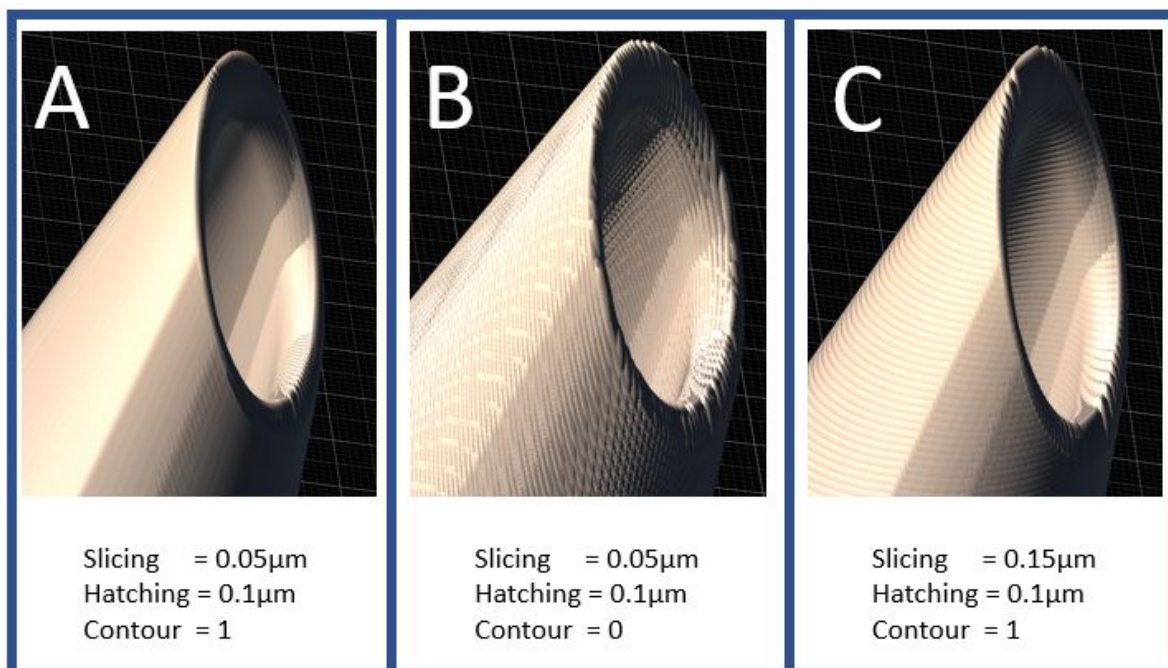


Figure B.9.48: Tips with various settings in Describe. The smaller the hatching and slicing, the smoother the surface and the smaller the feature sizes. Adding a contour layer smoothens the tip even further. **A)** and **B)** show the difference between a contour and no contour respectively. **C)** shows the result of increasing the slicing distance. Scale not relevant (illustration purpose).

A smaller slicing results in a longer print. A printing comparison should be made to see if the smoothness and resolution is worth the additional print time.

The effects of slicing are even more noticeable with a different design. Figure B.9.49 shows a comparison between the print result, the CAD model and the Describe slicer. The sharp tip becomes blunt due to the slicing.

After the cantilever has finished printing, the objectives moves down slightly before the tip starts to print. This causes slight bending of the cantilever, which is restored after a few seconds. Therefore, a wait command was used to allow the cantilever to bend back before the tip is printed.

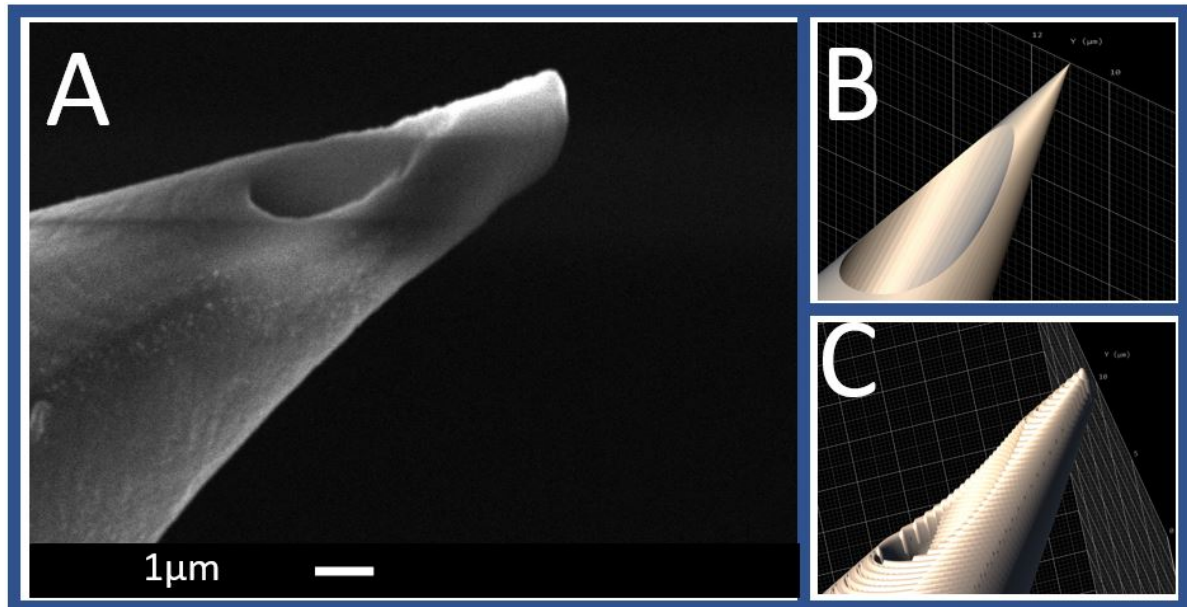


Figure B.9.49: Comparison between print, model and describe. **A)** The printed tip (SEM image), **B)** The CAD model, **C)** Sliced model in Describe. Figure B and C illustrate the effect of slicing, making the tip less sharp. Scale not relevant (illustration purpose).

B.9.3. Dose test for the tip

The laser power and the scanning speed also have a considerable influence on the printing result of the tip. To test a wide range of doses (varying powers and scanning speed), an array of tips were printed on 2PP printed pedestals to mimic printing on a cantilever.

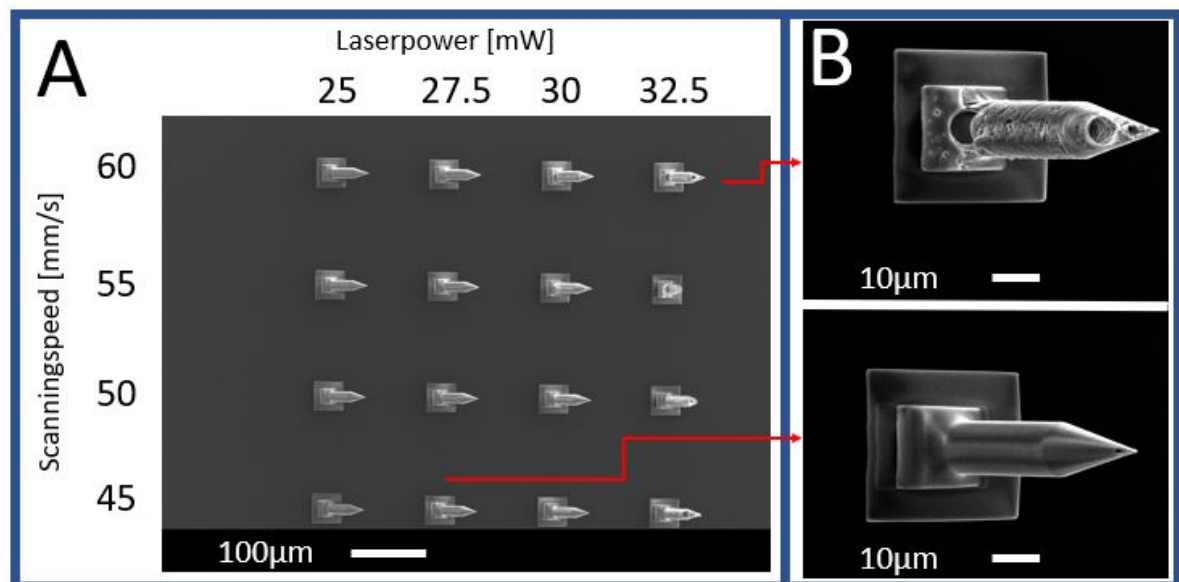


Figure B.9.50: Array of tips on pedestals on fused silica substrate (SEM image). **A)** Overview of the dose test, **B)** Highlight of two prints. Top = too high dose resulting in a bad print, Bottom = proper dose resulting in a good print.

It is clear that a correct dose is of paramount importance. Smaller features could be achieved with lower doses. Repeated scanning of the same area with low laser powers and ending with a single voxel point can decrease the

feature sizes even further, but this has not been tested.

B.9.4. Print results

The resulting tips can be seen in figure B.9.51 to B.9.53.

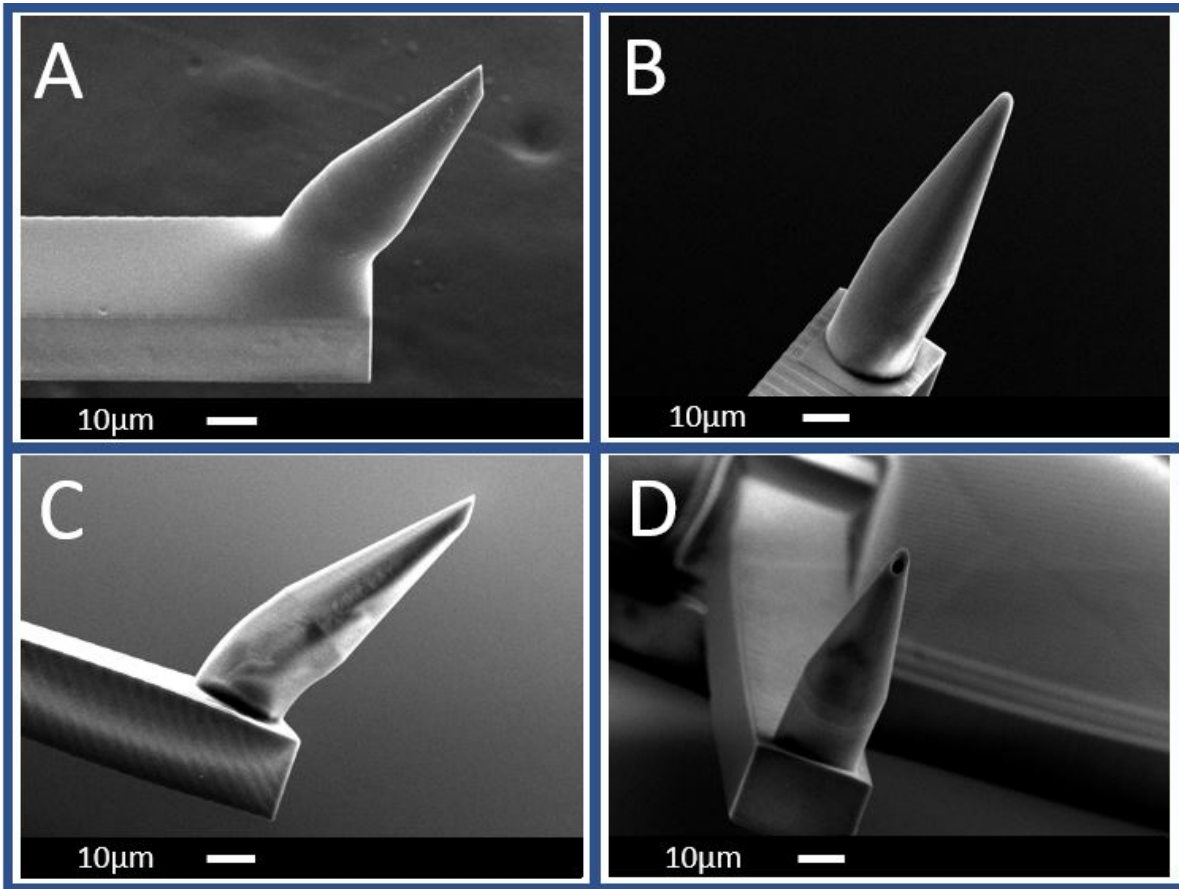


Figure B.9.51: SEM images of tips from different views. **A)** Side view, **B)** Back view **C)** Side view at angle **D)** Front view

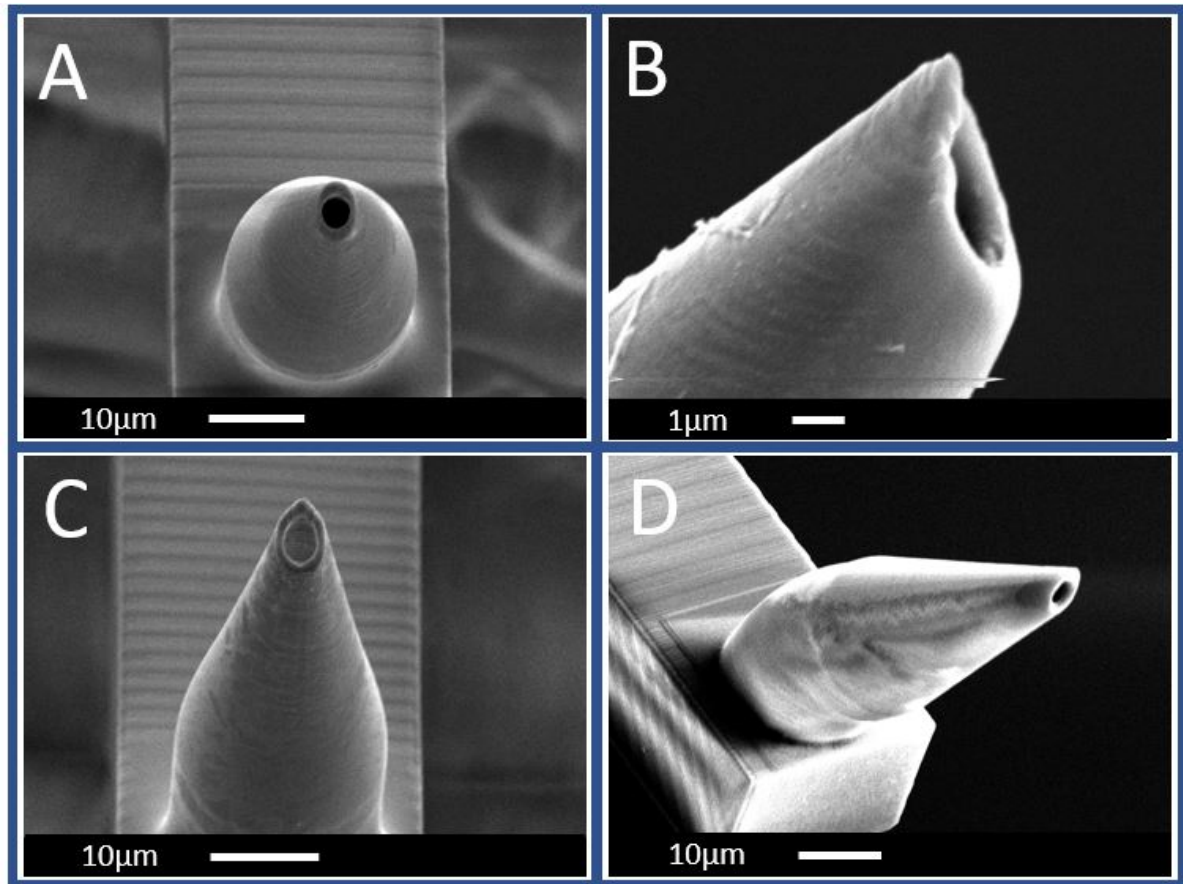


Figure B.9.52: SEM images of tips with the aperture from different views. **A)** Front view at 45 degree, **B)** Side view **C)** Front view at 60 degrees (sharper point) **D)** Isometric view

It is important to note that shrinkage of the aperture was observed for almost all prints (compared to the design). On average, the diameter of the aperture decreased with $1 \mu\text{m}$. This should be taken into account for designs for future prints.

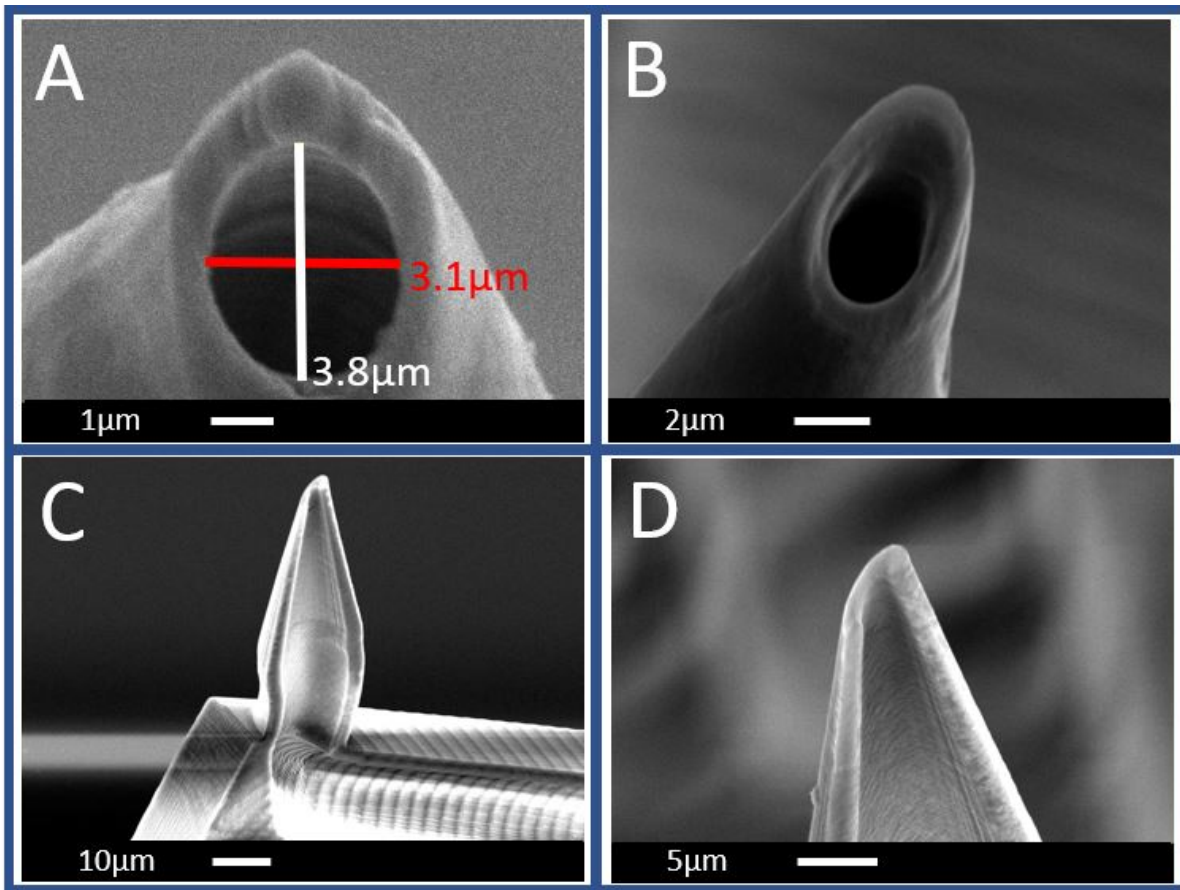


Figure B.9.53: SEM images of apertures and cross-section of tips from different views. **A)** Front view of aperture, **B)** Front view with tilt, **C)** Side view of cross-section of tip, **D)** Side view of cross-section near the aperture

Figure B.9.54 shows the smallest achieved tip diameter. Smaller tip diameters can be achieved by changing the design and print parameters (e.g. scan tip multiple times with a small dose, or make sure that the tip ends in a single voxel which results in a tip radius with the curvature of the voxel). FIB can also be investigated for reducing the tip size, as used by Yum et al. [4].

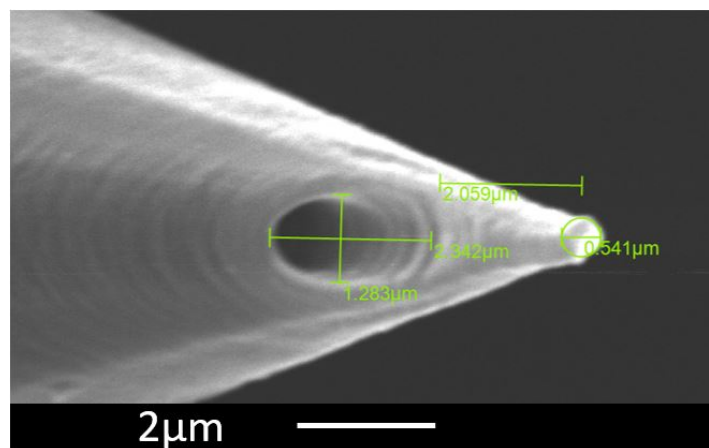


Figure B.9.54: SEM images achieved tip dimensions

Figure B.9.55 shows a tipless cantilever used for the cell adhesion experiments (aperture diameter of $7\mu\text{m}$).

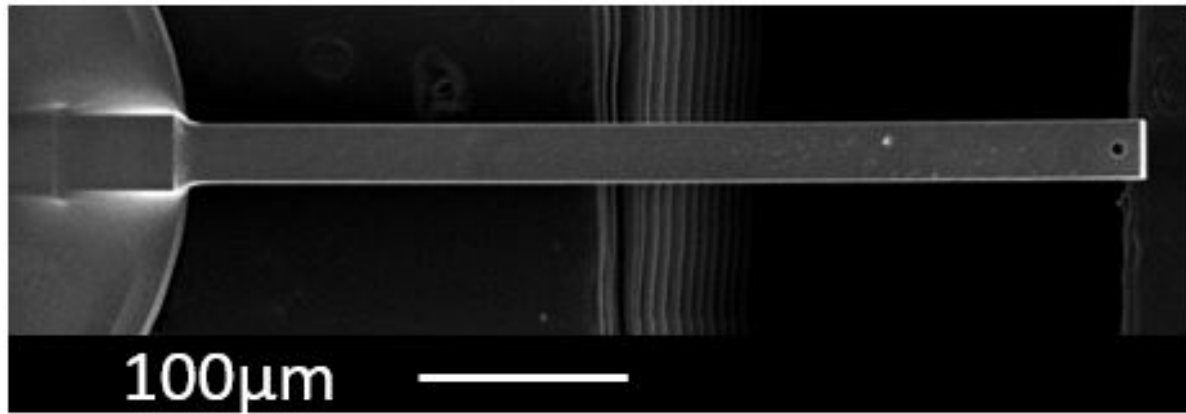


Figure B.9.55: SEM images with tipless cantilever for adhesion experiment with a $7\mu\text{m}$ aperture

The forward tilt of the tip meant that it was clearly visible from above while mounted on the AFM. This allows simultaneous visualisation of the nucleus and the tip. Figure B.9.56 shows that both the nucleus and the tip can be seen simultaneously during an experiment. If it is necessary that the tip is not tilted forward, markers can be printed on the side of the cantilever to align the tip with respect to the cell properly. This could be helpful in adhesion studies.

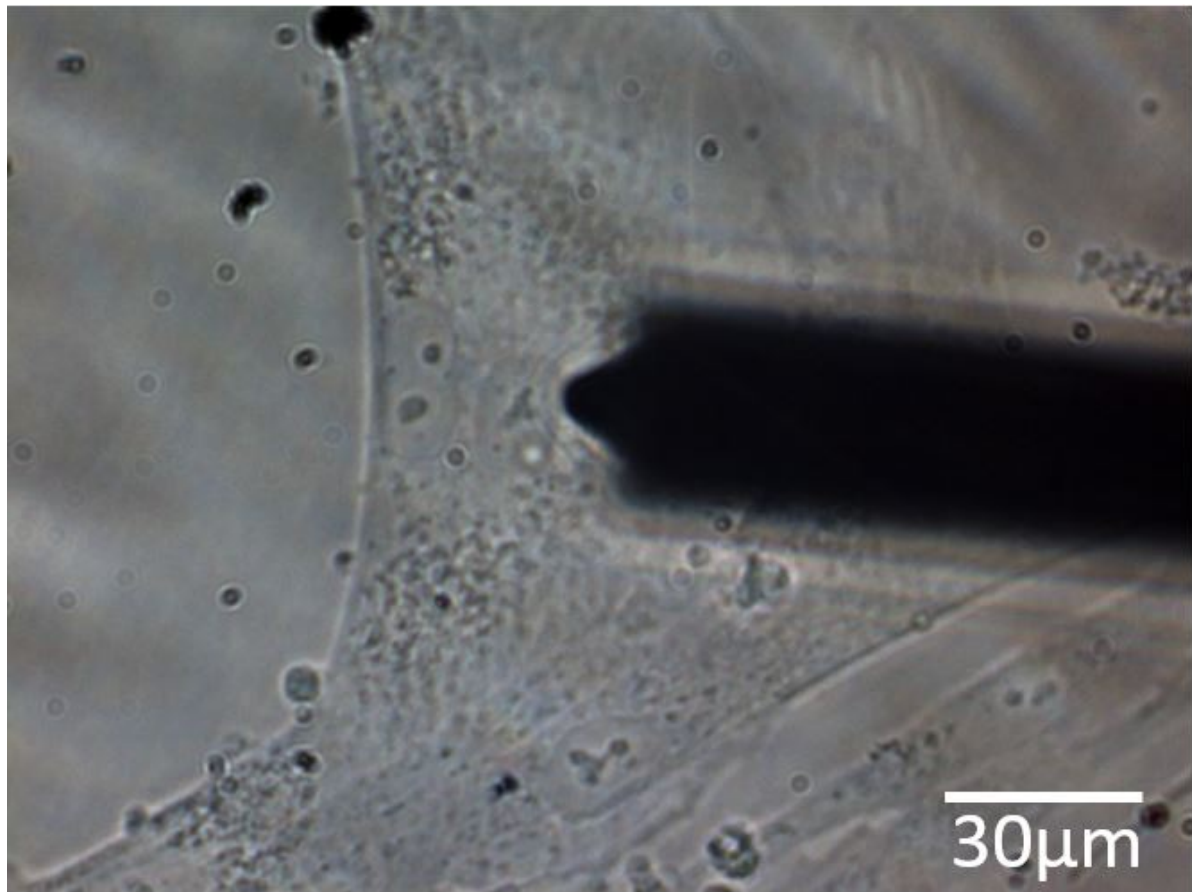


Figure B.9.56: Tip of the cantilever visible during an experiment on the AFM. The nucleus and tip are visible at the same time.

B.9.5. Other tip ideas

The smallest aperture achieved had a diameter of $2\ \mu\text{m}$ in the design, but was printed as $1\ \mu\text{m}$ (fig. B.9.57). Unfortunately, the cantilever was clogged due to insufficient development and could not be used.

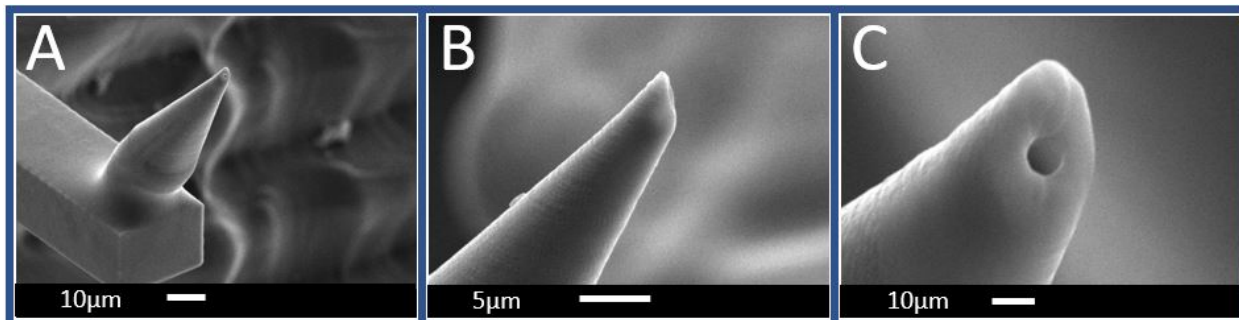


Figure B.9.57: SEM images of a tip with the smallest printed aperture. **A)** isometric view of the tip **B)** Side view, **C)** Zoom in at the aperture

Many other tip geometries are possible. For example, pyramidal or cylindrical tips can be printed. Three suggested tips that can be explored in future projects are shown in figure B.9.58. The tip in figure B.9.58A can be used to study the adhesion of cells to a substrate. The slope of the surface around the aperture results in good contact with the cell (as the holder is tilted 10 degrees). Figure B.9.58B shows an aperture that has a larger width than its height. As a result, the entire aperture to be inside the cell to perform the nucleus aspiration.

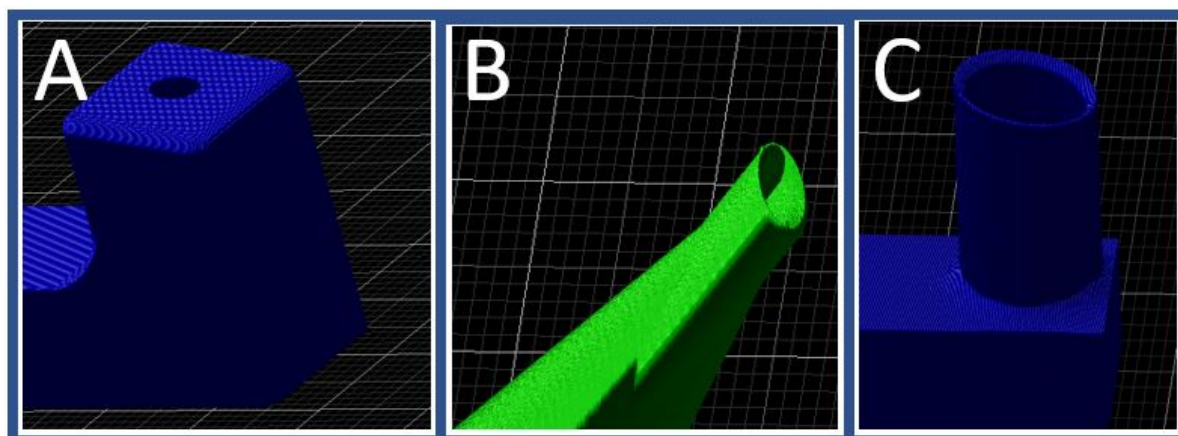


Figure B.9.58: Alternative tip geometries, **A)** Tip for cell adhesion studies. Surface around the aperture can be tilted for better contact, **B)** Aperture that is wider than its height, **C)** Tip that seals the nucleus in a membrane vesicle.

Figure B.9.58C is a tip that uses an entirely new approach. When it is aligned with the nucleus, it is moved downwards until the sides hit the substrate. This means that the upper and lower membranes of the cell are pushed together and fuse. This encloses the nucleus in a membrane vesicle and protects it during aspiration. This allows for minimally invasive nucleus removal. The proposed tips have been printed but have not been tested on cells.

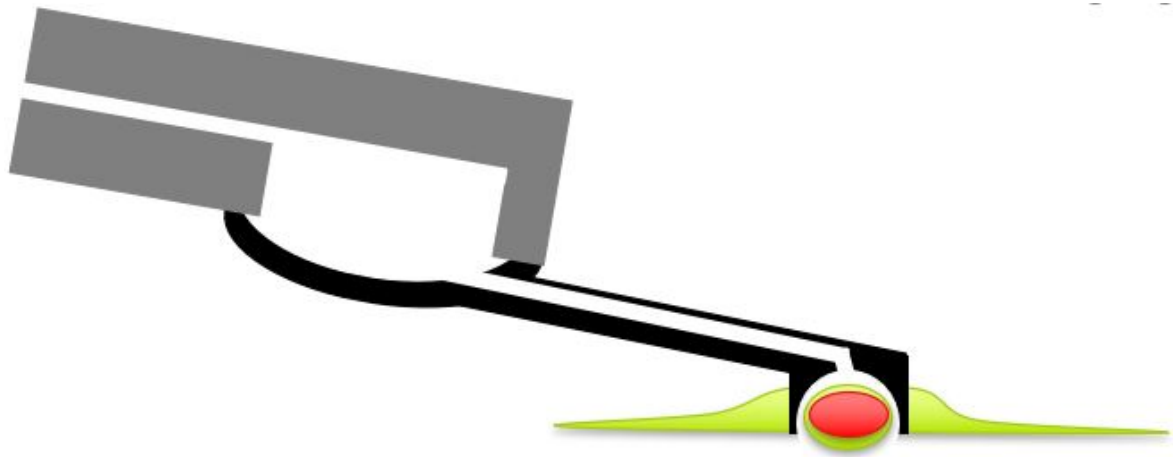


Figure B.9.59: Schematic drawing of sealing a nucleus (red) in a vesicle (cell=green). Figure B.9.58C shows the tip that could be used. By merging the top and bottom membrane, a protective vesicle is formed around the nucleus for transport.

Bifurcated needles can be printed for the precise handling of liquids. These needles, as seen in figure B.9.60, can hold a drop of liquid by their capillary forces. When printed at the microscale, it could be used to manipulate small amounts of liquid. Printed on a DLP print, it could even be used for manual liquid dispensing.



Figure B.9.60: Bifurcated needle which could be printed with at microscale for precise liquid handling. [22]

To create much sharper tips, e.g. for AFM imaging, it would be possible to create a tip of which a part of the tip can be broken off. The remaining part of the tip can then be sharper than printed (as it can have a sharp fracture line). This requires the development of a new design and a tip breaking protocol. Another possibility is to grow a tip directly onto the cantilever using a technique other than 3D printing. These possibilities can be explored in the future.

B.10. Overview of final print parameters

A total of 25 devices were printed for the cell experiment. Of these devices, one was clogged before the experiment began, and one had leaks originating from the channel of the DLP print. Some devices clogged during the experiments or broke due to human error. As can be concluded, all modules have their own optimal parameters depending on geometry, requirements, and boundary conditions. Figure B.10.61 shows the laser power and scanning speed of the different parts of the print. There are only minor differences in the laser power, but the differences are greater in the scanning speed.

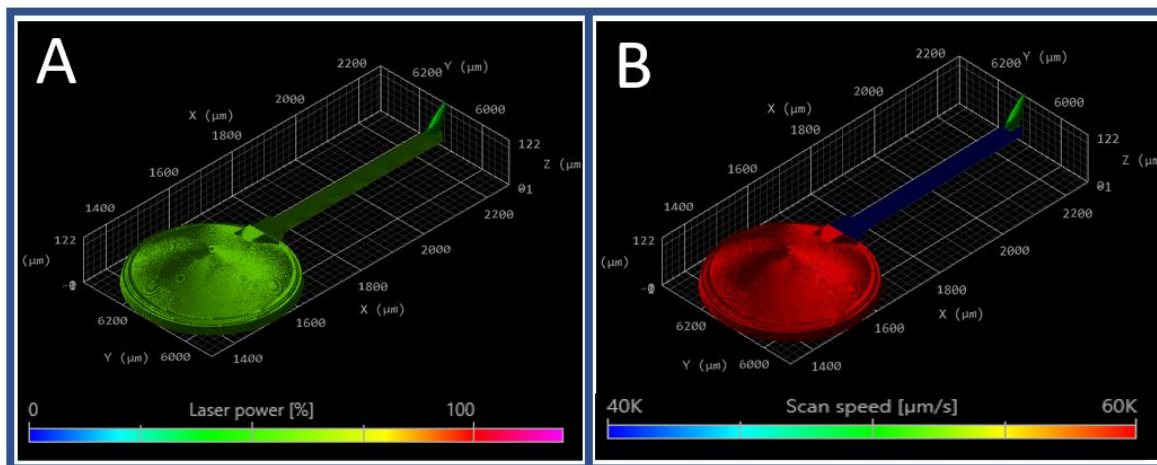


Figure B.10.61: Laser power and scan speed visualized in Describe. **A)** Laser power visualization, **B)** Scanning speed visualization

The used parameters for successful prints with IP-Dip and the 63X lens on 3DM Tough Clear substrates are listed below in table B.1.

Parameter [unit]	Dome	Cantilever	Tip
Laserpower [mW]	31.25	30	25
Laserpower [%]	62.5	60	50
Scanningspeed [mm/s]	60	40	50
Slicing distance [μm]	0.35	0.2	0.05
Hatching distance [μm]	0.25	0.2	0.1
Contour count	3	-	1
Contour distance [μm]	0.15	-	-
Galvoacceleration [V/ms^2]	6	6	2
Blocksplitting X-Y-Z [μm]	124 x 125x 69	4 x 81 x 41	-
Blocksplitting offset X-Y-Z [μm]	13 x 0 x 23*	-1 x -21 x 0	-
Block splitting shear angle [deg]	20	45	-
Blocksplitting overlap XY [μm]	2	2	-
Blocksplitting overlap Z [μm]	1*	1	-
Hatchlines	oneway	alternate	oneway
Find interface at [μm]	8	-	-
Hatching angle [deg]	90	0	90
Hatching angle offset [deg]	90	0	90

Table B.1: Parameters for successful prints with IP-Dip and the 63X lens on 3DM Tough Clear substrates. * = second layer of blocks moved 1 extra micron down into first layer of blocks by altering add z drive position in data file

B.11. Developing

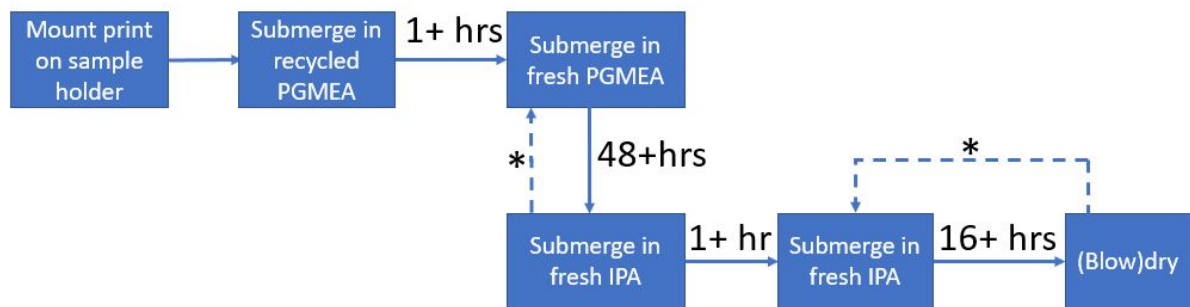


Figure B.11.62: 2PP development workflow. *Repeat previous step for couple of hours if required

The development of the prints is a time-consuming task. The main problem is the resin inside the channel of the cantilever. To remove this resin, PGMEA has to diffuse into the channel. This takes a long time (48+ hours), depending on the dimensions of the channel. During development, the PGMEA must be refreshed to achieve greater differences in concentration. Heating or stirring the PGMEA or agitating it in another way can speed up this process. There are three ways to agitate the PGMEA: Ultrasonic cleaner, sample shaker (e.g. IKA-VIBRAX-VXR) and magnetic stirrer. Heating increases the diffusion rate but can deform the DLP print. Ultrasonic cleaning damaged the cantilevers because it was too rough. The magnetic stirrer did not cause any problems, but it was not clear whether it reduced the development time. The shaker was not tried. The development workflow is shown in figure B.11.62 Figure B.11.63 shows a holder which was used to hold the three interface holders during the development.

Flushing the channel with PGMEA by connecting a syringe to the interface can reduce the development time to less than an hour, but requires manual labour and one risks damaging the print. A syringe pump could prevent damage, and more than one interface could be connected simultaneously via tubing couplings by using the microfluidic coupler developed for this research to connect tubing.



Figure B.11.63: 2PP development sample holder with three interface holders.

B.12. Coding

After slicing the model, six files are stored in the folder with the .STL file (shown in figure B.12.64). After rendering the print, an additional folder with called “gwlc” is added.







 xyzCalibration_cube_files	21-8-2021 11:34	Bestandsmap
 xyzCalibration_cube.recipe	21-8-2021 11:34	RECIPE-bestand
 xyzCalibration_cube.stl	2-2-2016 23:11	3D Object
 xyzCalibration_cube_data.gwl	21-8-2021 11:34	GWL document
 xyzCalibration_cube_job.gwl	21-8-2021 11:34	GWL document
 xyzCalibration_cube_job.recipe	21-8-2021 11:34	RECIPE-bestand

Figure B.12.64: Files generated by Describe

The “.recipe” files can be used for future prints to automatically set the Describe slicing settings to the same values as before.

The file with the extension “_data.gwl” lists the blocks to be printed and the required distance the stage must travel between two blocks. In this file, two things have to be changed for the printing of the dome. First, at the beginning of the file is the “FindInterfaceAt \$interfacePos” command. For the dome, the printer must find the interface next to the aperture. Therefore, it must move to a location, find the interface and move back to the centre of the aperture. An example is shown in figure B.12.65A, with the added commands highlighted in red. Note that if block splitting is used, the “FindInterfaceAt \$interfacePos” command may be present in several places in the .data file. These need to be removed by removing all of them except for the first one. For the cantilever and sharp tip, one should remove the “FindInterfaceAt \$interfacePos” command everywhere in the file.

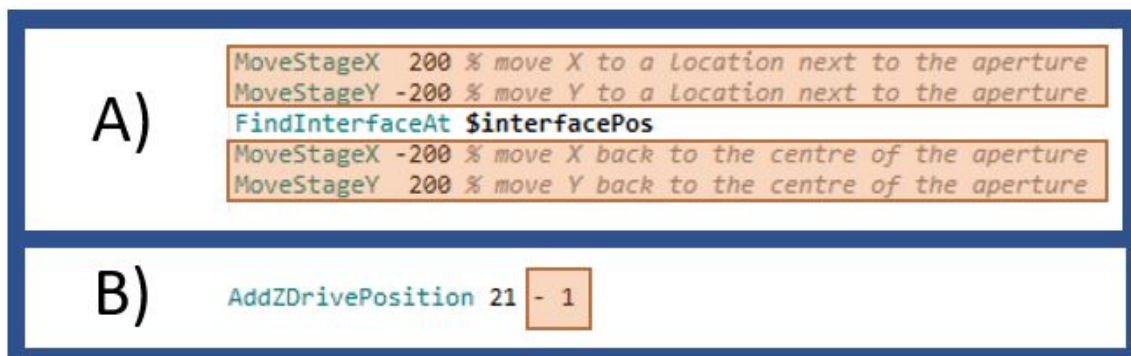


Figure B.12.65: Additions to data file marked in red. **A) and B)** explained in text

One more thing needs to be changed in the data file of the dome. The first “AddZDrivePosition” command (after the first blocks of the ring have been printed) should be changed to print 1 to 2 microns deeper into the previous row of blocks. To do this, subtract 1 or 2 microns from the value in the code shown in figure B.12.65B.

If there are unnecessary “MoveStage” commands at the beginning of the data file, they can be removed (this has to do with the (0,0) point in the Describe slicer).

After all parts have been sliced (into the same folder), each part has its own files in the folder. To combine them, a new job file is created in Describe.

First, add the system initialization part (can be copied from another job file). No changes are required to this part. Figure B.12.66 shows the initialization parameters in the red box. The blue field contains the depth at which the interface should be found and the positioning commands to align the dome with the aperture. This part is only required for the dome. The green field contains the print parameters, the print data and the commands to move the stage. These movement commands move the stage to the position where the next part is to be printed (found by rendering in Describe). The green part should be repeated for each part of the print with its own optimal settings.

```

% System initialization
InvertZAxis 1

% Writing configuration
GalvoScanMode
ContinuousMode
PiezoSettlingTime 10
GalvoAcceleration 6
StageVelocity 200

% Scan field offsets
XOffset 0
YOffset 0
ZOffset 0

% Writing parameters
PowerScaling 1.0

%%%%%%%%%%%%%%%%%%%%%%%%%%%%%%%%%%%%%%%%%%%%%%%%%%%%%%%%%%%%%%%%%%%%%%%%

var $interfacePos = 8           %% The print will start 8 microns into the found interface (only dome)
StageGotoX -5000               %% Move to the desired X coordinate for the center of the print
StageGotoY 2500                %% Move to the desired Y coordinate for the center of the print

%%%%%%%%%%%%%%%%%%%%%%%%%%%%%%%%%%%%%%%%%%%%%%%%%%%%%%%%%%%%%%%%%%%%%%%% Repeat from here to add other parts
GalvoAcceleration 6           %% Set the galvoacceleration for each part seperately

var $baseLaserPower = 62.5     %% Laserpower for the baselayers (number of layers set during slicing)
var $baseScanSpeed = 60000     %% Scanningspeed for the baselayers

var $solidLaserPower = 62.5    %% Laserpower for the solid
var $solidScanSpeed = 60000    %% Scanningspeed for the solid

var $contourLaserPower = 62.5  %% Laserpower for the contour
var $contourScanSpeed = 60000  %% Scanningspeed for the contour

include xyzCalibration_cube_data.gwl %% includes the blocks and prints them

MoveStageX -50                %% move to the location where the cantilever print needs to start (align using render)
MoveStageY 25                 %% move to the location where the cantilever print needs to start (align using render)
AddZDrivePosition 30          %% move to the location where the cantilever print needs to start (align using render)

%% repeat from galvoacceleration for other parts of the print

```

Figure B.12.66: Describe Job file. The red box marks the system initialization, this part is only required at the beginning of the print. The blue part contains the initial positioning commands (centre with aperture) and interface finding parameter. The blue part is only required for the dome (in combination with the green part) The green part contains the printing parameters, calls the data file and moves to the position for the next part of the print. The green part should be repeated for every part of the print.

B.12.1. Galvo acceleration

By changing the galvo acceleration, the printing time could be reduced considerably. The printing time is highly dependent on the galvoacceleration, printing speed and the geometry. It is advisable to optimize the galvo acceleration for each project. The maximum galvoacceleration is around $10\text{V}/\text{ms}^2$. Figure B.12.67 shows the decrease in print time at higher galvo accelerations. It also shows that the print time estimation is better at higher galvoaccelerations. Mainly valid for the 63X objective.

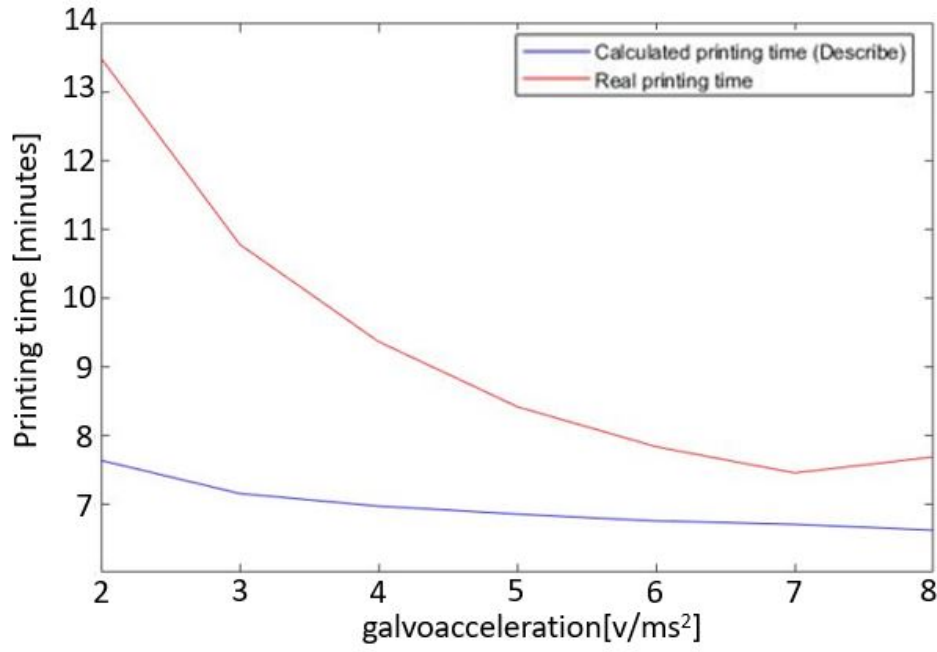


Figure B.12.67: Print time with various galvo accelerations, a comparison between the estimated print time and the real printing time. A block split test structure was used with 63X objective

Appendix C: Atomic force microscopy (AFM)

C.1. Introduction

The JPK BioAFM Nanowizard 4 was used for the experiments testing the functionality of the cantilever. The design of the microfluidic interface was optimized for use with the BIOAFM cantilever holder. This appendix explains the procedures and results of the AFM experiments.

C.2. Protocol

Figure C.2.1 shows the protocol for setting up and performing the experiment.

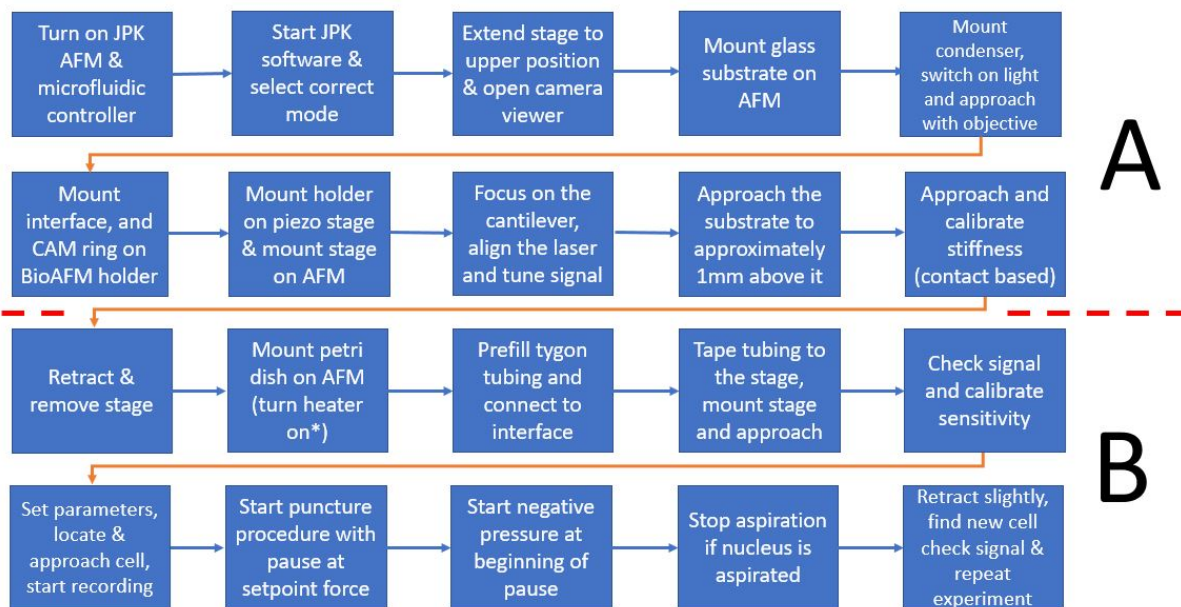


Figure C.2.1: AFM setup and experiment protocol. Part A is sufficient for experiments in air (experiment can be performed after setting the right parameters), part B is required for the cell experiments. *For the cell experiments, no heater was used due to the poor heat resistance of the DLP print.

Prolonged experiments sometimes resulted in cell debris in the Petri dish. If this was the case, part of the medium was removed with a pipette and fresh medium was added to the Petri dish. The old medium was disposed of with the cells in the biowaste. The procedure for disposing of the cells, and the cleaning procedure are described in figure C.2.2.

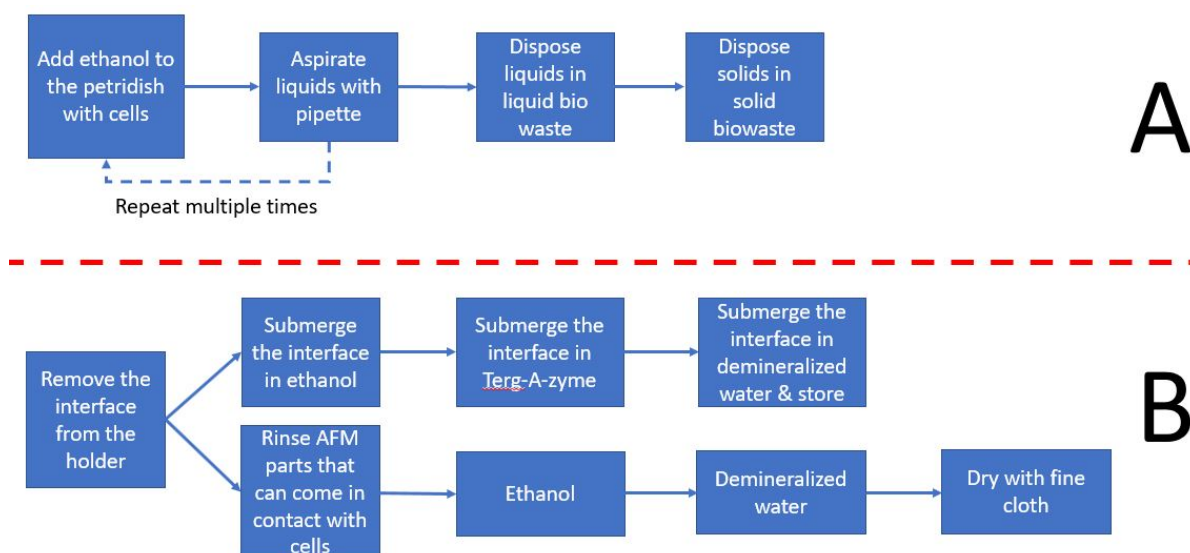


Figure C.2.2: Cell disposal and AFM cleaning procedure. **A)** Cell disposal procedure, **B)** AFM cleaning procedure. NOTE: cleaning instructions of technicians should always be followed!

C.3. Signal

The signal strength is crucial for AFM and vibrometer measurements. Increasing the thickness of the gold coating on the back of the cantilever directly leads to a higher signal strength. The maximum sum signal strength achieved was 0.9 volts. In the cell experiments, signals in the range of 0.2-0.5 volts were typically observed. Figure C.3.3A shows that too short a sputter coating results in an insufficient gold layer that does not reflect all the light (still transparent cantilever). Figure C.3.3B shows that the cantilever is no longer transparent, and the gold layer reflects the light.

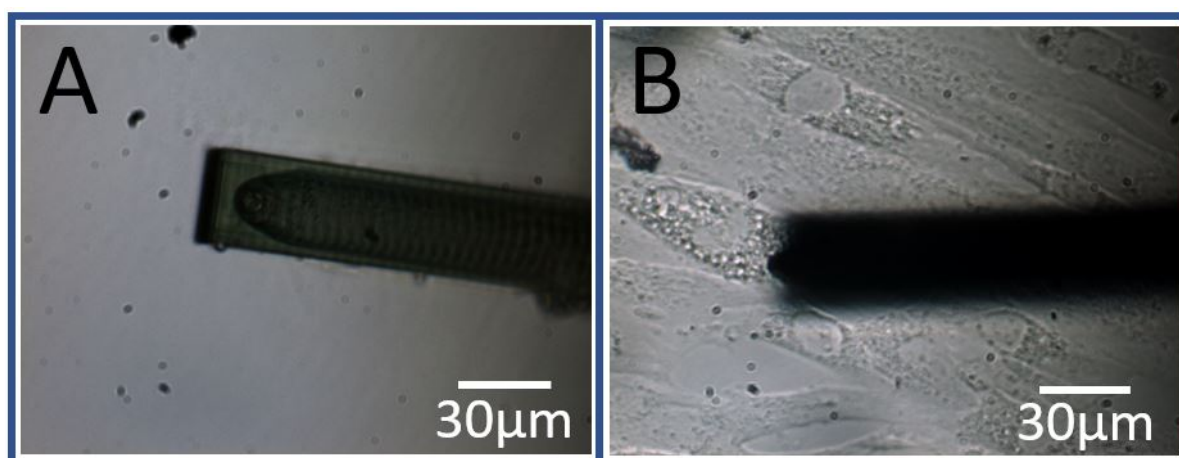


Figure C.3.3: Two cantilevers with different gold coating layer thickness. **A)** Thin coating, resulting in weak signal (1x 120second at 20mA). Transparency clearly visible, **B)** Cantilever with thick gold coating, not transparent any more, (5x 120second at 20mA).

C.3.1. Drift

During the experiments in liquid, a drift of the vertical deflection was observed (towards negative saturation voltage). The drift was worse in the experiments which used heated cells (37 degrees Celsius), but "stabilized" after approximately half an hour. The exact cause of the drift remains unknown, but four possibilities were identified: Swelling of the polymer (DLP or 2PP print), hydrodynamic influences, flow into the cantilever and interactions between the DLP print and the 2PP print. The drift was visible in the JPK laser alignment viewer (moving slowly to negative saturation for the vertical deflection), but the drift was also visible in some of the measurements. In the signal viewer of the detector, the drift rate was about twice as fast when the medium was heated.

Figure C.3.4 shows the result of the drift in one measurement. Due to the drift, no clear contact point with the cell can be determined.

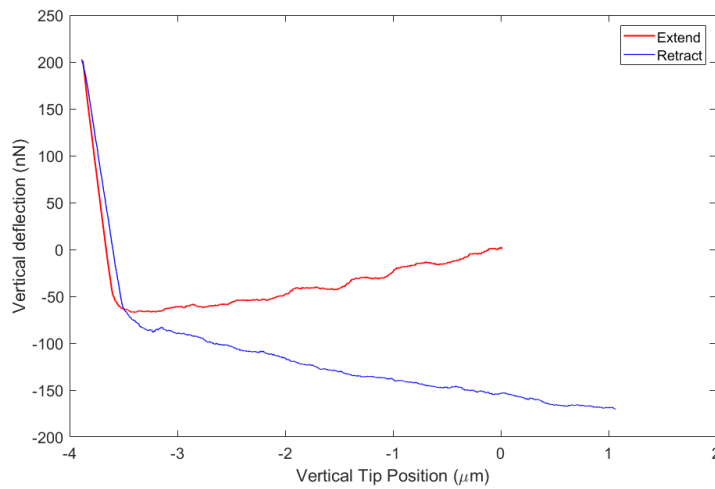


Figure C.3.4: Signal drift showing in a measurement. The decreasing extend line and the decreasing retract line, with a constant slope, show that a drift occurs (should be horizontal).

C.4. Force curve on a flat substrate

After the laser has been aligned with both the cantilever and the detector (by adjusting laser position and adjusting the detector and the mirror to get an optimal signal), the substrate can be approached. When the cantilever has approached the substrate, the cantilever can be calibrated using the contact-based method. This method uses the slope of the approach force curve to calculate the sensitivity and the thermal noise to determine the stiffness. For measurements in liquid, the sensitivity has to be recalibrated after the cantilever has been immersed.

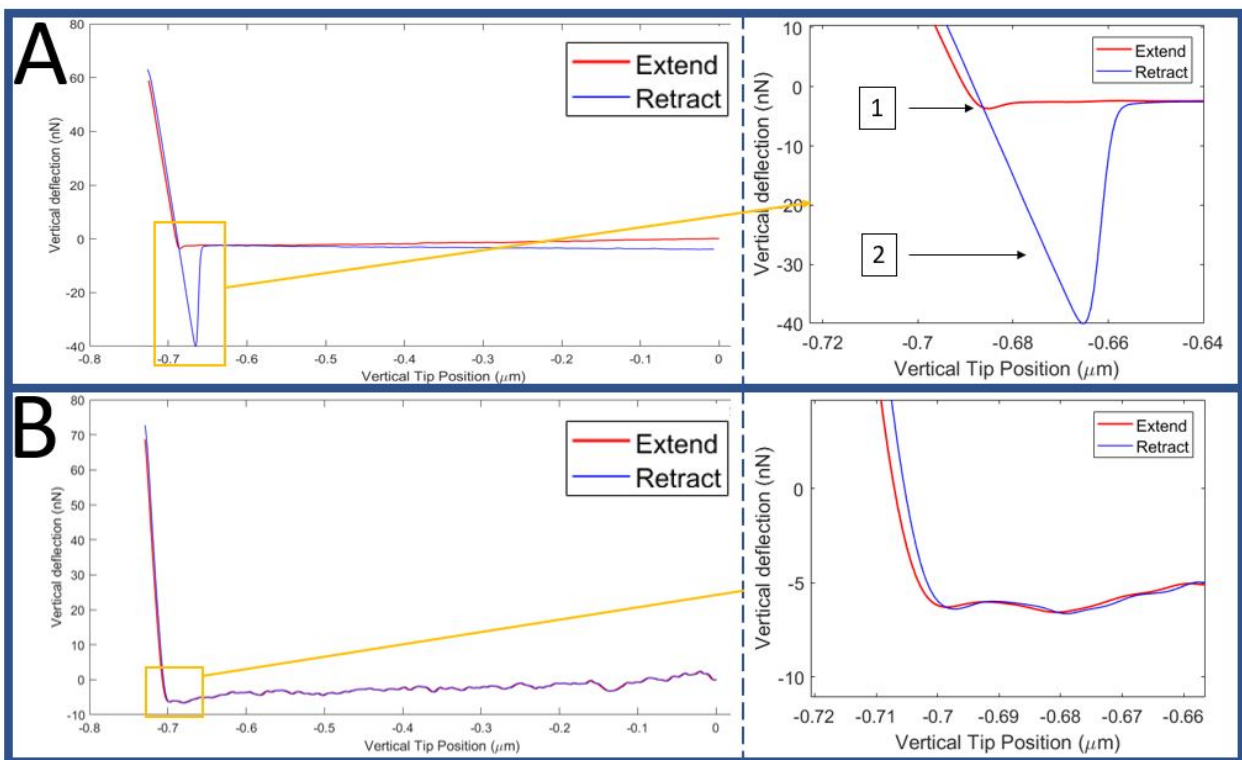


Figure C.4.5: Force curves in air and liquid (PBS). **A)** Force curve in air with zoom in at important region. 1 = Small jump into contact, 2 = Adhesion. **B)** Force curve in PBS (liquid) with zoom in at important region. No jump or adhesion distinguishable.

After calibration, experiments can be performed. One of these experiments is making force curves on substrates and cells. Figure C.4.5 shows the force curves of the cantilever both in air and in liquid on a flat surface (here: Petri dish). The measurement in air clearly shows a jump into contact and adhesion behaviour, both of which are not present when measuring water.

The contact-free method of the JPK system, which uses the Sader method [23] in combination with the thermal noise method [24, 25], does not give reliable results for a hollow polymeric cantilever. This is due to the assumption of a solid rectangular cantilever in Sader's method [26]. Although Sader et al. [23] propose a method for indirectly calibrating a cantilever, it was not used for this research.

C.5. Imaging

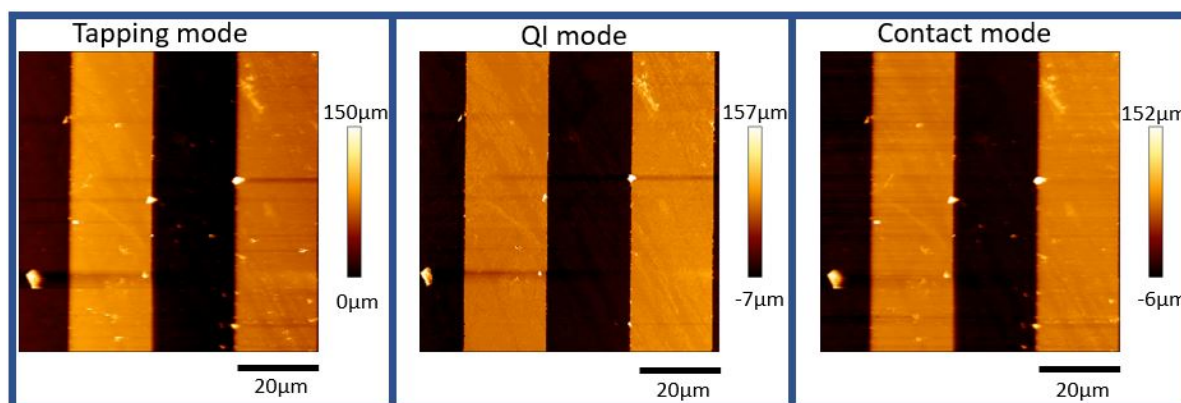


Figure C.5.6: Three modes (tapping, QI and contact mode) used to image a test substrate with $20\mu\text{m}$ wide ridges.

The cantilevers could also be used to image test substrates and capture the surface topology. With the 3D-printed cantilevers, it was possible to image rigid test substrates. However, it was not possible to get an accurate image of a cell. This is due to the stiffness of the cantilever. Normally, cantilevers with a stiffness of 0.06 N/m are used for imaging cells. With the 3D-printed cantilever, the high stiffness of the cantilever caused the cell to deform during imaging, either indenting the cell or detaching it.

Three modes were used for imaging a test substrate in air: tapping mode (AC), Quantitative Imaging (QI mode) and contact mode. The results of the imaging of a test substrate can be seen in figure C.5.6. The QI mode gave the best results and was also used to image the grid seen in C.5.7. Further, fine-tuning of the printing parameters can reduce the tip radius and provide higher resolution images.

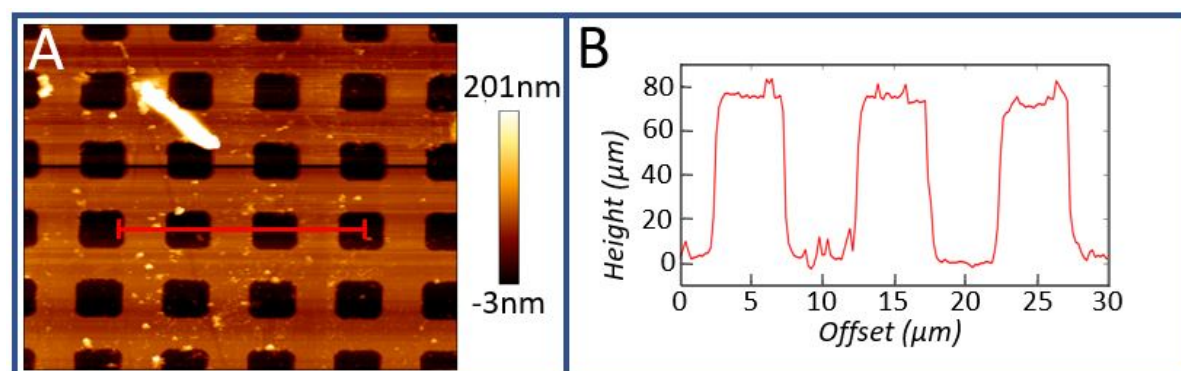


Figure C.5.7: AFM imaging of test grid substrate with $10\mu\text{m}$ ridges and $10\mu\text{m}$ spacing. The average roughness (R_a) was 34.06 nm and the peak-to-valley roughness (R_t) was 85.8 nm . **A)** Resulting AFM image, **B)** Height profile along red line in A.

Another test substrate with ridges spaced $3\mu\text{m}$ wide was imaged using the QI mode. The measured height is smaller than the specifications of the test substrate, as it should be 100 nm . However, ir. R. Kramer had similar results with the same substrate (possibly the substrate is damaged or the 3D printed cantilever tips are not able to capture the surface precisely enough). The results can be seen in figure C.5.8.

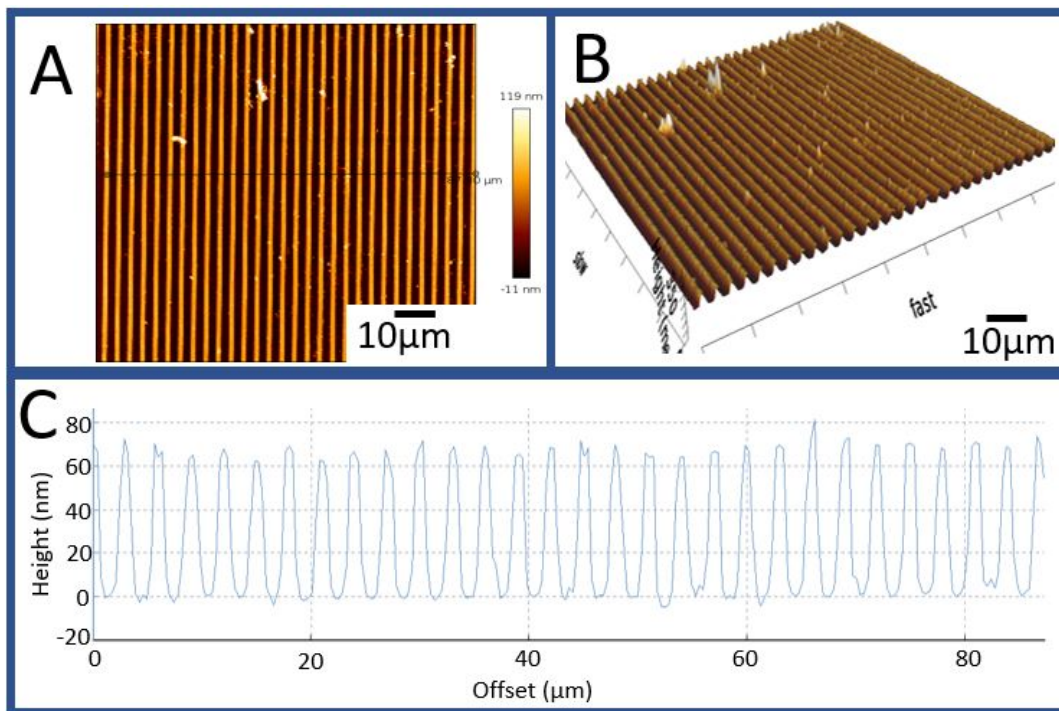


Figure C.5.8: QI mode used to image a test substrate with ridges $3\mu\text{m}$ apart. **A)** Top view of AFM image, **B)** 3D view of AFM image, **C)** Measured height of AFM image.

Since the cantilever was not specifically designed for imaging, the results are relatively good. Worse results were observed when imaging cells. As already mentioned, this is to be expected, as cantilevers with a stiffness of 0.06 N/m are normally used for imaging soft cells. The resulting images can be seen in figure C.5.9.

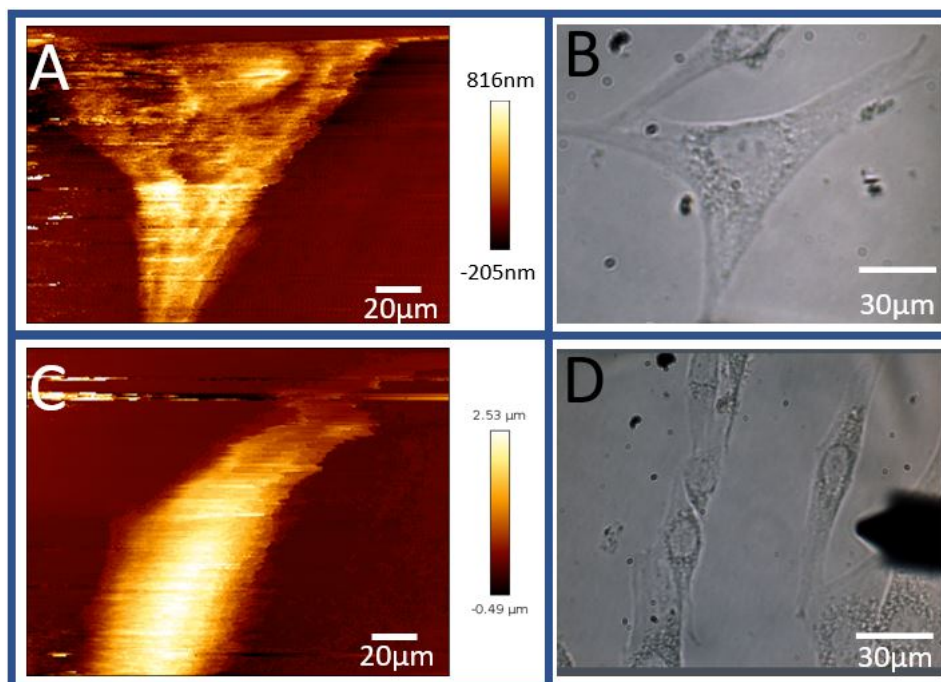


Figure C.5.9: QI mode used to image cells. **A & B)** Cell with A the AFM image and B the cell before imaging (optical microscope). The measured height is not realistic as the cantilever deformed the cell during imaging. **C & D)** Cell with C the AFM image and D the cell before imaging. Bending of the cell in the AFM image (in the direction of the cantilever movement) caused by detachment of the cell by the cantilever

The cantilever did not correctly measure the height of the cell on the AFM image. However, the overall shape of the cell was correctly recorded, and the nucleus is also recognisable in the image. The main reason for this seems to be that the cantilever is too stiff and deforms the cell too much. During the imaging, it was clear that the cantilever was scraping the cell and detaching it from the Petri dish. In some experiments, the cell membrane also seemed to stick to the tip, so coating the tip with an anti-stick compound (e.g. Sigmacote) might be necessary.

Short cantilevers with high stiffness, high natural frequency and low Q-factor can be used for high-speed imaging [6]. The required tip dimensions should be investigated, including the possibilities of growing tips on 3D-printed cantilevers.

C.6. Flow from cantilever

To determine whether the aperture was not clogged, one can look at the flow. The flow was clearly visible near cells as it displaced parts of them. The flow can be visualized far away from the substrate and close to it. The latter is shown in figure C.6.10.

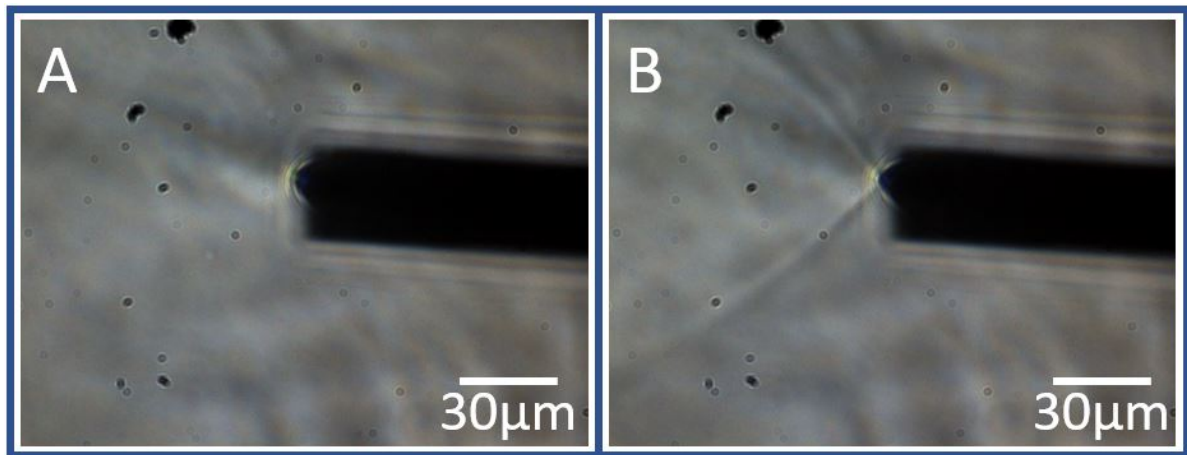


Figure C.6.10: No flow versus flow from the aperture in an AFM experiment. **A)** Pressure controller switched off, **B)** Flow visible, pressure controller set to 1000mbar

C.7. Puncture

The cell puncture experiments could provide information about two important properties of the cell: the force required to puncture the cell and Young's modulus of the cell. Punctures in the range of 20 to 80 nN have been observed in various experiments. Figure C.7.11 shows three peaks in the force curve, of which the peak with the highest force (left) is the most prominent.

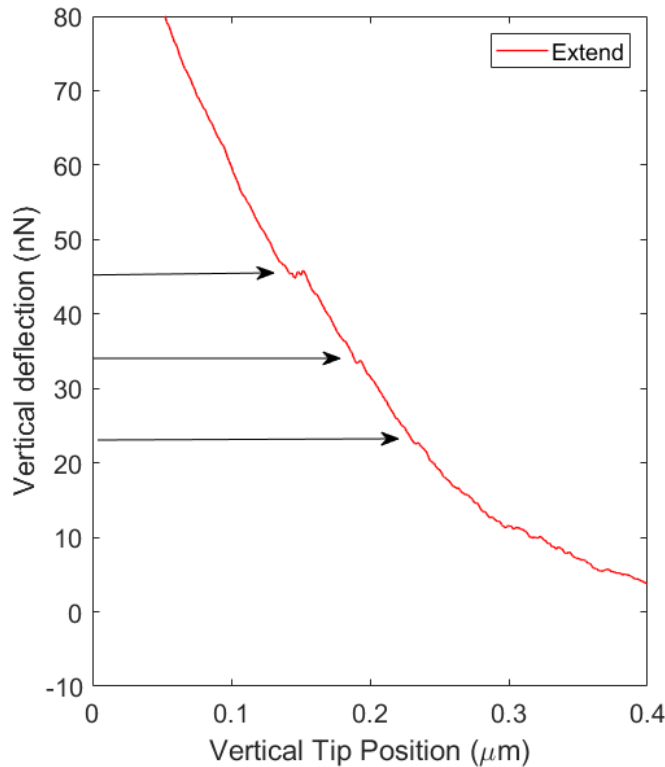


Figure C.7.11: Force curve of cell puncture experiment with tip positioned on top of a nucleus

Comparing the result with the work of McCreery et al. [27], the large peak (membrane puncture) should occur at the lower forces and then be followed by a smaller peak (nucleus puncture) at higher forces. Figure C.7.12 shows a typical force curve from McCreery et al. [27]. Note that the magnitude of the puncture force is in the same range as measured in this study.

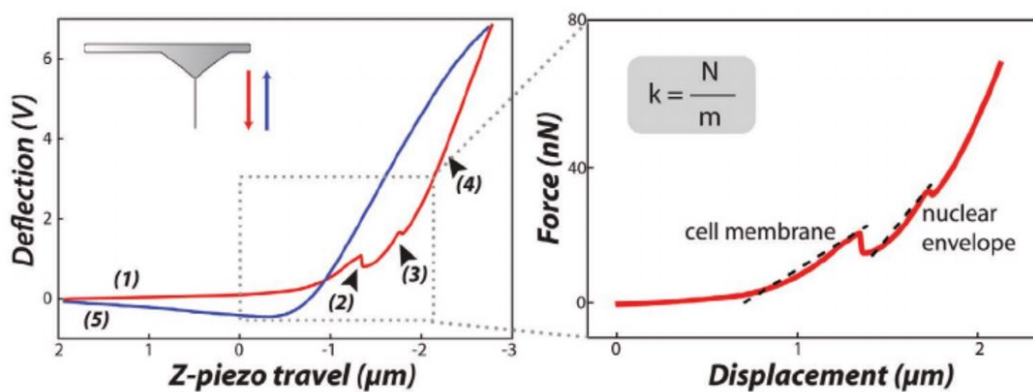


Figure C.7.12: Typical force curve of cell puncture experiment on top of the nucleus [27].

To accurately determine the Young's modulus of the cells, it is necessary to determine the tip radius at the apex. Due to the complex geometry of the tip, this cannot be determined from images or from the design. A

comparative study is required to determine an effective radius value. For this experiment, one can use a soft test substrate (e.g. PDMS or a gel) and compare the results of both a commercial and a 3D-printed tip. Without the approximate radius, no conclusions can be made about the Young's modulus of the cells. After puncturing, no clear hole was visible in the membrane, which would indicate that the cells sealed immediately. The cells did also not detach after a puncture, which indicates the cells are still alive.

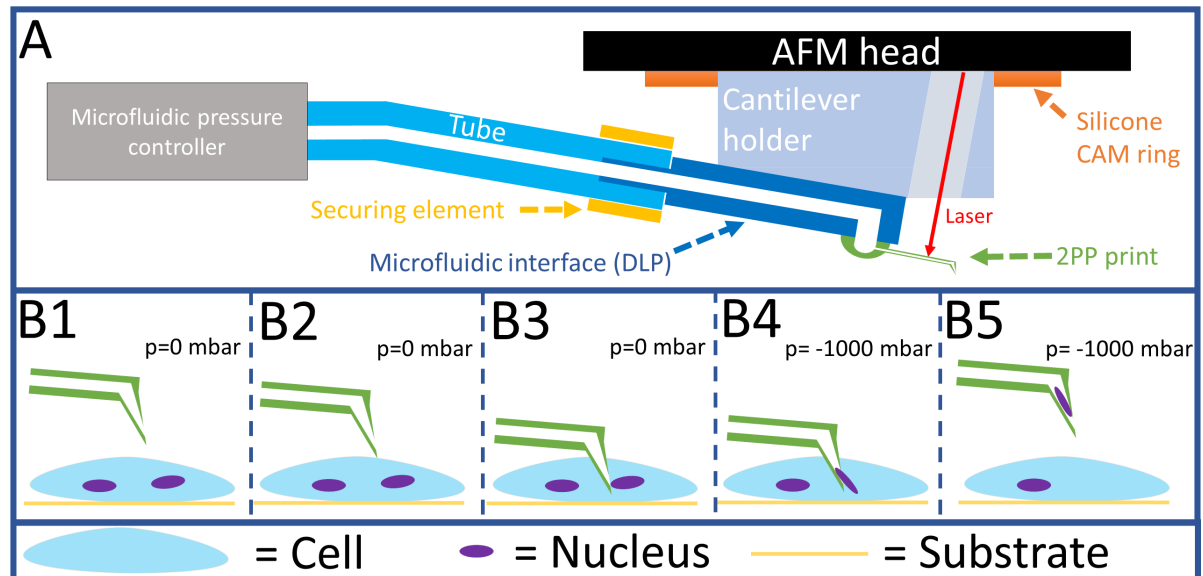


Figure C.7.13: Schematic diagram of the nucleus aspiration experiment (not to scale). **A)** Schematic of the AFM setup with the DLP-printed microfluidic interface mounted on the cantilever holder. The cantilever of the 2PP print, which is printed on the DLP print, reflects the laser. The tubing and securing element connect the DLP print to the microfluidic pressure controller. **B1-5)** Shows the procedure for aspirating a cell nucleus. First, the tip is positioned over the cell at the location of the nucleus (B1), then the cell is approached (B2). The piezos are extended until the set point force is reached. In the meantime, the cell is punctured (B3). The microfluidic controller pressure is set to -1000mbar for 30 seconds to aspirate the nucleus (B4). When the entire nucleus is aspirated, the piezos retract the cantilever with the nucleus inside (B5).

C.8. Aspiration

Figure C.7.13 shows the puncture procedure again for the nucleus aspiration study. For this aspiration of the nucleus, the tip was positioned on top of the nucleus. As the aperture is at an angle of 10 degrees (AFM holders is at an angle), this will ensure the aperture is positioned against the nucleus after a puncture. A setpoint force of 80 nN was used to ensure the tip was inside the cell. If the tip also hits the substrate, that should not be a problem as the aperture is 1 μm from the tip. Therefore, the aperture will be as deep in the cell as possible. After reaching the setpoint, a pause was started, and a negative pressure was applied. A total of three nuclei were partially aspirated, and five nuclei were successfully aspirated. Partial aspiration had two reasons that go hand in hand: the pause was too short to aspirate the nucleus fully, or the magnitude of the pressure was too low. Increasing either of the two helped to aspirate the nucleus. During some experiments with small cells, sometimes cell detachment or cell rupture was observed during the aspiration. With smaller pressure differences and longer pause, this could be minimized. Figure C.8.14 shows the rupturing of a cell during aspiration.

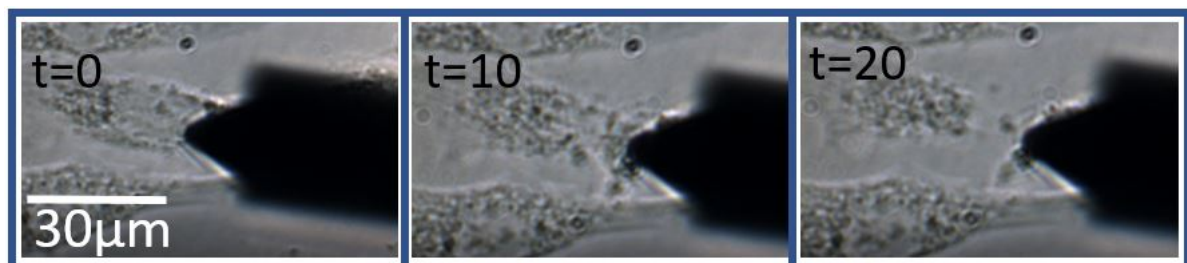


Figure C.8.14: Rupture of a cell during aspiration (AFM experiment). Scale bar applies to all figures.

In two experiments, a total of five cell nuclei were aspirated. In addition, in the experiments to determine the aspiration pressure, some nuclei were only partially aspirated. Figure C.8.15 shows the same nucleus extraction as in the paper but enlarged.

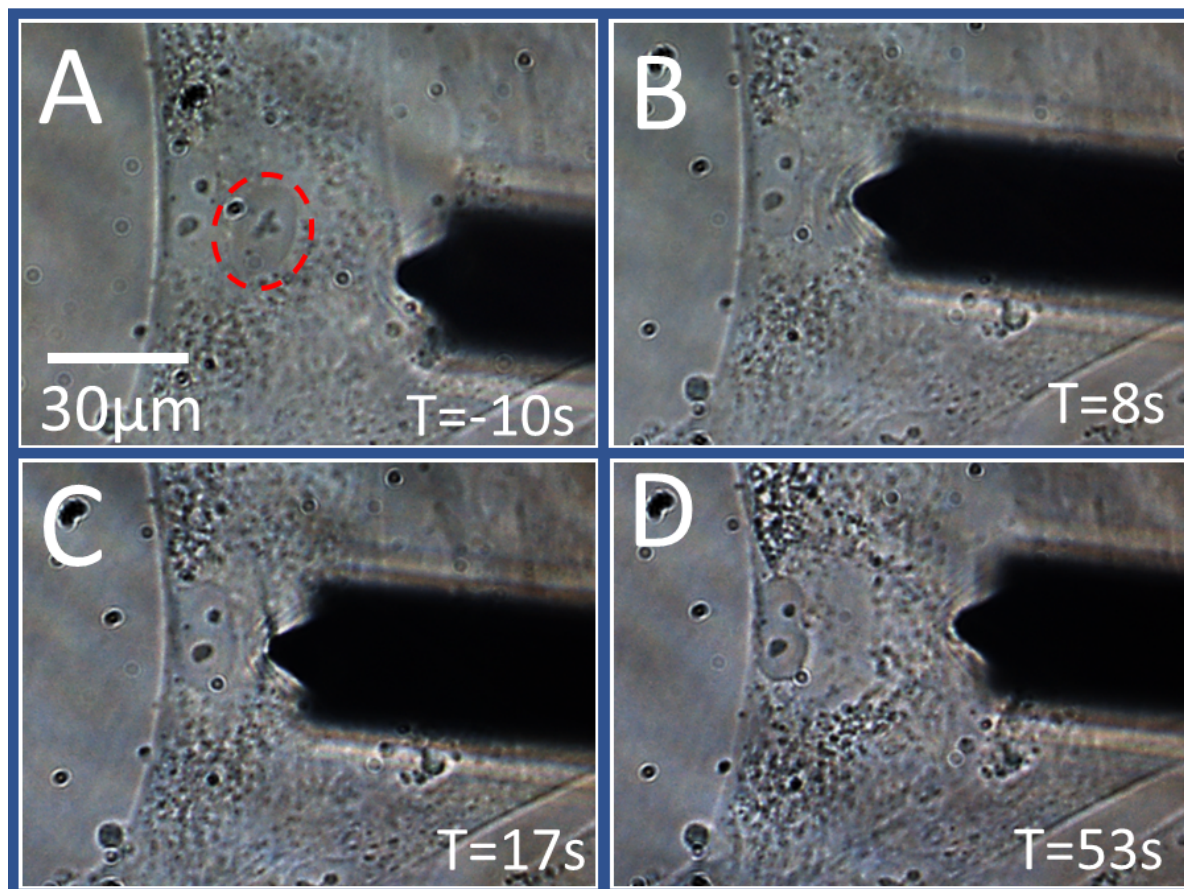


Figure C.8.15: Nucleus aspiration using -1000 mbar pressure (AFM experiment). Same figure as in the paper. Scale bar applies to all figures.

Figure C.8.16 shows another aspiration. This aspiration was performed on what appears to be a mononuclear cell. Note the overall deformation (contraction) of the cell after aspiration of the nucleus.

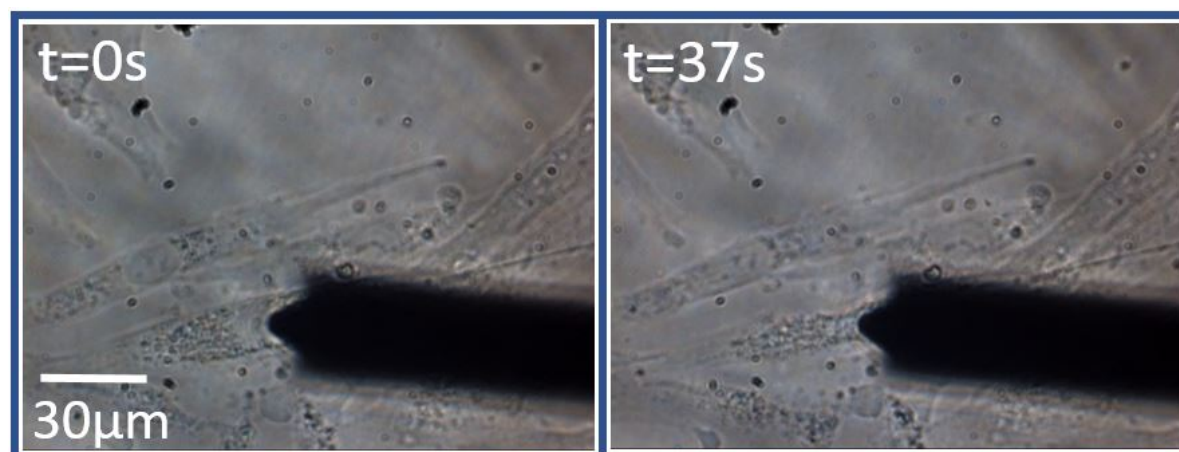


Figure C.8.16: Nucleus aspiration using -1000mbar pressure with large overall deformation of the cell.

Figure C.8.17 shows a partial aspiration of a nucleus. Note the deformation of the nucleus after the tip is removed and the hole in the membrane. This could be due to the constant aspiration pressure, even during the retraction of the tip. Aspiration of the nuclei is possible with pressures smaller than -1000 mbar, but a longer pause should be used.

Partial aspiration could be a new approach for removing the nucleus. If the nucleus is far in the tip, the cantilever can be retracted during aspiration and the nucleus removed. This makes it easier to deposit the nucleus in a microwell as it stays at the tip.

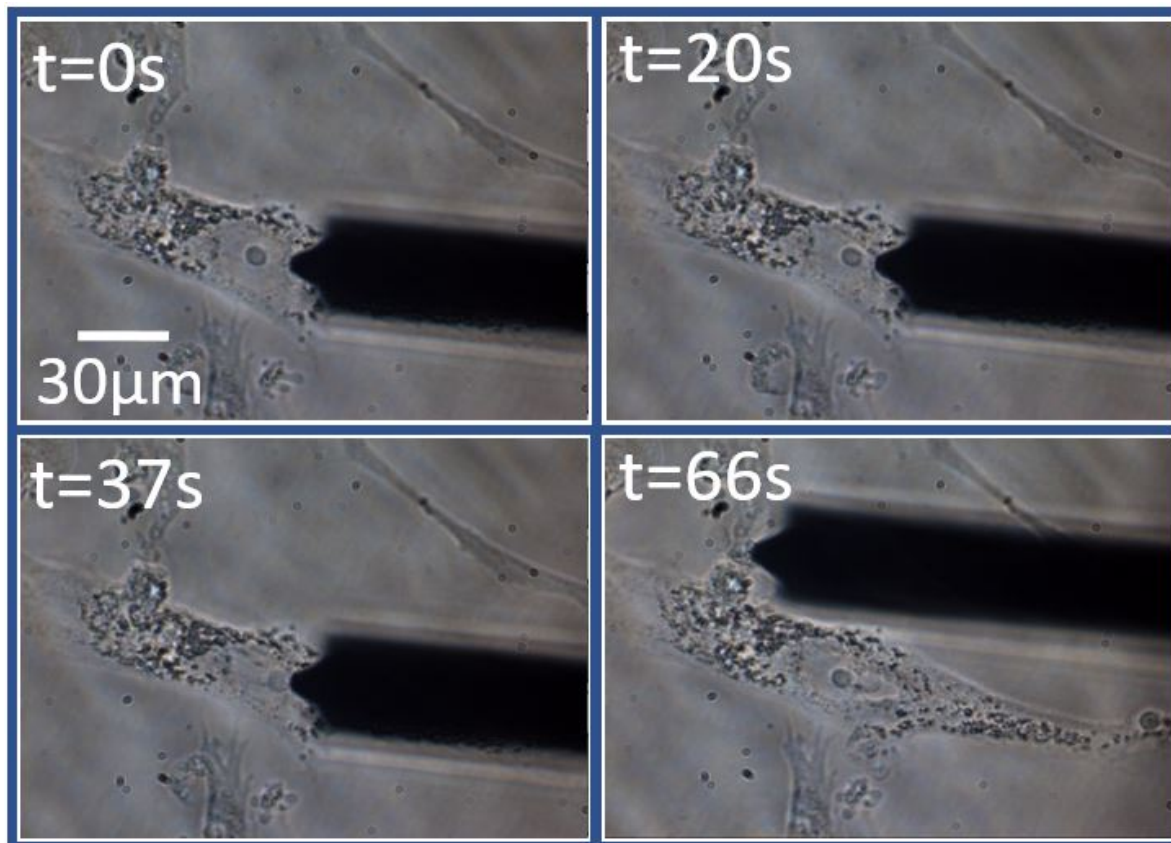


Figure C.8.17: Partial Nucleus aspiration using -800mbar pressure. Note the residual deformation after the tip has been moved away. A hole in the membrane is still visible. Scale bar applies to all figures.

C.9. Adhesion

The experiments on cell adhesion were challenging to perform with the current design of the cantilever. The results were already shown in the paper. It is suggested that the aperture did not make proper contact with the cells during the experiments, as other parts of the 2PP print probably hit the substrate before the cantilever (the sharp tips were relatively high and therefore did not have this problem). It is suggested to change the height of the attachment of the cantilever to the dome or to change the tip as suggested in appendix B to achieve better adhesion experiment results. Only one experiment was successful with partial detachment, as shown in figure C.9.18 and figure C.9.19.

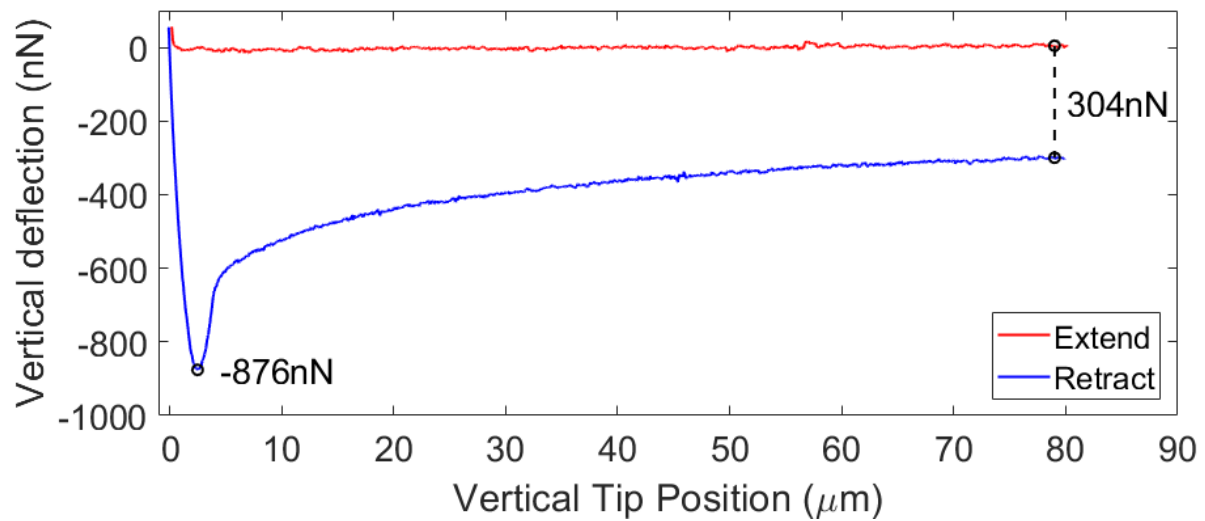


Figure C.9.18: Partial detachment of a cell (mouse preosteoblast). A tipless cantilever with an aperture of $7 \mu\text{m}$ was used (see fig C.9.20).

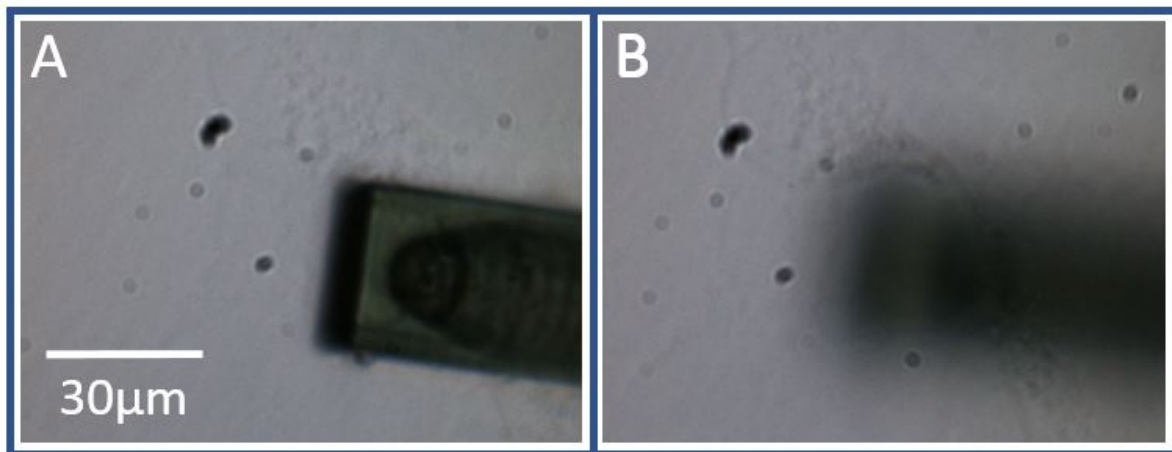


Figure C.9.19: Partial detachment of a cell (mouse preosteoblast) on the optical microscope of the AFM. A tipless cantilever with an aperture of $7 \mu\text{m}$ was used (see fig. C.9.20). **A)** before aspiration, **B)** During retraction

Figure C.9.20 shows again the tipless cantilever used for the cell adhesion experiments (aperture diameter of $7 \mu\text{m}$).

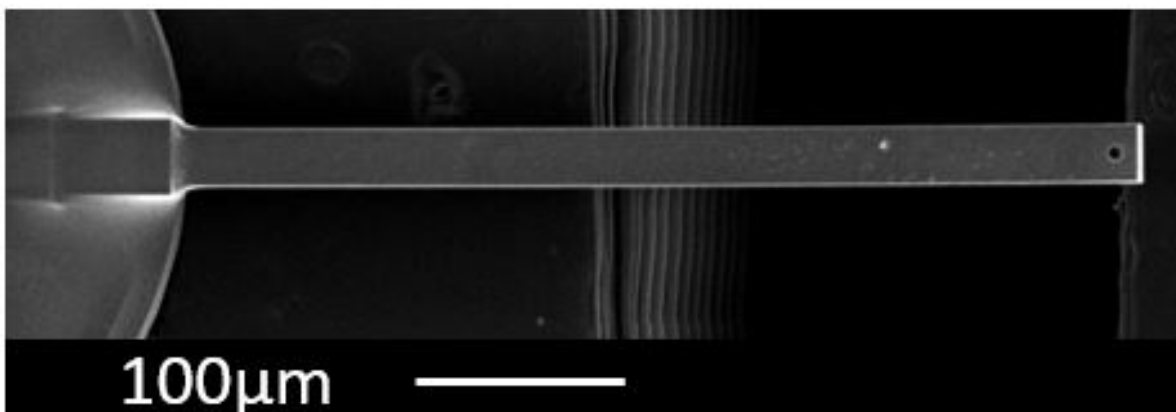


Figure C.9.20: SEM images with tipless cantilever for adhesion experiment with a $14 \mu\text{m}$ aperture

C.10. Measurement of the gold layer on prints

The thickness of the gold layer was measured using an NCLR cantilever with a stiffness of 27.7N/m for two different sputter settings. The 5 seconds at 10mA setting was used to coat the DLP print for the automatic interface finding (approximately 3nm, figure C.10.21A). The 60 seconds at 20mA setting was used to coat the back of the cantilever for laser reflection of the AFM (repeated 5-10 times, approximately 150-315 nm, figure C.10.21B). The AFM measurements of the gold layer height can be seen in figure C.10.21. Another measurement was made for a layer sputtered at 10 mA for 20 seconds. The result was a layer thickness of 13.2nm. Assuming that the sputtering rate is constant, this would result in a slightly thicker layer of 3.3 nm for the 5-second case.

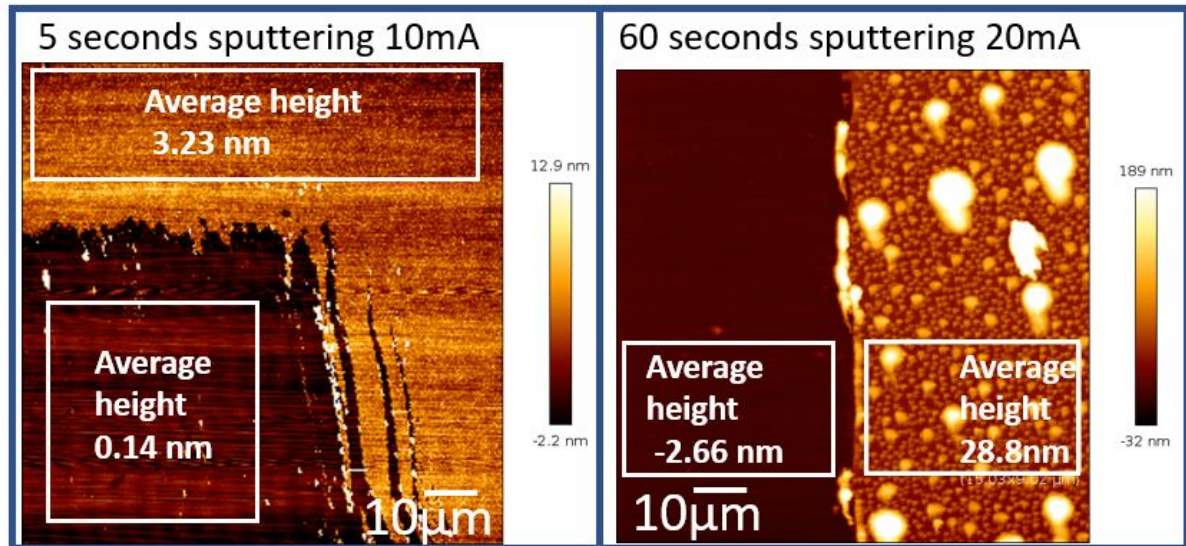


Figure C.10.21: Gold film thickness measured using an NCLR cantilever with a stiffness of 27.7N/m with two settings. The 5 seconds at 10mA setting was used to coat the DLP print for the interface finding (approximately 3 nm). The 60 seconds at 20mA setting was used to coat the backside of the cantilever for the laser reflection (repeated 5-10 times).

C.11. Recommendations

In the AFM experiments, the stiffness measurement (using the contact based method) showed a relatively large scatter ($k=1.84 \pm 0.24$ N/m). If the outliers are removed (1.6 N/m k 2.2 N/m), the resulting stiffness is $k=1.71 \pm 0.12$ N/m. A large number of samples should be studied in exactly the same way to determine the stiffness of the cantilever on the JPK more accurately.

In this research, both plastic and glass substrates were used for the approach and sometimes, the cantilever was already attached to the tubing before calibrating the cantilever. These factors could cause calibration errors, but also the variability of the printing process could also introduce this scatter.

Sader et al. [23] suggest calibrating a solid rectangular cantilever and then using this to calibrate a cantilever with a different geometry indirectly. This method could be explored in future work.

Appendix D: Laser Doppler vibrometer (LDV)

D.1. Introduction

The Polytec MSA-400-PM2-D laser Doppler vibrometer (LDV) was used to measure the stiffness and natural frequency of the cantilever. The interface was mounted upside down on a piezo (PZT) for these measurements using carbon tape. The piezo could be controlled directly via the Polytec system. Two different measurements were made to determine the behaviour of the cantilever at two different piezo settings. First, a measurement was performed while the piezo was actuated with a pseudo-random signal. This measurement was used to determine the frequency response of the cantilever. In the second measurement, the piezo was switched off, and the thermal noise was measured. The power spectral density at the base level and at the peak (at the resonant frequency) could be determined from this measurement. These measurements were carried out both in air and in a vacuum.

D.2. Laser Doppler vibrometer

The LDV system extracts the amplitude and vibration of the surface of interest, by comparing the reflected (NIR) laser signal with a reference beam. The laser is reflected from the surface of interest, whose movement causes a Doppler shift compared to the reference beam. The output of the LDV system is an analogue voltage proportional to the target velocity. To achieve the required reflection, the back of the cantilever was coated with gold.

To determine the behaviour of the entire cantilever, several points can be measured in succession. Figure D.2.1, shows the cantilever in the viewer and the selected locations where the laser will perform a measurement. Note that the block splitting of the cantilever is clearly visible in the image.

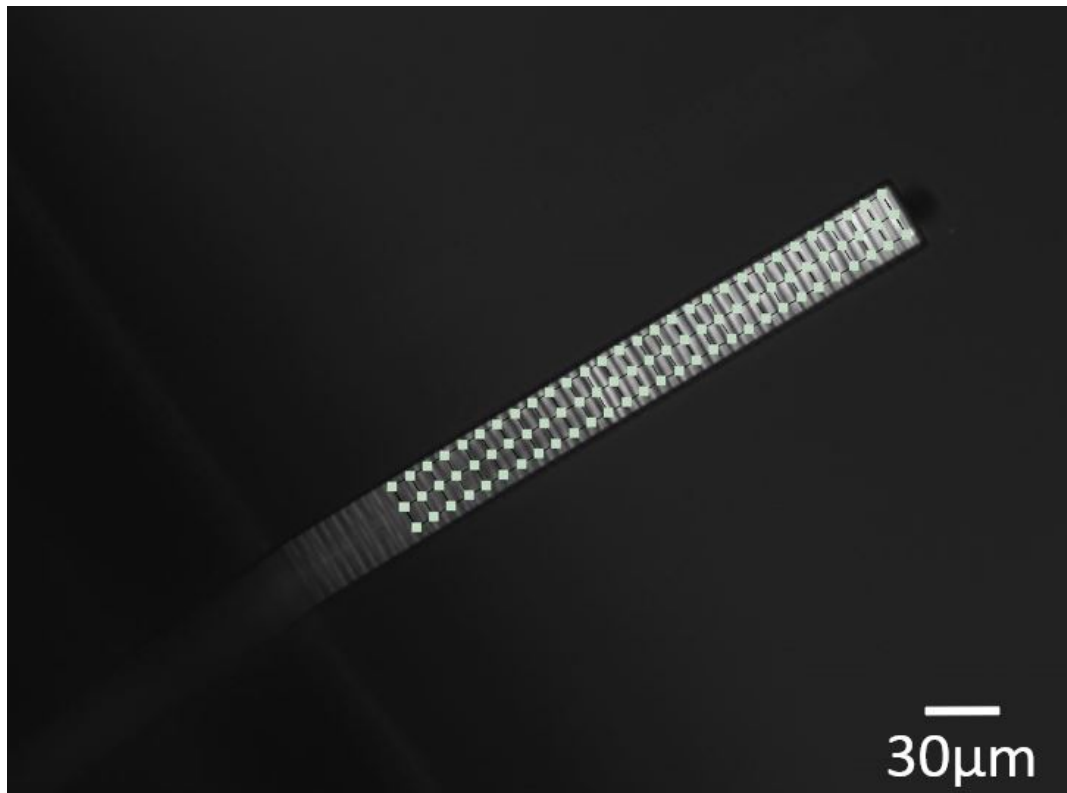


Figure D.2.1: View of the cantilever during a Polytec experiment. The squares indicate the locations at which the laser will perform measurements (all with optimal signal strength).

Figure D.2.2 shows the Polytec program, including the results of a measurement in the analyser. The laser can also be seen in this image.

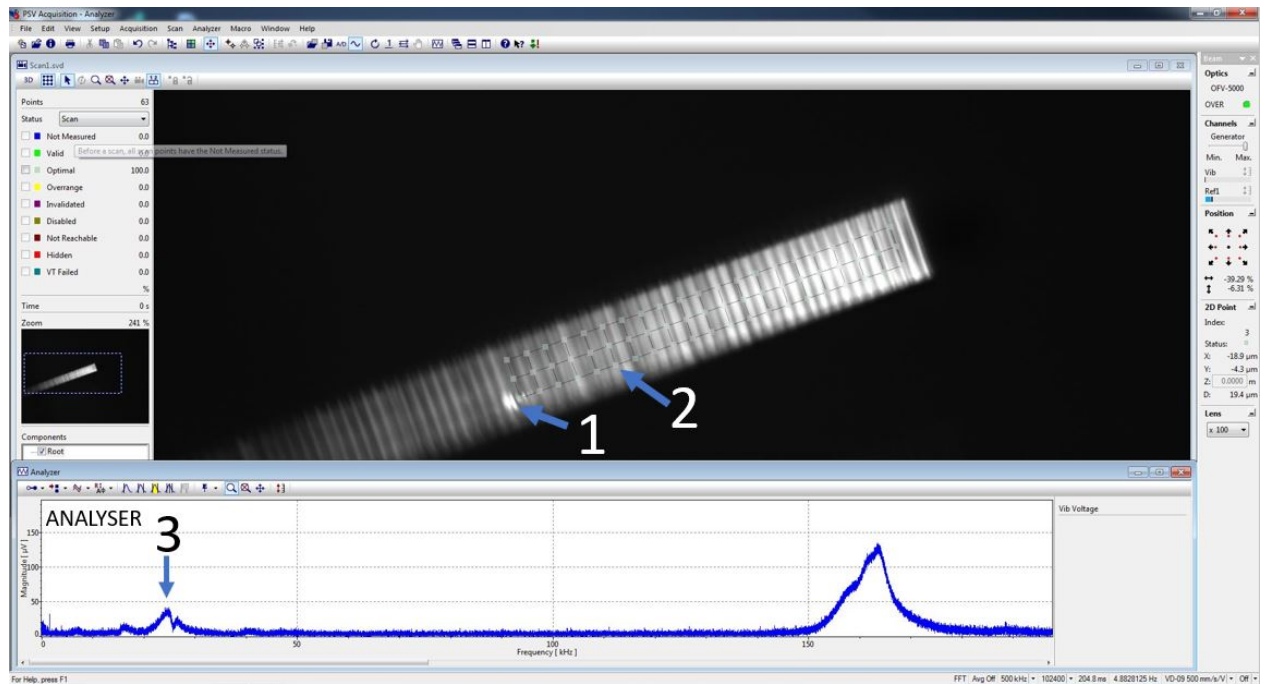


Figure D.2.2: Polytec cantilever and laser view. 1 = The laser spot, 2 = A point of the grid that is measured, 3 = Resonant frequency indicated in the analyser.

D.3. Frequency spectrum measurement

Using the grid measurement, the frequency response of the cantilever can be determined by applying a pseudo-random signal. Figure D.3.3 shows the results of the measurement in air.

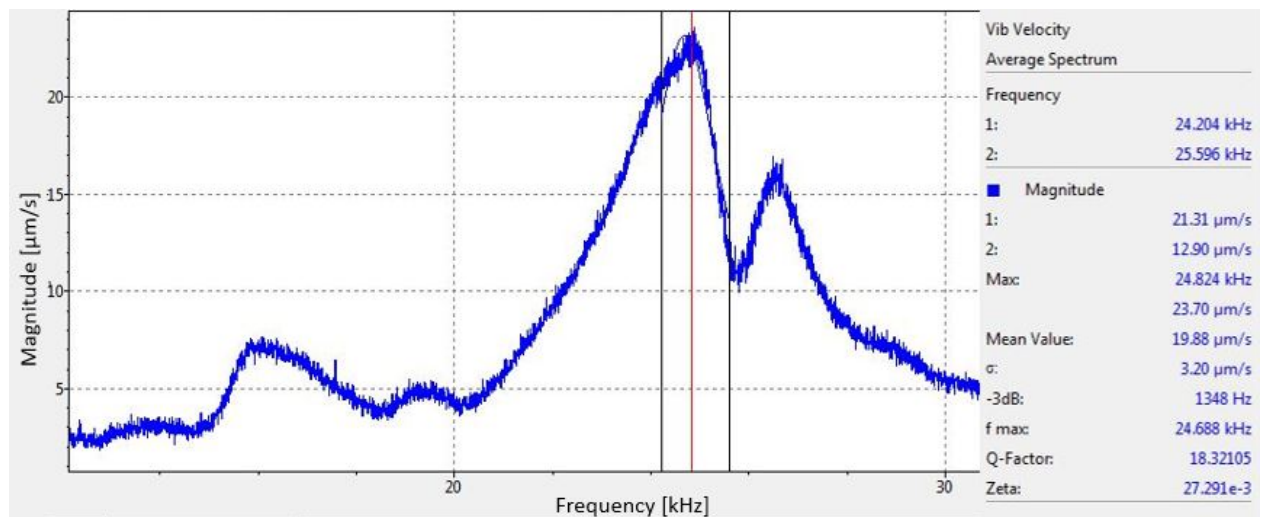


Figure D.3.3: Part of the frequency spectrum of the cantilever measured in air. Resonant frequency indicated by vertical red line.

For the measurements in a vacuum, the unit was placed in a vacuum chamber. Note that a different piezo-electric element was installed in this chamber, which may contribute to differences in the measurements.

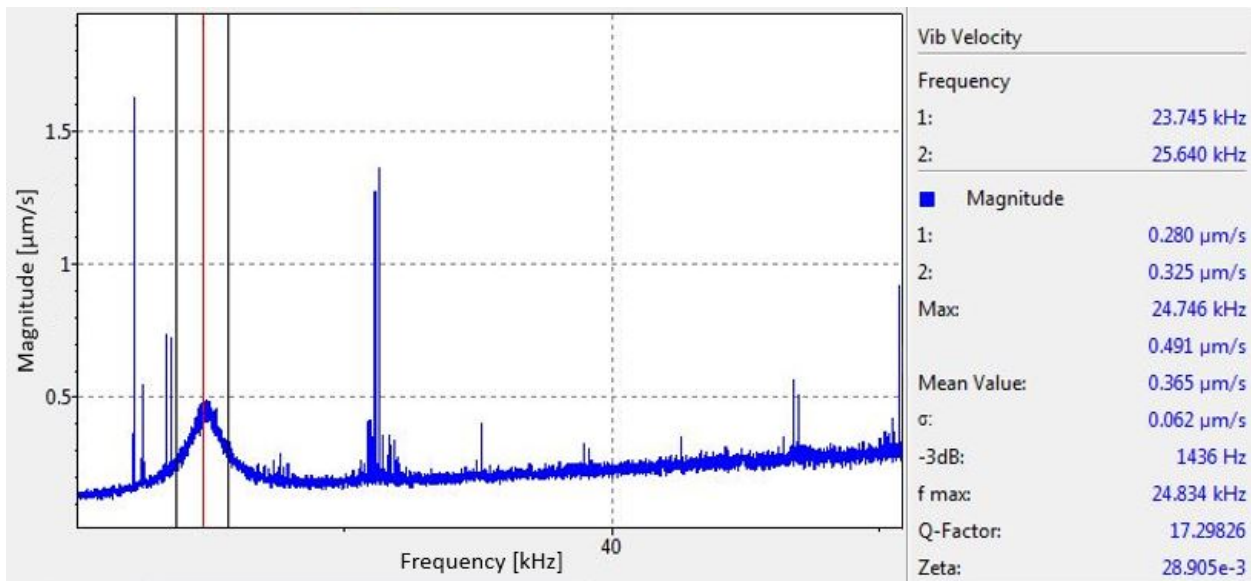


Figure D.3.4: Part of the frequency spectrum of the cantilever measured in vacuum (pressure = $9e-3$ mbar). Resonant frequency indicated by vertical lines.

If we compare the measurements in air with those in a vacuum, the resonance frequencies are in the same range. However, directly after the resonant frequency, the second peak is not present in the measurements in a vacuum. This could be due to differences in the mounting or the different piezos. It is suspected that the difference between the piezos falsifies the results, as the measurements are much more similar with the piezos switched off (thermal noise measurement). Also, one would expect an increase of the Q factor instead of a decrease when the same device is measured in vacuum, as can be seen in figures D.3.3 and D.3.4.

D.4. Power spectral density measurement

To determine the stiffness of the cell, the power spectral density was measured at the resonant frequency (peak) and far away from the resonant frequency (baseline). From this data, the stiffness was calculated using [28]:

$$X(\omega) = \frac{\sqrt{4k_b T \frac{\omega_0}{mQ}}}{\sqrt{(\omega_0^2 - \omega^2)^2 + \left(\frac{\omega\omega_0}{Q}\right)^2}} \quad (\text{D.17})$$

with X the auto spectral density, $\omega = \omega_0$ the resonance frequency, Q the damping coefficient, T the ambient temperature, k_b the Boltzmann constant and with m equal to:

$$m = \frac{k}{\omega_0} \quad (\text{D.18})$$

with k the cantilever stiffness.

The auto spectral density X can be calculated using:

$$X^2 = \sqrt{PSD_{peak}^2 - PSD_{base}^2} \quad (\text{D.19})$$

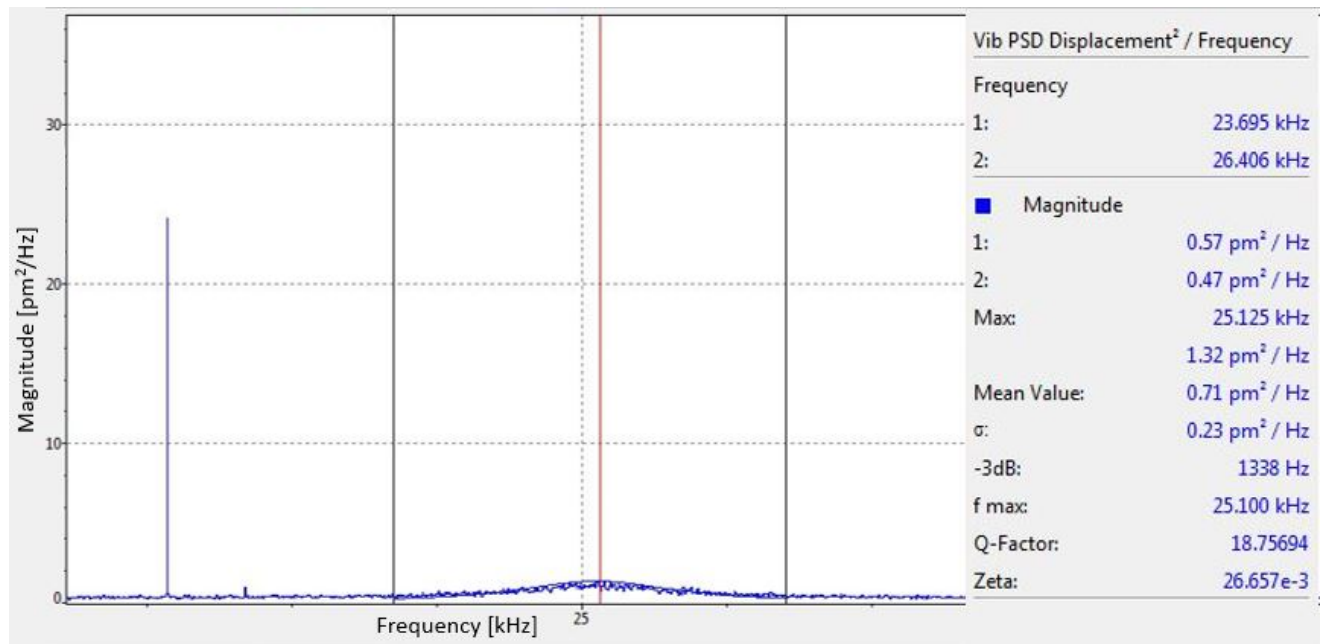


Figure D.4.5: Polytec power spectral density measurement in air. Note the outlier on the left of the resonant frequency (Q=8000).

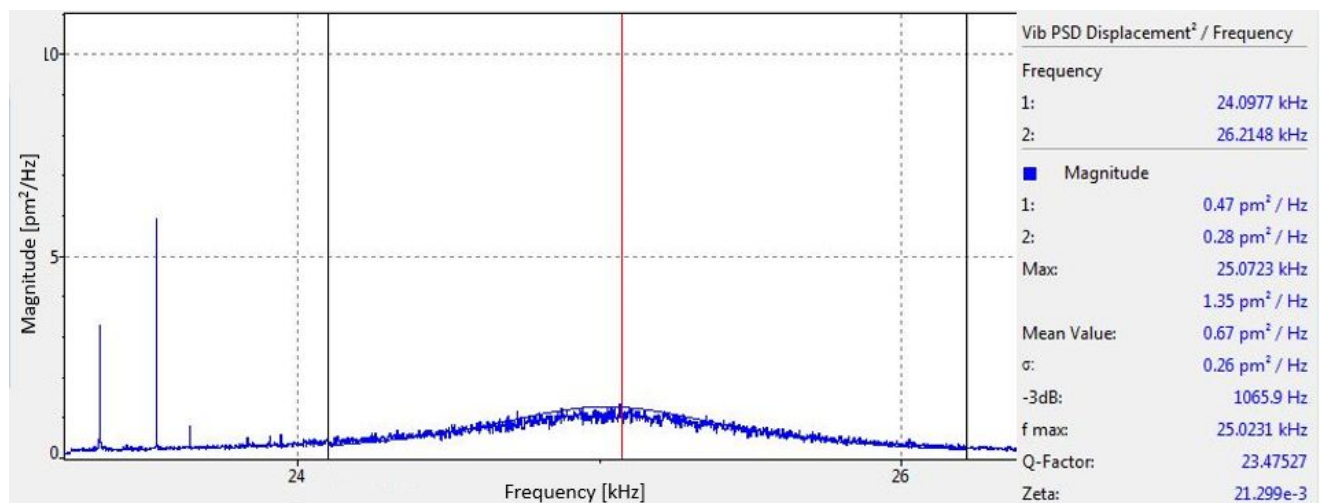


Figure D.4.6: Polytec power spectral density measurement in vacuum (pressure = 9e-3 mbar). Note the outlier again on the left of the resonant frequency.

Using the spectral densities, a stiffness of 1.64 N/m was determined for the cantilever in air and 1.90 N/m in vacuum (the fit of the measurement in vacuum was suboptimal).

An interesting aspect is that for the PSD measurements (no perturbation by the piezo) is that the Q-factor is higher in a vacuum than for a cantilever in air, while it is lower when a pseudo-random noise actuates the piezo. One possible explanation is the difference in piezo actuators and the mounting of the cantilevers.

$$Q = 2\pi \frac{\text{energy stored}}{\text{energy dissipated per cycle}} \quad (\text{D.20})$$

Using equation D.20, a higher Q is expected for the measurements in vacuum as the dissipated energy is less (less viscous damping).

D.5. Influences on the measurement

Since a polymer is used for the cantilever, one would expect a low Q-factor, which was also shown in the measurements. However, several parts of the setup should be improved to achieve more accurate measurements. First of all, the tape that is used to mount the DLP print on the piezo. This could lead to artefacts in the measurements, as it can introduce damping. A more rigid solution should be designed. In addition, the influence of the DLP print and the dome on the measurements should be investigated. Furthermore, measurements should be made in air, in a vacuum and in liquid, using the same piezo.

Appendix E: Simulations - COMSOL

E.1. Introduction

COMSOL was used to simulate the mechanical behaviour of the cantilever but also to characterize the flow through the channel of the device. The simulations of the mechanical behaviour were used to verify that the design met all the requirements and, in the experimental phase, to compare the data with the simulations. The flow simulations were performed to ensure that no strange flow phenomena occurred.

E.2. COMSOL for mechanical characterization

A finite volume model (FVM) was used to simulate the mechanical behaviour of the cantilever. The Solidworks design part was imported into COMSOL and the material properties of IP-Dip were added to the geometry ($E = 4.5 \cdot 10^9 \text{ Pa}$, $\nu = 0.3$ and $\rho = 1170 \text{ kg/m}^3$). A linear elastic model was used to solve the FVM equations. The boundary conditions are shown in figure E.2.1.

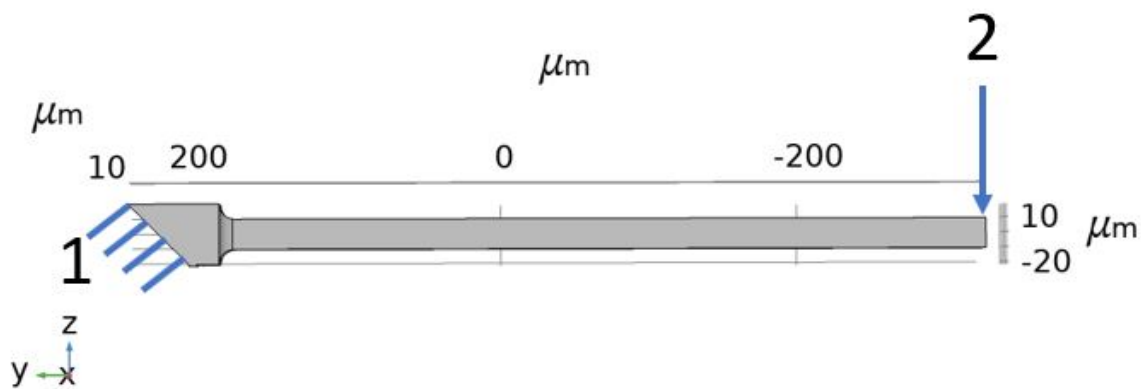


Figure E.2.1: Boundary conditions for cantilever simulation. 1 = Fixed end of the cantilever (zero displacement), 2 = Force of 60nN on the cantilever (set to zero for resonant frequency simulations).

For the deflection simulations, a force of 60 nN was applied to the free end of the cantilever to simulate the forces that would occur during the cell experiments. The resulting deflection can be used to calculate the stiffness of the cantilever.

To perform the simulations, a mesh had to be generated for the cantilever. A tetrahedral mesh was created with the default extra-fine physics-based settings. The mesh can be seen in figure E.2.2.

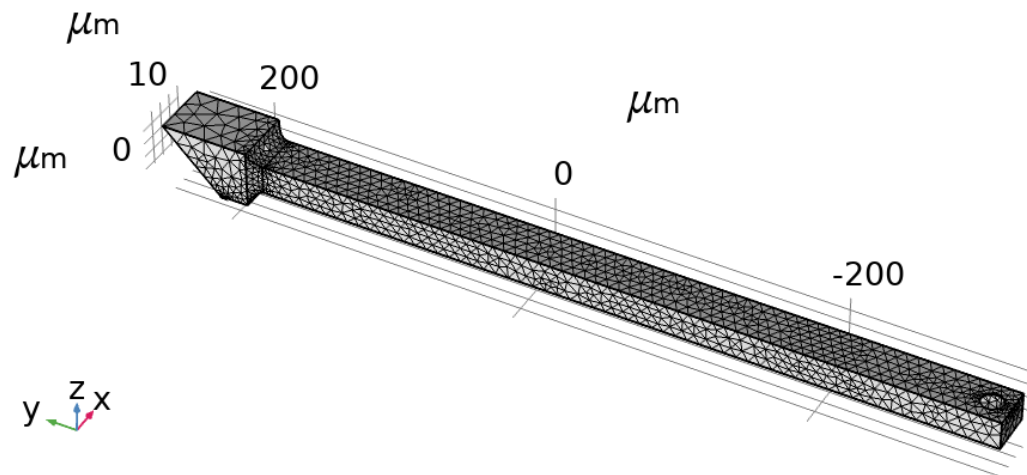


Figure E.2.2: Tetrahedral mesh of the cantilever in COMSOL

With the force at the free end of the cantilever set to -60 nN in the Z-direction, the deflection could be simulated. Figure E.2.3 shows the result of this simulation. Based on the deflection and the force, the stiffness of the cantilever can be calculated.

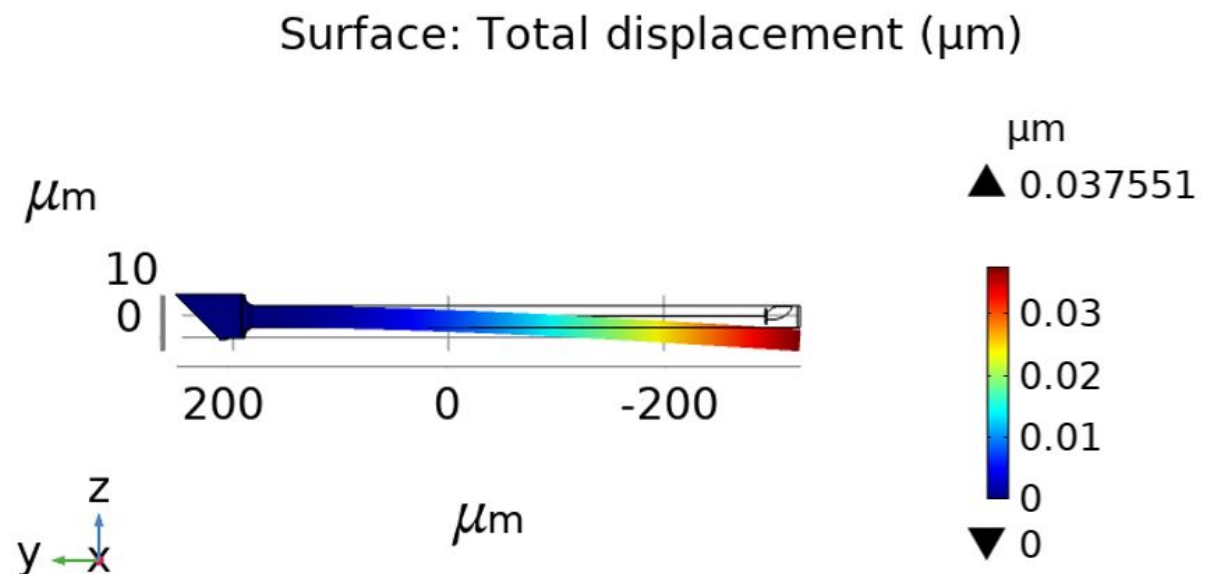


Figure E.2.3: Simulation of deflection of the cantilever with a force of -60nN in the Z-direction

The stiffness of the cantilever can be calculated using $k = F/\delta$, (where k is the stiffness, F is the force and δ is the deflection), resulting in a stiffness of 1.62 N/m. With the force at the tip set to zero, the natural frequencies of the cantilever were determined. Note that only modes in the vertical direction (z) were taken into account, as only these were measured in the experiments and are of interest. The first four modes can be seen in the figure E.2.4 to E.2.7.

Eigenfrequency=28707 Hz Surface: Total displacement (μm)

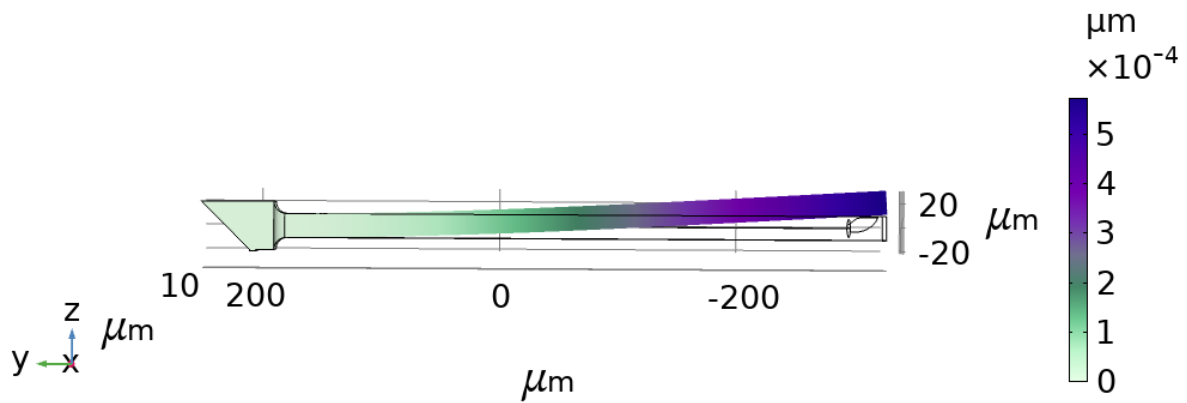


Figure E.2.4: Simulation of the first mode of the cantilever

Eigenfrequency=1.7815E5 Hz Surface: Total displacement (μm)

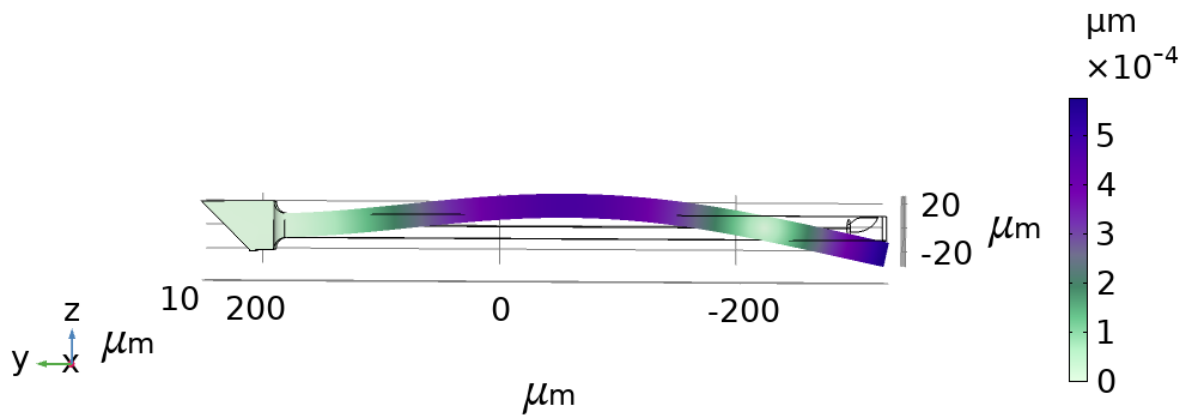


Figure E.2.5: Simulation of the second mode of the cantilever

Eigenfrequency=4.8755E5 Hz Surface: Total displacement (μm)

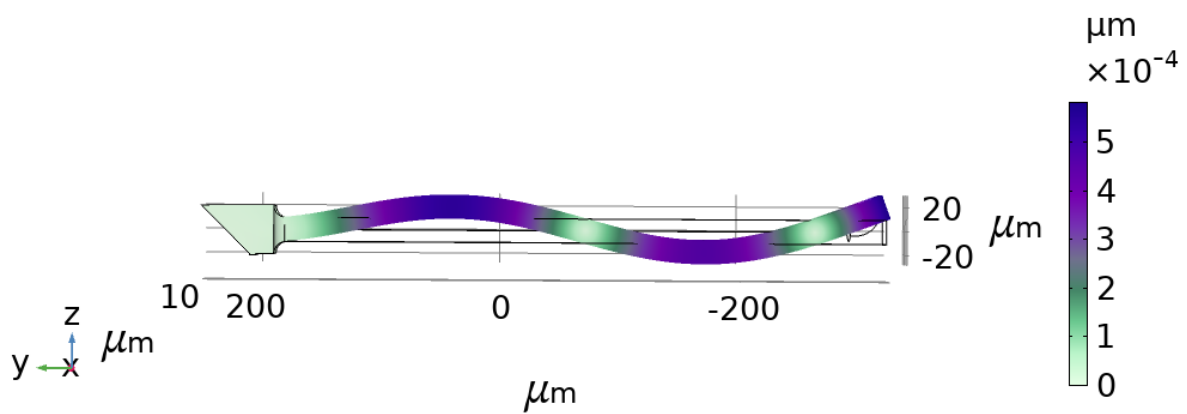


Figure E.2.6: Simulation of the third mode of the cantilever

Eigenfrequency=9.1438E5 Hz Surface: Total displacement (μm)

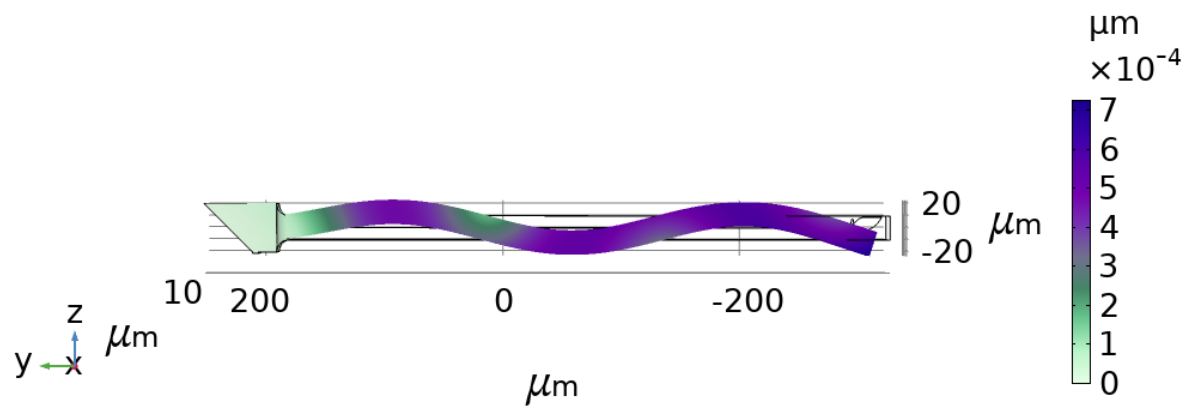


Figure E.2.7: Simulation of the fourth mode of the cantilever

The convergence plot for the resonant frequency simulations can be seen in figure E.2.8.

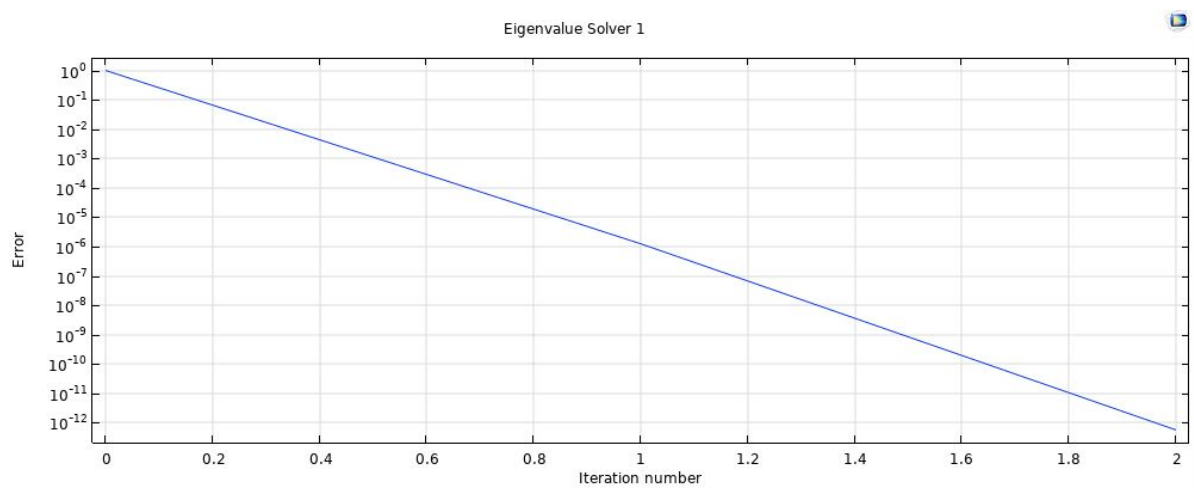


Figure E.2.8: Convergence plot of the COMSOL cantilever simulation

E.3. COMSOL for fluidic characterisation

COMSOL simulations can be used to characterize the flow. These simulations can provide information on flow velocity and pressure throughout the channel. In this section, the COMSOL simulations are discussed. These simulations have only been used to get a general idea of the flow characteristics.

E.3.1. Laminar flow justification

To verify that the laminar assumption is valid, the Reynolds number was calculated. The Reynolds number is defined as [29]:

$$Re = \frac{\rho u d_h}{\mu} \quad (\text{E.21})$$

with ρ the density of the fluid, u the velocity of the fluid, d_h the hydraulic diameter of the channel and μ the dynamic viscosity of the fluid.

For water, the following parameters were used:

- $\rho = 1000 \text{ kg/m}^3$
- $\mu = 10^{-3} \text{ Ns/m}^2$

The hydraulic diameter of the channel through the cantilever was calculated using [29]:

$$d_h = \left| \frac{4wh(64 - 16e^2)}{(w + h)(64 - 3e^4)} \right| \quad (\text{E.22})$$

$$e = \frac{w - h}{w + h}$$

with w the width of the ellipse and h the height of the ellipse. This results in a hydrodynamic diameter of $d_h = 2.027 \cdot 10^{-4}$.

To estimate the velocity in the channel, a laminar simulation was performed. Laminar flows always result in a higher velocity compared to turbulent flows because less viscous dissipation occurs. In the laminar flow simulation, the maximum velocity in the channel was determined to be 0.59 m/s. Using equation E.21 and the above parameters, the Reynolds number is calculated to be: $Re = 119$.

According to Rands et al. [30], the flow in microchannels transitions from laminar to turbulent at Reynolds numbers in the range of 2100-2500. This means that the flow can be assumed laminar.

E.3.2. Flow simulations

For the simulations, the channel was extracted as a separate part from the model CAD. Figure E.3.9 shows the channel model. The walls of the channel were also defined as walls for the boundaries of the simulation. An inlet was defined in COMSOL at the location marked with the "1" in Figure E.3.9. A pressure of 1000mbar was applied to this inlet. At the outlet (marked by the "2") the pressure was set to 0. This mimics the dispensing part of the experiments.

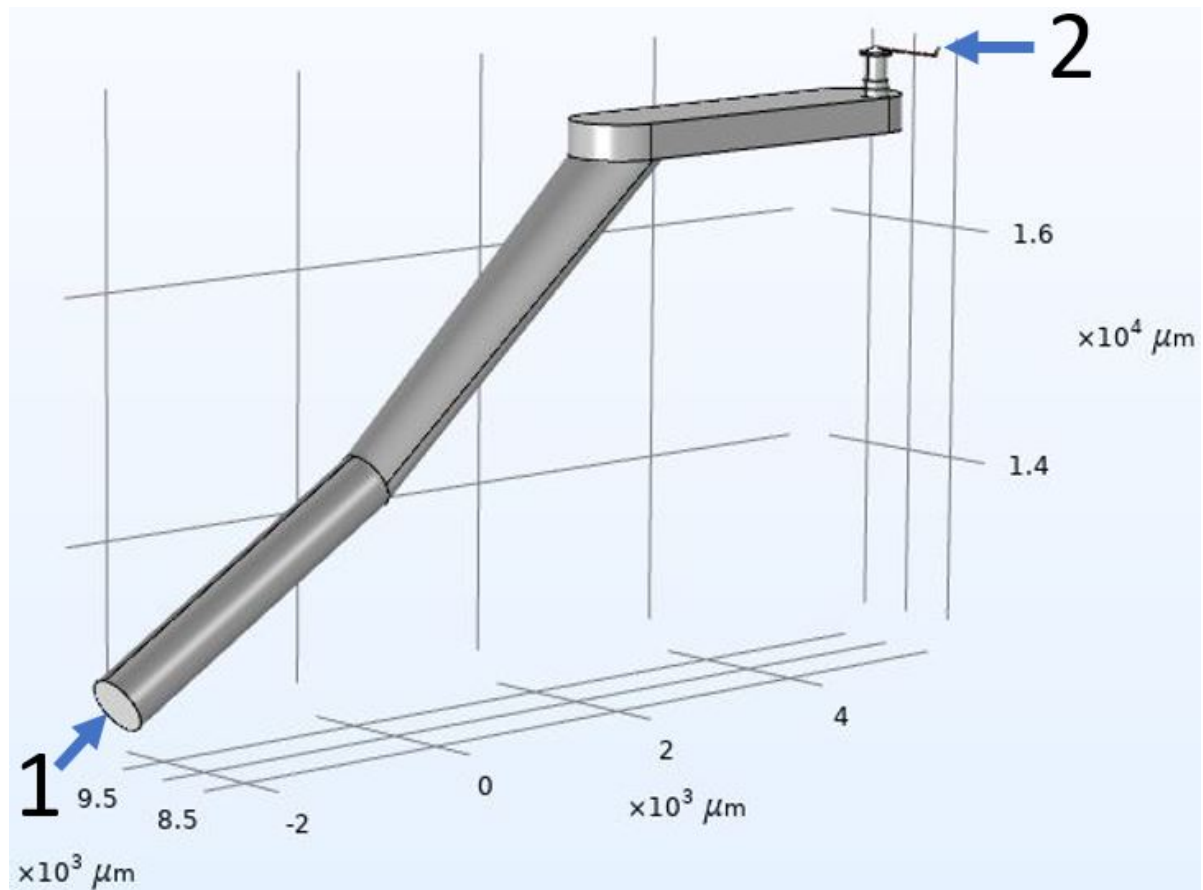


Figure E.3.9: Channel for the COMSOL simulation 1 indicates the inlet of the channel and 2 indicates the outlet (at the aperture of the tip of the cantilever).

The channel was meshed with an extra-fine physics-based tetrahedral mesh with a minimum mesh size of $1\ \mu\text{m}$, a maximum mesh size of $300\ \mu\text{m}$ and a maximum element growth rate of 1.3 (see figure E.3.10). The COMSOL standard properties of liquid water were applied to the geometry.

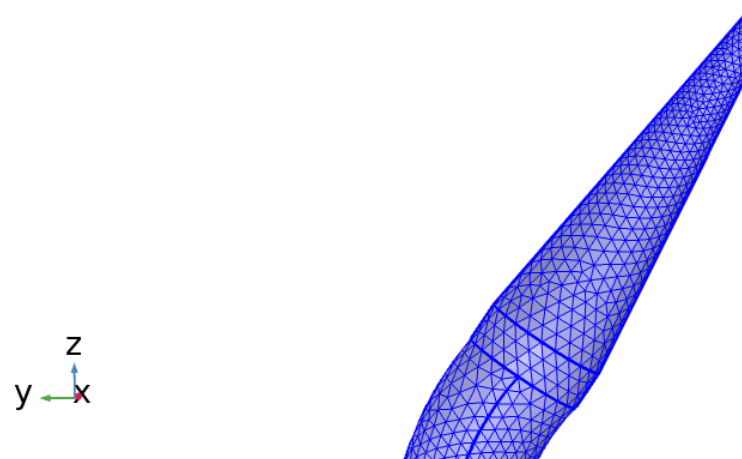


Figure E.3.10: Tetrahedral mesh of the channel in the tip

The simulation of the flow took approximately 20 minutes to converge. The resulting convergence plot is shown in figure E.3.11 and E.3.12. The convergence plots show the error estimate as a function of the iteration number for the iterative linear system solver (GMRES) and for the nonlinear solver as well as for the iterative linear system solver.

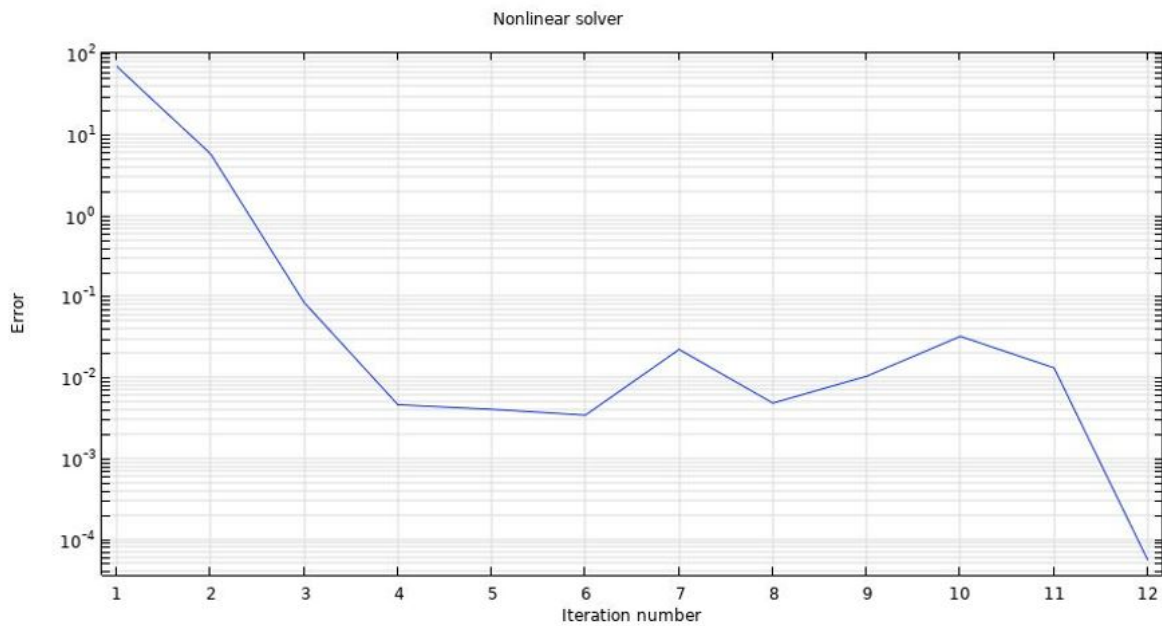


Figure E.3.11: Convergence plot of the flow simulation in COMSOL for the nonlinear solver

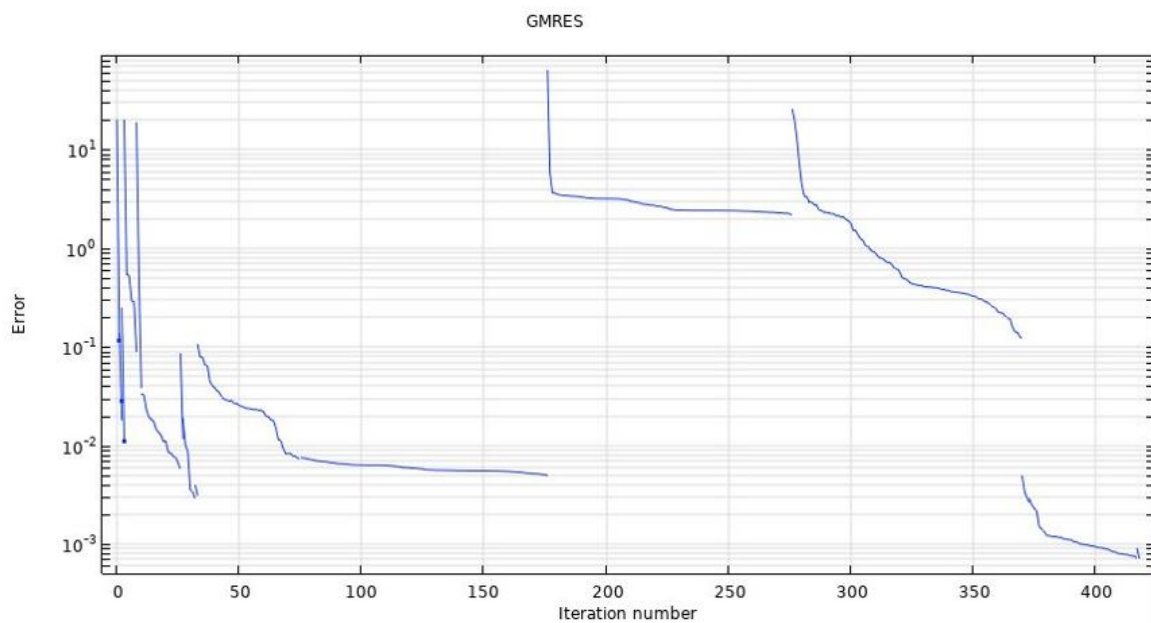


Figure E.3.12: Convergence plot of the COMSOL simulation for the Generalized minimal residual method (GMRES) solver. GMRES is an iterative linear system solver, thus uses an initial value to generate a sequence of constantly improving approximations of the solutions.

The convergence plots show that the solution of the simulations are valid. Figure E.3.13 and E.3.15 show the velocity profiles of the simulations throughout the channel.

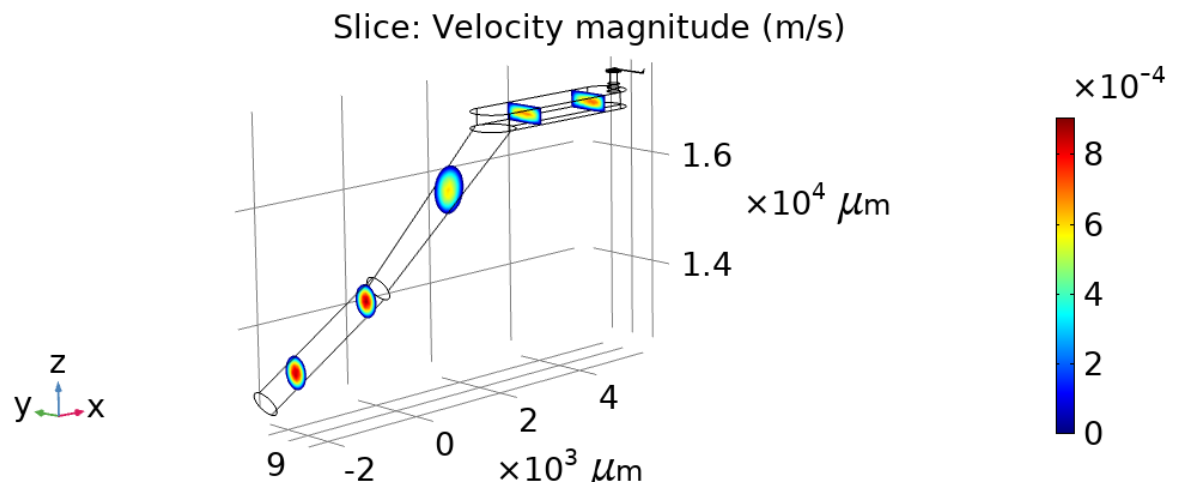


Figure E.3.13: COMSOL velocity simulation plot (laminar flow model)

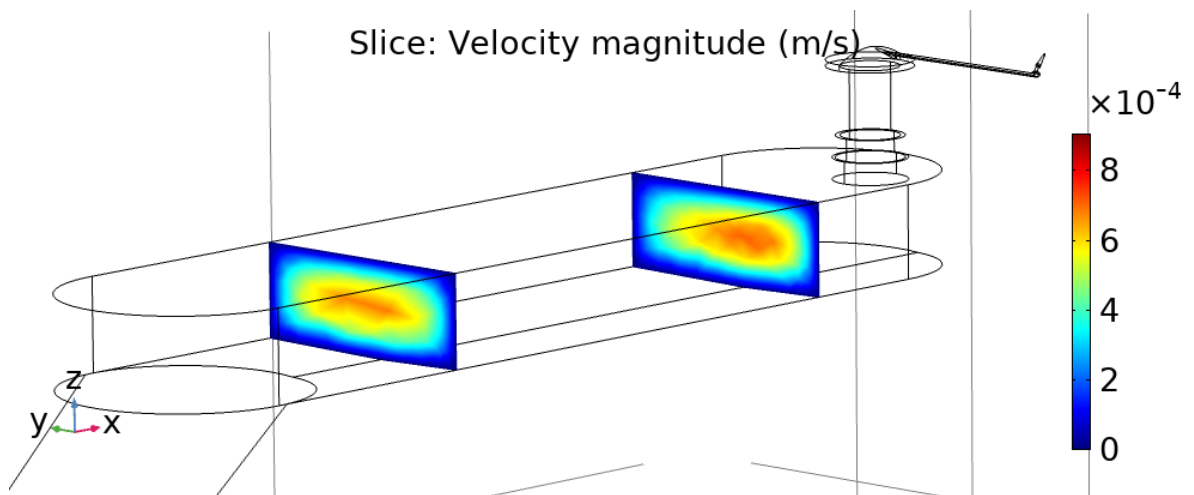


Figure E.3.14: COMSOL velocity simulation plot (laminar flow model) in the rectangular channel of the DLP print

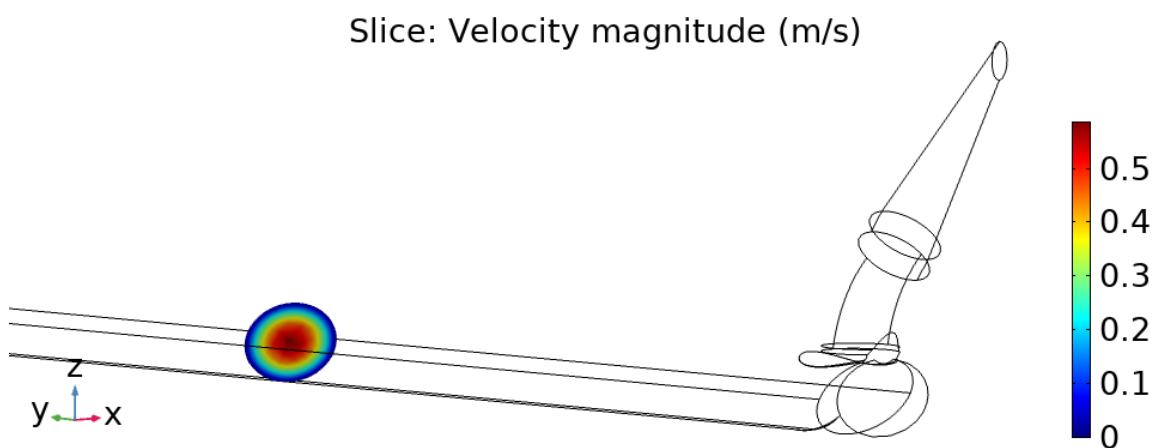


Figure E.3.15: COMSOL velocity simulation plot in the channel of the cantilever (laminar flow model).

The pressure contours only have significant changes in the channel of the cantilever and the tip, the pressure barely changes in the channel of the DLP print. The pressure contours are shown in figure E.3.16 and E.3.17.

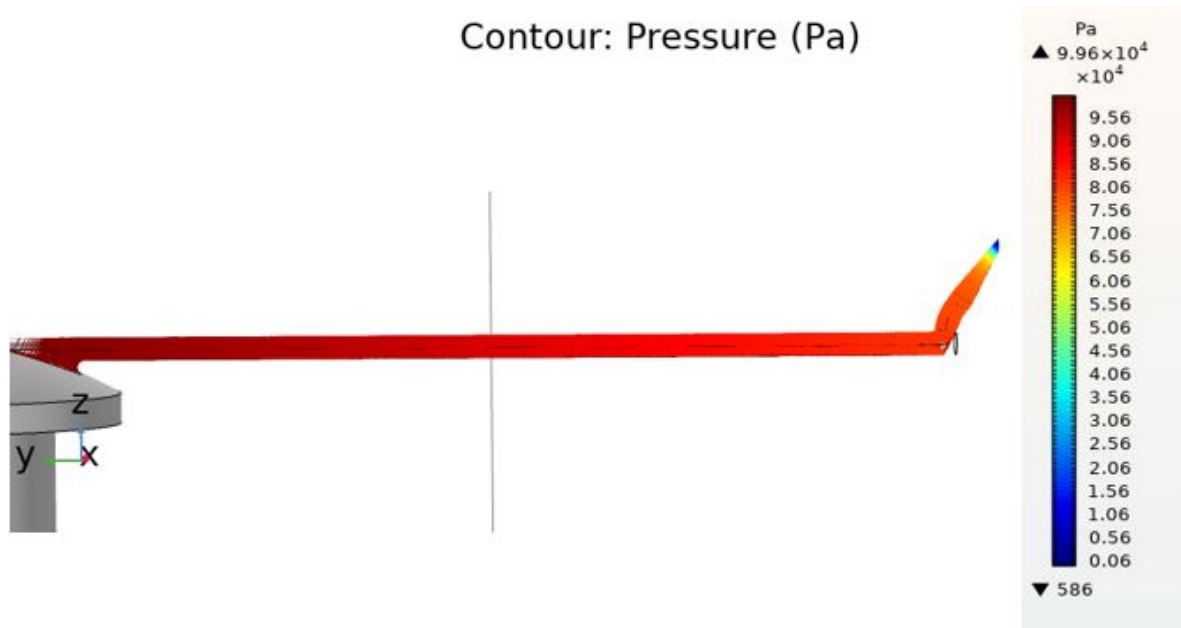


Figure E.3.16: COMSOL simulation of pressure contours of the cantilever channel (laminar flow model).

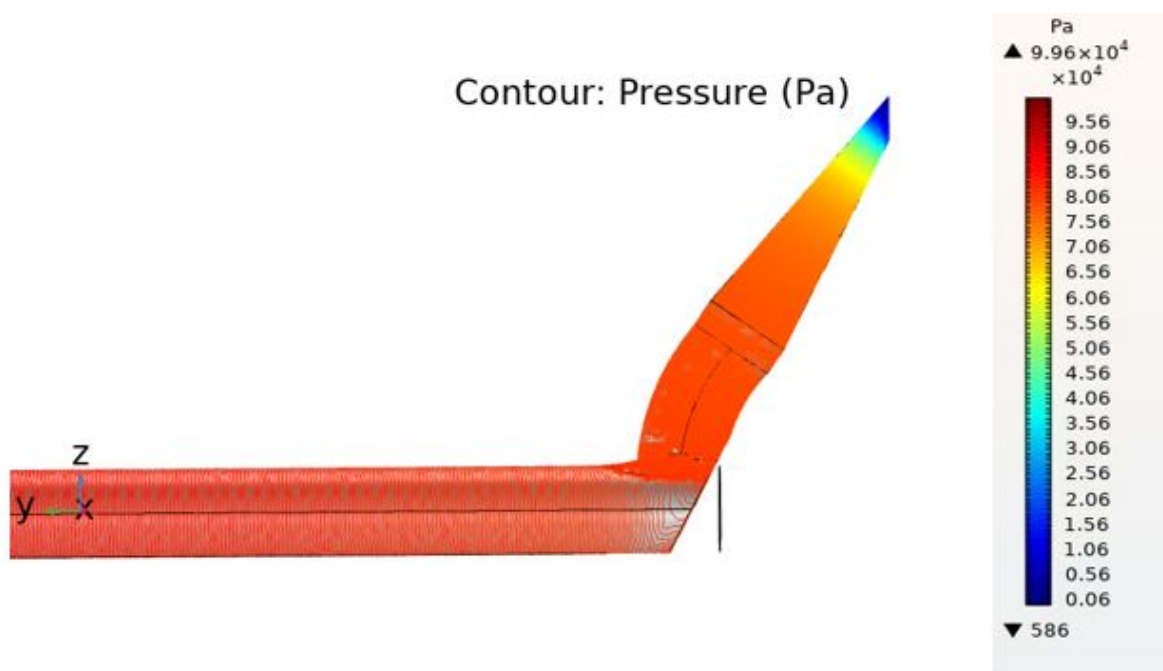


Figure E.3.17: COMSOL simulation of pressure contours of the tip channel (laminar flow model).

Figure E.3.16 shows that the pressure at the base of the cantilever is approximately equal to the pressure at the inlet. Therefore, the pressure drop in the channel of the DLP print is negligible. Figure E.3.17 shows that the most significant pressure drop is caused by the converging channel (as one would expect). However, it is difficult to determine the exact resulting pressure at the tip aperture. According to the simulations, the pressure drop is approximately in the range of 80-95 kPa, which is not comparable to the 600 mBar found in the flow experiments (pressure at which the first drops were observed at the aperture). The simulations did not converge when applying a 600mbar pressure at the inlet, meaning there would be no flow possible. These results indicate that the real

pressure drop is smaller compared to the simulations. For the new research, simulations should be performed that focus more on the tip and the aperture region. This could include flow from the aperture and aspiration of a flexible sphere (mimicking a nucleus). However, this was outside the scope of this research.

The simulations confirm that the flow is relatively stable, and no strange phenomena seem to occur.

E.4. Comparison simulations and Polytec experiment

A few aspects were not modelled in the COMSOL simulation but did influence the LDV (Polytec) experiment (e.g. tape and DLP substrate deformations). However, comparing the data from the experiments on the LDV with the COMSOL simulations, there are three frequencies that match the frequencies found in COMSOL. Some higher frequencies that match the simulations could also be seen in the experimental data (e.g. 250kHz) but were not included in the comparison as the experimental data was too limited.

Figure E.4.18 shows the frequency plot and the corresponding natural frequencies from the simulations. Note that the natural frequency at 41kHz is an in-plane motion. Polytec is only able to measure out-of-plane motions only. It is suspected that because the cantilever is mounted on carbon tape, it is not completely flat (the top surface of the cantilever is not perpendicular to the Z-axis that Polytec measures). This leads to more modes appearing in the experiments than one would expect (in summary: it is suspected that the cantilever's tilt shows natural frequencies in other directions).

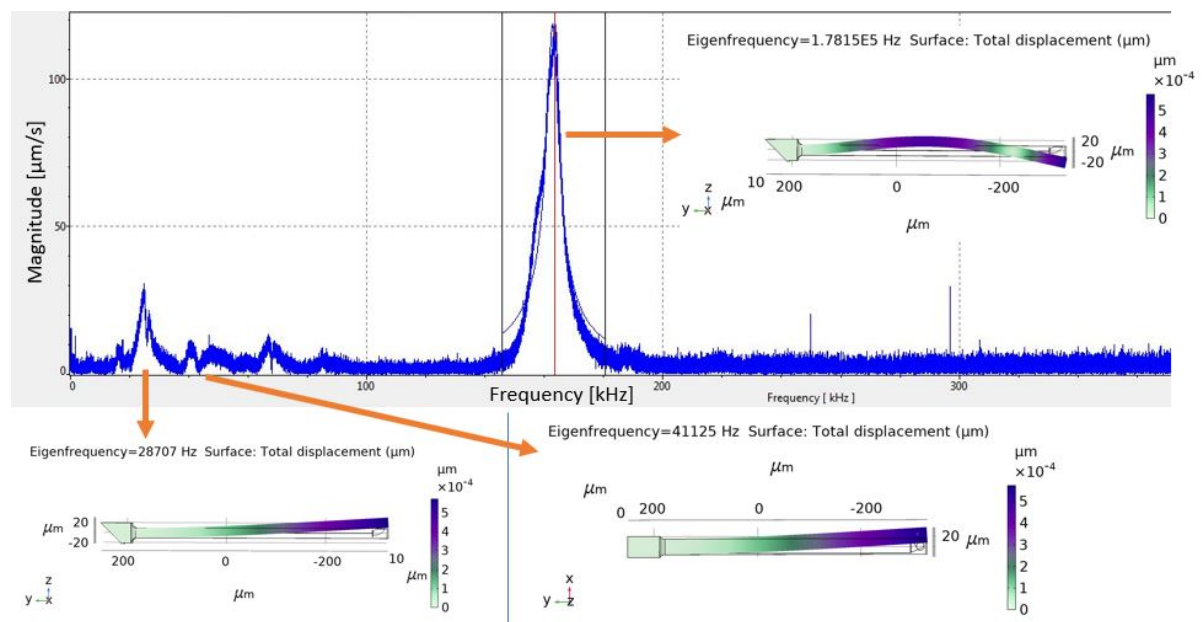


Figure E.4.18: Comparison between the simulations (COMSOL) and the experimental data (POLYTEC). Frequency plot found during experiments with matching simulation results. Important is to note that the 41kHz simulation is in plane and not out of plane.

The data of the modes, at 25kHz and 165kHz, were imported into the Polytec data processing software and are comparable to the COMSOL simulations. Figure E.4.19 and E.4.20 show the processed data of the modes at 25kHz and 165kHz respectively.

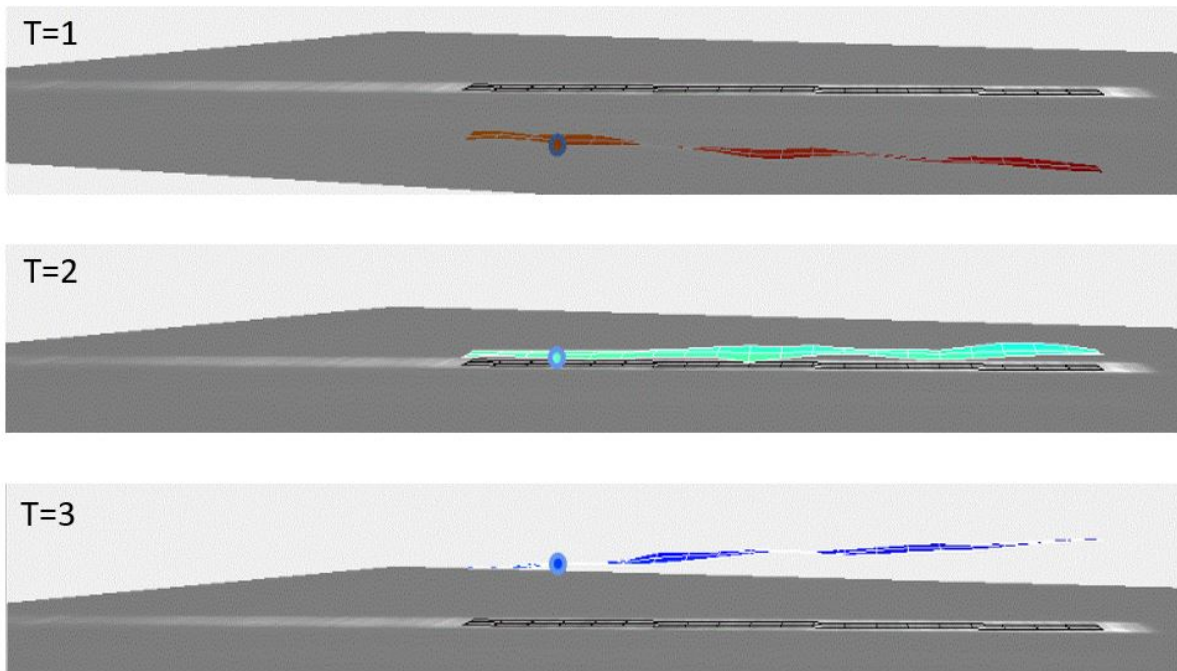


Figure E.4.19: Simulated cantilever using Polytec data at 25kHz. Images at three different positions of the cantilever during one cycle of the mode. Note: the base of the cantilever is far to the left of the image

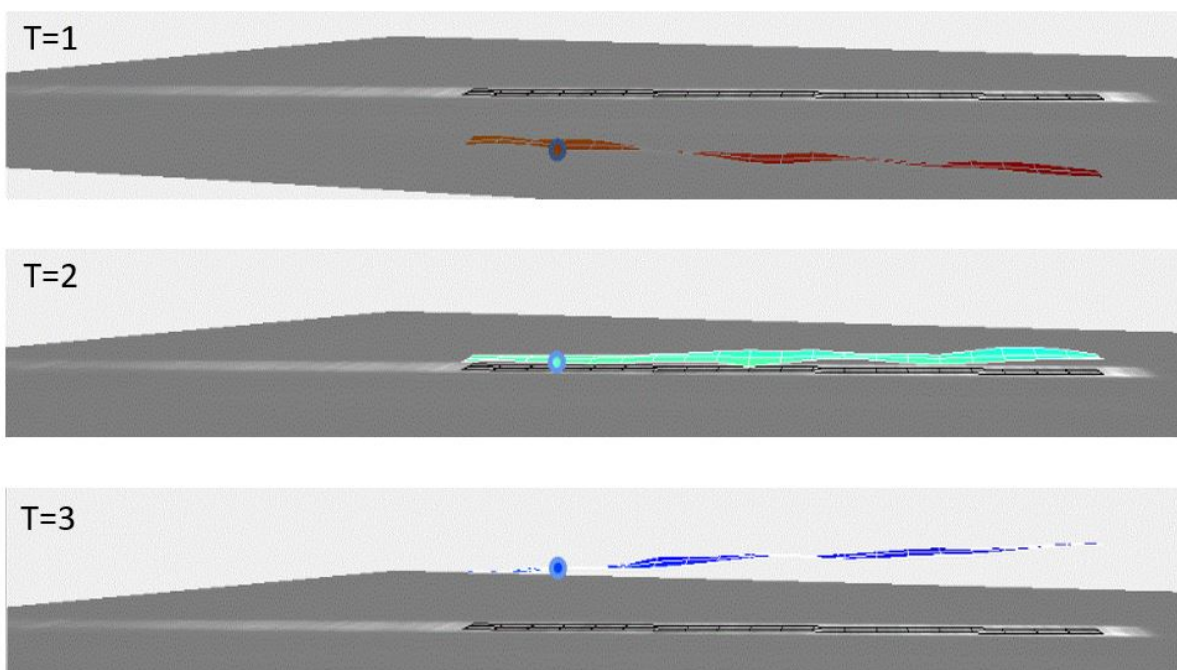


Figure E.4.20: Simulated cantilever using Polytec data at 165kHz. Images at three different positions of the cantilever during one cycle of the mode. Note: the base of the cantilever is far to the left of the image

E.5. Influence of gold on the stiffness measurement

An aspect that was not taken into account for the simulations is the gold layer on the back of the cantilever. The following equations can be used to determine the influence on the resonant frequency and the stiffness of the cantilever [26]:

$$\frac{\omega_1}{\omega_0} \cong \sqrt{\frac{1}{1 + (\rho_{Au}/\rho_{Cant}) (h_{Au}/h_{Cant})}} \quad (E.23)$$

where ω_1 is the resonance frequency of the gold coated cantilever, ω_0 the resonance frequency of the uncoated cantilever, ρ_{Au} and h_{Au} the density and height of the gold layer respectively and ρ_{cant} and h_{cant} the density and height of the cantilever respectively.

$$k_1 = k_0 \left(\frac{h_{Au} + h_{Cant}}{h_{Cant}} \right)^3 \frac{E_e}{E_{Cant}} \quad (E.24)$$

where k_1 and k_0 are the spring constants of the coated cantilever and uncoated cantilever respectively, E_{cant} the Young's modulus of the cantilever and E_e as defined in equation E.25.

$$E_e = \frac{E_{Au}h_{Au} + E_{Cant}h_{Cant}}{h_{Au} + h_{Cant}} \quad (E.25)$$

where E_{Au} is the Young's modulus of the gold.

For a gold coating with a thickness of 100 nm, this would result in an increase in stiffness from 1.6 to 1.75 N/m (factor 1.0953) and the resonant frequency would decrease by approximately 4%. The gold coating was more than twice as thick on the cantilevers used on the JPK (to get a proper signal) compared to the Polytec experiments, which might explain the large stiffness range in the measurements. The influence of the gold layer should be investigated further. If a silicon nitride probe was used instead of a polymer probe, the stiffness would only increase to 1.62 (factor 1.0123). The influence of the gold layer on the cantilever stiffness is thus much more significant for polymeric probes. The material properties for gold were taken from Sader et al. [26] ($E_{Au} = 78 \text{ GPa}$, $\rho_{Au} = 18800 \text{ kg/m}^3$).

E.6. Recommendations

In the future, the DLP print, the dome and the tip, should be included in the mechanical behaviour simulation. These can influence the resonant frequencies and damping. For the fluid simulations, more cases should be studied. It would be of great value if a simulation could be setup (in 2D) that simulates the aspiration of a flexible ball (nucleus like properties) and optimize the tip with that data.

Bibliography

- [1] P.J.E.M. Van Der Linden, A.M. Popov, and D. Pontoni. Accurate and rapid 3D printing of microfluidic devices using wavelength selection on a DLP printer. *Lab on a Chip*, 20(22):4128–4140, 2020.
- [2] G.L. Roth, S. Rung, C Esen, and R. Hellmann. Microchannels inside bulk pmma generated by femtosecond laser using adaptive beam shaping. *Opt. Express*, 28(4):5801–5811, Feb 2020.
- [3] Sigma-aldrich. Sigmacote siliconizing reagent for glass and other surfaces: Sigma-aldrich. <https://www.sigmaaldrich.com/NL/en/product/sigma/sl2>, 2021.
- [4] K. Yum, N. Wang, and M.F. Yu. Nanoneedle: A multifunctional tool for biological studies in living cells. *Nanoscale*, 2(3):363–372, 2010.
- [5] H. Plank, R. Winkler, C.H. Schwalb, J. Hütner, J.D. Fowlkes, P.D. Rack, I. Utke, and M. Huth. Focused electron beam-based 3d nanoprinting for scanning probe microscopy: A review. *Micromachines*, 11(1), 2020.
- [6] J.D. Adams, B.W. Erickson, J. Grossenbacher, J. Brugger, A. Nievergelt, and G.E. Fantner. Harnessing the damping properties of materials for high-speed atomic force microscopy. *Nature Nanotechnology*, 11(2):147–151, 2016.
- [7] Y. Wang, H. Wang, and S. Bi. Real time drift measurement for colloidal probe atomic force microscope: a visual sensing approach. *AIP Advances*, 4(5):057130, 2014.
- [8] J. C. Bruusgaard, K. Liestøl, M. Ekmark, K. Kollstad, and K. Gundersen. Number and spatial distribution of nuclei in the muscle fibres of normal mice studied in vivo. *Journal of Physiology*, 551(2):467–478, 2003.
- [9] R.C. L. N. Kramer, E. J. Verlinden, L. Angeloni, A. van den Heuvel, L. E. Fratila-Apachitei, Si. M. van der Maarel, and M.K. Ghatkesar. Multiscale 3D-printing of microfluidic AFM cantilevers. *Lab on a Chip*, pages 311–319, 2020.
- [10] ADMAT. 3DM Tough Clear. <https://www.3dm-shop.com/product-page/3DM-TOUGH>, 2021.
- [11] B. Steyrer, B Buseti, G. Harakály, R. Liska, and J. Stampfl. Hot lithography vs. room temperature dlp 3d-printing of a dimethacrylate. *Additive Manufacturing*, 21:209–214, 2018.
- [12] J.T. Fourkas. Chapter 1.3 - fundamentals of two-photon fabrication. In Tommaso Baldacchini, editor, *Three-Dimensional Microfabrication Using Two-photon Polymerization*, Micro and Nano Technologies, pages 45–61. William Andrew Publishing, Oxford, 2016.
- [13] J. Campbell, N. Petta, O. Stein, Y. Liu, Y. Lu, and L. J. Jiang. Three-dimensional printing and deformation behavior of low-density target structures by two-photon polymerization. page 66, 08 2017.
- [14] E. D. Lemma, F. Rizzi, T. Dattoma, B. Spagnolo, L. Sileo, A. Quattieri, M. De Vittorio, and F. Pisanello. Mechanical properties tunability of three-dimensional polymeric structures in two-photon lithography. *IEEE Transactions on Nanotechnology*, 16(1):23–31, 2017.
- [15] Y. Liu, J.H. Campbell, O. Stein, L. Jiang, J. Hund, and Y. Lu. Deformation behavior of foam laser targets fabricated by two-photon polymerization. *Nanomaterials*, 8(7):1–20, 2018.
- [16] Nanoscribe GmbH & Co. KG. Nanoguide - applications overview. <https://support.nanoscribe.com/hc/en-gb/articles/360003162893-Applications-Overview>, 2021.
- [17] T.Q. Qiu and C.L. Tien. Femtosecond laser heating of multi-layer metals—i. analysis. *International Journal of Heat and Mass Transfer*, 37(17):2789–2797, 1994.
- [18] V. Rai and A. Srivastava. Correlation between optical and morphological properties of nanostructured gold thin film. *JSM Nanotechnology & Nanomedicine*, 4, 09 2016.
- [19] F. Widdascheck, M. Kothe, A.A. Hauke, and G. Witte. The effect of oxygen plasma treatment of gold electrodes on the molecular orientation of cupc films. *Applied Surface Science*, 507:145039, 2020.

- [20] Cytosurge. Fluidfm nanosyringe stiffness. <https://www.cytosurge.com/shop/product/fluidfm-nanosyringe-855?category=1#attr=84>, 2020.
- [21] J.X.J. Zhang and K. Hoshino. Chapter 6 - mechanical transducers: Cantilevers, acoustic wave sensors, and thermal sensors. In J.X.J. Zhang and K. Hoshino, editors, *Molecular Sensors and Nanodevices (Second Edition)*, Micro and Nano Technologies, pages 311–412. Academic Press, second edition edition, 2019.
- [22] B. Hansen. D.A. henderson and the who smallpox eradication campaign of 1966–1979. <https://nyamcenterforhistory.org/2016/09/15/d-a-henderson-and-the-who-smallpox-eradication-campaign-of-1966-1979/>, Sep 2016.
- [23] J.E. Sader, J.W.M. Chon, and P. Mulvaney. Calibration of rectangular atomic force microscope cantilevers. *Review of Scientific Instruments*, 70(10):3967–3969, 1999.
- [24] R. Proksch, T. E. Schäffer, J. P. Cleveland, R. C. Callahan, and M. B. Viani. Finite optical spot size and position corrections in thermal spring constant calibration. *Nanotechnology*, 15(9):1344–1350, 2004.
- [25] T.F.D. Fernandes, O. Saavedra, E. Margeat, P.E. Milhiet, and L. Costa. Synchronous, Crosstalk-free Correlative AFM and Confocal Microscopies/Spectroscopies. *Scientific Reports*, 10(1):1–12, 2020.
- [26] J.E. Sader, I. Larson, P. Mulvaney, and L.R. White. Method for the calibration of atomic force microscope cantilevers. *Review of Scientific Instruments*, 66(7):3789–3798, 1995.
- [27] K.P. McCreery, X. Xu, A.K. Scott, A.K. Fajrial, S. Calve, X. Ding, and C.P. Neu. Nuclear Stiffness Decreases with Disruption of the Extracellular Matrix in Living Tissues. *Small*, 17(6):1–11, 2021.
- [28] J.M.L. Miller, A. Ansari, D.B. Heinz, Y. Chen, I.B. Flader, D.D. Shin, L. Guillermo Villanueva, and T.W. Kenny. Effective quality factor tuning mechanisms in micromechanical resonators. *Applied Physics Reviews*, 5(4):041307, 2018.
- [29] A.F. Mills and C.F.M Coimbra. *Basic heat and mass transfer*. Temporal Publishing, 2015. ISBN: 9780996305303.
- [30] C. Rands, B. W. Webb, and D. Maynes. Characterization of transition to turbulence in microchannels. *International Journal of Heat and Mass Transfer*, 49:2924–2930, 2006.